

A theoretical study of meson transition form factors

Dissertation
zur Erlangung des Grades
„Doktor der Naturwissenschaften“

am Fachbereich Physik, Mathematik und Informatik
der Johannes Gutenberg-Universität Mainz



JOHANNES GUTENBERG
UNIVERSITÄT MAINZ

Pablo Sanchez-Puertas
geboren in Granada (Spanien)

Mainz, 2016

Abstract

This thesis studies the lightest pseudoscalar mesons, π^0 , η , and η' , through their transition form factors. Describing the underlying structure of hadrons is still a challenging problem in theoretical physics. These form factors, which can be experimentally measured, provide valuable information on the pseudoscalar meson inner structure and are of fundamental interest for describing their elementary interactions. Obtaining a precise description for these form factors has become a pressing subject given their role in one of the finest tests of our understanding of particle physics: the anomalous magnetic moment of the muon. The foreseen experimental precision for this observable challenges the available theoretical descriptions so far.

Still, incorporating the available experimental information into a theoretical framework becomes increasingly difficult as the experimental precision improves, challenging simplified frameworks. In this work, we propose to use the framework of Padé theory in order to precisely describe these form factors in the space-like region, which provides a well-founded mathematically-based and data-driven approach for this task.

The first part of our study is devoted to extract the parameters relevant to our approach using the available single-virtual space-like data. The accuracy of the method, beyond that of previous approaches, has been latter confirmed in experiments performed in the low-energy time-like region for the η and η' cases. To give consideration to these new results, we incorporated the corresponding data into our analysis. The extension of the formalism to the most general double-virtual case is subsequently discussed, which requires the introduction, for the first time in this context, of Canterbury approximants, the bivariate version of Padé approximants.

As a direct application of our results, the $\eta - \eta'$ mixing parameters have been extracted from the single-virtual transition form factors. The employed method provides an alternative to the traditional ones, obtaining competitive results while minimizing modeling errors.

Besides, our double-virtual description is employed for describing the rare decays of the pseudoscalar mesons into a lepton pair. The latter process offers an opportunity to test the doubly virtual pseudoscalar mesons transition form factors as well as an opportunity to discuss possible new physics contributions in light of the present discrepancies.

Finally, our approach is used to obtain a precise calculation for the pseudoscalar-pole contribution to the hadronic light-by-light piece of the anomalous magnetic moment of the muon. This includes, for the first time, a systematic error and meets the required precision in foreseen experiments.

Zusammenfassung

Die vorliegende Dissertation befasst sich mit dem Studium der leichtesten pseudoskalaren Mesonen π^0 , η , and η' via deren Übergangsformfaktoren. Eine Beschreibung der zugrunde liegenden Struktur der Hadronen stellt in der theoretischen Physik immer noch eine Herausforderung dar. Diese Formfaktoren, die experimentell bestimmt werden können, stellen eine wichtige Informationsquelle über die innere Struktur pseudoskalarer Mesonen dar und sind von grundlegendem Interesse für die Beschreibung ihrer elementaren Wechselwirkungen. Der Erhalt einer präzisen Beschreibung für diese Formfaktoren ist, mit Blick auf ihre Rolle in einem der genauesten Tests unseres Verständnisses der Teilchenphysik: dem anomalen magnetischen Moment des Myons, zu einem dringlichen Thema geworden.

Die Einarbeitung der verfügbaren, experimentell ermittelten, Informationen in einen theoretischen Rahmen wird nach wie vor mit zunehmender Genauigkeit der Experimente schwieriger, was vereinfachte Modelle auf die Probe stellt. Im Rahmen dieser Arbeit schlagen wir vor, sich der Padé-Approximation, ein sowohl mathematisch als auch auf Daten basierender und somit wohlgegründeter Zugang zu diesem Problem ist, zu bedienen, um diese Formfaktoren in raumartigen Bereichen präzise beschreiben zu können.

Im ersten Teil unserer Betrachtungen widmen wir uns unter Ausnutzung von Messwerten raumartiger Prozesse mit einem virtuellen Photon, der Extraktion der für unseren Zugang relevanten Parameter. Die Genauigkeit dieser Methode, die über bisherige Versuche hinausgeht, wurde später durch Experimente die im raumartigen Niedrigenergiesektor für die Fälle von η und η' durchgeführt wurden, bestätigt. In der Folge wird die Ausweitung des Formalismus auf den allgemeinsten Fall zweier virtueller Photonen diskutiert, was die in diesem Kontext erstmalige Einführung der Canterbury-Approximation, der zweidimensionalen Padé-Approximation, erfordert.

Als eine direkte Anwendung unserer Ergebnisse, wurden die Parameter der Mischung $\eta - \eta'$ aus dem Übergangsformfaktor eines virtuellen Photons ermittelt. Die verwendete Methode bietet eine Alternative zu traditionell verwendeten, wobei wir konkurrenzfähige Ergebnisse erhalten und zugleich modellbezogene Fehler minimieren.

Zudem wird unsere Beschreibung von Prozessen mit zwei virtuellen Photonen auf die Beschreibung der seltenen Zerfälle eines pseudoskalaren Mesons in ein Leptonen-Paar angewendet. Der genannte Prozess bietet die Gelegenheit die Übergangsformfaktoren pseudoskalarer Mesonen für zwei virtuelle Photonen zu testen.

Schlussendlich wird unsere Vorgehensweise dazu verwendet, eine genaue Berechnung für den Beitrag des pseudoskalaren Pols zum Anteil der hadronischen Licht-Licht-Streuung des anomalen magnetischen Moments des Myons zu erhalten. In dieser mitinbegriffen ist erstmalig ein systematischer Fehler und sie entspricht der für Experimente geforderten, benötigten Genauigkeit.

Acknowledgements

I would like to express my gratitude to Pere Masjuan for his guidance during these four years of doctoral studies. His door was always open when looking for help and I have profited from his knowledge in physics in countless and interesting discussions. This work would not have been possible without his guidance and great enthusiasm. The realization of this thesis would have not been possible either without the help of Marc Vanderhaeghen, to whom I thank for his support, reading and interesting comments concerning this manuscript.

During my time at Mainz, I could profit as well from the help and comments from many people at the Nuclear Physics department; a very special thanks goes to Tobias Beranek, Mikhail Gorchtein, Nikolay Kivel and Oleksandr Tomalak, for many and valuable discussions and for sharing their wisdom with me. Besides, I am particularly indebted to my office mates, Patricia Bickert and Nico Klein for the hours stolen in trying to understand the basic concepts of chiral perturbation theory and to Hans Christian Lange for helping with the German translation. In addition, and besides Mainz, I was lucky to have a pleasant collaboration with R. Escribano, without whom one chapter of this thesis could not have been possible, and his PhD student Sergi Gonzalez-Solís, whom which I was luck to share my office and many discussions.

Finally, the greatest acknowledgement goes to my wife, for her support, love and encouragment, and for reading this manuscript since the early times.

Contents

Preface	xi	
1	Quantum Chromodynamics and related concepts	1
1.1	Introduction	1
1.2	Quantum Chromodynamics	2
1.3	Low energy QCD: χ PT	3
1.4	Closing the gap: large- N_c QCD	10
1.5	Padé approximants	15
1.6	The pseudoscalar transition form factors	21
2	Data analysis with Padé approximants	27
2.1	Introduction	27
2.2	Padé approximants as a fitting tool	28
2.3	Estimation of a systematic error	30
2.4	Space-like data: η and η' LEPs	34
2.5	Time-like data: η and η' LEPs	41
2.6	Conclusions	52
3	Canterbury Approximants	55
3.1	Introduction	55
3.2	Canterbury approximants	57
3.3	Practical examples	60
3.4	Canterbury approximants as a fitting tool	70
3.5	Conclusions	73
4	$\eta - \eta'$ mixing	75
4.1	Introduction	75
4.2	One-angle approximation	76
4.3	Two-angle mixing schemes	77
4.4	Determining the $\eta - \eta'$ mixing from the TFFs	81
4.5	Applications	89

4.6	Conclusions and outlook	95
5	Pseudoscalar to lepton pair decays	97
5.1	Introduction	97
5.2	The process: basic properties and concepts	98
5.3	A rational description for $F_{P\gamma^*\gamma^*}(Q_1^2, Q_2^2)$	105
5.4	Final results	112
5.5	Implications for χ PT	116
5.6	Implications for new physics contributions	120
5.7	Conclusions and outlook	127
6	The muon ($g - 2$): pseudoscalar-pole contribution	129
6.1	Introduction	129
6.2	Standard Model contributions to a_μ	130
6.3	Generic HLbL contribution to a_μ	136
6.4	The pseudoscalar-pole contribution	138
6.5	Beyond pole approximation	154
6.6	Final results for a_μ^{HLbL}	161
6.7	Conclusions and outlook	162
7	Conclusions and outlook	165
A	Definitions and conventions	169
A.1	Conventions	169
A.2	Feynman rules and spinors	169
A.3	S -matrix, cross sections and decay rates	170
B	Supplementary material	171
B.1	Formulae for the $g_{VP\gamma}$ couplings	171
B.2	Cutcosky rules for additional vector states in $P \rightarrow \bar{\ell}\ell$	172
B.3	Fierz transformations	174

Preface

The past decades of fundamental research in particle physics have established the standard model (SM) of particle physics as the microscopic theory of fundamental interactions, encompassing the strong, weak and electromagnetic forces in a $SU(3)_c \times SU(2)_L \times U(1)_Y$ gauge theory¹. Even if its formulation fits in a few lines, it provides the most successful theory ever formulated in the history of particle physics, and still stands in a good shape after thorough tests over the years —some of them standing to astonishing precision.

However, the SM as it is, was known to provide an incomplete description of nature even before its last piece remaining, the Higgs boson, was discovered in 2012 at the LHC experiment [3, 4]. Firstly, the SM fails to incorporate Einstein’s theory of general relativity —quantizing gravity is still a fundamental problem in theoretical physics. Secondly, there is great evidence that the ordinary matter which is described within the SM cannot explain the rotational galaxy curves, which seems to require the existence of dark matter —actually, the SM only describes the visible matter, which corresponds with around 5% of the energy content of the universe, whereas dark matter [5] would account for 26% [6, 7]. At larger cosmological scales, it is hard to explain the observed curvature of the universe without the presence of dark energy [8] —accounting for the remaining 69% energy content of the universe— for which the vacuum energy is a possible candidate; the SM however provides a number which is far too large as compared to the observational requirements. Furthermore, the SM is not able to describe baryogenesis —the CP violation within the SM is not large enough— nor inflation. Asides, the SM does not contain a mass term for the neutrinos, which is required to explain neutrino oscillations; the origin of neutrino mass and whether neutrinos are Dirac or Majorana particles is still an open question. There exist in addition theoretical reasons for which the SM is thought to be just the low-energy manifestation of an ultraviolet (UV) completion including, at the very least, gravity —known to be important at energies around the Planck scale $\Lambda_{\text{Planck}} \sim 10^{19}$ GeV. Furthermore, one

¹See Refs. [1, 2] for a detailed review.

of the most renowned issues has to deal with the so called hierarchy problem [9]. This is related to the large radiative corrections which the Higgs mass receives. These make natural to expect a mass close to the next scale of new-physics —say Λ_{Planck} — in contrast with its (now) well known mass $m_H = 125.09(24)$ GeV [10]. Furthermore, our current SM knowledge suggests that the SM vacuum is only metastable. Besides, the SM does not explain the large hierarchies of masses and the existence of three family generations. All in all, an evidence strong enough to stimulate speculations on different kind of physics scenarios beyond the standard model (BSM).

It has been a while right now since the first supersymmetric [9] and technicolor [11, 12] models appeared as a plausible realization of nature providing an UV completion of the SM. Since then, they have been intensively searched for at the most energetic colliders of their time, such as SPS@CERN, SLC@SLAC, LEP@CERN, Tevatron@Fermilab and, at this moment, LHC@CERN. Each of these new theories share the SM as their low-energy limit, but differ in their additional (heavier) particle spectra. Positive observations at colliders would immediately shed light into the uttermost structure of particle physics and represents the main tool to search for new physics. The negative results for these searches so far has led to the development of some alternative models such as Little(st) Higgs [13, 14], and extra dimensions [15], which so far have not been found either. This situation in the world of particle physics has led to the envisioning of new powerful colliders which would produce such hypothesized heavy particles. Nevertheless, it may be that such particles are too heavy to be produced at any envisaged collider so far, which poses a distressing scenario for the community.

Fortunately, quantum field theory provides alternative approaches to look for even heavier physics at lower energies. The quantum vacuum, with its fluctuations, offer us the opportunity to test the effects of these new particles at lower energies. Diagrammatically, this occurs through loop processes where heavy particles are virtually created and destroyed. From the modern point of view of effective field theories, this can be easily understood as a consequence of integrating-out the heavy fields, which produces additional higher-dimensional operators non-present in the SM. An outstanding example are those operators which drive the proton decay —a process which is forbidden in the SM due to the accidental baryon number conservation. Actually, the stringent bounds for the —so far unobserved— proton decay, provide strong limits to the scales of Grand Unified theories as high as 10^{15} GeV, which is inconceivable to test at any collider. Additional examples of these tiny contributions appear as well within the SM, such as in flavor physics, where the effective contribution from the charm and top quark in $\bar{K}^0 - K^0$ [16] and $\bar{B}^0 - B^0$ [17, 18] mixing, respectively, already pre-

dicted the order of the charm quark mass as well as a heavy top mass prior to their discoveries. Even preciser estimates were obtained both for the top and the Higgs masses based on electroweak precision observables [19] before they were discovered. The list of processes potentially sensitive to new physics effects is long, especially in flavor physics. Still at far lower energies, there is a world-famous observable which, given its experimental precision, plays an important role in looking for new physics and constraining BSM theories: the anomalous magnetic moment of the muon ($g_\mu - 2$) [20]. The latter is related to the magnetic dipole moment of the muon μ_m governing its interaction with a classical magnetic field \mathbf{B} through the Hamiltonian

$$\mathcal{H} = -\mu_m \cdot \mathbf{B}(\mathbf{x}), \quad \mu_m = g_\mu \left(\frac{eQ}{2m_\mu} \right) \mathbf{S}, \quad (1)$$

with $\mathbf{S}(Q)$ the muon spin(charge) and g_μ its gyromagnetic ratio, which classical value can be predicted from Dirac theory, obtaining $g_\mu = 2$. Such quantity receives however quantum corrections —arising within the SM of particle physics— implying deviations from the $(g_\mu - 2) = 0$ value. Similarly, new kind of physics would produce additional corrections to this observable. Therefore, a very precise measurement of $(g_\mu - 2)$ would allow to test BSM physics provided we are able to calculate the SM contributions to this observable, including quantum electrodynamics (QED), quantum chromodynamics (QCD) and electroweak (EW) contributions, to the astonishing precision to which $a_\mu \equiv (g_\mu - 2)/2$ is measured [21],

$$a_\mu^{\text{exp}} = 116592091(63) \times 10^{-11}. \quad (2)$$

The current theoretical estimation for the SM contribution reads²

$$a_\mu^{\text{th}} = 116591815(57) \times 10^{-11}, \quad (3)$$

and leads to a 3.2σ discrepancy among theory and experiment. This has motivated speculations on BSM physics contributing to this observable. For this reason, two new experiments have been projected at Fermilab [22] and J-PARC [23] aiming for an improved precision $\delta a_\mu = 16 \times 10^{-11}$ in order to sort out the nature of the discrepancy —note that even a negative result in the search for new physics effects would provide then a valuable constraint on BSM theories. However, this effort will be in vain unless a similar theoretical improvement is achieved, the current limiting factor being the SM hadronic corrections, among which, the leading order hadronic vacuum polarization (HVP) and hadronic light-by-light (HLbL) contributions dominate. Improving the current errors represents however an extremely difficult task, as these calculations involve non-perturbative hadronic physics which cannot be obtained from a first principles calculation —the exception is of

²See Chapter 6 for detailed numbers and references.

course lattice QCD which nevertheless requires some advances, specially for the HLbL, in order to improve current theoretical estimates.

The main objective of this thesis is to improve on a particularly large contribution dominating the HLbL—the pseudoscalar-pole contribution—at the precision required for the new projected $(g_\mu - 2)$ experiments. To this end, it is necessary to carefully describe the pseudoscalar meson interactions with two virtual photons. These are encoded in their transition form factors (TFFs), that must be described as precisely and model-independent as possible—including an accurately defined error—in order to achieve a precise and reliable result. Their study concerns the first part of this thesis. To this end, the methodology of Padé approximants and multivariate extensions relevant for the double-virtual TFFs description are considered.

Closely related to the HLbL, we address the calculation of the rare $P \rightarrow \bar{\ell}\ell$ decays, where $P = \pi^0, \eta, \eta'$ and $\ell = e, \mu$. These processes, showing a similar dependence on the pseudoscalar TFFs as the HLbL, not only offer a valuable check on our TFF description, but represent the only source of experimental information on the double-virtual TFF up to day—describing the double-virtual TFF behavior is very important in order to achieve a precise HLbL determination. Beyond that, the large suppression of these processes within the SM offers an opportunity to search for possible new physics effects in these decays. In the light of the present experimental discrepancies, we carefully describe and discuss them together with their implications in $(g_\mu - 2)$.

Despite of the theoretical relevance and hype for new physics searches, there are still some interesting questions within the SM that need to be addressed—the QCD spectrum among others. Whereas R. L. Jaffe affirmed that “the absence of exotics is one of the most obvious features of QCD” [24], which can be supported from large- N_c arguments, this is not clear at all as the recent discovery of a new plethora of the so-called *XYZ* exotic states [25], or even the possible pentaquark states in the charm quark sector [26] shows. Even more elusive is the question of gluonium states—purely gluonic quarkless bound states—for which several candidates exist. Given their quantum numbers, it is possible that some gluonium admixture exists in the η' . Elucidating the η and η' structure has been a very interesting and controversial topic, which relevance is not only theoretical but phenomenological, as it enters a number of heavy mesons decays. The electromagnetic interactions, encoded in their TFFs, offer a probe to test the internal η and η' structure which we use in order to obtain a new determination for the $\eta - \eta'$ mixing parameters.

Outline

The thesis is structured as follows: the fundamental concepts on QCD and TFFs employed in this thesis are presented in Chapter 1 along with the theory of Padé approximants, which we adopt to describe the pseudoscalar TFFs. In Chapter 2, we use the available data for the η and η' in order to extract the required low-energy parameters (LEPs). The excellent prediction that the method provides for the low-energy time-like region—based on space-like data and proving the power of the approach—is discussed and later incorporated into our analysis. This allows for an improvement in our LEPs extraction and provides a single description for the whole space-like and low-energy time-like regions. In Chapter 3, the generalization of Padé approximants to the bivariate case is introduced for the first time in this context and carefully discussed, thus providing a framework to reproduce the most general doubly-virtual TFF. In Chapter 4, we discuss as a first application from our outcome an alternative extraction for the $\eta - \eta'$ mixing parameters, which overcomes some problematics of previous approaches and incorporates subleading large- N_c and chiral corrections. In Chapter 5, we discuss a first application based on our TFF parameterization: the calculation of $P \rightarrow \ell\ell$ decays, which are of interest given current experimental discrepancies. Our method improves upon previously existing VMD-based models, specially for the η and η' . As a closure, a careful discussion on possible new-physics effects is presented. Finally, in Chapter 6, we use our approach to calculate the pseudoscalar-pole contribution to the hadronic light-by-light ($g_\mu - 2$) contribution. For the first time, a systematic method properly implementing the theoretical constraints, not only for the π^0 , but for the η and η' mesons and including a systematic error is achieved. Besides, the resulting calculation succeeds in obtaining a theoretical error in accordance to that which is foreseen in future ($g_\mu - 2$) experiments, which is the main goal of this thesis.

Quantum Chromodynamics and related concepts

Contents

1.1	Introduction	1
1.2	Quantum Chromodynamics	2
1.3	Low energy QCD: χ PT	3
1.4	Closing the gap: large- N_c QCD	10
1.5	Padé approximants	15
1.6	The pseudoscalar transition form factors	21

1.1 Introduction

In this chapter, we introduce the essential concepts of Quantum Chromodynamics (QCD) that will be required along this thesis. First, we introduce QCD, the quantum-field theory (QFT) of the strong interactions. We discuss then one of its central properties, asymptotic freedom. This feature, allowing to perform a perturbative expansion at high-energies, forbids at the same time a similar application at low energies. For this reason, we introduce chiral perturbation theory (χ PT), the effective field theory of QCD at low energies, which is our best tool to describe the physics of pions (π), kaons (K) and eta (η) mesons at low-energies, providing the relevant framework for discussions in this thesis. None of the previous descriptions are able to describe the intermediate energy region at around 1 GeV though. A successful framework providing some insight in this intermediate energy regime, encompassing both the chiral expansion and perturbative QCD limits, is the limit of large number of colors, large- N_c . We argue that the

success of resonant approaches inspired from such limit may be connected to the mathematical theory of Padé approximants (PAs), which is subsequently introduced. Finally, we briefly describe the pseudoscalar transition form factors.

1.2 Quantum Chromodynamics

QCD is the microscopic theory describing the strong interactions in terms of quarks and gluons. The former are the matter building blocks of the theory, whereas the latter represent the force carriers. It consists of a Yang-Mills $SU(3)_c$ — c standing for color— theory which Lagrangian is given as¹

$$\mathcal{L}_{\text{QCD}} = \sum_f \bar{q}_f (i\cancel{D} - m_q) q_f - \frac{1}{4} G_{\mu\nu}^c G^{c,\mu\nu}, \quad (1.1)$$

where q_f represent the quark spinor fields transforming under the fundamental $SU(3)_c$ representation; as such, they are said to come in $N_c = 3$ colors. Quarks come in addition in $n_f = 6$ different species or flavors f , up (u), down (d), strange (s), charm (c), bottom (b) and top (t), with different masses m_q spanning over five orders of magnitude. The symbol $\cancel{D} = \gamma^\mu D_\mu$, with γ^μ the Dirac matrices (see Appendix A) and D_μ the covariant derivative

$$D_\mu = \partial_\mu - ig_s A_\mu^c t^c, \quad (1.2)$$

with g_s the strong coupling constant, $t^c = \lambda^c/2$ the fundamental representation group generators and A_μ^c the $N_c^2 - 1 = 8$ gluon fields transforming in the adjoint $SU(3)_c$ representation. Finally, the $G_{\mu\nu}^c$ term stands for the field strength tensor²

$$G_{\mu\nu}^c = \partial_\mu A_\nu^a - \partial_\nu A_\mu^a + g_s f^{abc} A_\mu^b A_\nu^c. \quad (1.3)$$

The central property promoting QCD as the theory of the strong interactions is asymptotic freedom. In any QFT, renormalization effects lead to a non-constant coupling which is said to run with the energy. Such dependence is described with the help of the renormalization group (RG) equations for the coupling constant $\alpha_s = g_s^2/(4\pi)$ [27],

$$\mu^2 \frac{d\alpha_s}{d\mu^2} = \beta(\alpha_s) = -\alpha_s \left(\beta_0 \frac{\alpha_s}{4\pi} + \beta_1 \left(\frac{\alpha_s}{4\pi} \right)^2 + \beta_2 \left(\frac{\alpha_s}{4\pi} \right)^3 + \dots \right), \quad (1.4)$$

where $\beta_0 = (\frac{11N_c}{3} - \frac{2n_f}{3})$, being n_f the number of active flavors; additional $\beta_{1,2,\dots}$ terms can be found, up to β_4 , in Refs. [27, 28]. The remarkable property in Eq. (1.4) is the overall negative sign for $\beta_0 > 0$,

¹Section based in Refs. [1, 27].

²The structure constants f^{abc} are defined from $[t^a, t^b] = if^{abc}t^c$.

i.e. for $n_f < \frac{11}{2}N_c < 17$, deserving a Nobel prize in 2004 to D. J. Gross, H. D. Politzer and F. Wilczek³. This sign implies the decreasing of the strong coupling constant at high energies —asymptotic freedom— and allows for an easy and standard perturbative expansion in terms of quarks and gluons degrees of freedom. This property will be used in Section 1.6.1 to derive the high energy behavior for the pseudoscalar transition form factors (TFFs). In contrast, at low energies α_s increases, leading to a non-perturbative behavior and a strong-coupling regime, which is thought to be responsible for confinement, this is, the fact that free quarks and gluons are not observed in nature; instead, they bind together to form color-singlet states known as hadrons —the pions and proton among them. It must be emphasized at this point that confinement cannot be strictly explained on the basis of Eq. (1.4), which is based on a perturbative calculation. Indeed, describing confinement represents a still unsolved major theoretical challenge in mathematical physics as formulated for instance by the Clay Math institute [29]. Describing QCD at low-energies therefore represents a formidable task. So far, a first principles calculation based on Eq. (1.1) has only been achieved through Lattice QCD [30], an expensive computational numerical method based on the ideas from K. Wilson [31] consisting in a four dimensional euclidean space-time discretization of the QCD action. Additional, Dyson-Schwinger equations provides for a continuum non-perturbative approach to quantum field theories, which have been solved within some further approximation schemes. However, even if lattice calculations have shown a tremendous progress in the recent years, not all type of observables are at present accessible in lattice QCD. Furthermore, they are extremely costly and require some guidance when performing the required extrapolations. A viable and successful analytic approach comes by the hand of χ PT, the low-energy effective field theory of QCD.

1.3 Low energy QCD: χ PT

At the Lagrangian level, Eq. (1.1) is invariant by construction under Lorentz and local $SU(3)_c$ transformations. Eq. (1.1) is invariant too under the discrete charge conjugation (C), parity (P), and time reversal (T) transformations. In addition, there exists on top an almost-exact accidental symmetry which is not obvious or explicit in the construction, this is, the chiral symmetry; using the left-handed $P_L = \frac{1-\gamma_5}{2}$ and right-handed $P_R = \frac{1+\gamma_5}{2}$ projectors, the QCD Lagrangian may be written as⁴

$$\mathcal{L}_{\text{QCD}} = i\bar{q}_L \not{D} q_L + i\bar{q}_R \not{D} q_R - \bar{q}_L \mathcal{M} q_R - \bar{q}_R \mathcal{M} q_L - \frac{1}{4} G_{\mu\nu}^c G^{c,\mu\nu}, \quad (1.5)$$

³Interesting enough, at order α_s , Eq. (1.4) leads to the solution $\alpha_s(\mu) = 2\pi/(\beta_0 \ln(\mu/\Lambda_{\text{QCD}}))$, which defines an intrinsic (certainly non-perturbative) scale Λ_{QCD} .

⁴Most of the notations and concepts in this section are taken from Ref. [32].

where $\mathcal{M} = \text{diag}(m_u, m_d, m_s, m_c, m_b, m_t)$ and $q_{L(R)} = P_{L(R)}q$ with $q = (u, d, s, c, b, t)^T$. If the quark masses were left apart, the Lagrangian would be symmetric as well under the chiral global⁵ transformations $q_{L(R)} \rightarrow U_{L(R)}q_{L(R)}$, where $U_L \neq U_R$ represents a unitary matrix in flavor space, mixing then different flavors. This is, QCD does not distinguish among chiral quark flavors. Whereas the massless quark limit would represent a bad approximation for the heavy (c, b, t) quarks, this is not the case for the light (u, d, s) ones; the fact that the light hadrons are much heavier than the light quark masses points that the light quark masses should have little, if anything, to do with the mechanism conferring light hadrons their masses. The origin of the latter should be traced back to confinement, and is responsible for generating most of the visible particle masses in the universe. Chiral symmetry should be therefore a good approximation for the light-quarks sector.

Consequently, at the low energies where the heavy quarks do not play a role, we should find an approximate $U(3)_L \times U(3)_R$ symmetry. Through the use of Noether theorem, this would imply a set of 18 conserved currents and associated charges. These are conveniently expressed in terms of the vector and axial currents

$$J_\mu^a = L_\mu^a + R_\mu^a = \bar{q}\gamma_\mu \frac{\lambda^a}{2}q \quad J_{5\mu}^a = R_\mu^a - L_\mu^a = \bar{q}\gamma_\mu \gamma_5 \frac{\lambda^a}{2}q, \quad (1.6)$$

where $\lambda^a/2$ are the group generators. There is an octet corresponding to the eight λ^a Gell-Mann matrices and a singlet which, for later convenience, we define as $\lambda^0 = \sqrt{2/3} \mathbb{1}_{3 \times 3}$. The symmetry group may be rewritten then as $U(3)_L \times U(3)_R = U(1)_V \times U(1)_A \times SU(3)_V \times SU(3)_A$. However, the previous symmetry group holds only at the classical level; quantum corrections break the axial $U(1)_A$ symmetry. Precisely, the axial current divergence is given as [1]

$$\partial^\mu J_{5\mu}^a = \{\mathcal{P}^a, \mathcal{M}\} - \frac{g_s^2}{16\pi^2} \epsilon^{\alpha\beta\mu\nu} G_{\alpha\beta}^b G_{\mu\nu}^c \text{tr} \left(\frac{\lambda^a}{2} t^b t^c \right), \quad (1.7)$$

where the pseudoscalar current $\mathcal{P}^a = \bar{q}i\gamma_5 \frac{\lambda^a}{2}q$ has been used, $t^{b,c}$ are the $SU(3)_c$ generators associated to the strong interactions and $\lambda^a/2$ those associated to the chiral transformations. For $SU(3)_A$, the associated generators are traceless matrices in flavor space, producing a vanishing trace for the rightmost term; this contrasts with the (flavor singlet) $U(1)_A$ transformations, which generator is proportional to the unit matrix in flavor space⁶. Consequently, the singlet axial current is not conserved even in the chiral limit of vanishing quark masses $\mathcal{M} = 0$; it is called therefore an anomalous symmetry.

⁵Global means that, unlike in gauge theories, $U_{L,R} \neq U_{L,R}(x)$, i.e., the transformation does not depend on the space-time coordinate.

⁶Note that $\text{tr}(t^a t^b) = (1/2)\delta^{ab}$.

All in all, at the quantum level we should have an approximate $U(1)_V \times SU(3)_V \times SU(3)_A$ symmetry. The $U(1)_V$ symmetry is related to the baryon number conservation in the SM and is as important as to forbid the proton decay. The $SU(3)_V$ symmetry would imply the existence of degenerate-mass flavor multiplets in the hadronic spectrum, whereas the $SU(3)_A$ would imply analogous multiplets with opposite parity. However, the latter is not realized in nature: degenerate opposite parity multiplets are not found, indicating that the axial symmetry is spontaneously broken. This is thought to be related to the fact that, whereas the QCD Lagrangian is invariant under these transformations, the vacuum of the theory is not —the complex structure of the QCD vacuum is thought to be the ultimate responsible for the spontaneous breaking of the chiral symmetry. An important consequence of this feature comes by the hand of Goldstone's theorem. Goldstone's theorem dictates that, whenever a global symmetry is spontaneously broken, massless goldstone bosons with the quantum number of the broken generators appear. In nature, it seems that the symmetry breaking pattern is $U(1)_V \times SU(3)_V \times SU(3)_A \rightarrow U(1)_V \times SU(3)_V$ and 8 pseudoscalar Goldstone bosons should appear in correspondence with the 8 broken $SU(3)_A$ generators. In nature, there are no massless particles to which such hypothetical states could be associated to. There exists however, an octet of pseudoscalar particles much lighter than the standard mesons. These are the π 's, K 's and η mesons. It is believed that in the chiral limit $m_{u,d,s} \rightarrow 0$ such particles would correspond to the massless Goldstone bosons of the spontaneously broken chiral symmetry. In the real world, the explicit symmetry breaking by the quark masses is thought to give masses to these mesons, which are dubbed as pseudo-Goldstone bosons.

Before proceeding to describe χ PT, it is worth to take a brief detour anticipating some of the consequences of the large- N_c limit of QCD. Particularly, we are interested in the $U(1)_A$ axial anomaly. As we will comment in Section 1.4, 't Hooft showed that in the large- N_c limit, the strong coupling constant should be replaced as $g_s \rightarrow \tilde{g}_s/\sqrt{N_c}$, where \tilde{g}_s is to be fixed as $N_c \rightarrow \infty$ [33]. Consequently, in the chiral limit ($\mathcal{M} \rightarrow 0$), Eq. (1.7) reads

$$\partial^\mu J_{5\mu}^a = -\frac{\tilde{g}_s^2}{16\pi^2 N_c} \epsilon^{\alpha\beta\mu\nu} G_{\alpha\beta}^b G_{\mu\nu}^c \text{tr} \left(\frac{\lambda^a}{2} t^b t^c \right) \xrightarrow{N_c \rightarrow \infty} 0, \quad (1.8)$$

and the singlet axial current is conserved too as $N_c \rightarrow \infty$. In such limit, the $U(1)_A$ anomalous symmetry would be recovered, and the spontaneously breaking of the chiral symmetry would come with an additional Goldstone boson, the η' . Consequently, considering N_c as a parameter large enough, the η' could be incorporated to the χ PT Lagrangian in a combined chiral and large- N_c expansion, which is known as large- N_c chiral perturbation theory ($\ell N_c \chi$ PT). More formal arguments for the vanishing η' mass in the large- N_c chiral limit can be found in Ref. [34].

1.3.1 The chiral expansion

In the chiral limit of QCD, we believe in the existence of 8 massless Goldstone bosons associated to the breaking of the chiral symmetry —9 if the large- N_c limit is considered. Above this, there is a mass gap below the intrinsic scale that is generated in QCD, call it Λ_χ , where the full zoo of hadronic particles appears. Quantitatively, this spectrum starts around 0.5 GeV for scalar mesons, around 0.8 GeV for vector mesons and around 1 GeV for baryons. This situation calls for an effective field theory description of QCD at low-energies, in which the heavy hadrons above Λ_{QCD} are integrated out from the theory, which is effectively described in terms of the relevant degrees of freedom, the Goldstone bosons. The effect of the physics above Λ_χ are encoded in a plethora of terms appearing in the effective Lagrangian —actually, as many of them as the underlying symmetries allow to include. Of course, writing down the most general effective Lagrangian allowed by the assumed symmetry principles of the theory represents a formidable —if not impossible— task, as it contains an infinite number of terms. The second ingredient for constructing a useful effective field theory is the presence of an expansion parameter, according to which only a finite number of terms is required in order to achieve a prescribed precision. For effective field theories of spontaneously broken symmetries, this is an expansion in terms of small momenta p^2/Λ_χ^2 . In the real world, the small quark masses are non-zero, giving mass to the pseudo-Goldstone bosons. Still, these are much smaller than Λ_χ , which allows to systematically incorporate additional terms accounting for the explicit symmetry breaking as an expansion in terms of m_q/Λ_χ — χ PT is therefore an effective field theory description of QCD in terms of small momenta and quark masses.

The theoretical framework to describe such theories was initiated by Weinberg [35], Coleman, Wess and Zumino [36] and in collaboration with Callan in [37]. It generally implies that the Goldstone boson fields, $\phi(x)$, transform non-linearly upon the symmetry group; they are described then in terms of the $U(x)$ matrix

$$U(x) = \exp \left(\frac{i\phi(x)}{F} \right) = 1 + i \frac{\phi(x)}{F} + \dots \quad (1.9)$$

with F a parameter required to obtain a dimensionless argument and $\phi(x)$ the matrix associated to the Goldstone bosons

$$\phi(x) = \sum_{a=1}^8 \phi^a \lambda^a = \begin{pmatrix} \pi^0 + \frac{1}{\sqrt{3}}\eta & \sqrt{2}\pi^+ & \sqrt{2}K^+ \\ \sqrt{2}\pi^- & -\pi^0 + \frac{1}{\sqrt{3}}\eta & \sqrt{2}K^0 \\ \sqrt{2}K^- & \sqrt{2}\bar{K}^0 & -\frac{2}{\sqrt{3}}\eta \end{pmatrix}, \quad (1.10)$$

which serves as a building block of the theory. In this way, one can write the most general Lagrangian according to the powers of momentum p^n —what is equivalent, the number of derivatives ∂^n — and powers of the quark

masses (accounting that $m_q \sim p^2$). Due to Lorentz invariance, derivatives appears in even numbers, $2n$, leading to the decomposition

$$\mathcal{L} = \mathcal{L}_2 + \mathcal{L}_4 + \mathcal{L}_6 + \dots + \mathcal{L}_{2n} + \dots . \quad (1.11)$$

In addition, any of the pieces displayed above produces an infinite number of contributions —Feynman diagrams— to some given specific process. Consequently, an additional scheme classifying these pieces according to their relevance is required. This is achieved using Weinberg’s power counting [38], which assigns a chiral dimension D to every amplitude \mathcal{M} (see Appendix A) arising from a particular diagram according to its properties upon momenta, p , and quark masses, m_q , scaling

$$\mathcal{M}(p_i, m_q) \rightarrow \mathcal{M}(tp_i, t^2 m_q) = t^D \mathcal{M}(p_i, m_q). \quad (1.12)$$

The final result is given, in four space-time dimensions, in terms of the number of internal pseudo-Goldstone boson propagators, N_I , number of loops, N_L , and the number of vertices N_{2k} from \mathcal{L}_{2k} (see Eq. (1.11)) as

$$D = 4N_L - 2N_I + \sum_{k=1}^{\infty} 2kN_{2k}. \quad (1.13)$$

1.3.2 Leading order Lagrangian

The most general Lagrangian at leading order, \mathcal{L}_2 , reads [39, 40]

$$\mathcal{L}_2 = \frac{F^2}{4} \text{tr} \left(D_\mu U D^\mu U^\dagger \right) + \frac{F^2}{4} \text{tr} \left(\chi U^\dagger + U \chi^\dagger \right), \quad (1.14)$$

where F is known as the pion decay constant in the chiral limit due to its relation at LO with the π^\pm decay. The covariant derivative is defined as

$$D_\mu U = \partial_\mu U - ir_\mu U + iUl_\mu = \partial_\mu U - i[v_\mu, U] - i\{a_\mu, U\} \quad (1.15)$$

and allows to couple the pseudo-Goldstone bosons to external left (l_μ) and right (r_μ) handed —alternatively vector (v_μ) and axial (a_μ)— currents. Finally $\chi = 2B(s+ip)$, where B is related to the quark condensate $\langle \bar{q}q \rangle_0$ in the chiral limit and $s(p)$ are the external (pseudo)scalar currents⁷. This allows to introduce the finite quark masses effects via $s \rightarrow \mathcal{M} = \text{diag}(m_u, m_d, m_s)$.

The most general Lagrangian construction at the next order, \mathcal{L}_4 , was discussed in the seminal papers from Gasser and Leutwyler [39, 40].

Finally, the large- N_c limit allows to include the η' as a ninth degree of freedom, giving birth to $\ell N_c \chi$ PT, a low-energy description of QCD in terms of small momenta, quark masses and the large number of colors. In this

⁷The elements v_μ, a_μ, s, p are defined in terms of generating functional external currents $\mathcal{L}_{\text{ext}} = v_\mu \bar{q} \gamma^\mu \frac{\lambda^a}{2} q + a_\mu \bar{q} \gamma^\mu \gamma_5 \frac{\lambda^a}{2} q - s^a \bar{q} \lambda^a q + p^a \bar{q} i \gamma_5 \lambda^a q \equiv \bar{q} \gamma^\mu (v_\mu + \gamma_5 a_\mu) q - \bar{q} (s - i \gamma_5 p) q$.

framework, the expansion parameters are $p^2 \sim m_q \sim N_c^{-1} \sim \mathcal{O}(\delta)$ and the expansion reads

$$\mathcal{L} = \mathcal{L}^{(0)} + \mathcal{L}^{(1)} + \mathcal{L}^{(2)} + \dots + \mathcal{L}^{(\delta)} + \dots . \quad (1.16)$$

In addition, the N_c scaling has to be incorporated to Eq. (1.12). As a result, it can be obtained among others that $F \sim \mathcal{O}(N_c^{1/2})$, or that loop processes as well as additional flavor traces are N_c -suppressed in this framework. The leading order Lagrangian is given as [41]

$$\mathcal{L}^{(0)} = \frac{F^2}{4} \text{tr} \left(D_\mu U D^\mu U^\dagger \right) + \frac{F^2}{4} \text{tr} \left(\chi U^\dagger + U \chi^\dagger \right) - \frac{1}{2} \tau (\psi + \theta)^2 , \quad (1.17)$$

where Eq. (1.10) is to be replaced by

$$\phi(x) = \sum_{a=0}^8 \phi^a \lambda^a = \begin{pmatrix} \pi^0 + \frac{1}{\sqrt{3}}\eta + \frac{F}{3}\psi & \sqrt{2}\pi^+ & \sqrt{2}K^+ \\ \sqrt{2}\pi^- & -\pi^0 + \frac{1}{\sqrt{3}}\eta + \frac{F}{3}\psi & \sqrt{2}K^0 \\ \sqrt{2}K^- & \sqrt{2}\bar{K}^0 & -\frac{2}{\sqrt{3}}\eta + \frac{F}{3}\psi \end{pmatrix} \quad (1.18)$$

with $\lambda^0 = \sqrt{2/3} \mathbb{1}_{3 \times 3}$ and $\psi \equiv \frac{\sqrt{6}}{F} \phi^0$, being ϕ^0 the field to be related to the singlet Goldstone boson in the chiral large- N_c limit. The τ term in Eq. (1.17) is connected with the $\langle 0 | T\{\omega(x)\omega(0)\} | 0 \rangle$ two-point function in the pure gluonic theory⁸ and θ , the vacuum angle [41], represents an external current —similar to the $2Bs$ term in χ .

1.3.3 The effective Wess-Zumino-Witten action

The Lagrangians described above—including the higher order in Eqs. (1.11) and (1.16)—can be shown to be invariant under $\phi \rightarrow -\phi$ transformations if no external currents are considered, meaning that they always contain interactions with an even number of pseudo-Goldstone bosons. This remains the case even if vector currents are included in the formalism. The preceding Lagrangians cannot describe the $\pi^0 \rightarrow \gamma\gamma$ and related decays. The $\pi^0 \rightarrow \gamma\gamma$ decay has indeed been a fascinating process in the history of particle physics, the underlying mechanism driving this decay remaining a mystery until the independent discovery of the anomalies—the breaking of classical symmetries in QFT—in 1969 by Adler [42] and Bell-Jackiw [43] (ABJ anomaly). The ABJ anomaly can be used then to predict the $\pi^0 \rightarrow \gamma\gamma$ decay in the chiral limit of QCD—see for instance [44]. The systematic incorporation of anomalies into chiral Lagrangians is accomplished by the use of the Wess-Zumino-Witten (WZW) action [45, 46], which introduces additional terms involving an odd number of Goldstone bosons as well as terms

⁸The winding number density is defined as $\omega = -\frac{g_s^2}{32\pi^2} \epsilon^{\mu\nu\rho\sigma} G_{\mu\nu}^c G_{\rho\sigma}^c = -\frac{\alpha_s}{4\pi} G^c \tilde{G}^c$ with the dual tensor $\tilde{G}^{c,\mu\nu} = \frac{1}{2} \epsilon^{\mu\nu\rho\sigma} G_{\rho\sigma}^c$.

such as $\phi\gamma\gamma$, $\phi^3\gamma$, etc (see Ref. [32, 41]). For our case of interest, we refer to the leading term inducing $P \rightarrow \gamma\gamma$ decays [47]

$$\mathcal{L}_{\text{WZW}} = \frac{N_c \alpha}{8\pi} \epsilon^{\mu\nu\rho\sigma} F_{\mu\nu} F_{\rho\sigma} \text{tr}(\mathcal{Q}^2 \phi) \quad (1.19)$$

which is valid both, for χ PT and $\ell N_c \chi$ PT, where it appears at order \mathcal{L}_4 and $\mathcal{L}^{(1)}$, respectively. In the expression above, $\mathcal{Q} = \text{diag}(2/3, -1/3, -1/3)$ is the charge operator and $\phi = \lambda^a \phi^a$.

1.3.4 Basic leading order results: masses and decay constants

As an example, we outline here the LO results for the pseudoscalar masses and decay constants in $\ell N_c \chi$ PT. From the Lagrangian Eq. (1.17), and taking $\chi \rightarrow 2B\mathcal{M}$, we obtain for the kinetic terms at LO

$$\begin{aligned} \mathcal{L}_{\text{kin}}^{(0)} = & \partial_\mu \pi^+ \partial^\mu \pi^- - 2B\hat{m} \pi^+ \pi^- + \frac{1}{2} (\partial_\mu \pi^0 \partial^\mu \pi^0 - 2B\hat{m} \pi^0 \pi^0) \\ & + \partial_\mu K^+ \partial^\mu K^- + \partial_\mu \bar{K}^0 \partial^\mu K^0 - B(\hat{m} + m_s)(K^+ K^- + \bar{K}^0 K^0) \\ & + \frac{1}{2} (\partial_\mu \eta_8 \partial^\mu \eta_8 - B(\frac{2\hat{m}+4m_s}{3}) \eta_8 \eta_8) - \frac{1}{2} (\eta_8 \eta_0 + \eta_0 \eta_8) \frac{2\sqrt{2}}{3} (\hat{m} - m_s) \\ & + \frac{1}{2} (\partial_\mu \eta_0 \partial^\mu \eta_0 - B(\frac{4\hat{m}+2m_s}{3}) \eta_0 \eta_0 - \frac{6\tau}{F^2} \eta_0 \eta_0). \end{aligned} \quad (1.20)$$

In the expression above, the isospin-symmetric limit $m_u = m_d \equiv \hat{m}$ has been used. Eq. (1.20) allows to identify the pions and kaons masses at LO

$$m_{\pi^\pm}^2 = m_{\pi^0}^2 \equiv \dot{M}_\pi^2 = 2B\hat{m} \quad m_{K^\pm}^2 = m_{K^0}^2 \equiv \dot{M}_K^2 = B(\hat{m} + m_s). \quad (1.21)$$

The η and η' masses require additional work since the terms from the third line in Eq. (1.20) are non-diagonal, leading to the $\eta - \eta'$ mixing. This will be discussed in more detail in Chapter 4. For the moment, let us note that in standard χ PT $\eta = \eta_8$, which receives mass from the quarks alone. The singlet component η_0 acquires a large topological mass $M_\tau^2 = 6\tau/F^2$ absent in the octet terms.

Finally, we define the pseudoscalar decay constants, which are of major interest for discussing the $\eta - \eta'$ mixing in Chapter 4 as well as for calculating new physics contributions to $P \rightarrow \bar{\ell}\ell$ decays in Chapter 5, where $P = \pi^0, \eta, \eta'$. The pseudoscalar decay constants are defined in terms of the matrix elements of the pseudoscalars with the axial current

$$\langle 0 | J_{5\mu}^a | P(p) \rangle \equiv i p_\mu F_P^a, \quad J_{5\mu}^a = \bar{q} \gamma_\mu \gamma_5 \frac{\lambda^a}{2} q. \quad (1.22)$$

They can be obtained at LO from Eq. (1.17) taking an external axial current $a_\mu \equiv a_\mu^a \frac{\lambda^a}{2}$, see Eq. (1.15). The relevant term reads

$$-F \text{tr}(\partial^\mu \phi a_\mu) = -\frac{F}{2} \text{tr}(\partial^\mu \phi \lambda^a) a_\mu^a. \quad (1.23)$$

Identifying λ^a with the relevant $SU(3)$ matrix, i.e., λ^3 for the π^0 , one obtains in χ PT that $F_{\pi^\pm} = F_{\pi^0} = F_{K^\pm} = F_{K^0} = F_\eta \equiv F$. In $\ell N_c \chi$ PT, the $\eta - \eta'$ mixing makes this picture more complicated for the η and η' mesons.

The success obtained in χ PT at higher orders (state of the art is $\mathcal{O}(p^6)$) in predicting different observables shows a good performance of the theory, which is to day our best tool to produce analytical calculations for low-energy hadronic physics. Still, the theory is not expected to be valid above some scale, often defined as $\Lambda_\chi \equiv 4\pi F$, which is below the pQCD applicability range. For a particular process, the natural scale at which one can expect a poor performance is given by the closest relevant hadronic resonance which has not been included in the theory as an active degree of freedom. Unfortunately, this avoids to match the theory with pQCD.

1.4 Closing the gap: large- N_c QCD

Describing all the QCD phenomenology with its great complexity represents a challenging task. The complex analytic structure which QCD requires — think about reproducing all nuclear physics as a part — makes an analytic description nonviable. Consequently, so far, only perturbative expansions have reached success in analytically describing particular sectors of QCD, but the lack of an apparent perturbative parameter of the theory at all scales avoids the whole QCD description within a single framework. However, 't Hooft pointed out that there might be such a candidate for an expansion parameter in QCD, this is, the limit of large number of colors, large N_c [33]. Its phenomenological success and the fact that it is the only framework justifying some known features of QCD, such as Regge theory or the OZI rule among others, makes this approximation to QCD very useful even if so far it only produces a qualitative picture of QCD rather than a quantitative one⁹.

The large- N_c limit of QCD is based on the combinatorics $SU(N_c)$ group factors arising in diagrammatic calculations. Recall for instance the RG equation for the strong coupling constant α_s in Eq. (1.4). There, N_c plays a relevant role in the leading coefficient for the β -function $\beta_0 = \frac{1}{3}(11N_c - 2n_f)$. In the large- N_c limit, the first part dominates. Actually, if a smooth and non-trivial behavior is desired in such a limit, the strong coupling constant should be taken as $g_s \rightarrow \bar{g}_s/\sqrt{N_c}$, where \bar{g}_s is kept fixed as $N_c \rightarrow \infty$. Then, the RG equation for $\bar{\alpha}_s \equiv \bar{g}_s^2/4\pi$ would resemble that in Eq. (1.4) with β_0 defined as $\beta_0 = \frac{1}{3}\left(11 - \frac{2}{N_c}n_f\right)$ — otherwise, \bar{g}_s would tend to 0 inducing a trivial theory¹⁰. This means that any interacting process in the large- N_c limit will not survive unless the combinatoric factors of the relevant dia-

⁹This introduction is mainly based on Refs. [48–50].

¹⁰In addition, this guarantees that the induced QCD scale, Λ_{QCD} , as well as the hadron masses, remain N_c -independent.

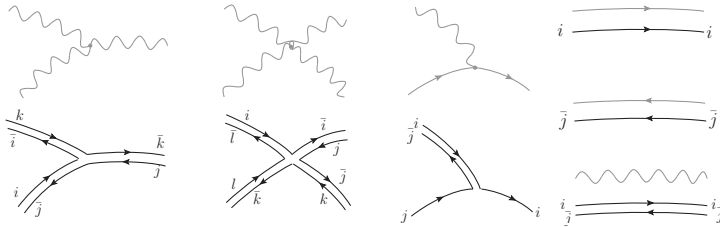


Figure 1.1: The different QCD vertices and propagators (gray) in the color-lines notation (black). The indices i, j, k, l stand for color indices.

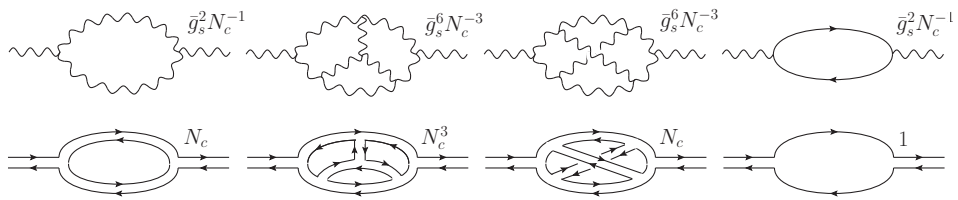


Figure 1.2: Examples of diagrams contributing to the gluon self-energy. Upper graphs show the vertex suppression, $\bar{g}_s/\sqrt{N_c}$, and the lower ones the combinatoric $SU(N_c)$ enhancement arising from closed color lines $\sim N_c$.

grams are large enough to compensate for the $\bar{g}_s/\sqrt{N_c}$ factors. It turns out that only a certain class of diagrams, which can be classified according their topology, survive in this limit (in the purely gluonic theory these are the so called planar diagrams). To figure this out, it is convenient to employ the color-line notation introduced by 't Hooft [33], according to which the quarks propagators can be illustrated as color lines, the gluons propagators as color-anticolor lines and a similar representation holds for the vertices, see Fig. 1.1.

As an example, we show in Fig. 1.2 different contributions to the vacuum polarization appearing in the α_s running together with their N_c counting. From those diagrams, only the first and second ones have a combinatoric factor arising from closed color lines large enough to counteract the vertices suppression; the third and fourth are suppressed with respect to the previous ones by factors of N_c^{-2} and N_c^{-1} , respectively. The leading diagrams belong to the so called planar diagrams. In contrast to the third one, they can be drawn in such a way that color lines do not cross each other and are leading in the large- N_c expansion. Contrary, non-planar diagrams and quark loops are N_c^{-2} and N_c^{-1} suppressed, respectively.

Therefore, in order to obtain the gluon self-energy, it would be sufficient, at leading order in the large- N_c expansion, to take the planar diagrams contributions. The resummation of all the planar diagrams has only been achieved so far in a 1+1 space-time dimensions [51]. Therefore, it is difficult to obtain a quantitative answer in large N_c . Still, it is possible to obtain a qualitative picture for a variety of QCD phenomena. In this thesis, it is

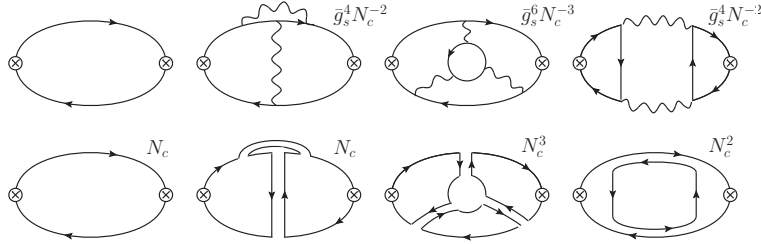


Figure 1.3: Different contributions to quark bilinear correlation functions, where the insertion is marked by a cross. Upper graphs indicate the strong-coupling suppression and the lower ones the combinatoric $SU(N_c)$ enhancement.

of interest what concerns Green's functions involving $\bar{q}\Gamma q$ bilinear currents, where Γ is a Dirac bilinear matrix. It turns out that planarity is not enough then. For the case of bilinear currents, *the leading diagrams are the planar diagrams with only a single quark loop which runs at the edge of the diagram* [48]. To see this, we refer to Fig. 1.3, where crosses refer to bilinear currents insertions. The first diagram is of order N_c ; the second, with a gluon at the edge, is N_c^{-2} suppressed; the third one, with an internal quark loop, is N_c^{-1} suppressed; the fourth is N_c^{-1} suppressed.

These observations have far reaching consequences once confinement is assumed: take a typical leading diagram such as that in Fig. 1.4 and cut it through to search for possible intermediate states, this is, intermediate quarks and gluons color singlet combinations. First of all, as quark loops are N_c suppressed, any intermediate state contains one and only one $q\bar{q}$ pair. Second, a closer look to Fig. 1.4 reveals that it is not possible to have two or more singlet configurations, say $q\bar{q}$ and some gluonic state —more precisely, these configurations are N_c suppressed. In conclusion, all the quarks and gluons must bind together to form one particle color-singlet states; the diagram in Fig. 1.4 represents thereby a perturbative approximation to a single hadron. As a conclusion, bilinear two-point correlation functions —such as the vacuum polarization— can be expressed in terms of single particle intermediate meson states with the appropriate quantum numbers:

$$\frac{1}{i} \int d^4x e^{ik \cdot x} \langle 0 | T\{J(x)J(0)\} | 0 \rangle \equiv \langle J(k)J(-k) \rangle = \sum_n \frac{a_n^2}{k^2 - m_n^2 + i\varepsilon}, \quad (1.24)$$

where the meson masses, m_n , are N_c independent. Furthermore, it is known that, in the perturbative regime, such function behaves logarithmically, requiring then an infinite number of mesons. In the large- N_c limit, correlation functions are given in terms of an infinite sum of narrow-width (stable) meson states. In addition, since the correlation function is of order N_c , $a_n = \langle 0 | J | n \rangle = \sqrt{N_c}$.

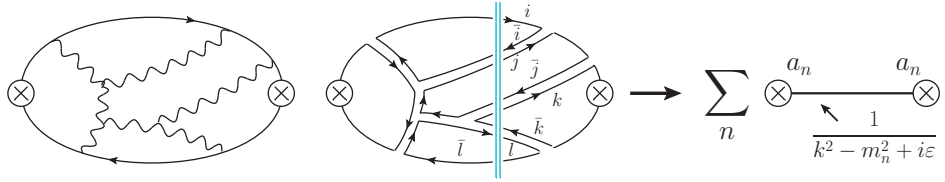


Figure 1.4: A typical N_c -leading contribution to a bilinear two-point function. Multiple singlet color intermediate states cannot appear at the leading order. Two-point functions can be understood then in the large- N_c limit as a sum over single meson states (right).

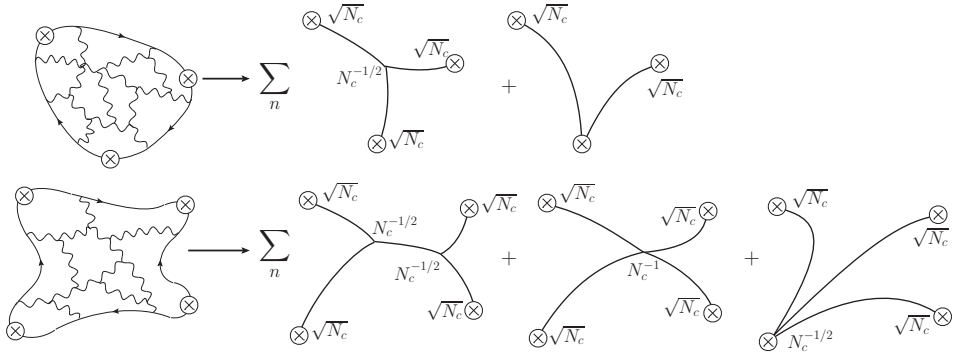


Figure 1.5: A typical N_c -leading contribution to the three- and four-point function (upper and lower row, respectively) and possible meson-exchange decomposition (crossed channels are implied).

The same reasoning can be extrapolated to higher order correlation functions for quark bilinears. As an example, we illustrate this for the three- and four-point functions¹¹ in Fig. 1.5. Again, the only possible intermediate color singlet states are single particles —multiparticle states being N_c suppressed. In addition, the large- N_c counting allows to obtain that the three(four) meson vertex is $1/\sqrt{N_c}(1/N_c)$ suppressed, leading to a large- N_c estimate for the meson decay widths. In general terms, it is found that any Green's function must contain, at the leading order, single-pole contributions alone —multiparticle states are suppressed. Actually, using crossing symmetry and unitarity arguments, the large- N_c limit implies that, at the leading order, every amplitude can be expressed as if arising from the tree level calculation from some local Lagrangian with the following properties:

- Green's functions for bilinear quark currents can be expressed as sums over single meson states —an analogous result holds for purely gluonic currents which can be expressed as a sum over purely gluonic bound states (glueballs).

¹¹Actually, these are of relevance for this thesis, as the pseudoscalar transition form factors can be defined in terms of the $\langle VV\mathcal{P} \rangle$ Green's function and the hadronic light-by-light tensor is related to the $\langle VVVV \rangle$ one.

- The amplitude for a bilinear current to create m mesons from the vacuum $\langle 0 | J | n^m \rangle$ is $\mathcal{O}(N_c^{1-m/2})$ —similarly, the amplitude for creating g glueball states $\langle 0 | J | n^g \rangle$ is $\mathcal{O}(N_c^{1-g})$.
- Vertices involving m mesons are $\mathcal{O}(N_c^{1-m/2})$ —for g glueball states they are of $\mathcal{O}(N_c^{1-g})$.
- Similarly, a meson-glueball vertex —and thereby meson-glueball mixing— can be obtained to be $\mathcal{O}(1/\sqrt{N_c})$.

The properties above, even qualitative, allow to understand many QCD phenomenological observations supporting the applicability of the large- N_c limit:

- Most of the observed mesons are (mainly) $q\bar{q}$ states and additional $q\bar{q}$ content seems suppressed.
- The dominance of narrow resonances over multiparticle continuum.
- Hadronic decays proceed, dominantly, via resonant states.
- It provides a natural explanation (the only one so far) for Regge phenomenology.
- It is the only framework justifying the Okubo-Zweig-Iizuka (OZI)¹² rule. It explains for instance why $\phi \rightarrow \bar{K}K$ dominates over $\phi \rightarrow \rho\pi$ or the approximate nonet symmetry in meson multiplets¹³.

Note that in the combined chiral and large- N_c limit not only may one expect the η' to be degenerate in mass with the pseudo-Goldstone bosons, but to decouple from glueball mixing effects, providing thus an ideal framework to implement the η' into the chiral description as previously said.

We concluded the previous sections observing that χ PT and pQCD could not provide a complete description of QCD at all scales. The large- N_c limit does not provide a quantitative answer either —as we do not know how to solve it yet— but it provides a qualitative description. In the region of interest between χ PT and pQCD, the relevant physics is provided by the role of intermediate resonances. One could interpolate the QCD Green's functions from the low energies —calculable within χ PT— to the high-energies using a rational function incorporating the minimum number of resonances required to reproduce the pQCD behavior. This approach has been known as the minimal hadronic approximation (MHA) [52] and has provided with successful and reasonable descriptions involving different phenomena.

¹²The OZI rule refers to the suppression of quark-disconnected contributions such as that in the fourth diagram in Fig. 1.3.

¹³Note that the mass difference from singlet against octet mesons would arise from diagrams such as the last one in Fig. 1.3, which are N_c suppressed.

1.5 Padé approximants

The large- N_c limit dictates that, to leading order, the QCD Green's functions are characterized in terms of the different poles arising from intermediate resonance exchanges and their residues, motivating the construction of some rational ansatz for them. Specializing to two-point functions, say, the hadronic vacuum polarization (HVP)

$$\int d^4x e^{iq \cdot x} \langle 0 | T\{J^{(\mu)}(x)J^{(\nu)}(0)\} | 0 \rangle \equiv i(q^2 g^{\mu\nu} - q^\mu q^\nu) \Pi(q^2), \quad (1.25)$$

the large- N_c limit suggests that, at leading order,

$$\widehat{\Pi}(q^2) \equiv \Pi(q^2) - \Pi(0) = \frac{A(q^2)}{(q^2 - M_{V_1}^2)(q^2 - M_{V_2}^2) \dots (q^2 - M_{V_n}^2) \dots}, \quad (1.26)$$

with $\widehat{\Pi}(q^2)$ the renormalized HVP, M_{V_n} the n -th vector meson resonance mass and $A(q^2)$ a polynomial¹⁴. Moreover, the residues from $\widehat{\Pi}(q^2)$ can be expressed in term of the vector resonances' decay constants F_{V_n} as

$$\lim_{q^2 \rightarrow M_{V_n}^2} (q^2 - M_{V_n}^2) \widehat{\Pi}(q^2) \equiv -F_{V_n}^2, \quad \langle 0 | J^\mu | V_n \rangle \equiv M_{V_n} F_{V_n} \epsilon^\mu. \quad (1.27)$$

Phenomenologically, one may adjust the required number of vector resonances to reproduce the pQCD behavior (MHA) to the physical ($N_c=3$) resonance masses¹⁵ and even to determine some coefficients in Eq. (1.27) from the physical vector meson decays. Alternatively, as in the real world the vector mesons have a finite width, one may obtain the parameters in Eq. (1.26) through a data-fitting procedure instead. The procedure outlined often provides a reasonable description, which, in some cases, may go beyond the large- N_c expectations. Still, when aiming for precision, large N_c is not enough and it would be desirable to be able to implement all the information at hand: the well-known low-energy behavior from χ PT — including multiparticle intermediate states — and the high-energy behavior from pQCD — via the operator product expansion (OPE). In this section, we introduce Padé approximants (PAs), which can be precisely used for this task. Padé theory defines then a rigorous mathematical approach which is applicable, at least, in the space-like region. As an outcome, this theory is able to justify the reason why, sometimes, the MHA provides such a good performance beyond large- N_c expectations¹⁶.

¹⁴the $\lim_{q^2 \rightarrow \infty} \Pi(q^2) \sim \ln(q^2)$ behavior requires an infinite number of resonances and therefore $A(q^2)$ should be an infinite degree polynomial as well.

¹⁵This is possible with a finite number of resonances if the anomalous dimensions vanish so no logarithmic corrections appear or, approximately, if they appear as correction to the leading Q^2 behavior [53]. This is not the case for the HVP; it is the case however for the Π_{LR} function [54] or the TFFs.

¹⁶This section is based on Ref. [55]. A thorough discussion of PAs can be found in Refs. [56, 57].

1.5.1 Padé theory essentials

Given a function $f(z)$ of complex variable z with a well defined power expansion around the origin¹⁷ and a radius of convergence $|z| = R$,

$$f(z) = \sum_{n=0}^{\infty} f_n z^n, \quad (1.28)$$

the Padé approximant [56, 57] is a rational function¹⁸

$$P_M^N(z) = \frac{Q_N(z)}{R_M(z)} = \frac{\sum_{n=0}^N a_n z^n}{\sum_{m=0}^M b_m z^m} \quad (1.29)$$

with coefficients a_n, b_m defined to satisfy the accuracy-through-order conditions up to order $N + M$

$$P_M^N(z) = f_0 + f_1 z + \dots + f_{M+N} z^{M+N} + \mathcal{O}(z^{L+M+1}). \quad (1.30)$$

Note that, without loss of generality, one can always choose $b_0 = 1$.

If the original function $f(z)$ has a radius of convergence $R \rightarrow \infty$, $f(z)$ is said to be an entire function and is given by its power series expansion, Eq. (1.28), everywhere in the complex plane. Employing PAs for this kind of functions may accelerate the convergence rate with respect to the series expansion, but the gain may not be dramatic. The situation changes for series expansions with a finite radius of convergence R_0 : the power series Eq. (1.28) represents a divergent series beyond R_0 and convergence deteriorates as one approaches this point. It is in this case where PAs become a powerful tool; they cannot only dramatically improve the convergence rate within $|z| < R$ with respect to Eq. (1.28), but may provide convergence in a larger domain $\mathcal{D} \subset \mathbb{C}$ ($\{|z| < R\} \subset \mathcal{D}$), which in some cases could extend (almost) to the whole complex plane —in such case, PAs would provide in a sense a formal tool to perform an analytic continuation of a given series expansion. This is very important, as the functions we want to deal with in QCD, are not analytic in the whole complex plane; as we saw, in the large- N_c limit these functions are characterized by an infinite set of resonances or poles, whereas in the real $N_c = 3$ world, multiparticle intermediate states imply the existence of branch cuts. In that sense, the applicability of Eq. (1.28) would be very limited (R would be given by the lowest (multi)particle production point). The study of convergence properties for PAs is much more complicated than for the cases of power expansions and represents an active field of research in applied mathematics. Nevertheless, there are some classes of functions for which convergence properties are very well-known. In the following, we describe the convergence properties for meromorphic and Stieltjes functions, which are representative cases of QCD Green's functions.

¹⁷The definition is not special for the origin ($z = 0$) and generally applies to any point z_0 in the complex plane as long as the series expansion is well-defined around $z = z_0$.

¹⁸In the mathematical literature $P_M^N(z)$ is commonly noted as $[N/M]$, $[N|M]$ or N/M .

The large- N_c limit of QCD: meromorphic functions

A particular class of functions we are interested in are meromorphic functions, this is, functions which are analytic in the whole complex plane except for a set of isolated poles and, therefore, represents the case of interest of large- N_c QCD. The convergence properties of PAs to this kind of functions are very well-known and can be summarized in terms of Montessus' and Pommerenke's theorems as given in Ref. [57]:

Montessus' theorem

Let $f(z)$ be a function which is meromorphic in the disk $|z| \leq R$, with m poles at distinct points z_1, z_2, \dots, z_m , where $|z_1| \leq |z_2| \dots \leq |z_m| \leq R$. Let the pole at z_k have multiplicity μ_k and let the total multiplicity $\sum_{k=1}^m \mu_k = M$. Then,

$$f(z) = \lim_{L \rightarrow \infty} P_M^L(z) \quad (1.31)$$

uniformly on any compact subset of

$$\mathcal{D}_m = \{z, |z| \leq R, z \neq z_k, k + 1, 2, \dots, m\}. \quad (1.32)$$

When dealing with Green's functions in the large- N_c limit of QCD, this means that a sequence of approximants $P_M^L(z)$ will provide an accurate description within a disk $|z| < R$ englobing the first M poles as long as $L \rightarrow \infty$. The advantage of the theorem is that it provides uniform convergence, which is a strong property as it implies that no spurious poles or “defects” —see the theorem below— will appear. In particular, the position of the m poles and their residues will be correctly determined as $L \rightarrow \infty$ (see Refs. [53, 54]). The disadvantage is that the theory does not say anything outside $|z| < R$ and the number of poles within must be anticipated —an information which might be unknown. If these requirements were too strong for some specific application, one may resort to Pommerenke's theorem instead.

Pommerenke's theorem

Let $f(z)$ be a function which is analytic at the origin and analytic in the entire complex plane except for a countable number of isolated poles and essential singularities. Suppose $\varepsilon, \delta > 0$ are given. Then, M_0 exists such that any P_M^L sequence with $L/M = \lambda$ ($0 < \lambda < \infty$) satisfies

$$|f(z) - P_M^{\lambda M}| \leq \varepsilon \quad (1.33)$$

for any $M \geq M_0$, on any compact set of the complex plane except for a set \mathcal{E}_M of measure less than δ . Consequently, convergence is found as $M \rightarrow \infty$. As an interesting corollary, previous theorem can be generalized to $P_N^{N+k}(z)$ sequences with $k \geq -1$ fixed.

The great advantage of this theorem is threefold: first, the poles do not have to be specified in advance; second, convergence is guaranteed for the

whole complex plane; third, it includes not only poles, but essential singularities. In contrast, one has to deal with the occurrence of artificial poles not present in the original function. Convergence implies that these poles either move away in the complex plane, or they pair with a close-by zero, forming what are known as “defects”¹⁹, for which convergence is not uniformly guaranteed but in measure. This means that the region in the complex plane where Eq. (1.33) is not satisfied becomes arbitrarily small. See Ref. [54] for a nice illustration of this feature and the use of Pommerenke’s theorem for the $\langle VV - AA \rangle$ QCD Green’s function.

Back to the $N_c=3$ real world: Stieltjes functions

As a consequence of the previous theorems, convergence of PAs to meromorphic functions can be guaranteed, and thereby, the convergence of PAs to QCD Green’s functions in the large- N_c limit of QCD follows. This allows to reconstruct and to extend the otherwise divergent series defined in Eq. (1.28) —which may be obtained from χ PT— up to an arbitrary large domain as long as enough terms in the power-series expansion are known. Of course, this does not guarantee an analogous performance in the real world with $N_c = 3$. For instance, the hadronic vacuum polarization $\hat{\Pi}(q^2)$, Eq. (1.25), does no longer consists of an infinite number of resonances; multiparticle channels starting at the $\pi\pi$ threshold manifest themselves instead as a cut along the real axis, allowing to express the vacuum polarization through a once-subtracted dispersion relation [58]

$$\begin{aligned}\hat{\Pi}(q^2) &= q^2 \int_{s_{th}}^{\infty} \frac{dt}{t(t - q^2 - i\varepsilon)} \frac{1}{\pi} \text{Im} \Pi(t + i\varepsilon) \\ &= z \int_0^1 \frac{du}{1 - uz - i\varepsilon} \frac{1}{\pi} \text{Im} \Pi\left(\frac{s_{th}}{u} + i\varepsilon\right),\end{aligned}\quad (1.34)$$

where $s_{th} = 4m_\pi^2$ is the lowest threshold for particle production, $z = q^2/s_{th}$, and a change of variables $t = s_{th}u^{-1}$ has been performed in the second line of Eq. (1.34). The fact that $\text{Im} \Pi(q^2)$ is related through the optical theorem to the $\sigma(e^+e^- \rightarrow \text{hadrons})$ cross section, a positive quantity, guarantees that such a function is of the Stieltjes kind.

Stieltjes functions are defined in terms of a Stieltjes integral [57],

$$f(z) = \int_0^{\infty} \frac{d\phi(u)}{1 + zu}, \quad |\arg(z)| < \pi, \quad (1.35)$$

where $\phi(u)$ is a bounded non-decreasing function²⁰ with finite and real-

¹⁹Defects are regions of the complex plane featuring a pole and a close-by zero —their effect is nevertheless limited to a neighborhood around it and not the whole complex plane.

²⁰Note that the function $\phi(u)$ is not even required to be continuous. As an example, $\phi(u) = \theta(u - u_0) \rightarrow d\phi(u) = \delta(u - u_0)du$, which is meromorphic and Stieltjes.

valued moments defining a formal expansion around the origin²¹

$$f_j = \int_0^\infty u^j d\phi(u), \quad j = 0, 1, 2, \dots \quad \Rightarrow \quad f(z) = \sum_{j=0}^{\infty} f_j (-z)^j. \quad (1.36)$$

Note that, given a continuous non-zero $d\phi(u)$ function non-vanishing along $0 \leq u \leq 1/R$, the Stieltjes function is not well defined in the real $-\infty < z \leq -R$ interval and a discontinuity $f(-z - i\varepsilon) \neq f(-z + i\varepsilon)$ appears along this, the reason for which Stieltjes functions are defined in the cut complex plane $|\arg(z)| < \pi$. Moreover, the original series expansion, Eq. (1.36), is convergent within the $|z| < R$ disk alone; for the vacuum polarization, $R = 4m_\pi^2$ corresponds to the threshold production, and the discontinuity at $4m_\pi^2 < z < \infty$ is related to the imaginary part or spectral function.

If a given function is of the Stieltjes kind, there is a well-known theorem in the theory of Padé approximants guaranteeing the convergence of the $P_N^{N+J}(z)$ sequence in the cut complex plane for $J \geq -1$. In addition, the poles (and zeros) of the approximant are guaranteed to lie along the negative real axis and to have positive residues.

An additional property that Stieltjes functions can be shown to obey is that the diagonal(subdiagonal) $P_{N(+1)}^N(z)$ sequence decreases(increases) monotonically as N increases, having a lower(upper) bound. Indeed, if $f(z)$ is a Stieltjes function,

$$\lim_{N \rightarrow \infty} P_{N+1}^N \leq f(z) \leq \lim_{N \rightarrow \infty} P_N^N(z), \quad (|\arg(z)| < \pi). \quad (1.37)$$

More generally, any P_N^{N+J} ($J \geq -1$) sequence is monotonically increasing(decreasing) for J odd(even).

The condition that a function is Stieltjes is a very strong one and guarantees the possibility to reconstruct such a function through the use of PAs. Moreover, poles and zeros from PAs are guaranteed to pile along the negative real axis, excluding the possibility of defects. This allows to reconstruct certain hadronic functions, like the vacuum polarization, in the whole cut complex plane. This reconstruction excludes nevertheless the threshold and resonance region (which is ill-defined as well in the original function) and PAs poles cannot be associated therefore to physical resonances but to analytic properties of the underlying function. The PA zeros and poles conspire thereby to mimic the effects from the discontinuity at the cut. We illustrate such effect in Fig. 1.6 for the Stieltjes function $z^{-1} \ln(1+z)$. These properties explain therefore the excellent performance of rational approaches beyond the naive large- N_c estimation. As a final remark, let us note that a function could be meromorphic and Stieltjes at the same time (i.e., if every pole has a positive-defined residue). In such a case, Stieltjes properties would apply as well.

²¹In addition, Stieltjes functions can be shown to obey certain determinantal conditions [55, 57]. See Ref. [58] for an application of them.

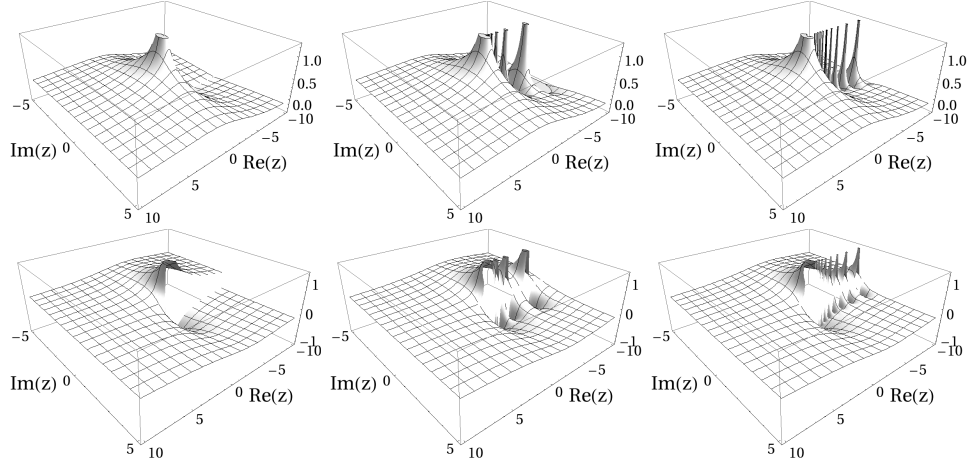


Figure 1.6: The $z^{-1} \ln(1+z)$ function (first column) is compared to the $P_{11}^{10}(z)$ and $P_{31}^{30}(z)$ PAs (second and third column). Upper(lower) row illustrates the real(imaginary) parts.

1.5.2 Extensions of Padé approximants

So far, we have only discussed the implementation of PAs based on the low-energy expansion Eq. (1.28). However, in the large- N_c approximation, or even in the real $N_c = 3$ world, one may wish to include the information about some resonances' position. Additionally, further information away from the origin could be available —the high-energy expansion among others. In this section, further extensions of PAs are presented allowing to incorporate this kind of information.

Padé type and partial Padé approximants

As said, from Montessus's and Pommerenke's theorems, it follows that, eventually, the poles and residues of the underlying function are reproduced by the approximant. However, it would be interesting to incorporate this information from the beginning whenever this is known. This possibility is brought by Padé type and partial Padé approximants.

Partial Padé approximants

If the lowest-lying K poles at $z = z_1, z_2, \dots, z_K$ from the underlying function are known in advance, this information could be incorporated from the beginning using the so called Partial Padé approximants defined as

$$\mathbb{P}_{M,K}^N(z) = \frac{Q_N(z)}{R_M(z)T_K(z)}, \quad (1.38)$$

where $Q_N(z)$, $R_M(z)$ are degree N and M polynomials and $T_K(z) = (z - z_1)(z - z_2)\dots(z - z_K)$ is a degree K polynomial defined as to have all the

zeros exactly at the first K -poles location.

Padé type approximants

Padé type approximants is another kind of rational approximant

$$\mathbb{T}_M^N(z) = \frac{Q_N(z)}{T_M(z)} \quad (1.39)$$

in which all the poles of the approximant are fixed in advance to the original function lowest-lying poles. This is, $T_M(z) = (z - z_1)(z - z_2)\dots(z - z_M)$. This requires however the knowledge of every pole of the original function if one is aiming to construct an infinite sequence ($N, M \rightarrow \infty$).

An interesting discussion and illustration of partial Padé and Padé type approximants is illustrated for a physical case, the $\langle VV - AA \rangle$ function, in Refs. [54, 59]. Here we only note that these approximants could justify why the MHA has often such a good performance—and a slower convergence—wrt PAs that offer an improvement based on a mathematical framework.

N-point Padé approximants

Eventually, one could have analytical information of a particular function, not only at the origin, but at different points, say, z_0 and z_1

$$f(z) = \sum_{n=0}^{\infty} a_n(z - z_0)^n, \quad f(z) = \sum_{n=0}^{\infty} b_n(z - z_1)^n, \quad (1.40)$$

which belongs to what is known as the rational Hermite interpolation problem. Typical cases is when low-energy, high energy or threshold behavior are known in advance. It is possible then to construct an N-point PA, $P_M^N(z)$, in which $J(K)$ terms are fixed from the series expansion around $z_0(z_1)$ from Eq. (1.40), where $J + K = N + M + 1$. Note that, for $N + M + 1$ points, this would correspond to a fitting function interpolating between the given points. In general, N-point PAs will produce an improved overall picture with respect to typical (one-point) PAs of the same order, whereas the latter will provide a more precise description around their expansion point.

1.6 The pseudoscalar transition form factors

The central object of interest in this thesis are the transition form factors (TFFs) describing the interactions of the lowest-lying pseudoscalar mesons (P) with two (virtual) photons and as such characterize the internal pseu-

doscalar structure. From the S -matrix element²²

$$\begin{aligned} \langle \gamma^* \gamma^* | S | P \rangle &\equiv i\mathcal{M}(P \rightarrow \gamma^* \gamma^*)(2\pi)^4 \delta^{(4)}(q_1 + q_2 - p) \\ &= \frac{(ie)^2}{2!} \int d^4x \int d^4y \langle \gamma^* \gamma^* | T \{ A_\mu(x) j_{\text{em}}^\mu(x), A_\nu(y) j_{\text{em}}^\nu(y) \} | P \rangle \\ &= -e^2 \int d^4x e^{iq_1 \cdot x} \int d^4y e^{iq_2 \cdot y} \langle 0 | T \{ j_{\text{em}}^\mu(x), j_{\text{em}}^\nu(y) \} | P \rangle \\ &= -e^2 \int d^4x e^{iq_1 \cdot x} \langle 0 | T \{ j_{\text{em}}^\mu(x), j_{\text{em}}^\nu(0) \} | P \rangle (2\pi)^4 \delta^{(4)}(q_1 + q_2 - p) \end{aligned} \quad (1.41)$$

where p, q_1 and q_2 represent the pseudoscalar and photon momenta, the relevant amplitude defining the pseudoscalar TFF can be extracted:

$$\begin{aligned} i\mathcal{M}(P \rightarrow \gamma^* \gamma^*) &= -e^2 \int d^4x e^{iq_1 \cdot x} \langle 0 | T \{ j_{\text{em}}^\mu(x), j_{\text{em}}^\nu(0) \} | P(p) \rangle \\ &\equiv ie^2 \epsilon^{\mu\nu\rho\sigma} q_{1\rho} q_{2\sigma} F_{P\gamma^*\gamma^*}(q_1^2, q_2^2), \end{aligned} \quad (1.42)$$

which represents a purely hadronic object. For the case of real photons, the TFFs can be related in the chiral (and, for the η' , combined large N_c) limit to the ABJ anomaly [1], obtaining for $F_{P\gamma^*\gamma^*}(0, 0) \equiv F_{P\gamma\gamma}$

$$\begin{aligned} F_{P\gamma\gamma} &= \frac{N_c}{4\pi^2 F} \text{tr}(\mathcal{Q}^2 \lambda^P) \Rightarrow \mathcal{M}(P \rightarrow \gamma\gamma) = e^2 \epsilon^{\mu\nu\rho\sigma} \epsilon_{1\mu}^* \epsilon_{2\mu}^* q_{1\rho} q_{2\sigma} F_{P\gamma\gamma} \\ &\Rightarrow \Gamma(P \rightarrow \gamma\gamma) = \frac{\pi \alpha^2 m_P^3}{4} F_{P\gamma\gamma}^2, \end{aligned} \quad (1.43)$$

where F is the decay constant in the chiral limit defined in Eq. (1.22) and $\lambda^P = \lambda^{3,8,0}$ for the π , η_8 and η_0 , respectively. For an elementary particle, the TFF would be constant, whereas for composite particles is expected to exhibit a q^2 -dependency providing valuable information on the pseudoscalar meson structure. To study the TFF from first principles in the most general q^2 regime poses a formidable task, for which the only firm candidate so far is lattice QCD —there exist some promising results in Refs. [60–62] within a limited energy range. Still, there exists some knowledge at some particular energy regimes where different approaches apply.

1.6.1 High-energies: perturbative QCD

At large space-like energies, the TFF can be calculated as a convolution of a perturbatively calculable hard-scattering amplitude T_H and a gauge invariant meson distribution amplitude (DA) $\phi_P^{(a)}$ encoding the non-perturbative dynamics of the pseudoscalar bound state [63] (summation over flavor $a = 3, 8, 0$ implied; alternatively $a = 3, q, s$ in the flavor basis, see Chapter 4),

$$F_{P\gamma^*\gamma^*}(Q_1^2, Q_2^2) = \text{tr}(\mathcal{Q}^2 \lambda^a) F_P^a \int_0^1 dx T_H(x, Q_{1,2}^2, \mu) \phi_P^{(a)}(x, \mu), \quad (1.44)$$

²² $j_{\text{em}}^\mu = \frac{2}{3}\bar{u}\gamma^\mu u - \frac{1}{3}\bar{d}\gamma^\mu d - \frac{1}{3}\bar{s}\gamma^\mu s \equiv \mathcal{Q}\bar{q}\gamma^\mu q$ defines the electromagnetic current —sum over quarks and colors is implicit.

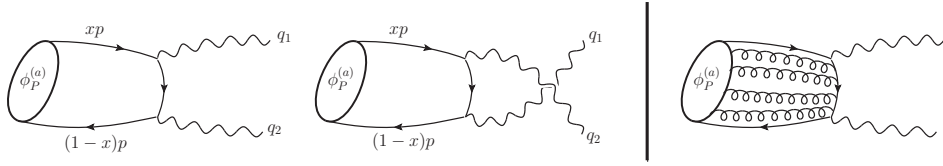


Figure 1.7: Left: leading order diagrams in pQCD contributing to the hard-scattering amplitude T_H . Right: gluon exchanges inducing a gauge link or Wilson line.

with $\bar{x} = 1 - x$. The hard scattering amplitude at LO²³ (see Fig. 1.7) reads

$$T_H^{\text{LO}} = \frac{1}{\bar{x}Q_1^2 + xQ_2^2} + (x \rightarrow \bar{x}), \quad (1.45)$$

whereas the DA can be defined in terms of the matrix element [67]²⁴

$$\langle 0 | \bar{q}(z_2) \gamma^\mu \gamma_5 [z_2, z_1] \frac{\lambda^a}{2} q(z_1) | P(p) \rangle = i p^\mu F_P^a \int_0^1 dx e^{-iz_{21} \cdot p} \phi_P^{(a)}(x, \mu), \quad (1.46)$$

where $z_{21} = \bar{x}z_2 + xz_1$ and obeys $\phi_P^{(a)}(x) = \phi_P^{(a)}(\bar{x})$. As a non-perturbative object, its particular shape is unknown from first principles at an arbitrary (renormalization) scale μ . However, its asymptotic behavior at large energies is well-known: the DA follows the ERBL evolution [63, 68] which allows for a convenient decomposition in terms of Gegenbauer polynomials

$$\phi_P^{(a)}(x, \mu) = 6x(1-x) \left(1 + \sum_{n=1}^{\infty} c_{2n, P}^{(a)}(\mu) C_{2n}^{3/2}(2x-1) \right), \quad (1.47)$$

with coefficients evolving at LO as^{25,26}

$$c_n^{(a)}(\mu) = \left(\frac{\alpha_s(\mu)}{\alpha_s(\mu_0)} \right)^{\gamma_n/\beta_0} c_n^{(a)}(\mu_0), \quad (1.48)$$

As a result, asymptotic freedom implies that at large $\mu^2 \sim Q_1^2 + Q_2^2$ the DA tends to the asymptotic one, $\phi^{\text{as}}(x) = 6x(1-x)$. Consequently, the high-energy behavior follows trivially from Eqs. (1.44) and (1.45), implying

$$\lim_{Q^2 \rightarrow \infty} F_P \gamma^* \gamma^*(Q^2, 0) = \frac{6F_P^a}{Q^2} \text{tr}(\mathcal{Q}^2 \lambda^a), \quad (1.49)$$

$$\lim_{Q^2 \rightarrow \infty} F_P \gamma^* \gamma^*(Q^2, Q^2) = \frac{2F_P^a}{Q^2} \text{tr}(\mathcal{Q}^2 \lambda^a). \quad (1.50)$$

²³The NLO result was calculated in Refs. [64, 65]. See also Ref. [66].

²⁴ $[z_2, z_1]$ represents a gauge link or Wilson line, see Fig. 1.7, right.

²⁵The LO anomalous dimensions read $\gamma_n = C_F \left(4 [\psi(n+2) + \gamma_E] - \left[3 + \frac{2}{(n+1)(n+2)} \right] \right)$,

$C_F = \frac{N_c^2 - 1}{2N_c} = \frac{4}{3}$ and $\alpha_s(\mu)$ evolution should be at LO. β_0 has been defined below Eq. (1.4).

²⁶An additional effect has to be accounted for the singlet component —a careful description can be found in Ref. [67]. Whereas it has a non-negligible effect, we postpone its discussion to Chapter 4 as it does not change the conclusions outlined below.

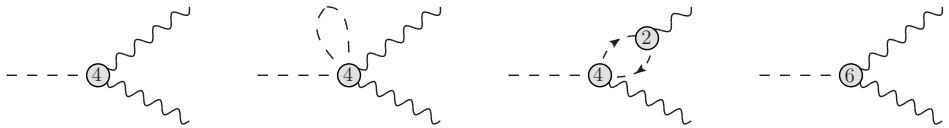


Figure 1.8: The different contributions up to $\mathcal{O}(p^6)$ to the $P\gamma\gamma$ process. First is LO $\mathcal{O}(p^4)$ contributions, while the other are NLO.

The first one is known as the Brodsky-Lepage (BL) asymptotic behavior, whereas the second one can be obtained independently from the OPE of two electromagnetic currents [69] which are solid pQCD predictions.

Even if the DA shape is largely unknown —the c_2 coefficient has been estimated from lattice QCD for the π^0 [70–72]— it can be modeled to reproduce the available experimental data for the space-like single-virtual TFF at Q^2 large enough (the double-virtual TFF has not been measured so far). This has been studied for the π^0 in light-cone pQCD [73], using light-cone sum rules, both for the π^0 [66, 74, 75] and η, η' [67], or using flat DAs —which became popular after the *BABAR* data release for the π^0 [76]— among others [77–80]. In addition, transverse momentum effects have been studied [81, 82]. Alternatively, the TFF has been analyzed using Dyson-Schwinger equations [83], from Holographic models [84] and employing anomaly sum rules [85, 86]. The agreement among different parameterizations and the conclusions drawn from different authors is not clear at all, except for the solid results Eqs. (1.49) and (1.50). Particularly, there is no consensus on the range on applicability of pQCD and the onset of the asymptotic behavior. In addition, the pQCD approach cannot be extended down to $Q^2 \rightarrow 0$ as the theory becomes non-perturbative there. In such limit, an appropriate candidate to describe the TFF is χ PT.

1.6.2 Low-energies: χ PT

At low-energies, χ PT can be used to provide the TFF behavior. At leading order $\mathcal{O}(p^4)$ ($\mathcal{O}(1)$ in $\ell N_c \chi$ PT), this is described via the WZW Lagrangian Eq. (1.19), which exactly reproduces the ABJ result Eq. (1.43). Remarkably, this is a free-parameter prediction once the decay constant F has been fixed from other processes. In order to probe the pseudoscalar structure, higher orders bringing mass and q^2 (and large- N_c) corrections are required. At NLO in χ PT, $\mathcal{O}(p^6)$, the TFF result arises from the diagrams in Fig. 1.8 and wave-function renormalization, and can be found in Refs. [87–89]. Using the

$\mathcal{L}_{6,\epsilon}$ Lagrangian from Ref. [90], the TFF reads ($p_{1,2}^2$ is a time-like quantity)

$$\begin{aligned} F_{P\gamma^*\gamma^*}(p_1^2, p_2^2) = & \frac{N_c \text{tr}(\mathcal{Q}^2 \lambda^P)}{4\pi^2 F_P} \left(1 - \frac{512\pi^2}{3} \left[2L_8^{6,\epsilon} c_P^8 + 2L_9^{6,\epsilon} c_P^9 + L_{19}^{6,\epsilon;r}(p_1^2 + p_2^2) \right] \right. \\ & + \frac{1}{96\pi^2 F^2} \left[- \left(\ln \left(\frac{m_\pi^2}{\mu^2} \right) + \ln \left(\frac{m_K^2}{\mu^2} \right) + \frac{2}{3} \right) p_1^2 + (p_1^2 - 4m_\pi^2) \right. \\ & \left. \times H \left(\frac{p_1^2}{m_\pi^2} \right) + (p_1^2 - 4m_K^2) H \left(\frac{p_1^2}{m_K^2} \right) + (p_1^2 \rightarrow p_2^2) \right] \right). \end{aligned} \quad (1.51)$$

At $q_1^2 = q_2^2 = 0$, corrections arise from the $L_{8,9}^{6,\epsilon}$ counterterms²⁷ which are nevertheless not necessary to render the $P \rightarrow \gamma\gamma$ amplitude finite since the divergence is reabsorbed in the wave-function renormalization upon $F \rightarrow F_P$ replacement, a result which holds only at NLO [91]. Furthermore, these corrections vanish in the chiral limit and they are commonly dismissed. For finite virtualities, an additional counterterm, $L_{19}^{6,\epsilon;r}$ is required to absorb the divergencies²⁸, incorporating a $p_{1,2}^2$ -dependency together with the $H(s)$ loop function (see Eq. (3.10) in Ref. [2])

$$H(s) = \begin{cases} 2 + \beta(s) \ln \left(\frac{\beta(s)-1}{1+\beta(s)} \right), & s \leq 0 \\ 2 + |\beta(s)| (2 \tan^{-1}(|\beta(s)|) - \pi), & 0 < s < 4 \\ 2 + i\pi\beta(s) + \beta \ln \left(\frac{1-\beta(s)}{1+\beta(s)} \right), & s \geq 4 \end{cases} \quad (1.52)$$

with $\beta(s) = \sqrt{1 - 4s^{-1}}$. A naive extrapolation to incorporate the η_0 singlet state would yield an analogous result to that in Eq. (1.51) with an extra $1/2$ factor in the second line. However, the inclusion of the singlet state requires invoking large N_c . It turns out that, in the $\ell N_c \chi$ PT counting, loops and the $L_9^{6,\epsilon}$ contributions are N_c suppressed. Consequently, the chiral logarithms and loop function should be absent together with $L_9^{6,\epsilon}$. Moreover, an additional purely singlet OZI-violating term Λ_3 [47] appears²⁹, which in contrast to $L_8^{6,\epsilon}$ cannot be avoided in order to cancel the F_0 QCD scale dependency. Describing the physical η and η' TFFs requires though to introduce the mixing, which we discuss in Chapter 4. It is well known that the TFF $p_{1,2}^2$ dependency in Eq. (1.51) is fully dominated by $L_{19}^{6,\epsilon}$ instead of the (a priori large) chiral logarithms [91, 92] —a sign that such a process is dominated from vector resonance effects, with the consequent breakdown of the chiral expansion at energies close to the resonance. Given the lowest-lying ρ and ω resonances, one cannot expect the chiral theory to work beyond 0.6 GeV² —even if including an infinite number of terms— and this cannot be matched to pQCD to provide a full-energy range description.

²⁷ $c_\pi^8 = \dot{M}_\pi^2$ and $c_\pi^9 = 0$; $c_{\eta_8}^8 = \frac{7\dot{M}_\pi^2 - 4\dot{M}_K^2}{3}$ and $c_{\eta_8}^9 = 8(\dot{M}_\pi^2 - \dot{M}_K^2)$; in a naive η_0 implementation, $c_{\eta_0}^8 = \frac{2\dot{M}_\pi^2 + \dot{M}_K^2}{3}$ and $c_{\eta_0}^9 = (\dot{M}_\pi^2 + \dot{M}_K^2)$.

²⁸ $L_{19}^{6,\epsilon} \rightarrow L_{19}^{6,\epsilon;r} + \frac{\delta}{8192\pi^4 F^2}$ with $\delta = (\frac{2}{\epsilon} + \ln(4\pi\mu^2) + \gamma_E + 1)$.

²⁹ Which amounts to replace $\frac{3\text{tr}(\mathcal{Q}^2 \lambda^0)}{4\pi^2 F_0} (1 - [...]) \rightarrow \frac{3\text{tr}(\mathcal{Q}^2 \lambda^0)}{4\pi^2 F_0} (1 + \Lambda_3 - [...])$ in Eq. (1.51).

1.6.3 Alternatives approaches and Padé theory

As previously stated, the presence of resonances limits the applicability of the chiral effective field theory which begs for the presence of additional degrees of freedom. One possibility is to parametrize these contributions into the chiral theory in terms of pseudoscalar mesons rescattering effects which are experimentally known [89]. Actually, this can be generalized advocating for a fully a dispersive framework [93–96] incorporating different time-like information. Note however that such approaches have in practice either a limited range of applicability or require some modeling assumptions.

Alternatively, the situation can be analyzed within the large- N_c limit of QCD in which the resonances are far more important than those effects which may be accounted for in χ PT or pQCD. From this point of view, one could describe the TFFs through modeling the infinite tower of vector resonances [97]. Alternatively, it has been customary to employ the MHA to saturate the TFF with a minimal finite amount of well-known resonances [98, 99]. Furthermore, there have been attempts to incorporate the resonances (within large N_c) explicitly into χ PT in what is known as resonance chiral perturbation theory [100, 101].

From an orthogonal point of view, PAs can be used to directly address the problem posed at the end of Sections 1.6.1 and 1.6.2, this is, to provide an interpolation between χ PT and pQCD (at least in the full space-like region) without the necessity of invoking large N_c —which is ultimately an approximation and requires some modeling. Recall that PAs do not only apply in the large- N_c limit of meromorphic functions, but offer an opportunity to go beyond this and to apply them to the real world, as it was shown for the case of Stieltjes functions. In this way, PAs allow to improve upon ideas as old as the MHA or the Brodsky-Lepage (BL) interpolation formula [102]. Moreover, having a limited amount of information, they provide improved convergence properties with respect to typical resonant approaches used nowadays. For the case of the TFF, the analytic properties of the function are much more intricate than for two-point Green's functions, and therefore we cannot anticipate convergence —note however that the salient features such as the $\pi\pi$ elastic rescattering and different resonances are of the Stieltjes kind. We can however check this a posteriori and estimate a systematic error from the convergence pattern, which we anticipate to be excellent, which provides an advantage with respect to previous methods. From this point of view, all the required information is encapsulated in the TFF series expansion

$$F_{P\gamma^*\gamma}(Q^2) = F_{P\gamma\gamma}(0, 0) \left(1 - b_P \frac{Q^2}{m_P^2} + c_P \frac{Q^4}{m_P^4} - d_P \frac{Q^6}{m_P^6} + \dots \right), \quad (1.53)$$

which can be determined from data as it is explained in the next chapter.

Chapter 2

Data analysis with Padé approximants

Contents

2.1	Introduction	27
2.2	Padé approximants as a fitting tool	28
2.3	Estimation of a systematic error	30
2.4	Space-like data: η and η' LEPs	34
2.5	Time-like data: η and η' LEPs	41
2.6	Conclusions	52

2.1 Introduction

For the phenomenological applications of pseudoscalar transition form factors (TFFs) covered in this thesis, we find that a very accurate description of these TFFs at very low energies —where no available experimental data exists— is required. For this reason, and regarding our approach based on Padé approximants (PAs) to reconstruct the TFFs, it is extremely important to our work to know the series expansion for the TFF at zero energies. For the moment, we will restrict ourselves to the simpler single virtual case

$$F_{P\gamma^*\gamma}(Q^2) \equiv F_{P\gamma^*\gamma^*}(Q^2, 0) = F_{P\gamma\gamma} \left(1 - b_P \frac{Q^2}{m_P^2} + c_P \frac{Q^4}{m_P^4} - d_P \frac{Q^6}{m_P^6} + \dots \right), \quad (2.1)$$

where b_P , c_P and d_P are referred to as slope, curvature and third derivative, respectively. The value for $F_{P\gamma\gamma} \equiv F_{P\gamma^*\gamma}(0)$ is well known for every pseudoscalar, as it is related to the Adler [42]-Bell-Jackiw [43] anomaly and can be theoretically related in χ PT to the meson decay constants for the

π^0, η and η' (the mixing parameters are required for the last two though, see Chapter 4). Furthermore, they can be experimentally extracted from the measured $P \rightarrow \gamma\gamma$ two-photon decays[10, 103–105]. In contrast, the additional low-energy parameters (LEPs) b_P, c_P, \dots cannot be obtained from first principles in QCD or predicted from χ PT, as their values are given in terms of unknown low-energy constants. Moreover, they are not directly related to any experimental quantity. Consequently, these parameters have always been obtained after modelization. For instance, with quark-loop models [88], Brodsky-Lepage interpolation formula [88, 102], resonance models [101] or χ PT supplied with vector meson dominance (VMD) ideas [87, 106].

A possible venue to address this problem would be to use low-energy experimental data so that χ PT or the series expansion, Eq. (2.1), apply. Then, the above parameters could be extracted from a fitting procedure in a model-independent way. However, these data at very low energies are, in general, not available, rather scarce, or not precise, and one relies then on fits to models from high-energy data to extract these parameters. Such procedure is model-dependent and implicitly includes a systematic error which has never been considered. Actually, depending on the fitted data set, inconsistencies seem to appear in some cases, for instance, when comparing space-like and time-like data-based extractions for the slope parameter b_η .

In this chapter, we show how PAs can be used as a data-fitting tool to extract valuable information of the underlying function —the single-virtual TFF— including, among others, the desired LEPs in Eq. (2.1). We illustrate that current inconsistencies cannot only be understood, but actually solved within a Padé framework. The results from this chapter represents the starting point of the following ones, as it provides the basic inputs for reconstructing the TFFs which are used in our calculations, as well as for extracting the $\eta - \eta'$ mixing parameters. We proceed as follows: in Section 2.2, we outline the procedure to obtain the LEPs from a fitting procedure. The corresponding systematic error is estimated in Section 2.3 through the use of different well-motivated models. Then, we apply our approach to the real case for the η and η' mesons using space-like data in Section 2.4. In Section 2.5, we argue, in view of the recent Dalitz decay measurements, why PAs could be applied to the low-energy time-like region as well, reevaluating our LEPs extraction. We give our conclusions and main results in Section 2.6.

2.2 Padé approximants as a fitting tool

Traditionally, the lack of low-energy data for the TFF has implied that the LEPs have been determined from phenomenological fits to high-energy data.

There, the vector meson dominance (VMD) fitting function

$$F_{P\gamma^*\gamma}^{VMD}(Q^2) = F_{P\gamma\gamma} \frac{\Lambda^2}{\Lambda^2 + Q^2} \quad (2.2)$$

has been employed [107, 108], which then —upon expansion— allowed to extract a determination for the slope b_P parameter, which for this model is given by $b_P = m_P^2/\Lambda^2$. Additional LEPs were not discussed in this context though as they are all fixed in the ansatz above (i.e. $c_P = b_P^2$). Moreover, given the quality and precision of previous data, this discussion was irrelevant then, a situation which has changed with the recent release of new and more precise data in a wider energy regime, which makes timely a study of this kind. The possible deficiencies and model dependencies from this approach can be easily understood from Padé theory, where the old VMD determinations can be understood as the simplest step in a systematic and convergent expansion [54, 109]. As such, this implies that previous fitting approaches —implying large systematic uncertainties as we illustrate below— can be systematically improved, which makes possible not only a more accurate determination for b_P , but a meaningful extraction for additional parameters such as c_P and d_P in a model-independent way after performing the expansion of Eq. (2.1) for the fitted approximants.

Certainly, previous assertion relies on the assumption that the underlying function is such that some convergence to a given PA sequence exists, so our fits and the LEPs extracted from them will converge to the real ones. Having incomplete analytical information about the TFFs, this cannot be guaranteed beforehand. Note however that the prominent features around $Q^2 = 0$ and the space-like region seem dominated by the role of the lowest-lying resonances —of almost meromorphic nature— and the $\pi\pi$ rescattering effects, essentially accounting for the ρ width —basically of Stieltjes nature. The existing convergence theorems, see Section 1.5.1, would justify then an excellent performance, at least, in the space-like region, of main interest for our applications. Finally, even in the case where convergence to the underlying function cannot be guaranteed —nor disproved—, the PAs practitioner can still judge on the convergence of a given sequence *a posteriori* after the fitting procedure. We illustrate this in the following with the help of three different well-motivated models, where the different scenarios described above apply. This exercise will provide not only helpful to describe and get familiar with the procedure we use to extract the LEPs, but to assess a systematic error that we will employ when determining the LEPs from real data.

The last point to discuss is the kind of sequences that should be used then for the fitting procedure. A glance at time-like data reveals that the first resonance effects are dominating the low-energy time- and space-like

description, meaning that including a single pole is enough to achieve a precise description and motivates the use of the P_1^N sequence. It is important to note however that such description violates unitarity at high energies as it diverges as $(Q^2)^{N-1}$. This motivates the use of a second sequence, P_{N+1}^N , which can be thought of as a two-point PA (see Section 1.5.2) and incorporates the appropriate high-energy BL behavior, see Eq. (1.49), $F_{P\gamma^*\gamma}(Q^2) \sim Q^{-2}$. Given the uncertainty about convergence, cross-checking the results from both sequences will reassure the consistency of the method. In what follows, we restrict our attention to these two sequences. Alternative choices exist, as for instance, Padé- or partial Padé-type approximants, see Section 1.5.2. Their arbitrariness in choosing a pole, and their slower convergence as compared to the previous ones make them less attractive, and we do not further consider their study.

2.3 Estimation of a systematic error

For testing the convergence of our chosen P_1^N and P_{N+1}^N sequences, we propose the use of three different motivated theoretical models out of the vast literature, which will illustrate the performance of our approach in different representative situations. These are, the large- N_c Regge model from Refs. [97, 110], the logarithmic model in Ref. [111]—which finds inspiration in flat distribution amplitudes [77] and quark models [112]— and the holographic model proposed in Refs. [84, 113]. For studying the convergence pattern, we generate a set of pseudo-data points in a similar manner to how real experimental data are distributed. As this is to represent the ideal case where the function is known up to arbitrary precision, we don't ascribe any error to the data for our fitting procedure, and therefore it does not make sense to give the χ^2 from the fits. Finally, we perform the expansion in Eq. (2.1) to extract the LEPs from our fits and compare.

2.3.1 Large- N_c Regge model

The large- N_c model from Refs. [97, 110] consists of an infinite sum of vector resonances, which sum can be expressed in terms of the polygamma function $\psi^{(n)} = \frac{d^{n+1}}{z^{n+1}} \ln \Gamma(z)$ with $\Gamma(z)$ the Gamma function,

$$F_{P\gamma^*\gamma}(Q^2) = \frac{a F_{P\gamma\gamma}}{Q^2 \psi^{(1)}\left(\frac{M^2}{a}\right)} \left[\psi^{(0)}\left(\frac{M^2 + Q^2}{a}\right) - \psi^{(0)}\left(\frac{M^2}{a}\right) \right]. \quad (2.3)$$

The parameters above have been slightly renamed for convenience with respect to those appearing in Refs. [97, 110]. To reproduce the physical case, we choose the experimental $F_{P\gamma\gamma} \equiv F_{P\gamma\gamma}(0, 0)$ together with $a = 1.3 \text{ GeV}^2$ and $M^2 = \lambda \times 0.64 \text{ GeV}^2$ [111, 114] where $\lambda = 1, 0.95, 1.05$ for the π^0, η, η' ,

	P_1^0	P_1^1	P_1^2	P_1^3	P_1^4	P_1^5	P_1^6	P_1^7	P_2^1	P_3^2	Exact
$F_{P\gamma\gamma}$	0.268	0.273	0.274	0.275	0.275	0.275	0.275	0.275	0.275	0.275	0.275
b_P	0.332	0.373	0.394	0.404	0.411	0.416	0.419	0.421	0.413	0.425	0.426
c_P	—	0.143	0.163	0.173	0.182	0.188	0.192	0.195	0.185	0.201	0.204
d_P	—	—	0.067	0.074	0.081	0.085	0.088	0.091	0.083	0.097	0.100

Table 2.1: LEPs determination from the space-like pseudo-data set for the large- N_c Regge model. $F_{P\gamma\gamma}$ is expressed in GeV^{-1} ; additional quantities are dimensionless.

respectively¹. In what follows, we focus in the η case, though very similar results are obtained for the η' as it shares a similar TFF and available data sets. Actually, the results for the π^0 are similar too, see Ref. [111]. For this model convergence is expected as it is a meromorphic function, which in addition represents the interesting case in which the large- N_c limit applies.

Adopting the points defined in Ref. [114] —10 points in the region $0.6 < Q^2 < 2.2 \text{ GeV}^2$, 15 points in the region $2.7 < Q^2 < 7.6 \text{ GeV}^2$ and 10 points in the region $8.9 < Q^2 < 34 \text{ GeV}^2$ — which resembles the experimental situation, we obtain the results in Table 2.1. We find the expected convergence pattern we anticipated (note that the curvature and third derivative are not extracted up to P_1^1 and P_1^2 , respectively). Moreover, we find an hierarchy: there is a faster convergence for $F_{P\gamma\gamma} \equiv F_{P\gamma^*\gamma}(0)$, then for b_P , and so on. An important observation at this point is that no matter whether strong correlations and, possibly, a tiny χ^2 value in the real case appear, the highest the element within a sequence, the better the extraction for the LEPs becomes—a feature common to all the models and characteristic of PAs. Therefore, we should aim for the largest possible element in our sequence when fitting real data for extracting our desired parameters. In addition, we find that the P_{N+1}^N sequence has the better performance—note though that this sequence increases its number of parameters in units of two, so the P_2^1 should be compared with the P_1^2 and so on. This can be understood from the fact that, even if at these energies it is the influence of the first pole that dominates, there are additional higher resonances. Not less, this sequence implements as well the appropriate high-energy behavior, relevant for the data range we are using. In Section 2.5, we will employ also some very low-energy time-like data points in addition to the space-like ones. Given their small q^2 values, we expect that they significantly improve the accuracy from our determination, which demands a new systematic error evaluation. For this, we add to our previous pseudo-data set 8 points in the $(0.045)^2 < q^2 < (0.100)^2 \text{ GeV}^2$ region, 15 points in the $(0.115)^2 < q^2 < (0.200)^2 \text{ GeV}^2$ region and 31 points in the $(0.230)^2 < q^2 < (0.470) \text{ GeV}^2$ region in order to reproduce the experimental

¹The parameter a is taken from the analysis of different Regge trajectories in Ref. [115]. For the π^0 , M is roughly the ρ and ω meson masses. For the η and η' there is an interplay of ρ , ω and ϕ resonances [116] which effectively translates in the λ parameter.

	P_1^0	P_1^1	P_1^2	P_1^3	P_1^4	P_1^5	P_1^6	P_1^7	P_2^1	P_3^2	Exact
$F_{P\gamma}$	0.279	0.276	0.275	0.275	0.275	0.275	0.275	0.275	0.275	0.275	0.275
b_P	0.415	0.433	0.437	0.437	0.436	0.435	0.435	0.434	0.435	0.433	0.426
c_P	—	0.196	0.204	0.207	0.209	0.210	0.210	0.210	0.210	0.210	0.204
d_P	—	—	0.095	0.098	0.101	0.102	0.102	0.103	0.102	0.104	0.100

Table 2.2: LEPs determination from the space- and time-like pseudo-data set for the large- N_c Regge model. $F_{P\gamma\gamma}$ is expressed in GeV^{-1} ; additional quantities are dimensionless.

	P_1^0	P_1^1	P_1^2	P_1^3	P_1^4	P_1^5	P_1^6	P_1^7	P_2^1	P_3^2	Exact
$F_{P\gamma}$	0.268	0.273	0.274	0.275	0.275	0.275	0.275	0.275	0.275	0.275	0.275
b_P	0.159	0.196	0.217	0.227	0.233	0.238	0.241	0.243	0.233	0.247	0.250
c_P	—	0.040	0.052	0.058	0.063	0.068	0.071	0.073	0.064	0.078	0.083
d_P	—	—	0.012	0.015	0.017	0.020	0.021	0.023	0.018	0.026	0.031

Table 2.3: LEPs determination from the space-like pseudo-data set for the logarithmic model. $F_{P\gamma\gamma}$ is expressed in GeV^{-1} ; additional quantities are dimensionless.

situation [117]. Our results are displayed in Table 2.2. We find very similar conclusions together with an improved accuracy —to be expected from the increased amount of low-energy data points.

2.3.2 Logarithmic model

This model finds inspiration in quark models [112] or flat distribution amplitudes [77], which have been proposed ever since the puzzling *BABAR* data for the π^0 TFF [76] were released. The model includes a logarithmic enhancement with respect to the BL asymptotic behavior,

$$F_{P\gamma^*\gamma^*}(Q^2) = \frac{F_{P\gamma\gamma} M^2}{Q^2} \ln \left(1 + \frac{Q^2}{M^2} \right), \quad (2.4)$$

with $M^2 = 0.6 \text{ GeV}^2$ [77] to reproduce *BABAR* data [76] and $F_{P\gamma\gamma}$ to reproduce the physical value. This second model is known to belong to the class of Stieltjes functions, which guarantees the performance of the method and allows to test the effects of perturbative logarithms as well, representing therefore an interesting case of study. Taking the pseudo-data points discussed above, we find the results in Table 2.3. Again, we can reach to very similar conclusions as those in the Regge model. Moreover, we find that in this case the P_{N+1}^N sequence has even better performance with respect to the P_1^N than in the previous case. This can be understood from the convergence theorems for Stieltjes functions existing for the P_{N+1}^N sequence (see Section 1.5.1) and from the much more involved analytic structure which a cut implies with respect to a single pole. Once more, we reanalyze the systematic error for the case where we include the time-like data points on top and display the results in Table 2.4

	P_1^0	P_1^1	P_1^2	P_1^3	P_1^4	P_1^5	P_1^6	P_1^7	P_2^1	P_3^2	Exact
$F_{P\gamma}$	0.281	0.278	0.276	0.276	0.275	0.275	0.275	0.275	0.281	0.275	0.275
b_P	0.199	0.230	0.245	0.251	0.253	0.253	0.253	0.253	0.253	0.251	0.250
c_P	—	0.057	0.068	0.075	0.079	0.081	0.082	0.083	0.081	0.084	0.083
d_P	—	—	0.019	0.022	0.025	0.027	0.028	0.029	0.027	0.031	0.031

Table 2.4: LEPs determination from the space- and time-like pseudo-data set for the logarithmic model. $F_{P\gamma\gamma}$ is expressed in GeV^{-1} ; additional quantities are dimensionless.

	P_1^0	P_1^1	P_1^2	P_1^3	P_1^4	P_1^5	P_1^6	P_1^7	P_2^1	P_3^2	Exact
$F_{P\gamma}$	0.279	0.277	0.276	0.276	0.275	0.275	0.275	0.275	0.275	0.275	0.275
b_P	0.376	0.357	0.342	0.334	0.327	0.322	0.319	0.316	0.307	0.311	0.311
c_P	—	0.126	0.114	0.107	0.101	0.096	0.092	0.090	0.078	0.083	0.083
d_P	—	—	0.038	0.034	0.031	0.028	0.026	0.025	0.018	0.017	0.021

Table 2.5: LEPs determination from the space-like pseudo-data set for the holographic model. $F_{P\gamma\gamma}$ is expressed in GeV^{-1} ; additional quantities are dimensionless.

2.3.3 Holographic model

Finally, we take a model based on light-front holographic QCD from Ref. [84] and we restrict ourselves, for simplicity, to the simplest leading twist result (though similar patterns are found for the other models in [84])

$$F_{P\gamma^*\gamma^*}(Q^2) = \frac{P_{q\bar{q}}}{\pi^2 F_\pi} \int_0^1 \frac{dx}{(1+x)^2} x^{Q^2 P_{q\bar{q}}/(8\pi^2 F_\pi^2)} \quad (2.5)$$

with $P_{q\bar{q}} = 1/2$ in order to reproduce the anomaly result. This model represents a particularly interesting case as, in contrast to previous models, no convergence-theorem is known for it, which represents a similar situation to that in the real world. Taking the previous pseudo-data points, we obtain the results in Table 2.5. Remarkably, we can reach similar conclusions to those in previous sections even if no convergence theorem could be provided in this case. Again, we use in addition the combined time- and space-like pseudo-data points obtaining the results in Table 2.6

2.3.4 Final results

To summarize, we find after comparing to different well-motivated models that, both, P_1^N and P_{N+1}^N sequences have a great performance for extracting the LEPs through a fitting procedure from experimental data. We emphasize that this may be the case even when convergence is not guaranteed, see Section 2.3.3. As an important result, we show that in order to have the most accurate prediction, we should reach the highest element in each sequence regardless of correlations or $\chi^2_\nu \ll 1$ values. In this respect, we remark that we do not aim for the best fitting-function rather than for the best LEPs extraction. In addition, we find that it is the P_{N+1}^N sequence which has the better performance, though it increases its number of parameters in units of two, making the fitting procedure more complicated than for

	P_1^0	P_1^1	P_1^2	P_1^3	P_1^4	P_1^5	P_1^6	P_1^7	P_2^1	P_3^2	Exact
$F_{P\gamma}$	0.271	0.273	0.274	0.274	0.275	0.275	0.275	0.275	0.275	0.275	0.275
b_P	0.334	0.323	0.316	0.313	0.310	0.310	0.310	0.310	0.311	0.311	0.311
c_P	—	0.102	0.095	0.091	0.087	0.085	0.084	0.083	0.082	0.083	0.083
d_P	—	—	0.028	0.026	0.024	0.023	0.022	0.022	0.020	0.020	0.021

Table 2.6: LEPs determination from the space- and time-like pseudo-data set for the holographic model. $F_{P\gamma\gamma}$ is expressed in GeV^{-1} ; additional quantities are dimensionless.

	P_1^0	P_1^1	P_1^2	P_1^3	P_1^4	P_1^5	P_1^6	P_1^7	P_2^1	P_3^2
$F_{P\gamma}$	6/0	2/0	1/0	0.5/0	0.1/0	0/0	0/0	0/0	0.1/0	0/0
b_P	40/20	20/10	15/5	10/5	5/1	5/1	5/1	5/0.5	5/1	1/0
c_P	—	50/30	40/20	30/10	25/5	20/1	15/1	10/1	25/3	5/0
d_P	—	—	60/40	50/30	45/20	40/15	30/10	30/5	45/15	15/2

Table 2.7: Our final systematic errors in % for the SL/(SL+TL) data sets

the P_1^N sequence. In order to estimate the systematic errors, we adopt a conservative approach and take those arising from the quark model, which shows the slowest convergence pattern, obtaining the results in Table 2.7—such table represents the main result from this section. At this point, we find that it is possible to have a meaningful extraction for the slope and curvature parameters in both data sets, whereas an accurate extraction for the third derivative is only possible and considered in our combined space- and time-like data set study. In addition, an analogous procedure shows that experimental determinations for b_P based on time-like data alone should be ascribed an additional 5% systematic error.

2.4 Space-like data: η and η' LEPs

Having demonstrated the excellent performance of Padé approximants as fitting functions to extract the LEPs, and having estimated a systematic error for the procedure, we proceed to their extraction in the real case. This was done for the π^0 in Ref. [111] and we extend this approach to the η and η' below [114]. For that, we start using all the available data in the space-like region in which convergence is expected. This comprises the measurements from CELLO [107], CLEO [108] and *BABAR* [118] for the η and η' , and the additional L3 Collaboration [105] data-set at low-energies for the η' . In addition, we use the measured two-photon decay widths $\Gamma_{\eta \rightarrow \gamma\gamma} = 0.516(18)$ keV [10] and $\Gamma_{\eta' \rightarrow \gamma\gamma} = 4.35(14)$ keV [10], dominated from the recent KLOE-2 [104] and L3 [105] measurements, respectively. For the fitting procedure, we take the function $Q^2 F_{\eta^{(\prime)}\gamma^*\gamma}(Q^2)$ rather than $F_{\eta^{(\prime)}\gamma^*\gamma}(Q^2)$, since this is the standard way in which experimental data has been published, with the exception of L3 and CELLO² collaborations. For

²The CELLO Collaboration does not report a systematic error for each bin of data. While for the η' case such error is 16% of the total number of events (which we translate

these, we transform their results into $Q^2 F_{\eta^{(\prime)}\gamma^*\gamma}(Q^2)$. Moreover, we relate the two-photon decay widths to $F_{\eta^{(\prime)}\gamma^*\gamma}(0)$ using the relation

$$|F_{P\gamma\gamma}|^2 = \frac{64\pi}{(4\pi\alpha)^2} \frac{\Gamma_{P\rightarrow\gamma\gamma}}{m_P^3}, \quad (2.6)$$

obtaining $F_{\eta\gamma\gamma} = 0.2738(47)$ GeV $^{-1}$ and $F_{\eta'\gamma\gamma} = 0.3437(55)$ GeV $^{-1}$.

For the fitting procedure, we employ the P_1^N and P_{N+1}^N sequences motivated in the previous sections, which translate into the P_1^N and P_N^N sequences for the $Q^2 F_{\eta^{(\prime)}\gamma^*\gamma}(Q^2)$ published data. Then, we must reach the highest possible element within a sequence as to maximally reduce the systematic uncertainty for the LEPs extraction as shown in the previous section. However, when using real data, it is not possible to go all the way up to an arbitrary large N element. At some point, some of these parameters from which our PAs are built become statistically compatible with zero, meaning that its extraction is meaningless. We must stop at this point and take this result as our better extraction, and ascribe a systematic error as estimated from our results in the previous section.

In order to show the performance of our method, we employ a bottom-up approach. We start fitting the $Q^2 F_{\eta^{(\prime)}\gamma^*\gamma}(Q^2)$ space-like data without any information at $Q^2 = 0$. This means in particular that the mathematical limit $\lim_{Q^2 \rightarrow 0} Q^2 F_{\eta^{(\prime)}\gamma^*\gamma}(Q^2) = 0$ is not imposed but extracted from data. In a second step, we impose such limit making use of PAs whose numerator starts at order Q^2 (i.e. there is no constant term). This study allows then to extract the TFFs at zero, and therefore predict the two-photon partial decay widths in addition to the slope and curvature parameters. Finally, as a last step, we incorporate the measured two-photon partial widths in our set of data, to be fitted together with the space-like data points. This approach will show the robustness of our results.

Starting then without constraining the $\lim_{Q^2 \rightarrow 0} Q^2 F_{\eta^{(\prime)}\gamma^*\gamma}(Q^2) = 0$ limit, we find that our fits “see the zero” for the η and η' cases within two and one standard deviations for the η and η' , respectively. Particularly, we find $P_1^1(0) = 0.059(29)$ and $P_1^3(0) = -0.02(3)$ for the η and η' , respectively. Once this is seen to be zero, the next coefficient in its series expansion is associated with the TFF normalization. We find $F_{\eta'\gamma\gamma}(0) = 0.38(6)$ GeV $^{-1}$, which translates into $\Gamma_{\eta'\rightarrow\gamma\gamma} = 5.3(1.7)$ keV. This illustrates the potential of space-like data, which are ranging from 0.6 to 35 GeV 2 in the η case and

into 32% for each bin), for the η case only 12% for the two-photon channel is reported. Accounting for all the different systematic sources we could find in the publication, we ascribe a 12% of systematic error for the hadronic η decay which leads to a 6% error for the global number of events (implying 12% systematic error for each bin).

η					η'					
N	b_η	c_η	$F_{\eta\gamma\gamma}$, GeV $^{-1}$	χ_ν^2	N	$b_{\eta'}$	$c_{\eta'}$	$F_{\eta'\gamma\gamma}$, GeV $^{-1}$	χ_ν^2	
$P_1^N(Q^2)$	2	0.45(13)	0.20(12)	0.235(53)	0.79	5	1.25(16)	1.57(42)	0.339(17)	0.70
$P_N^N(Q^2)$	1	0.36(6)	0.13(4)	0.201(28)	0.78	1	1.19(6)	1.42(15)	0.332(15)	0.68

Table 2.8: LEPs for the η and η' TFFs obtained from our fits *without including* information on $\Gamma_{P \rightarrow \gamma\gamma}$. The first column indicates the type of sequence used for the fit and N is the highest order achieved. We also present the quality of the fits in terms of χ_ν^2 . Errors are only statistical and symmetrized.

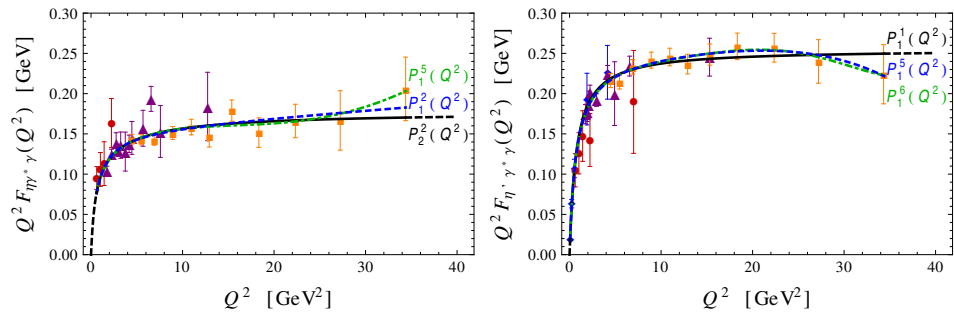


Figure 2.1: η (left panel) and η' (right panel) TFFs best fits. Blue-dashed lines show our best $P_1^L(Q^2)$ *without including* the $\Gamma_{P \rightarrow \gamma\gamma}$ information in our fits; green-dot-dashed lines show our best $P_1^L(Q^2)$ when *including* the $\Gamma_{P \rightarrow \gamma\gamma}$ information in our fits; black-solid lines show our best $P_N^N(Q^2)$ in the latter case, which extrapolation down to $Q^2 = 0$ and $Q^2 \rightarrow \infty$ is shown as a black-dashed line. Experimental data points are from CELLO (red circles) [107], CLEO (purple triangles) [108], L3 (blue diamonds) [105], and BABAR (orange squares) [118] collaborations.

from 0.06 to 35 GeV 2 for the η' , to predict LEPs, which are our main aim for further applications in this work [114].

Next, we make use of $\lim_{Q^2 \rightarrow 0} Q^2 F_{\eta^{(\prime)}\gamma^*\gamma}(Q^2) = 0$, meaning that the PAs numerator starts already at order Q^2 . This simple constraint allows for an improved LEPs determination, shown in Table 2.8. In this case, we reach up to the second and fifth elements of the P_1^L sequence for the η and η' , respectively, which TFFs are shown in Fig. 2.1. Unfortunately, it is not possible to go beyond the first element for the P_N^N sequence in both cases: for higher elements, the fit places poles in the space-like region, mimicking statistical fluctuations in the data —such results should not be considered and the sequence should be truncated at this point. Remarkably, in this approach we obtain $\Gamma_{\eta \rightarrow \gamma\gamma} = 0.38(17)$ keV and $\Gamma_{\eta' \rightarrow \gamma\gamma} = 4.22(42)$ keV, at 0.8 and 0.3 standard deviations from their physical values.

Finally, we include in our fits the two-photon decay widths through Eq. (2.6). In this case, we reach, for the P_1^L sequence, up to the fifth and sixth element for the η and η' , respectively. On the other hand, *including*

	η				η'			
	N	b_η	c_η	χ^2_ν	N	$b_{\eta'}$	$c_{\eta'}$	χ^2_ν
$P_1^N(Q^2)$	5	0.58(6)	0.34(8)	0.80	6	1.30(15)	1.72(47)	0.70
$P_N^N(Q^2)$	2	0.66(10)	0.47(15)	0.77	1	1.23(3)	1.52(7)	0.67
Final		0.60(6)	0.37(10)			1.30(15)	1.72(47)	

Table 2.9: LEPs for the η and η' TFFs obtained from our fits when *including* information on $\Gamma_{P \rightarrow \gamma\gamma}$. The first column indicates the type of sequence used for the fit and N is the highest order achieved. The last row shows our final result for each LEP —find details in the text. We also present the quality of the fits in terms of χ^2_ν . Errors are only statistical and symmetrized.

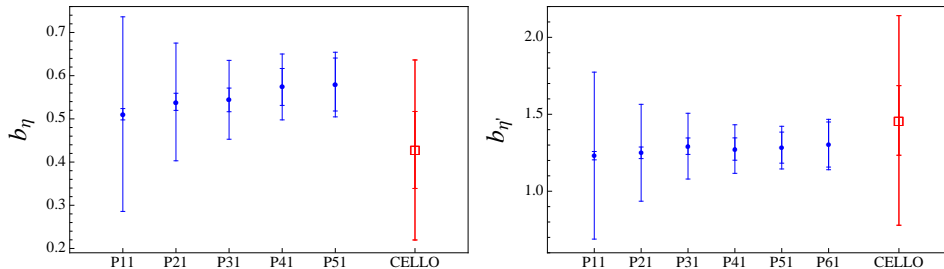


Figure 2.2: Slope predictions for the η (left panel) and η' (right panel) TFFs using the $P_1^L(Q^2)$ sequence (blue circles). The inner error bars correspond to the statistical error of the different fits. The outer error bars are the combination of statistical and systematic errors determined as explained in the main text. The CELLO determination is also shown for comparison (empty-red squares).

$\Gamma_{P \rightarrow \gamma\gamma}$ allows to reach up to the second element in the P_N^N sequence for the η , whereas this is not possible for the η' . The obtained TFFs are shown in Fig. 2.1. The LEPs obtained for these cases are shown in Table 2.9. The similarity for these results and those found previously *without including* the two-photon decay widths, Table 2.9, are quite reassuring. On top, we show our convergence results for the slope b_P and curvature c_P parameters within the P_1^L sequence in Figs. 2.2 and 2.3, where the systematic errors are taken from Table 2.7. The observed pattern shows an excellent convergence. In these plots, we show in addition the results from CELLO for $b_{\eta(\eta')}$ obtained from a VMD model fit [107]. To perform an appropriate comparison, we add to their determinations an additional 40% error corresponding to the P_1^1 element as determined in Table 2.7.

In addition, we comment on the fitted poles obtained from the P_1^N sequence, which we show in Fig. 2.4, and range from $\sqrt{s_p} = (0.71 - 0.77)$ GeV and $\sqrt{s_p} = (0.83 - 0.86)$ GeV for the η and η' respectively. We note that such pole does not correspond to a particular physical resonance. It corresponds instead to an effective parameter which effectively accounts for the presence of different resonances, threshold effects and analytic structure

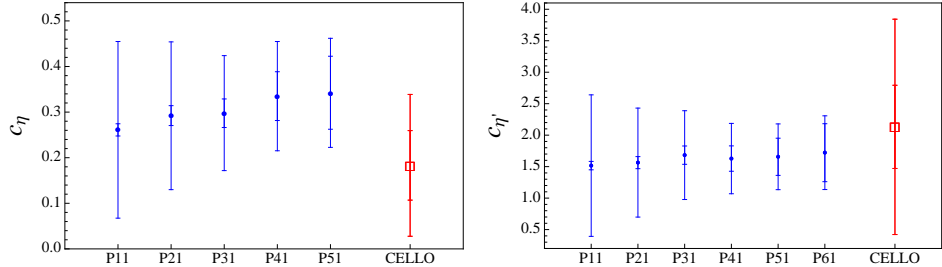


Figure 2.3: Curvature predictions for the η (left panel) and η' (right panel) TFFs using the $P_1^L(Q^2)$ sequence (blue circles). The inner error bars correspond to the statistical error of the different fits. The outer error bars are the combination of statistical and systematic errors determined as explained in the main text. The CELLO determination is also shown for comparison (empty-red squares).

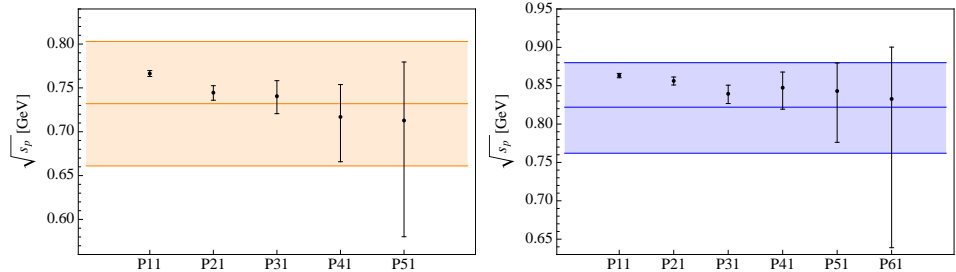


Figure 2.4: Pole-position predictions for the η (left panel) and η' (right panel) TFFs using the $P_1^L(Q^2)$ sequence. For comparison, we also display (orange and blue bands) the range $m_{\text{eff}} \pm \Gamma_{\text{eff}}/2$ corresponding to the effective VMD meson resonance evaluated using the half-width rule (see main text for details).

of the whole function in general. For comparison, we show as orange and blue bands what would correspond to the effective VMD meson resonance, m_{eff} [116] using $m_\rho = 0.775$ GeV, $\Gamma_\rho = 0.148$ GeV, $m_\omega = 0.783$ GeV, $\Gamma_\omega = 0.008$ GeV, $m_\phi = 1.019$ GeV and $\Gamma_\phi = 0.004$ GeV and a mixing angle in the flavor basis $\phi = 39^\circ$ (see Chapter 4). Alternatively, see Ref. [119] or the updated values of Ref. [120] in [114]). The bands represent the range of such mass implied by the half-width rule [115, 121, 122], i.e., $m_{\text{eff}} \pm \Gamma_{\text{eff}}/2$, which offers a nice estimation of large- N_c corrections to typical resonance approaches. We obtain $m_{\text{eff}} = 0.732(71)$ GeV and $m_{\text{eff}} = 0.822(58)$ GeV for the η and η' . As already indicated in Refs. [54, 59, 109, 111], fitting space-like data in resonant models does not produce an accurate determination for resonance parameters. We do not recommend then this method for such determination. For an alternative model-independent method, we refer to the interested readers to Refs. [123, 124].

Finally, it is possible from the P_N^N sequences to extrapolate beyond the available data up to arbitrary large Q^2 values (dashed lines in Fig. 2.1),

which allows for extracting the asymptotic behavior. For the η , we reach up to the second element, while for the η' we reach only up to the first element due to the appearance, once more, of space-like poles mimicking statistical noise in the data. We obtain [114]

$$\lim_{Q^2 \rightarrow \infty} Q^2 F_{\eta\gamma^*\gamma}(Q^2) = 0.160(24) \text{ GeV}, \quad (2.7)$$

$$\lim_{Q^2 \rightarrow \infty} Q^2 F_{\eta'\gamma^*\gamma}(Q^2) = 0.255(4) \text{ GeV}. \quad (2.8)$$

We emphasize here that previous errors—which are statistical alone—could be deceptive. While the results for the η , arising from a higher element, suggest a larger error than for the η' counterpart, the last has an intrinsic larger systematic error and it would be desirable as well for the η' to reach a higher element, an achievement which is not possible with the available data so far. For completeness, if we would have used the P_1^1 element for extracting the asymptotic behavior of the η , we would have obtained 0.160(3) GeV instead. The similarity with Eq. (2.7) is reassuring.

Finally, combining in weighted average our results in Table 2.9 from the different sequences when *including* the information on $\Gamma_{P \rightarrow \gamma\gamma}$, we obtain [114]

$$b_\eta = 0.60(6)_{\text{stat}}(3)_{\text{syst}} \quad c_\eta = 0.37(10)_{\text{stat}}(7)_{\text{syst}}, \quad (2.9)$$

$$b_{\eta'} = 1.30(15)_{\text{stat}}(7)_{\text{syst}} \quad c_{\eta'} = 1.72(47)_{\text{stat}}(34)_{\text{syst}}, \quad (2.10)$$

where the second error is systematic, of the order of 5% and 20% for b_P and c_P , respectively. When the spread of the central values for the weighted averaged result is larger than the error after averaging, we enlarge this error to cover the spread³. For the η' case, we could only reach the first element within the P_N^N sequence. Since the first error of each sequence has a large systematic uncertainty, this should not be used, and consequently, we do not include it in our averaged result.

For the η , the slope of the TFF obtained in Eq. (2.9) can be compared with $b_\eta = 0.428(89)$ from CELLO [107] and $b_\eta = 0.501(38)$ from CLEO [108]. The TFF was also measured in the time-like region with the results $b_\eta = 0.57(12)$ from Lepton-G [125], $b_\eta = 0.585(51)$ from NA60 [126], $b_\eta = 0.58(11)$ from A2 [127], and $b_\eta = 0.68(26)$ from WASA [128]. Recently, the A2 Collaboration reported $b_\eta = 0.59(5)$ [129], the most precise experimental extraction up to date. Note the tendency among space- and time-like determinations, the former always smaller than the latter. This can be understood having a look at Figs. 2.2 and 2.3, which shows the poor result which is obtained from VMD-like fits (P_1^1) to space-like data. Our

³We thank C.F. Redmer for discussions on the average procedure.

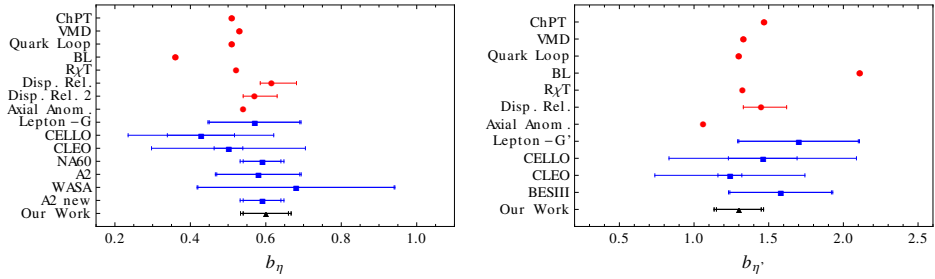


Figure 2.5: Slope determinations for η (left panel) and η' (right panel) TFFs from different theoretical (red circles) and experimental (blue squares) references discussed in the text. Inner error is the statistical one and larger error is the combination of statistical and systematic errors. ChPT [87, 106], VMD, Quark Loop, BL [88], $R\gamma T$ [101], Disp.Rel [95], Disp.Rel 2 [96, 131], Axial Anom. [86], Lepton-G [125], Lepton-G' [116], CELLO [107], CLEO [108], NA60 [126], A2 [127], WASA [128], A2 new [129], BESIII [130], Our Work [114].

rigorous mathematical and systematical approach improves on this issue. For the η' , the slope in Eq. (2.10) can be compared with $b_{\eta'} = 1.46(23)$ from CELLO [107], $b_{\eta'} = 1.24(8)$ from CLEO [108], $b_{\eta'} = 1.7(4)$ from the time-like analysis by the Lepton-G Collaboration (cited in Ref. [116]) and $b_{\eta'} = 1.58(35)$ from BES-III [130]. One should notice that all the previous collaborations used a VMD model fit to extract the slopes. In order to be consistent when comparing with our results, a systematic error of about 40% should be added to the experimental determinations based on space-like data (see Table 2.7) and a smaller one of about 5% on the ones based on time-like data. We present all these results in Fig. 2.5, where the smaller error is the statistical and the larger the quadratic combination of both statistical and systematic. For completeness, we include different existing theoretical results, $b_\eta = 0.51$ and $b_{\eta'} = 1.47$ from χ PT [87, 106] for $\sin \theta_P = -1/3$ [88], being θ_P the $\eta - \eta'$ mixing angle in the octet-singlet basis defined at lowest order; $b_\eta = 0.53$ and $b_{\eta'} = 1.33$, from vector meson dominance (VMD) [88]; $b_\eta = 0.51$ and $b_{\eta'} = 1.30$, from constituent-quark loops; $b_\eta = 0.36$ and $b_{\eta'} = 2.11$, from the Brodsky-Lepage interpolation formula [102]; $b_\eta = 0.521(2)$ and $b_{\eta'} = 1.323(4)$, from resonance chiral theory [101]; and recently, while our work in Ref. [114] was in progress, $b_\eta = 0.61^{+0.07}_{-0.03}$ and $b_{\eta'} = 1.45^{+0.17}_{-0.12}$ from a dispersive analysis [95]⁴.

Eventually, we want to comment on the effective single-pole mass determination Λ_P which Eq. (2.9) implies for the P_1^1 reconstruction. Using $b_P = m_P^2/\Lambda_P^2$ and the values in Eq. (2.9), we obtain $\Lambda_\eta = 0.706$ GeV and $\Lambda_{\eta'} = 0.833$ GeV. These values together with $\Lambda_\pi = 0.750$ GeV obtained in Ref. [111] lead to $\Lambda_\eta < \Lambda_\pi < \Lambda_{\eta'}$, in agreement with constituent-quark loops

⁴The dispersive results [95] neglected the a_2 tensor meson contribution [131]. After accounting for this, they obtain $b_\eta = 0.57^{+0.06}_{-0.03}$ [96, 131].

	t_0	t_1	t_2	t_3	t_4	t_5	r_1
η	0.274	0.011	-0.789×10^{-3}	0.229×10^{-4}	-0.169×10^{-6}	—	1.968
η'	0.343	0.007	-0.986×10^{-3}	0.744×10^{-4}	-0.252×10^{-5}	0.290×10^{-7}	1.442

Table 2.10: Fitted coefficients for our best $P_1^L(Q^2)$ for the η and η' TFFs in units of GeV^{-2i} for $t(r)_i$ and GeV^{-1} for t_0 .

and VMD model approaches [88].

Notoriously, our results for the LEPs would not be affected to the quoted precision if the additional high-energy data points measured by *BABAR* Collaboration at $q^2 = 112 \text{ GeV}^2$ [132] are included through the duality assumption that $\lim_{q^2 \rightarrow \infty} F_{P\gamma^*\gamma}(q^2) = \lim_{Q^2 \rightarrow \infty} F_{P\gamma^*\gamma}(Q^2)$ extends to large but finite energies. One would expect similarly that this is the case for the space-like *BABAR* data in the $(4 - 35) \text{ GeV}^2$ range [118]. However, this is not the case: the high-energy data are relevant in order to reach higher PA sequences leading to more constrained values of the LEPs. In the case at hand, only the *BABAR* Collaboration provides precise measurements in the region between 5 and 35 GeV^2 . For instance, the value of the η slope parameter shown in Eq. (2.9), $b_\eta = 0.60(6)(3)$, turns out to be $b_\eta = 0.65(9)(7)$ when the *BABAR* data are not included in the fits. In view of this behavior and having in mind the π^0 TFF controversy after the measurements of the *BABAR* [76] and *Belle* [133] collaborations, a second experimental analysis by the *Belle* Collaboration covering this high-energy region would be very welcome. Remarkably, we will find in Section 2.5 that even when including very low-energy time-like data, the *BABAR* data points are still of relevance.

For convenience, we also provide our parametrization of the highest P_1^L fits, which can be used to predict the TFF low-energy behavior. Defining the $P_1^L(Q^2)$ for $F_{\eta(\prime)\gamma^*\gamma}(Q^2)$ as

$$P_1^L(Q^2) = \frac{t_0 + t_1 Q^2 + \dots t_L(Q^2)^L}{1 + r_1 Q^2}, \quad (2.11)$$

the corresponding coefficients are given in Table 2.10

2.5 Time-like data: η and η' LEPs

Our space-like data-based description above [114] provides an accurate description for the TFF in the low-energy range, which is the reason why we could obtain such an accurate extraction for the LEPs. Of course, there is no special analytic property at $Q^2 = 0$ which prevents us to make a prediction for low time-like energies. It remains the question then on what low means here. It is well known that at larger time-like energies the appearance of production thresholds, starting with $\pi^+\pi^-$, imply the appearance

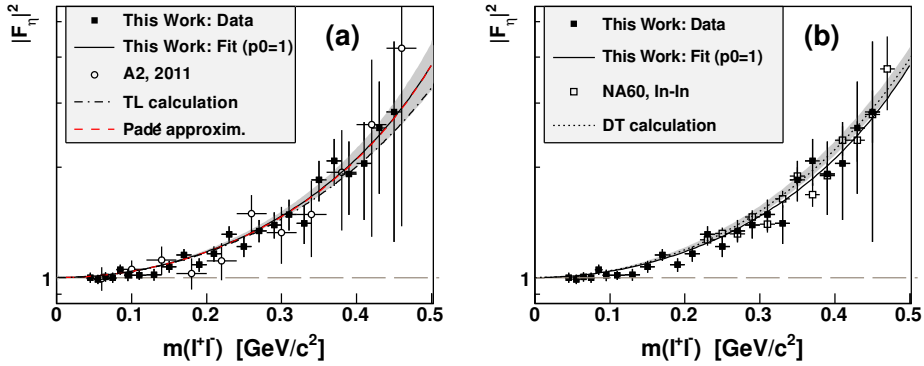


Figure 2.6: The normalized η TFF results obtained from A2 Collaboration at MAMI. Plot taken from Fig. 10 in [129]. Their results displayed as solid squares [129] are compared to NA60 [126] (open squares in (b)) and former A2 results [127] (open circles in (a)). The data and their fit is compared to different theoretical calculations: TL [134], dispersive theory (DT) [95] and our results [114] from Eq. (2.11) (red line in (a) with gray error band).

of additional singularities and cuts. The analytic structure of PAs in turn is given by a set of isolated poles, which would in principle forbid its use above threshold production and would question then the applicability of our approach to the $\eta^{(\prime)} \rightarrow \bar{\ell}\ell\gamma$ Dalitz decays above threshold.

Very recently, the A2 Collaboration at MAMI [129] reported a new measurement of the $\eta \rightarrow e^+e^-\gamma$ Dalitz decay with the best statistical precision up to date, which allowed them to extract the (normalized) η TFF, $\tilde{F}_{\eta\gamma^*\gamma}(q^2)$, in the low-energy time-like region, $q^2 \in (4m_e^2, m_\eta^2)$. In their study, they performed a comparison with different theoretical models, obtaining the results in Fig. 2.6. The agreement with our parameterization, Eq. (2.11), is excellent (we note that this would not have been the case for the simplest P_1^0 element). Moreover, we can see that our parameterization is superior compared with the different theoretical models considered in [129], though the precision from data does not allow to discard any of them.

Furthermore, new time-like data are also available from BESIII. They have been able to measure, for the first time, the $\eta' \rightarrow e^+e^-\gamma$ Dalitz decay⁵, allowing them to extract the normalized η' TFF in the $q^2 \in (4m_e^2, m_{\eta'}^2)$ region [130]. Since their last bin is at 0.75 GeV and our approximant pole, Eq. (2.11), lies at 0.83 GeV, we can extrapolate up to their last point, obtaining again an excellent agreement —though the current precision is not comparable to that in the η Dalitz decay— see Fig. 2.7.

⁵The $\eta' \rightarrow \mu^+\mu^-\gamma$ was measured before [135, 136] though with less precision, and in the higher range $q^2 \in (4m_\mu^2, m_{\eta'}^2)$.

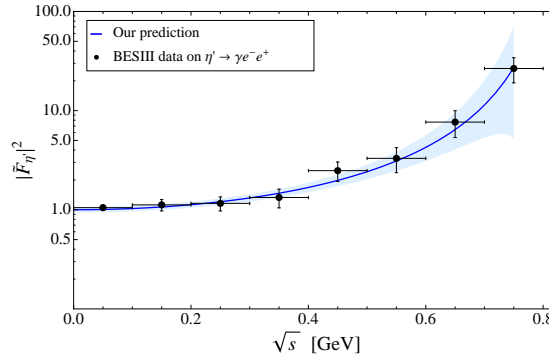


Figure 2.7: Our space-like P_1^N prediction (blue line), Eq. (2.11), for the η' TFF including statistical errors (blue-band) compared with the recent BESIII results [130].

The excellent agreement displayed above challenged our understanding of PAs and the underlying reason behind these findings [117, 137, 138]. Since PAs are analytic functions in the whole complex plane except at their poles location, they cannot reproduce the analytical structure which a branch cut requires. As an example, our construction above would not allow to open the second Riemann sheet and, consequently, it cannot be used to determine resonance parameters. The latter would be possible if constructing the approximant above the threshold [123, 124], which however would forbid the LEPs determination. For the particular case when the original function to be approximated is Stieltjes with a finite radius R of convergence around the origin, it is a well-known result in the theory of Padé approximants that the sequence $P_N^{N+J}(z)$ (with $J \geq -1$) converges to the original function as $N \rightarrow \infty$ on any compact set in the complex plane, excluding the cut at $R \leq z < \infty$, see Section 1.5.1 —where the poles of the approximant locate to emulate the cut effects, cf. Fig. 1.6. In other words, even though the $\pi\pi$ unitary cut driving the decay is of Stieltjes nature, there is *a priori* no reason why the PA should work above the branch cut. The surprising situation is, however, that at least the $P_1^L(s)$ sequence does seem to work well above the cut (cf. Figs. 2.6 and 2.7) for the two observables. One could speculate about the good agreement found above.

To qualitatively understand the situation, as a first approximation, it would be fair to say that the TFF is a meromorphic function —as it would in the large- N_c limit of QCD. In such scenario, PAs are an excellent approximation tool [54]. Particularly, if the TFF contains a single and isolated pole, the $P_1^L(s)$ sequence reproduces the pole of the TFF with infinite precision. As soon as the width is again switched on, the $\pi\pi$ threshold opens a branch cut responsible for that width. Then, at first, no mathematical theorem will guarantee convergence on this scenario. On the contrary, if the convergence theorem is to be satisfied, one would expect the single pole of the $P_1^L(s)$ to

be located closer and closer to the threshold point as soon as $L \rightarrow \infty$, since this is the first singular point the PA is going to find. However, the behavior of this $\pi\pi$ branch cut at threshold is well known as it comes from the $\pi\pi$ P-wave, implying the imaginary part expansion at threshold to behave as $(s - 4m_\pi^2)^{3/2}$ —such behavior can be easily obtained from Eqs. (1.51) and (1.52) and gives an estimate for the discontinuity size. Beyond, the well-studied $\pi\pi$ P-wave rescattering will be responsible to modulate such discontinuity, which is related to the well-studied $\pi\pi$ vector form factor. It is the smoothness of such discontinuity that explains the excellent performance found above. More precisely, taking the definition of a $P_1^L(s)$ given by

$$P_1^L(s) = \sum_{k=0}^{L-1} a_k(s)^k + \frac{a_L(s)^L}{1 - \frac{a_{L+1}(s)}{a_L(s)}}, \quad (2.12)$$

we would expect the PA pole to effectively account for the TFF pole, whereas the polynomial part would accurately reproduce the induced $\pi\pi$ P-wave effects subthreshold. The latter would guarantee a reasonable approximation above threshold as long as the discontinuity is mild, this is, as this does not become resonant. This happens basically at a distance of the pole given by the half-width rule [121], which can provide a simple estimate of the PAs applicability range. In a realistic situation with multiple cuts, the picture will develop new features, but the final result would be similar. The PA pole becomes an effective pole resulting from the combination of the absolute values of the different resonances entering the process, closer to the one with larger coupling in the particular reaction and with shifts produced by their respective widths.

For a quantitative discussion, we focus on the particular case of the η TFF. To illustrate our statements, we choose the dispersive approach from Ref. [95], which has the appropriate $\pi\pi$ branch cut implementation along with $\pi\pi$ rescattering effects⁶. We generate then a space-like data set analog to that in Section 2.3 with such model and perform a fit using the $P_1^N(Q^2)$ sequence of approximants. The results are shown in Fig. 2.8 left and display a perfect agreement below threshold with respect to the dispersive model and a smooth offset above. Both the dispersive model and the PA extrapolations to the time-like region can be compared to real experimental data for that channel. Interestingly enough, the observed offset is below the experimental resolution as can be inferred from Fig. 2.8 left, supporting our previous comments and justifying the observed performance of PAs. In addition, the relative difference of the fitted approximants with respect to the dispersive model is plotted in Fig. 2.8 right. The latter suggests that a precision around

⁶Our study requires an unsubtracted version of [95]; though this may deteriorate the accuracy to which the data is reproduced, it does not affect our discussion.

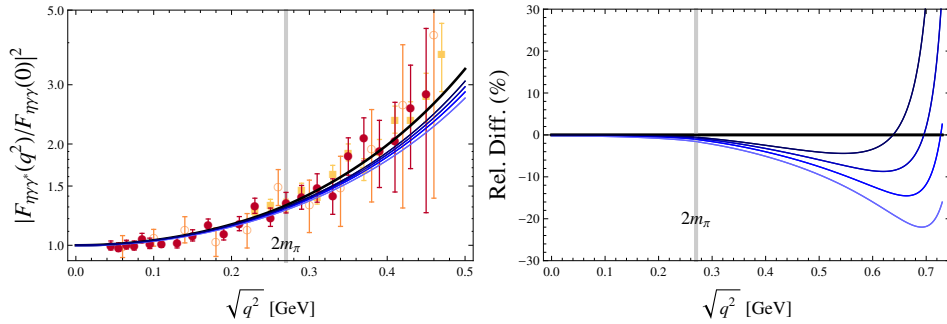


Figure 2.8: Dispersive model for the η TFF in the time-like region (thick-black line) compared to the fit to that model in the space-like region with $P_1^N(q^2)$ approximants, which is extrapolated to the time-like region (light to dark blue lines for $N = 0, 3, 7, 14$, respectively). The gray band represents the $\pi\pi$ threshold. The data corresponds to A2 2011 (empty orange circles) [127], NA60 (yellow squares) [126] and A2 2013 (red circles) [129] and are included to provide a context for the differences among the model and PAs.

5% and 10% could be achieved from our results at energies above threshold and close to the η mass, respectively; below this precision, it seems unlikely that experiments could spot deviations from our approach predictions. Still, PAs cannot differentiate among the different weights of the different contributions appearing in the TFF. However, being fitted to experimental data, all the possible pieces are included —as they are in the data. An interesting exercise would be to compare our predictions below threshold against dispersive approaches, where each contribution must be explicitly included. Incorporating every single contribution represents though a formidable task, for which only those expected to play the main role are included. In this respect, our approach would help on identifying if relevant pieces should be included, as well as potential model dependencies in such formalisms. More comments later in this section.

The discussion above already excludes the generalization of our results to any arbitrary Stieltjes function since one can immediately conclude that the clue feature of the function that would allow the PA to provide a good performance above the branch cut is its behavior around the threshold point. As an example, for a scalar resonance the effects would be larger. Particularly, the imaginary part behavior at threshold starts at order $(s - 4m_\pi^2)^{1/2}$. This, together with the broadness of scalar resonances [10], would anticipate an early and large disagreement above threshold between data and PAs.

In the light of the excellent prediction that PAs provide for the available time-like data and the discussion above, we proceed to include the time-like data in our study [117, 138]⁷. We take, on top of the previous space-like data

⁷The size of current errors for the TFFs in the time-like region played a relevant role in

set, the current available experimental results for the η and η' Dalitz-decays. For the first, this includes the $\eta \rightarrow \gamma e^+ e^-$ results from A2 Collaboration in 2011 [127], together with the more recent ones [129], as well as the NA60 Collaboration results [126] obtained from the $\eta \rightarrow \gamma \mu^+ \mu^-$ Dalitz decay⁸. These collaborations include as well their fitted VMD Λ parameter (cf. Eq. (2.2)) which includes both, statistic and systematic errors. Unfortunately, such systematic error is not included in the data. In order to obtain the combined statistical and systematic published error, one can define a new source of error defined in the following way: $\Delta_{\text{final}} = \sqrt{\Delta_{\text{stat}}^2 + (\epsilon |F(Q_i)|^2)^2}$ for each Q_i^2 datum, with ϵ some percentage. The specific value for ϵ is chosen as to reproduce their combined statistical and systematical error⁹. We find that for the different collaborations, $\Lambda^{-2} = (1.92 \pm 35_{\text{stat}} \pm 13_{\text{syst}})$ [127], $\Lambda^{-2} = (1.95 \pm 17_{\text{stat}} \pm 5_{\text{syst}})$ [126] and $\Lambda^{-2} = (1.95 \pm 15_{\text{stat}} \pm 10_{\text{syst}})$ [129], require $\epsilon = 6.8\%$, 1.9% and 4.8% , respectively. For the η' , the time-like data comprise only the BESIII results [130]¹⁰. Fortunately, this time they provided a systematic error for the data points. For the fitting procedure, we employ the χ^2 function

$$\chi^2 = \sum_{\text{SL}} \left(\frac{Q^2 P_M^{N-1}(Q^2) - Q^2 F_{P\gamma^*\gamma}^{\text{exp}}(Q^2)}{\sigma_{\text{exp}}} \right)^2 + \sum_{\text{TL}} \left(\frac{\tilde{P}_M^{N-1}(Q^2) - \tilde{F}_{P\gamma^*\gamma}^{\text{exp}}(Q^2)}{\sigma_{\text{exp}}} \right)^2 + \left(\frac{P_M^{N-1}(0) - F_{P\gamma^*\gamma}(0)}{\sigma_{\text{exp}}} \right)^2, \quad (2.13)$$

where $P_M^N(Q^2)$ is the PA to fit $Q^2 F_{P\gamma^*\gamma}^{\text{exp}}(Q^2)$ and $\tilde{f}(Q^2)$ means that $\tilde{f}(0) = 1$.

We next report on our results. We start by fitting with a $P_1^L(Q^2)$ sequence. We reach up to $L = 7$ both for η and η' , which is shown in Fig. 2.9 as a green-dashed line. The smaller plot in Fig. 2.9 is a zoom into the time-like region. The obtained LEPs are collected in Table 2.11 and shown in Figs. 2.10 and 2.11 together with our previous results in Figs. 2.2 and 2.3 when only space-like data were included in our fits. The stability observed for the LEPs with the $P_1^L(Q^2)$ sequence is remarkable, and the impact of the inclusion of time-like data is clear since it not only allows us to reach higher precision on each PA but also enlarges our PA sequence by two and one elements for the η and η' , respectively. The stability of the result is also

the previous discussion. If in the near future more precise data with discriminating power enough to discern branch cut effects become available, it may be necessary to carefully reconsider which data points could be used.

⁸More recently, NA60 presented an improved preliminary result, $\Lambda^{-2} = (1.951 \pm 0.059_{\text{stat}} \pm 0.042)_{\text{syst}} \text{ GeV}^{-2}$ [139], but the corresponding data are not yet published.

⁹We thank Marc Unverzagt for discussions on this subject.

¹⁰As said, previous results from Lepton-G from $\eta' \rightarrow \mu^+ \mu^- \gamma$ have rather large errors and are not available in their publication [135, 136].

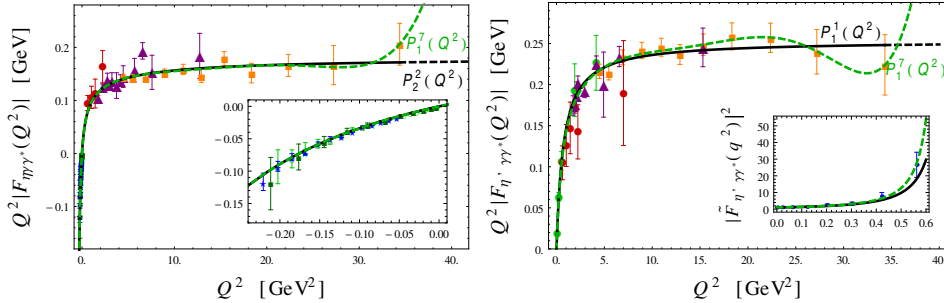


Figure 2.9: η and η' TFF best fits. Green-dashed line shows our best $P_1^L(Q^2)$ fit and black line our best $P_N^N(Q^2)$ fit. Experimental data points in the space-like region are from CELLO (red circles) [107], CLEO (purple triangles) [108], L3 (green points) [105], and BABAR (orange squares) [118] collaborations. Experimental data points in the time-like region are from NA60 (blue stars) [126], A2 2011 (dark-green squares) [127], A2 2013 (empty-green circles) [129], and BESIII (blue points) [130]. The inner plot shows a zoom into the time-like region.

	η					η'				
	N	b_η	c_η	d_η	χ_ν^2	N	$b_{\eta'}$	$c_{\eta'}$	$d_{\eta'}$	χ_ν^2
$P_1^N(Q^2)$	7	0.575(16)	0.338(22)	0.198(21)	0.6	7	1.31(4)	1.74(9)	2.30(19)	0.7
$P_N^N(Q^2)$	2	0.576(15)	0.340(20)	0.201(19)	0.6	1	1.25(3)	1.56(6)	1.94(12)	0.7
Final		0.576(11)	0.339(15)	0.200(14)			1.31(4)	1.74(9)	2.30(19)	

Table 2.11: Low-energy parameters for the η and η' TFFs obtained from the PA fits to experimental data. The first column indicates the type of sequence used for the fit and N is its highest order. The last row shows the weighted average result for each LEP. We also present the quality of the fits in terms of χ_ν^2 . Errors are only statistical and symmetrical.

reached earlier, the systematic error is reduced and our method allows to extract, for the first time, the LEPs from a combined fit to all the available data¹¹. In order to reproduce the asymptotic behavior of the TFF, we have also considered the $P_N^N(Q^2)$ sequence (second row in Table 2.11). The results obtained are in very nice agreement with our previous determinations. The best fit is shown as black-solid line in Fig. 2.9. We reach $N = 2(1)$ for the $\eta(\eta')$. Since these approximants contain the correct high-energy behavior built-in, they can be extrapolated up to infinity (black-dashed line in Fig. 2.9) and then predict the leading $1/Q^2$ coefficient [117, 138]

$$\lim_{Q^2 \rightarrow \infty} Q^2 F_{\eta \gamma^* \gamma}(Q^2) = 0.177^{+0.020}_{-0.009} \text{ GeV}, \quad (2.14)$$

$$\lim_{Q^2 \rightarrow \infty} Q^2 F_{\eta' \gamma^* \gamma}(Q^2) = 0.254(4) \text{ GeV}. \quad (2.15)$$

Even though the prediction for the η is larger—but compatible within errors—than our previous result from the space-like data, Eq. (2.7), it

¹¹The only exception is the Novosibirsk data [140–144] in the resonant region around $0.700 - 1.400$ GeV.

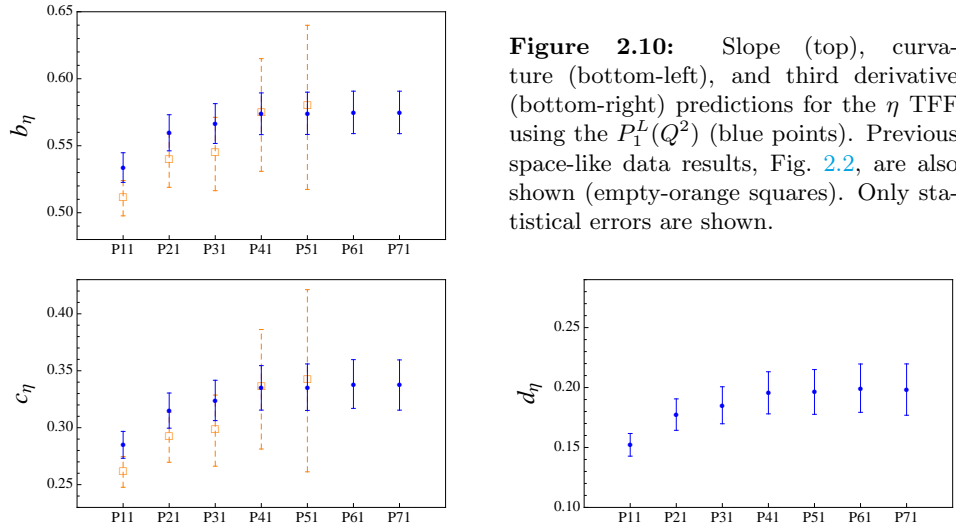


Figure 2.10: Slope (top), curvature (bottom-left), and third derivative (bottom-right) predictions for the η TFF using the $P_1^L(Q^2)$ (blue points). Previous space-like data results, Fig. 2.2, are also shown (empty-orange squares). Only statistical errors are shown.

is still far below the *BABAR* time-like measurement at $q^2 = 112$ GeV 2 , $F_{\eta\gamma^*\gamma}(112) = 0.229(30)(8)$ GeV [132]. The result for the η' is on the other hand similar to the previous space-like determination Eq. (2.8). See more discussions on *BABAR* time-like measurements below.

Our combined weighted average results from Table 2.11, taking into account both types of PA sequences, give [117, 138]

$$b_\eta = 0.576(11)_{\text{stat}}(4)_{\text{sys}} \quad b_{\eta'} = 1.31(4)_{\text{stat}}(1)_{\text{sys}} \quad (2.16)$$

$$c_\eta = 0.339(15)_{\text{stat}}(5)_{\text{sys}} \quad c_{\eta'} = 1.74(9)_{\text{stat}}(3)_{\text{sys}} \quad (2.17)$$

$$d_\eta = 0.200(14)_{\text{stat}}(18)_{\text{sys}} \quad d_{\eta'} = 2.30(20)_{\text{stat}}(21)_{\text{sys}} \quad (2.18)$$

where the first error is statistic and the second systematic, see Table 2.7. These results can be compared to our previous results from space-like data, Eqs. (2.9) and (2.10), which shows the great improvement not only on the statistical error, but on the systematic one as well, both by an order of magnitude. Our results, Eqs. (2.16) to (2.18), represent the most precise determination to date for the LEPs. As a further check, for the η' , we have checked the relevance of including the last data points in the time-like region. We have found that omitting them yields very similar results. Therefore, we believe this justifies their inclusion in our fitting procedure. For comparison, we update in Fig. 2.12 our previous Fig. 2.5 to include this additional determination. Note as said, that previous dispersive results [95] stands at one standard deviation from ours, both for η and η' . The reason being the omission of the a_2 tensor meson contribution, which was observed in [131] and recently included in their later analysis for the η [96], bringing their result closer to our value and confirming thereby our determination —the

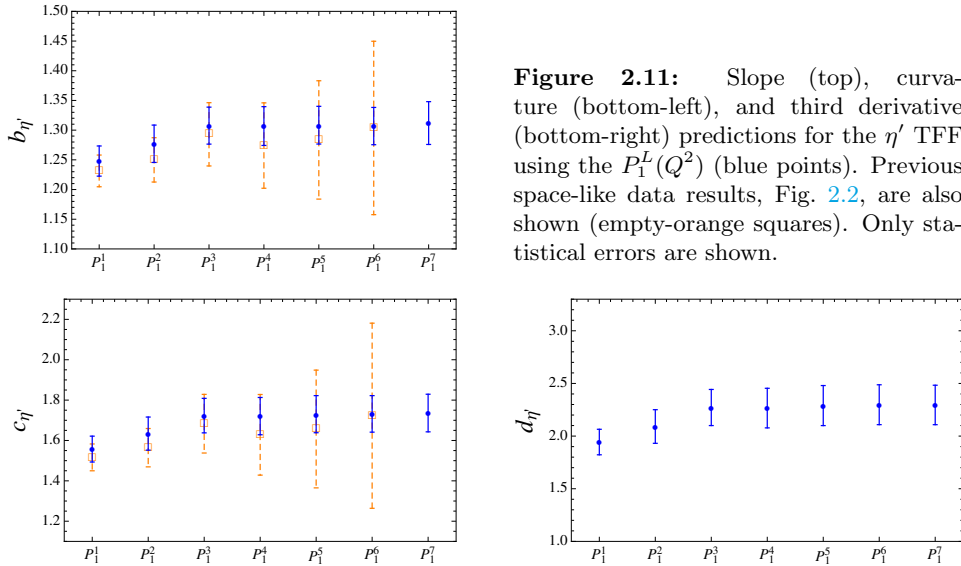


Figure 2.11: Slope (top), curvature (bottom-left), and third derivative (bottom-right) predictions for the η' TFF using the $P_1^L(Q^2)$ (blue points). Previous space-like data results, Fig. 2.2, are also shown (empty-orange squares). Only statistical errors are shown.

η' modified result has not been reported—which could have been predicted from our b_P determination and shows the potential of our method to estimate unaccounted effects in dispersive approaches. In addition, this result could be used as an input to perform further subtractions in their method.

After showing the excellent precision achieved in our study, we would like to comment on the role of data in our results. The models studied in Section 2.2 suggest that, due to the large amount of low-energy data, the presence of new data will not improve on the systematic errors achieved so far (except for the $d_{\eta(\eta')}$ parameter if higher elements are reached, see Table 2.7). However, since the current limitation, except for $d_{\eta(\eta')}$, is the statistical one, new precise data will be very welcome. In principle, one may think that it is the low-energy data which may be preferred. We notice however, that in order to reach large PA sequences—which allow for more accurate extractions—the high-energy data, which from 5 to 35 GeV² is dominated by *BABAR*, is also very important. To show the role of each collaboration, we report for the η case (similar results are obtained for the η') on the different results for the slope and asymptotic values arising from each one in Table 2.12. We find that a fit exclusively to *BABAR* data yields similar results both for the slope and asymptotic values than other space-like configurations. This contrast for instance for the asymptotic value obtained when only *CELLO* or time-like data is used. The role of *BABAR* data is then twofold, allowing to reach larger approximants, such as $P_2^2(Q^2)$ and determining basically the asymptotic value. In view of the π^0 puzzle between *BABAR* [76] and *Belle* [133] results, a second experimental measurement cov-

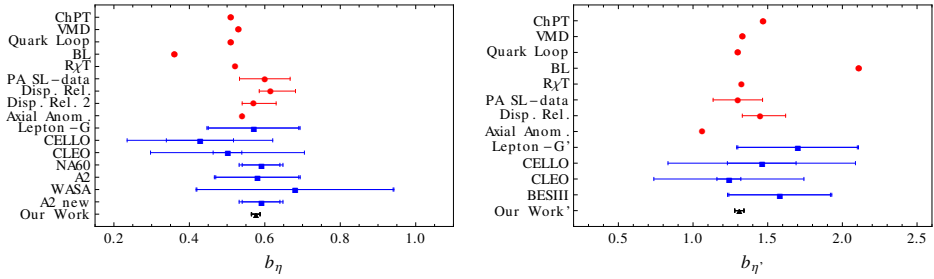


Figure 2.12: Slope determinations for the η from different theoretical (red circles) and experimental (blue squares) references discussed in the text. Inner error is the statistical one and larger error is the combination of statistical and systematic errors. ChPT [87, 106], VMD, Quark Loop, BL [88], R γ T [101], Disp. Rel. [95], Disp. Rel. 2 [96, 131], Axial Anom. [86], Lepton-G [125], Lepton-G' [116], CELLO [107], CLEO [108], NA60 [126], A2 [127], WASA [128], A2 new [129], BESIII [130], PA SL-data [114], Our Work [117], Our Work' [138].

ering the high-energy region would be very welcome here. In the future, the Belle II Collaboration may be able to provide such measurements.

To complete our previous discussion, we comment as well on the role of $\Gamma_{\eta \rightarrow \gamma\gamma}$ in our extractions given the current discrepancy among e^+e^- collider results and Primakoff measurements for this quantity. We find that our previous results are rather stable though mildly depend on this input. For instance, if we would have used the value measured through the Primakoff mechanism omitted in the PDG average [10] (i.e., $\Gamma_{\eta\gamma\gamma}^{\text{Primakoff}} = 0.476(62)$ keV [10]), we would find $b_\eta = 0.570(13)$, which represents half a standard deviation with respect to our result, Eq. (2.16). Even though this does not represent a puzzle as everything agrees within uncertainties, it may suggest to look again for a Primakoff measurement¹², specially given that both, $\Gamma_{\eta\gamma\gamma}$ and b_η , play a central role in our following calculations: $\eta - \eta'$ mixing, $P \rightarrow \bar{\ell}\ell$ decays and $(g-2)$.

Finally, we comment on the result from the *BABAR* Collaboration at very large time-like energies [132]. As already mentioned before, *BABAR* measured the process $e^+e^- \rightarrow \gamma^* \rightarrow \eta^{(\prime)}\gamma$ at the center of mass energies $\sqrt{s} = 10.58$ GeV. Its relation to the TFF [146],

$$\sigma(e^+e^- \rightarrow P\gamma) = \frac{2\pi^2\alpha^3}{3} \left(1 - \frac{m_P^2}{s}\right)^3 |F_{P\gamma^*\gamma}(s)|^2, \quad (2.19)$$

where s the center of mass energy squared, allowed them to extract a measurement for the TFF absolute value in the time-like region for $q^2 =$

¹²This kind of measurement is part of the experimental programme of *GlueX* Collaboration at CLAS in Jefferson Lab [145].

	Data range (GeV ²)	$P_1^L(Q^2)$		$P_N^N(Q^2)$		
		L	b_η	N	b_η	η_∞
CELLO [107]	0.62–2.23	2	0.48(20)	1	0.427(66)	0.193(30)
CLEO [108]	1.73–12.74	3	0.73(12)	1	0.522(19)	0.157(5)
BABAR [118]	4.47–34.38	4	0.53(9)	1	0.509(14)	0.162(3)
CELLO,CLEO	0.62–12.74	3	0.65(9)	2	0.704(87)	0.25(10)
SL	0.62–34.38	5	0.58(6)	2	0.66(10)	0.161(24)
A2-11,A2-13 [127, 129]	-0.212 – -0.002	2	0.475(76)	1	0.551(40)	0.149(11)
NA60 [126]	-0.221 – -0.053	3	0.640(77)	1	0.582(19)	0.141(5)
TL	-0.221 – -0.002	3	0.565(87)	1	0.576(17)	0.143(5)
CELLO,TL	-0.221 – 2.23	5	0.531(39)	2	0.533(30)	0.203(58)
CELLO,CLEO,TL	-0.221 – 12.74	6	0.567(22)	1	0.550(13)	0.152(3)
A2-11,A2-13,SL	-0.212 – 34.38	7	0.561(35)	2	0.569(28)	0.178(16)
TL,SL	-0.221 – 34.38	7	0.575(16)	2	0.576(15)	0.177(15)

Table 2.12: Role of the different sets of experimental data in determining slope and asymptotic values (η_∞) of the η TFF. SL refers to the space-like data set, i.e., data from CELLO,CLEO,BABAR [107, 108, 118] collaborations, and TL refers to the time-like data set, i.e., data from NA60+A2-11+A2-13 [126, 127, 129] collaborations. Bold numbers are our final result. No systematic errors included.

112 GeV², obtaining $q^2 F_{\eta\gamma^*\gamma}(q^2) = 0.229(31)$ GeV and $q^2 F_{\eta'\gamma^*\gamma}(q^2) = 0.251(21)$ GeV, where statistical and systematic errors have been added in quadrature. Taking into account the kinematical factor $(1 - m_P^2/s)^3$ (see Ref. [146]) that was missing in the *BABAR* expression, and assuming that duality $F_{P\gamma^*\gamma}(Q^2) = F_{P\gamma^*\gamma}(q^2)$ [132] holds at large but finite energies, implies

$$\begin{aligned} |Q^2 F_{\eta\gamma^*\gamma}(Q^2)|_{Q^2=112 \text{ GeV}^2} &= 0.231(31) \text{ GeV}, \\ |Q^2 F_{\eta'\gamma^*\gamma}(Q^2)|_{Q^2=112 \text{ GeV}^2} &= 0.254(21) \text{ GeV}. \end{aligned} \quad (2.20)$$

This suggests to include these data points in our fitting procedure, assuming that at this high-momentum transfer, the duality between space- and time-like region holds, and no extra error should be included. For the η' , given our results in Eqs. (2.8) and (2.15), in excellent agreement with *BABAR* results, it is clear that this won't change much. For the η case, its inclusion will mainly modify the asymptotic prediction from P_2^2 increasing its value up to $\lim_{Q^2 \rightarrow \infty} Q^2 F_{\eta\gamma^*\gamma}(Q^2) = 0.247$ GeV, higher than the *BABAR* result and with a good $\chi_\nu^2 < 1$. Curiously enough, the fit function at $Q^2 = 112$ GeV² is $Q^2 F_{\eta\gamma^*\gamma}(Q^2) = 0.219$ GeV, below Eq. (2.20). Even worse is the prediction (assuming duality) for the time-like counterpart at $q^2 = 112$ GeV², $q^2 F_{\eta\gamma^*\gamma}(q^2) = 0.307$ GeV. One may speculate in light of these results on the validity of duality assumptions and whether the asymptotic regime is reached or not. Actually, a recent analysis of the η and η' TFFs based on perturbative corrections [67] concludes that the difference between the time- and space-like form factors at $Q^2 = 112$ GeV² can be of the order (5 – 13)% for different pseudoscalar distribution amplitudes, and can be enhanced by Sudakov-type corrections. It may be surprising to find such a

P	$\sigma(e^+e^- \rightarrow P\gamma)$ (fb)		
	J/ψ	$\psi(2S)$	$\psi(3770)$
π^0	324(16)	192(14)	180(14)
η	237(24)	130(16)	120(14)
η'	456(34)	264(27)	245(28)

Table 2.13: The continuum cross sections for $\sigma(e^+e^- \rightarrow P\gamma)$ processes in fb at the center of mass energies of different charmonium resonances.

large error on duality assumptions at these energies. Notice however that, even at these high-energies, the TFFs are sensitive to soft scales for $x \simeq 0(1)$, see Section 1.6.1. These corrections become relevant if the pseudoscalar DAs are relatively broad, which seems the case for the π^0 and η cases, which TFFs, definitely not VMD-like, seems to require a broad DA [67]. Similar results are found from CLEO results [147], which measured cross sections at $q^2 = 14$ GeV 2 —assuming continuum contribution and duality— lead to

$$\begin{aligned} |Q^2 F_{\eta\gamma^*\gamma}(Q^2)|_{Q^2=14 \text{ GeV}^2} &= 0.203(41) \text{ GeV}, \\ |Q^2 F_{\eta'\gamma^*\gamma}(Q^2)|_{Q^2=14 \text{ GeV}^2} &= 0.249(29) \text{ GeV}, \end{aligned} \quad (2.21)$$

even though with potentially larger corrections being at lower energies. On the other hand, the η' seems not that affected, which may suggest a much narrower DA less sensitive to the end-point behavior. This would be reasonable given its heavier singlet nature, introducing an explicit scale that would drive the DA away from a flat shape. Still, to draw firmer conclusions, further and more precise experimental results are required. There is at the moment an ongoing analysis at BES III to measure such processes at $q^2 = 18.5$ GeV 2 [148].

Alternatively, we can use our TFF description to extract the cross section which duality arguments would imply for these processes when using Eq. (2.19). This contribution is of relevance when estimating background contribution to $\psi(nS) \rightarrow \gamma\eta^{(\prime)}$ decays. We obtain at the center of mass energies of the different resonances, the cross sections quoted in Table 2.13, where, for completeness, we include the π^0 results obtained from the work in Ref. [111]. This represents an improvement with respect to Ref. [146] as the latter assumes the asymptotic behavior to extrapolate down to the charmonium energies. Still, we note that these predictions are only valid in the case that duality holds (strictly as $Q^2 \rightarrow \infty$) and would require a more refined analysis in line of [67] in order to estimate for these corrections.

2.6 Conclusions

In this chapter we have described how PAs can be used as fitting functions in order to extract relevant information from the pseudoscalar TFFs,

	$F_{P\gamma\gamma}$ (GeV $^{-1}$)	b_P	c_P	d_P	P_∞ (GeV)
π^0 [111]	0.2725(29)	0.0324(12)(19)	0.00106(9)(25)	—	$2F_\pi$
η [117]	0.2738(47)	0.576(11)(4)	0.339(15)(5)	0.200(14)(18)	0.177(15)
η' [138]	0.3437(55)	1.31(3)(1)	1.74(9)(2)	2.30(20)(21)	0.254(4)
η^{SL} [114]	0.2738(47)	0.60(6)(3)	0.37(10)(7)	—	0.160(24)
η'^{SL} [114]	0.3437(55)	1.30(15)(7)	1.72(47)(34)	—	0.255(4)

Table 2.14: The main results from our work in this chapter. The numbers come from the combined space- and time-like data, Sections 2.4 and 2.5. We include the π^0 results from Ref. [111] and the TFFs at zero energies implied by experiments. In addition, we quote what would be obtained from space-like data alone, which is labelled as P^{SL} .

namely the LEPs and the asymptotic behavior. We have demonstrated this using three different models for the TFF, illustrating the PAs performance in cases where convergence theorems exist or not, that has allowed on top to estimate a systematic error, an unique property of our approach. The proposed method has been applied then to the real η and η' cases, obtaining an excellent performance in the space-like region. Moreover, we have discussed that our previous description can be extrapolated for these TFFs into the low-energy time-like region up to an excellent accuracy, allowing for the first combined description as well as an improved LEPs determination. All in all, our method has allowed a systematic and model-independent robust extraction for the central quantities that we need for later reconstructing the (single-virtual) pseudoscalar TFFs. Moreover, we were able to explain the existing discrepancies among space- and time-like data analysis from different collaborations on the basis of a systematic error. Our main results are the low-energy parameters for the TFF expansion

$$F_{P\gamma^*\gamma}(Q^2) = F_{P\gamma\gamma} \left(1 - b_P \frac{Q^2}{m_P^2} + c_P \frac{Q^4}{m_P^4} - d_P \frac{Q^6}{m_P^6} + \dots \right), \quad (2.22)$$

as well as the asymptotic behavior, $P_\infty \equiv \lim_{Q^2 \rightarrow \infty} Q^2 F_{P\gamma^*\gamma}(Q^2)$. We recapitulate them together with the π^0 results from space-like data, which were not analyzed here, but in Ref. [111], in Table 2.14. We expect to reanalyze the π^0 TFF as well in the near future once the new data from BESIII [149] in the low-energy space-like ($0.3 \leq Q^2 \leq 10$) GeV 2 range and time-like data from NA62 [150] and A2 [148] collaborations from the $\pi^0 \rightarrow \gamma e^+ e^-$ decay become available. Moreover, there are prospects to measure the π^0 TFF at even lower space-like energies at KLOE-2 [151] and *GlueX* [152] collaborations. This would allow for a statistical and systematic improvement for the π^0 LEPs. Additional data for the η and η' mesons is expected too in a similar range. Although this would not improve much the systematic error, an improvement on the statistical one—the dominant at the moment—is to be expected. For completeness, we also show the η and η' results using

space-like data alone, labelled as $\eta^{(i)SL}$, in order to compare the effects of including the time-like data. We remark that the value shown for the TFF at zero energies, $F_{P\gamma\gamma}$ in Table 2.14, is the experimental one obtained from the $\Gamma_{P\gamma\gamma}$ decay widths from PDG [10]. Actually, this result has changed for the π^0 with respect to Ref. [111], where the $\Gamma_{\pi^0\gamma\gamma}^{\text{PrimEx}}$ [103] value was used. We include however the subsequent PDG combination [10] including, among others, the value from Ref. [103]. In addition, the asymptotic behavior was not extracted there but included, since its theoretical prediction, $\pi_\infty = 2F_\pi$, is a clean one as compared to the η and η' , where the mixing and effects related to their singlet component obscure their calculation. This represents the first step in order to reconstruct our PAs describing the pseudoscalar TFFs in next chapters.

Chapter 3

Canterbury Approximants

Contents

3.1	Introduction	55
3.2	Canterbury approximants	57
3.3	Practical examples	60
3.4	Canterbury approximants as a fitting tool	70
3.5	Conclusions	73

3.1 Introduction

So far, we have carefully described how to reconstruct the single-virtual transition form factor (TFF) from the theory of Padé approximants (PAs). However, for almost every practical application in this thesis, see Chapters 5 and 6, it is the double-virtual TFF that is required. From the very basic principle of Bose symmetry, we know that $F_{P\gamma^*\gamma^*}(Q_1^2, Q_2^2) = F_{P\gamma^*\gamma^*}(Q_2^2, Q_1^2)$. Such symmetry principle certainly simplifies the most general form that the double-virtual TFF could have, but it is not constrictive enough as to fully predict the double-virtual TFF from its single-virtual version alone. We illustrate this assertion using two simple ansätze. A simple extension of the single-virtual TFF, which respects Bose symmetry, is the factorization approach

$$F_{P\gamma^*\gamma^*}^{\text{fact}}(Q_1^2, Q_2^2) = \frac{F_{P\gamma^*}(Q_1^2, 0) \times F_{P\gamma^*}(Q_2^2, 0)}{F_{P\gamma\gamma}}. \quad (3.1)$$

This construction was proposed back in the 60's based on vector meson dominance ideas [116, 153, 154] —and recently reconsidered in [96]. There, the form factor was given through vector resonance exchanges as depicted in Fig. 3.1 left, which implicitly uses factorization. Note however that

in a large- N_c framework additional diagrams exist —see Fig. 3.1 right or Ref. [100]— which break factorization. Still, from the study in Ref. [91], it seems that the leading logarithms in χ PT support the factorization approach at low energies, corrections appearing one loop higher than expected —and even two loops higher in the chiral limit. However, Eq. (3.1) cannot reproduce at the same time the high-energy single- and double-virtual behavior which is implied from pQCD, see Section 1.6.1. Namely, if the single-virtual TFF falls as Q^{-2} —as the BL, Eq. (1.49), implies—the double-virtual factorized version, Eq. (3.1), necessarily falls as Q^{-4} , in conflict with the OPE which predicts Q^{-2} , Eq. (1.50). This implies that, even if factorization would be appropriate at low-energies, it must fail at energies large enough.

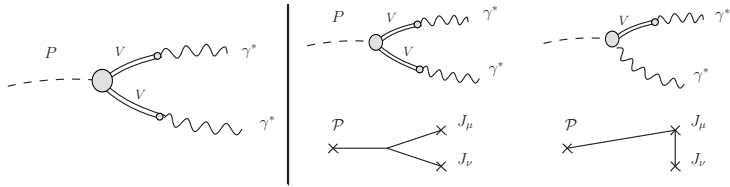


Figure 3.1: Left: standard vector meson dominance conception; factorization is implied. Right: resonant approach to the TFF; factorization is not implied. The graphics on top arise from the large- N_c pseudoscalar pole contribution to the (large- N_c) Green's functions sketched below (cf. Fig. 1.5).

An alternative idea, which would keep Bose symmetry without spoiling the high energy behavior, would be to extend the TFF as $F_{P\gamma^*\gamma^*}(Q_1^2, Q_2^2) = F_{P\gamma^*\gamma^*}(Q_1^2 + Q_2^2, 0)$. However, this would imply that, if the high-energy behavior for the single-virtual TFF is given as λQ^{-2} , its double-virtual counterpart would read $(\lambda/2)Q^{-2}$, whereas pQCD requires $(\lambda/3)Q^{-2}$ instead, see Eqs. (1.49) and (1.50). These examples illustrate that the TFF double-virtual extension cannot be trivially reconstructed from the single-virtual one, but will require a dedicated effort. From a Padé theory point of view, this amounts to the observation that, given the most general double-virtual TFF series expansion,

$$F_{P\gamma^*\gamma^*}(Q_1^2, Q_2^2) = F_{P\gamma\gamma} \left(1 - b_P \frac{Q_1^2 + Q_2^2}{m_P^2} + c_P \frac{Q_1^4 + Q_2^4}{m_P^4} + a_{P;1,1} \frac{Q_1^2 Q_2^2}{m_P^4} + \dots \right), \quad (3.2)$$

Bose symmetry only dictates that $a_{P;i,j} = a_{P;j,i}$, but does not enforce additional relations among the single-virtual parameters, b_P, c_P, \dots , and the double-virtual ones, $a_{P;i,j}$, which therefore must be provided as an additional input. In this chapter, we explore how to consistently generalize in the spirit of Padé theory our previous approach, which would provide then a model-independent framework to reconstruct the most general double-virtual TFF from the parameters in Eq. (3.2). Our method is described in Section 3.2, while its performance and properties are explored along Sec-

tion 3.3 using practical examples. Once more, experimental data, when available, would provide then the external required input to reconstruct the TFF. We investigate this possibility, in analogy to Chapter 2, in Section 3.4. Finally, we summarize the main results in Section 3.5.

3.2 Canterbury approximants

To extend the PAs to the bivariate case, we follow the approach from the Canterbury Group, started by Chisholm in Refs. [155, 156] and giving birth to what is known as Canterbury approximants (CAs) [57, 157]. This approach requires symmetrizing some equations, which is ideal in our case of study given the symmetry of our function. In this section, we review the basics of the method when applied to symmetric functions. Let's define a function $f(x, y) = f(y, x)$ analytic in a certain domain around $x = y = 0$, which series expansion reads

$$f(x, y) = \sum_{\alpha, \beta} c_{\alpha, \beta} x^{\alpha} y^{\beta}, \quad (c_{\alpha, \beta} = c_{\beta, \alpha}). \quad (3.3)$$

The Canterbury approximant is constructed from the rational function

$$C_M^N(x, y) = \frac{P_N(x, y)}{Q_M(x, y)} = \frac{\sum_{i, j=0}^N a_{i, j} x^i y^j}{\sum_{k, l=0}^M b_{k, l} x^k y^l} \quad (b_{1, 1} = 1). \quad (3.4)$$

Note that the rational function is constructed as to have the maximum power in each variable rather than a total maximum power in $x^i y^j$ with $i + j \leq N(M)$, essential for the construction [155]. Next, we need to set the defining equations for the bivariate approximant in analogy to Eq. (1.30). A natural extension from the univariate case would be

$$\sum_{i, j}^M b_{i, j} x^i y^j \sum_{\alpha, \beta}^{\infty} c_{\alpha, \beta} x^{\alpha} y^{\beta} = \sum_{k, l}^N a_{k, l} x^k y^l + \mathcal{O}(x^{\gamma} y^{n+m+1-\gamma}), \quad (3.5)$$

with $\gamma \in (0, n + m + 1)$. Such set of equations define (Bose symmetry is implied)

$$\sum_{i=0}^{N+M} = N + M + 1 \quad (c_{i, 0} \text{ terms}) \quad (3.6)$$

$$\sum_{\substack{i+j=N+M \\ (i \geq j)=1}} = \begin{cases} \frac{(N+M)^2}{4}, & N + M \in \text{even} \\ \frac{(N+M)^2-1}{4}, & N + M \in \text{odd} \end{cases} \quad (c_{i, j} \text{ terms}) \quad (3.7)$$

constraints for the single and double-virtual parameters, respectively, the first of which are reminiscent from the univariate case. To obtain the number

of equations for the double-virtual terms, note that each order $\mathcal{O}(L) \equiv \mathcal{O}(x^{L-i}y^i)$ involves, after using Bose symmetry, $L/2((L-1)/2)$ coefficients for $L \in \text{even(odd)}$, implying $\sum_{i=1}^{L/2} i + \sum_{i=1}^{L/2-1} i = L^2/4$ terms for $L \in \text{even}$ and $2\sum_{i=1}^{(L-1)/2} i = (L^2-1)/4$ terms for $L \in \text{odd}$. In turn, Eq. (3.4) involves

$$\sum_{i=0}^N + \sum_{j=1}^M = N + M + 1 \quad (a_{i,0}, b_{i,0} \text{ terms}) \quad (3.8)$$

$$\sum_{(i \geq j)=1}^N + \sum_{(i \geq j)=1}^M = \frac{1}{2}N(N+1) + \frac{1}{2}M(M+1) \quad (a_{i,j}, b_{i,j} \text{ terms}) \quad (3.9)$$

terms for the single-virtual and double-virtual parameters, respectively—to obtain the number of double-virtual terms, note that $\sum_{(i \geq j)=1}^L = \sum_{i=1}^L i = L(L+1)/2$. Expressing Eq. (3.9) as $(N+M)^2/4 + (N-M)^2/4 + (N+M)/2$, it becomes clear that additional constraints beyond Eq. (3.5) are required to fix the double-virtual terms as Chisholm noted [155].

In the following, we illustrate how to find the defining set of equations for CAs as in Refs. [157, 158]. For this, take a $C_M^N(x, y)$ approximant for which $N \geq M$ (an identical procedure applies for $M \geq N$). Its $P_N(x, y)$ numerator polynomial involves $N(N+1)/2$ double-virtual terms, which are classified according their total order in Table 3.1. All the terms $\sim x^N y^{M \leq N}$ are present and need to be included therefore in the defining equations. However, we find that for a given order $\mathcal{O}(L \leq 2N)$ not all the terms need to be filled in Table 3.1; the additional terms up to $\mathcal{O}(N+M+1)$ represent $M(M+1)/2$ terms which can be exactly matched from the $Q_M(x, y)$ polynomial double-virtual parameters, fixing every coefficient in Eq. (3.4). These represent the defining equations for CAs, which can be summarized as

$$\sum_{i,j}^M b_{i,j} x^i y^j \sum_{\alpha,\beta}^{\infty} c_{\alpha,\beta} x^{\alpha} y^{\beta} - \sum_{k,l}^N a_{k,l} x^k y^l = \sum_{\gamma,\delta}^{\infty} d_{\gamma,\delta} x^{\gamma} y^{\delta}, \quad (3.10)$$

$$\begin{aligned} d_{\gamma,\delta} &= 0 & 0 \leq \gamma + \delta \leq M + N \\ d_{\gamma,\delta} &= 0 & 0 \leq \gamma \leq \max(M, N), \\ && 0 \leq \delta \leq \max(M, N) \\ d_{\gamma,\delta} &= 0 & 1 \leq \gamma \leq \min(M, N), \\ && \delta = M + N + 1 - \gamma. \end{aligned} \quad (3.11)$$

The defining equations, Eqs. (3.10) and (3.11), represent the most important definition in this chapter as it is the basis to reconstruct the bivariate approximants. The definition above corresponding to the Canterbury group fulfills several properties [155, 157, 158]:

- If either x or y is taken to vanish, CAs reduce to PAs.

	$\mathcal{O}(2)$	$\mathcal{O}(3)$	$\mathcal{O}(4)$	$\mathcal{O}(5)$	$\mathcal{O}(6)$	$\mathcal{O}(7)$	$\mathcal{O}(8)$
C_M^0	—						
C_M^1	11	—	—, —				
C_M^2	11	21	22, —	—, —			
C_M^3	11	21	22,31	32, —	33, —, —	—, —, —	—, —, —, —
C_M^4	11	21	22,31	32,41	33,42, —	43, —, —	44, —, —, —
C_M^5	11	21	22,31	32,41	33,42,51	43,52, —	44,53, —, —
C_M^6	11	21	22,31	32,41	33,42,51	43,52,61	44,53,62, —
C_M^7	11	21	22,31	32,41	33,42,51	43,52,61	44,53,62,71

Table 3.1: Coefficients $b_{i,j} = b_{j,i} \equiv_{i,j}$ appearing in the degree N polynomial $P_N(x, y)$ from $C_M^N(x, y)$. The order \mathcal{O} stands for $i + j$.

- If the original function is symmetric, this is $f(x, y) = f(y, x)$, the resulting CAs preserve this symmetry as well.
- If the original function can be written $f(x, y) = g(x)h(y)$, the resulting CAs factorize in terms of the PAs for $g(x)$ and $h(y)$.
- The $C_M^N(x, y)$ approximant for $1/f(x, y)$ is identical to $1/\tilde{C}_N^M(x, y)$, being $\tilde{C}_N^M(x, y)$ the approximant for $f(x, y)$.
- The diagonal approximants are invariant under the group of homographic transformations, this is, if $C_N^N(x, y)$ is the approximant for $f(\frac{Ax}{1-Bx}, \frac{Ay}{1-Cy})$, this is identical to $\tilde{C}_N^N(\frac{Ax}{1-Bx}, \frac{Ay}{1-Cy})$, where $\tilde{C}_N^N(x, y)$ is the approximant to $f(x, y)$ —a well known property of diagonal PAs.

These properties are of relevance for us. In particular, reduction to PAs allows us to connect to our previous work; the second condition guarantees Bose symmetry; the third one is interesting regarding factorization discussions, whereas the last properties are reassuring in the sense that they extend important and well known properties of PAs to the bivariate case. In addition, Montessus theorem (cf. Section 1.5.1) as well as convergence to Stieltjes functions have been proved for CAs as well [57, 159, 160]. Note that the former guarantees convergence of CAs for the pseudoscalar TFFs in the large- N_c limit of QCD. As a final comment, there exist additional extensions of PAs to the multivariate case. Their relevance can be understood for example if considering non-symmetric functions, which substantially complicates the procedure outlined above (for more details see Ref. [161] and references therein). Note however that alternative approaches may not respect several of the properties quoted above.

3.3 Practical examples

In this section, we illustrate the performance and operation of CAs for the particular cases of two functions already discussed in Chapter 2 in their univariate case (i.e., one of their variables is taken to be zero) in the context of PAs, where excellent results were obtained¹. These are the Regge and logarithmic models discussed in Chapter 2.

The first one reads in its bivariate (double-virtual) form [97]

$$F_{P\gamma^*\gamma^*}^{\text{Regge}}(Q_1^2, Q_2^2) = \frac{a F_{P\gamma\gamma}}{Q_1^2 - Q_2^2} \frac{\left[\psi^{(0)}\left(\frac{M^2 + Q_1^2}{a}\right) - \psi^{(0)}\left(\frac{M^2 + Q_2^2}{a}\right) \right]}{\psi^{(1)}\left(\frac{M^2}{a}\right)}, \quad (3.12)$$

and we take $M = 0.8$ GeV and $a = 1.3$ GeV², see Section 2.3.1. We note that, whereas QCD evolution is necessary to restore the BL asymptotic behavior for one large virtuality [97], the asymptotic behavior for two equal and large virtualities is already built-in in the model. To see this, take

$$\lim_{Q_2^2 \rightarrow Q_1^2 \equiv Q^2} F_{P\gamma^*\gamma^*}^{\text{Regge}}(Q_1^2, Q_2^2) = \frac{F_{P\gamma\gamma}}{\psi^{(1)}\left(\frac{M^2}{a}\right)} \psi^{(1)}\left(\frac{M^2 + Q^2}{a}\right), \quad (3.13)$$

which asymptotic behavior Eq. (3.13) reads

$$\lim_{Q^2 \rightarrow \infty} F_{P\gamma^*\gamma^*}^{\text{Regge}}(Q^2, Q^2) = \frac{a F_{P\gamma\gamma}}{\psi^{(1)}\left(\frac{M^2}{a}\right)} Q^{-2} + \mathcal{O}(Q^{-4}). \quad (3.14)$$

The second (logarithmic) model is generalized to the bivariate (double-virtual) version as

$$F_{P\gamma^*\gamma^*}^{\log}(Q_1^2, Q_2^2) = \frac{F_{P\gamma\gamma} M^2}{Q_1^2 - Q_2^2} \ln\left(\frac{1 + Q_1^2/M^2}{1 + Q_2^2/M^2}\right), \quad (3.15)$$

with $M^2 = 0.6$ GeV², see Section 2.3.2. We note that this function arises as a natural extension of flat distribution amplitudes, in the line of [77, 78], to the double-virtual case. To see this, consider the representation

$$F_{P\gamma^*\gamma^*}^{\log}(Q_1^2, Q_2^2) = F_{P\gamma\gamma} M^2 \int_0^1 dx \frac{1}{x Q_1^2 + (1-x) Q_2^2 + M^2}, \quad (3.16)$$

which essentially corresponds to a flat DA $\phi_P(x) \equiv 1$ in Eqs. (1.44) and (1.45). In addition, Eq. (3.15) corresponds, up to normalization, to a particular case of the Appell hypergeometric function $F_1(1, 1, 1, 2; -Q_1^2/M^2, -Q_2^2/M^2)$.

¹As an additional source for practical applications and discussions, the reader is referred to a similar study of the Euler's Beta function in [158].

This function has a singularity at $Q_1^2 = Q_2^2 = -M^2$ and branch cut discontinuities for $Q_{1(2)}^2 < -M^2$, disappearing whenever both virtualities meet such condition at the same time. A nice feature from this model is again obtained in the limit

$$\lim_{Q_2^2 \rightarrow Q_1^2 \equiv Q^2} F_{P\gamma^*\gamma^*}^{\log}(Q_1^2, Q_2^2) = F_{P\gamma\gamma} \frac{M^2}{M^2 + Q^2}, \quad (3.17)$$

which fulfills the appropriate asymptotic behavior, even if the BL limit was not reproduced. A final interesting property, is that Eq. (3.16) can be re-expressed as

$$\frac{F_{P\gamma\gamma} M^2}{\frac{1}{2}(Q_1^2 + Q_2^2) + M^2} \int_{-\frac{1}{2}}^{+\frac{1}{2}} \frac{du}{uz + 1}; \quad z = \frac{Q_1^2 - Q_2^2}{\frac{1}{2}(Q_1^2 + Q_2^2) + M^2}, \quad (3.18)$$

which represents an extended Stieltjes function —see section 5.6 from Ref. [57]

3.3.1 Branch cuts: Stieltjes functions

The Stieltjes theorem for PAs proved to be a powerful tool in physical applications [58, 162]. It provides convergence for the whole complex plane —except for the cut, where the original function itself is ill-defined—as well as bounds ($P_{N+1}^N(x) \leq f(x) < P_N^N(x)$) for the (Stieltjes) function to be approximated, Section 1.5.1. In this subsection, we illustrate its performance for the bivariate case through the use of the logarithmic model in Eq. (3.15), which corresponds to a generalized Stieltjes function, for which convergence is guaranteed [57, 160].

As a first analysis, we check the convergence for the diagonal $C_N^N(Q_1^2, Q_2^2)$ and subdiagonal $C_{N+1}^N(Q_1^2, Q_2^2)$ sequences. The lowest order elements read

$$C_1^0(Q_1^2, Q_2^2) = \frac{F_{P\gamma\gamma}}{1 + \frac{Q_1^2 + Q_2^2}{2M^2} + \frac{Q_1^2 Q_2^2}{6M^4}}, \quad (3.19)$$

$$C_1^1(Q_1^2, Q_2^2) = \frac{F_{P\gamma\gamma} \left(1 + \frac{Q_1^2 + Q_2^2}{6M^2} + \frac{Q_1^2 Q_2^2}{18M^4}\right)}{1 + \frac{2(Q_1^2 + Q_2^2)}{3M^2} + \frac{7Q_1^2 Q_2^2}{18M^4}}, \quad (3.20)$$

$$C_2^1(Q_1^2, Q_2^2) = \frac{F_{P\gamma\gamma} \left(1 + \frac{Q_1^2 + Q_2^2}{2M^2} + \frac{4Q_1^2 Q_2^2}{5M^4}\right)}{1 + \frac{Q_1^2 + Q_2^2}{M^2} + \frac{14Q_1^2 Q_2^2}{15M^4} + \frac{Q_1^4 + Q_2^4}{6M^4} + \frac{2Q_1^2 Q_2^2 (Q_1^2 + Q_2^2)}{15M^6} + \frac{Q_1^4 Q_2^4}{90M^8}}. \quad (3.21)$$

The performance for these sequences is excellent up to large Q^2 values as it is illustrated in Fig. 3.2, where the relative deviation, defined as $C_M^N(Q_1^2, Q_2^2) / F_{P\gamma^*\gamma^*}^{\log}(Q_1^2, Q_2^2) - 1$, is shown for two selected cases. There, we observe—as anticipated—that the diagonal and subdiagonal sequences approach the original function from above and below, respectively. Recall in

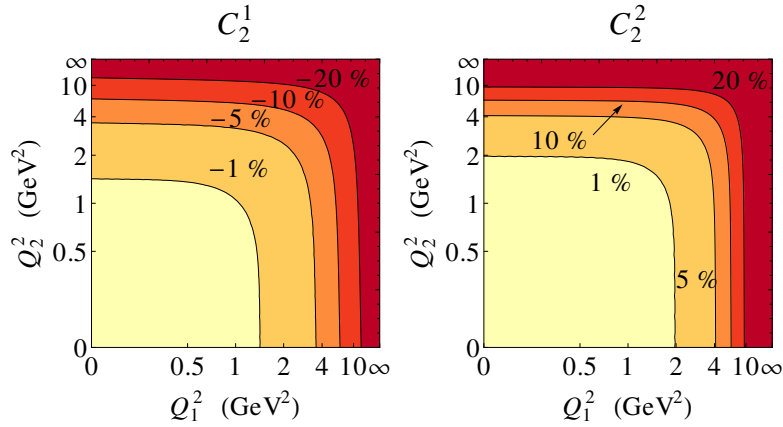


Figure 3.2: Convergence of the $C_{N+1}^N(Q_1^2, Q_2^2)$ and $C_N^N(Q_1^2, Q_2^2)$ sequences to the logarithmic model. We show the C_2^1 (left) and C_2^2 (right) elements, respectively. The first, second, third, and fourth contours, from light to dark red, stand for the relative $\mp 1, \mp 5, \mp 10$ and $\mp 20\%$ deviations. Both axis have been scaled as $Q^2/(1+Q^2)$. See discussion in the text.

this respect that the $C_N^N(Q_1^2, Q_2^2)$ sequence behaves as a constant for large Q^2 values, the $C_{N+1}^N(Q_1^2, Q_2^2)$ falls as $Q^{-2}(Q^{-4})$ for one (two) large virtualities, and the original function, as $\ln(Q^2)Q^{-2}$ and Q^{-2} , respectively, for one and two large virtualities.

An interesting implication from Stieltjes theorem is that the poles and zeros from the approximant must be located along the branch cut discontinuity, where the function itself is ill-defined. We check as a second step this property, and illustrate the poles and zeros for some elements of the diagonal and subdiagonal sequences in Fig. 3.3. There is no pole or zero in the space-like region and, in addition, these approach to the branch cut locations, as expected from the univariate case. There is an interesting remark though. As observed, there exist poles and zeros in the time-like region where no cut exists (light shaded time-like region in Fig. 3.3). Still, these poles and zeros are spurious in the sense that they approach the gray-shaded regions in Fig. 3.3 —where these should be located— as the order of the approximant increases, but indicate a slower convergence within this region. It would be interesting in this respect to find whether it is possible to accelerate such convergence. We note in this respect that the logarithmic model in Eq. (3.15) enjoys an additional symmetry,

$$F_{P\gamma^*\gamma^*}^{\log}(-Q_1^2 - 2M^2, -Q_2^2 - 2M^2) = -F_{P\gamma^*\gamma^*}^{\log}(Q_1^2, Q_2^2), \quad (3.22)$$

which actually relates the two space- and time-like light-shaded regions in Fig. 3.3. It is intuitive that, constraining such symmetry into the approximant, the excellent convergence which is obtained for the space-like region will be translated into the time-like one. We find that such symmetry can only be implemented —at least for the lowest approximants— for the sub-

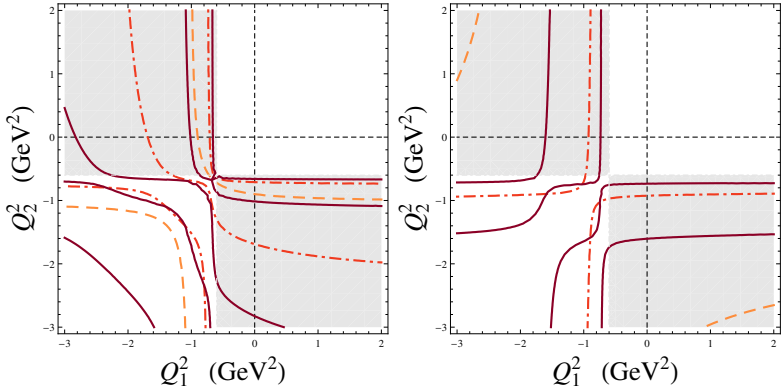


Figure 3.3: The poles (left) and zeros (right) for the C_1^1 , C_2^2 and C_3^3 elements as dashed, dash-dotted and full lines, respectively. The gray-shaded areas represent the regions for which a branch cut exists.

diagonal sequence, which lowest elements read

$$C_1^0(Q_1^2, Q_2^2) = \frac{F_{P\gamma\gamma}}{1 + \frac{(Q_1^2 + Q_2^2)}{2M^2}}, \quad (3.23)$$

$$C_2^1(Q_1^2, Q_2^2) = \frac{F_{P\gamma\gamma} \left(1 + \frac{(Q_1^2 + Q_2^2)}{2M^2}\right)}{1 + \frac{(Q_1^2 + Q_2^2)}{M^2} + \frac{(Q_1^4 + Q_2^4)}{6M^4} + \frac{2Q_1^2 Q_2^2}{3M^4}}, \quad (3.24)$$

$$C_3^2(Q_1^2, Q_2^2) = \frac{F_{P\gamma\gamma} \left(1 + \frac{(Q_1^2 + Q_2^2)}{M^2} + \frac{11(Q_1^4 + Q_2^4)}{60M^4} + \frac{19Q_1^2 Q_2^2}{30M^4}\right)}{1 + \frac{3(Q_1^2 + Q_2^2)}{2M^2} + \frac{3(Q_1^4 + Q_2^4)}{5M^4} + \frac{(Q_1^6 + Q_2^6)}{20M^6} + \frac{9Q_1^2 Q_2^2}{5M^4} + \frac{9Q_1^2 Q_2^2 (Q_1^2 + Q_2^2)}{20M^6}}. \quad (3.25)$$

It is amusing to check that, in addition, for $Q_1^2 = Q_2^2$ the equal-virtual behavior Eq. (3.17) is exactly reproduced in Eqs. (3.23) to (3.25) even if this was not imposed. Incidentally, we find that the polynomials in our approximants, Eqs. (3.23) to (3.25), can be constructed as $\sum_{i+j=0}^N c_{i,j} Q_1^{2i} Q_2^{2j}$, missing the elements $Q_1^{2i} Q_2^{2j}$ with $i+j > N$. We remark that this is a particular feature for this model, which cannot be generalized to other functions [160].

To end our discussion, we show the poles and zeros of Eqs. (3.23) to (3.25) in Fig. 3.4. In contrast to Fig. 3.3, there are no poles or zeros in the region $(x, y) < -(M^2, M^2)$ (time-like light shaded region in Fig. 3.4), which can now be described —as anticipated— to the same precision as the space-like one. As a conclusion, whenever a symmetry principle exists, its inclusion improves convergence. We shall not forget that such symmetry necessarily implies a connection among the single- and double-virtual parameters in Eq. (3.2). An interesting discussion along these lines is found in Ref. [163].

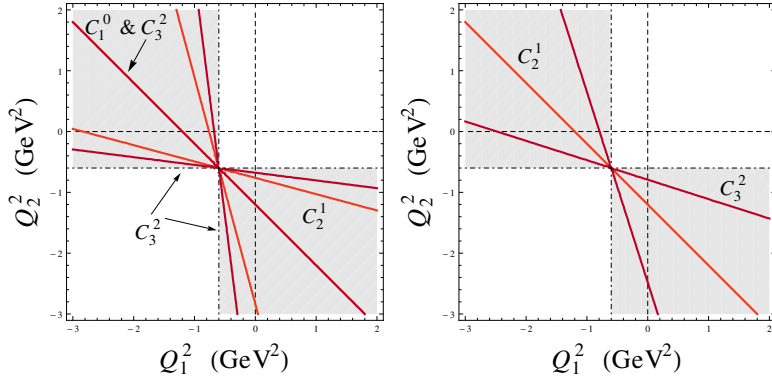


Figure 3.4: From lighter to darker full red lines, the poles (left) and zeros (right) for the C_1^0 , C_2^1 and C_3^2 elements once the symmetry of the original function has been constrained. The dotted-dashed lines represent the original logarithmic function branch cuts. We note that the pole for the C_1^0 approximant overlaps with one pole of the C_3^2 approximant. They gray-shaded areas represent the regions for which a cut is opened.

3.3.2 The large- N_c limit and meromorphic functions theorems: Montessus and Pommerenke

In this subsection, we employ the Regge model in Eq. (3.12) to discuss additional convergence theorems which apply to the large- N_c limit of QCD, in which the Green's functions become meromorphic. These are the Montessus' theorem and Pommerenke's theorem. As a brief summary from Section 1.5.1, we recall that, for the special case of meromorphic functions, Montessus theorem implies convergence within a disk containing M poles for the $P_M^N(x)$ sequence, whereas Pommerenke's theorem implies convergence in the whole complex plane for the $P_N^{N+M}(x)$ sequence. We shall not forget that Montessus theorem has been obtained already for the multivariate case [57, 159]. In addition, we recall that, if a meromorphic function have only positive residues (the same applies if all are negative), this is of the Stieltjes kind. As such condition is fulfilled for the Regge model, Stieltjes theorem applies here as well.

To discuss Montessus theorem, we reconstruct the C_1^N sequence for the Regge model, which for the first elements read

$$\frac{C_1^0(Q_1^2, Q_2^2)}{F_{P\gamma\gamma}} = \frac{1}{1 - \frac{(Q_1^2 + Q_2^2)\psi^{(2)}}{2a\psi^{(1)}} - \frac{Q_1^2 Q_2^2}{2a^2} \left(\frac{\psi^{(3)}}{3\psi^{(1)}} - \left(\frac{\psi^{(2)}}{\psi^{(1)}} \right)^2 \right)}, \quad (3.26)$$

$$\frac{C_1^1(Q_1^2, Q_2^2)}{F_{P\gamma\gamma}} = \frac{1 - \frac{Q_1^2 + Q_2^2}{a} \left(\frac{\psi^{(3)}}{3\psi^{(2)}} - \frac{1}{2} \frac{\psi^{(2)}}{\psi^{(1)}} \right) + \frac{Q_1^2 Q_2^2}{3a^2} \left(\frac{2}{3} \left(\frac{\psi^{(3)}}{\psi^{(2)}} \right)^2 - \frac{\psi^{(3)}}{2\psi^{(1)}} - \frac{\psi^{(4)}}{4\psi^{(2)}} \right)}{1 - \frac{(Q_1^2 + Q_2^2)\psi^{(3)}}{3a\psi^{(2)}} - \frac{Q_1^2 Q_2^2}{3a^2} \left(\frac{\psi^{(4)}}{4\psi^{(2)}} - \frac{2}{3} \left(\frac{\psi^{(3)}}{\psi^{(2)}} \right)^2 \right)}, \quad (3.27)$$

where $\psi^{(n)} \equiv \psi^{(n)}(M^2/a)$. The performance, as expected, resembles that of the univariate case. As an example, we show how the poles of the

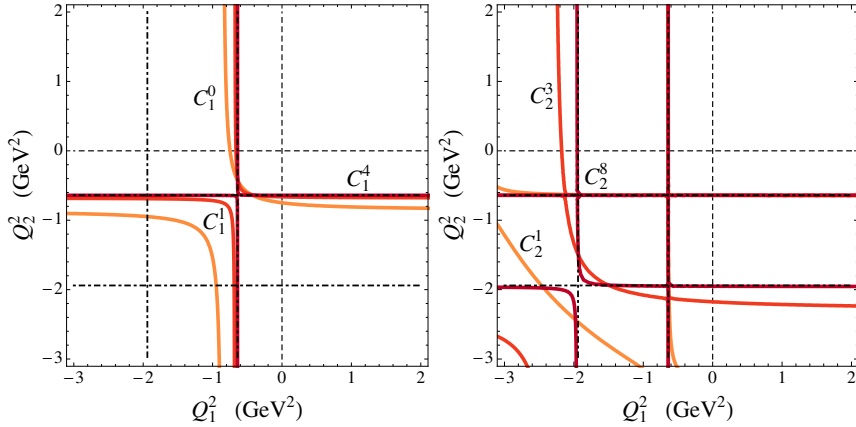


Figure 3.5: The poles from the $C_1^N(Q_2^2, Q_2^2)$ (left) and $C_2^N(Q_2^2, Q_2^2)$ (right) sequences for the C_1^0, C_1^1, C_1^4 and C_2^1, C_2^3, C_2^8 elements, (light to dark red lines). The original first and second poles are displayed as dashed-dotted lines.

$C_1^N(Q_1^2, Q_2^2)$ sequence approach those of the original function at $Q_1^2(Q_2^2) = -M^2$ in Fig. 3.5 left. As we move either further from the first pole, or far into the space-like region, convergence deteriorates and is eventually lost as we move away from the convergence disk. This is in accordance to Montessus theorem, and can be easily understood for this particular case from the power-like behavior of the approximant, which rapidly diverges as N is increased, in contrast to the original function. To enlarge such convergence disk beyond the second pole from the model, we need to go to the C_2^N sequence. The poles from such approximant are illustrated in Fig. 3.5 (right panel), where it can be observed the hierarchical convergence for the poles, which approach faster to those closer to the expansion point. This is to be expected, as the imprint from the poles far from the origin should be small.

Eventually, our goal is to reproduce the function in the whole complex plane or, at least, in the whole space-like region. To this aim, and dealing with meromorphic functions, we can appeal to Pommerenke's theorem and check if this seems to extend to the bivariate case too. As an example, we use the subdiagonal $C_N^{N-1}(Q_1^2, Q_2^2)$ sequence, for which the theorem applies. We show the relative error, defined as in the previous subsection in Fig. 3.6, obtaining excellent results and suggesting that Pommerenke's applies to the bivariate case too. Moreover, there we find that the original function is always approached from below in this sequence. The opposite would have been found for the diagonal sequence. This was to be anticipated as this function is not only meromorphic but Stieltjes, which places stronger constraints.

Given the observed ability of the approximants to reproduce the original pole, it is natural to ask ourselves whether its residue is approached at a similar convergence rate. Actually, this quantity is of physical relevance too.

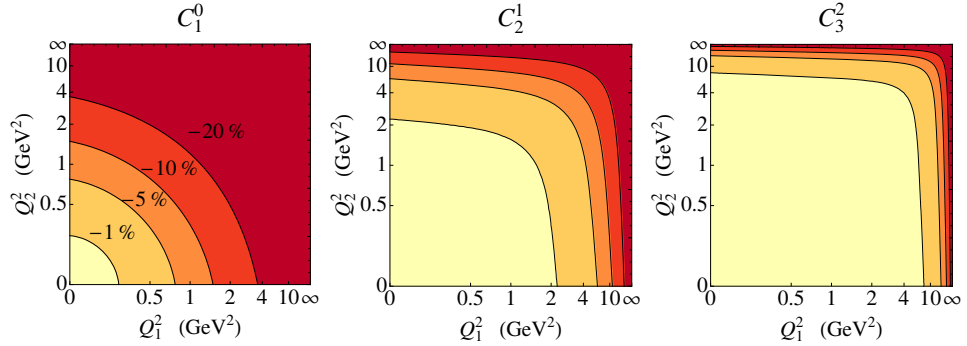


Figure 3.6: Convergence of the $C_N^{N-1}(Q_1^2, Q_2^2)$ sequence to the Regge model for different elements. The first, second, third, and fourth contours, from light to dark red, stand for the relative $-1, -5, -10$ and -20% deviations. Both axis have been scaled as $Q^2/(1+Q^2)$.

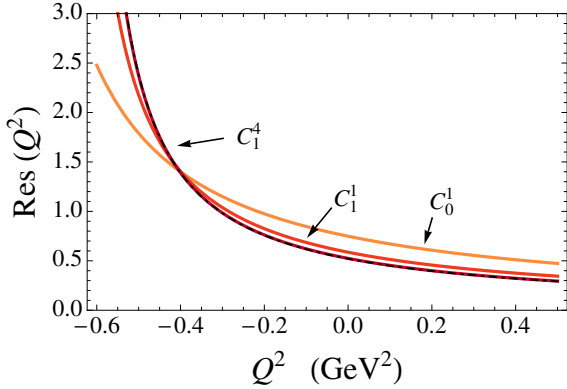


Figure 3.7: From lighter to darker full-red lines, the residue associated to the C_1^0, C_1^1, C_1^4 approximants whenever some virtuality hits a pole. The original residue, overlapping with the C_1^4 element, is plotted as dotted-dashed black line.

As an example, in our Regge model for the TFF, this would represent some vector meson form factor, say, the $\omega\pi^0\gamma^*$ TFF —of course, in the real world with finite-width resonances, this identification is misleading, and would only hold, approximately, for extremely narrow resonances. To this end, we take the residue from our $C_1^N(Q_1^2, Q_2^2)$, which is illustrated in Fig. 3.7. We find an excellent convergence too, even if the accuracy is smaller than that found for the pole position. If we would repeat the same exercise for the C_2^N sequence, we would find an excellent convergence for extracting the first pole —see Fig. 3.5— and its residue. For the second pole, as illustrated in Fig. 3.5, the convergence is slower and an even slower convergence rate is found for its residue. We conclude that, as in the univariate case of PAs, Canterbury approximants provide an excellent description for meromorphic functions in the space-like region, they are able to predict the poles position and, eventually, describe their residues as well, this is, they provide a

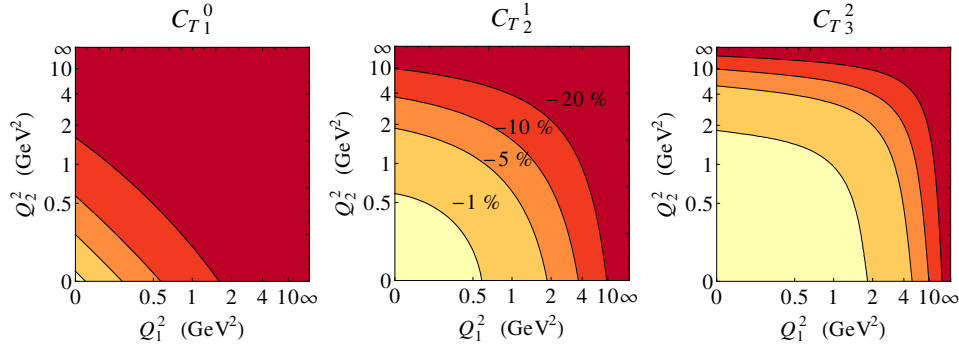


Figure 3.8: Convergence of the $C_{T_{N+1}}(Q_1^2, Q_2^2)$ sequence to the Regge model for different elements. The first, second, third, and fourth contours, from light to dark red, stand for the relative $-1, -5, -10$ and -20% deviations. Both axis have been scaled as $Q^2/(1+Q^2)$.

complete description of the original function.

3.3.3 Resonant approaches: Padé Type extensions

From the previous discussion, it seems that if the poles would have been known *a priori*, these could have been used from the very beginning, bringing additional parameters to our approach. This is interesting, as in the real situation we often know several poles from our function², but not its series expansion. In this section, we study the implications from this approach, in which the poles of the approximant are given in advance, and are in correspondence with the lowest-lying poles from the original function. This is known in the univariate case as Padé-Type approximants, see Section 1.5.2, and have been implicitly used in the past years in resonant approaches. For reconstructing these approximants, we build in our case the denominator from our Canterbury-Type approximant, $C_{T_M^N}$, as

$$\prod_{n=0}^{M-1} (Q_1^2 + M^2 + na)(Q_2^2 + M^2 + na), \quad (3.28)$$

whereas the remaining parameters from the $P_N(Q_1^2, Q_2^2)$ polynomial, Eq. (3.4), are fixed from the series expansion. The obtained results for the first approximants are shown in Fig. 3.8. Comparing with Fig. 3.6, it is easy to see that the achieved convergence rate is not as satisfactory as in the previous case, and the resulting systematic error from the approach is larger. This was easy to anticipate, as the position of the poles—specially those far from the expansion point—did not exactly correspond to the original pole location in our previous examples. This kind of approach may better reproduce the resonant region which is close to the fixed poles, but this comes at cost of the

²It must be noted that, in the real world, many of these poles may have a significant width. Including them as real zero-width poles implies then an additional error.

space-like region which we are interested in. We conclude then that fixing the poles in advance is not the best strategy to find a fast convergence, and we warn against its generalized use in phenomenological applications. An intermediate choice which may be competitive is that of using Partial-Padé approximants, Section 1.5.2, in which only a finite number of poles is fixed in advance, the others being constrained from the series expansion as usual.

3.3.4 High energy limit: two-point approximants

In the previous subsections, we found that the convergence from our approximants deteriorated at very large Q^2 values. This was easy to anticipate, as our models (Eqs. (3.12) and (3.15)) approached 0 for $Q_1^2 = Q_2^2 \equiv Q^2 \rightarrow \infty$ as Q^{-2} (cf. Eqs. (3.14) and (3.17)), whereas none of the approximants constructed above implemented such behavior. In this subsection, we discuss how such behavior—which could have been anticipated from the OPE expansion—can be implemented into our approximant. To this object, we review the concept of two-point PAs, see Section 1.5.2, applied to CAs, which in our case allows to describe both, the low- and the high-energy expansions, providing then a tool to unify our knowledge from χ PT and pQCD.

Our two expansions of interest for the Regge and logarithmic models are

$$F_{\pi^0\gamma^*\gamma^*}^{\text{Model}}(Q_1^2, Q_2^2) = \sum_{n,m=0}^{\infty} c_{n,m} Q_1^{2n} Q_2^{2m} \quad (Q_{1,2}^2 \rightarrow 0), \quad (3.29)$$

$$F_{\pi^0\gamma^*\gamma^*}^{\text{Model}}(Q^2, Q^2) = \sum_{n=0}^{\infty} c_n^{\text{OPE}} Q^{-2n} \quad (Q_1^2 = Q_2^2 \rightarrow \infty). \quad (3.30)$$

The first one represents the expansion at the origin of energies used in previous sections, whereas the second one represents the OPE expansion for equal large virtualities $Q_1^2 = Q_2^2 \equiv Q^2 \rightarrow \infty$. For illustrating the construction of two-point CAs, we make use of the diagonal and subdiagonal sequences, which high-energy behavior expansion reads (see Eq. (3.4))

$$C_N^N(Q^2, Q^2) = \frac{a_{N,N}}{b_{N,N}} + \frac{2a_{N,N-1}b_{N,N} - 2b_{N,N-1}a_{N,N}}{b_{N,N}^2} Q^{-2} + \dots, \quad (3.31)$$

$$C_{N+1}^N(Q^2, Q^2) = \frac{a_{N,N}}{b_{N+1,N+1}} Q^{-4} + \dots \quad (b_{N+1,N+1} \neq 0), \quad (3.32)$$

$$C_{N+1}^N(Q^2, Q^2) = \frac{a_{N,N}}{2b_{N+1,N}} Q^{-2} + \dots \quad (b_{N+1,N+1} = 0). \quad (3.33)$$

For both of our models $c_0^{\text{OPE}} = 0$, the first non-vanishing term in the high-energy expansion Eq. (3.30) being c_1^{OPE} . This implies $a_{N,N} = 0$ and $b_{N+1,N+1} = 0$ for the diagonal and subdiagonal sequences, respectively (cf. Eqs. (3.31) to (3.33)). If additional terms from the high-energy expansion are to be included in our two-point CA, say c_1^{OPE} , additional constraints are

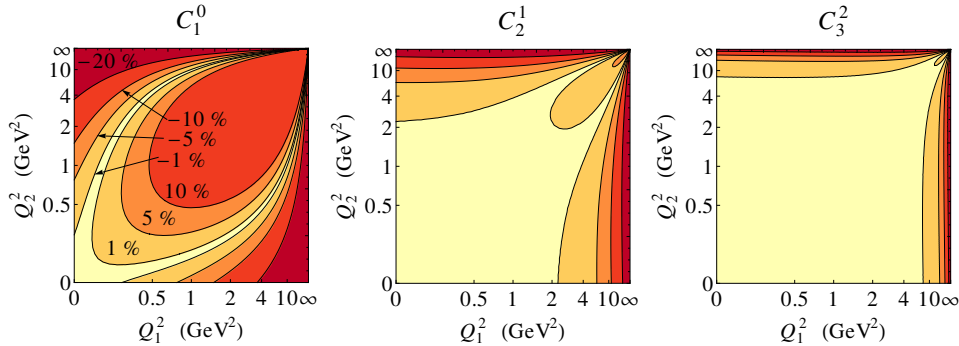


Figure 3.9: Convergence of the $C_{N+1}^N(Q_1^2, Q_2^2)$ sequence with the appropriate high-energy behavior to the Regge model for different elements. The first, second, third, and fourth outer(inner) contours, from light to dark red, stand for the relative $\pm 1, \pm 5, \pm 10$ and $\pm 20\%$ deviations. Both axis have been scaled as $Q^2/(1+Q^2)$.

	C_1^1	C_2^2	C_3^3	C_1^0	C_2^1	C_3^2	Exact
c_1^{OPE}	0.172	0.234	0.246	0.374	0.276	0.264	0.257

Table 3.2: The prediction for the leading c_1^{OPE} term in the high-energy expansion for the diagonal and subdiagonal sequences compared to the exact result for the Regge model.

present. The resulting equations are taken instead those arising from the higher order terms in the low-energy expansion. However, in contrast to PAs, for the bivariate case there are many different terms $c_{N,M}Q_1^{2N}Q_2^{2M}$ of the same order $L = N+M$. For our models, we find that the best convergence is achieved when the most asymmetric terms are replaced for the high-energy ones, this is, the terms $c_{L-1,1}, c_{L-2,2}, \dots$ are replaced by $c_0^{\text{OPE}}, c_1^{\text{OPE}}, \dots$.

As an illustration, we show the result from matching $c_0^{\text{OPE}} = 0$ alone. The resulting equation replaces the $c_{2N,1}$ ($c_{2N+1,1}$) matching condition for the diagonal (subdiagonal) sequence, respectively. The results obtained for the Regge model are illustrated in Fig. 3.9, and show the expected improved convergence along the $Q_1^2 = Q_2^2$ region. A similar improvement is achieved for the logarithmic model as well. Actually, we find that in this case the equal-virtual behavior Eq. (3.17) is exactly satisfied, reproducing then all the terms in Eq. (3.30) and reaching an infinite precision along $Q_1^2 = Q_2^2$. For the Regge model this is no longer possible, as its equal-virtual behavior Eq. (3.13) is not represented by a rational function, requiring then an infinite sequence to reproduce it. Still, additional terms in the high-energy expansion may be predicted even if these were not matched. As an example, we show the prediction for the c_1^{OPE} term in Eq. (3.30) in Table 3.2. As a conclusion, we find that CAs are able as well to use the information at zero and infinity, providing a reliable description of the underlying function in the whole-energy range.

3.4 Canterbury approximants as a fitting tool

Our knowledge about the double-virtual TFF is rather scarce. Theoretically, the situation resembles that of the single-virtual TFF. At high-energies, pQCD can be used to predict the leading $Q_1^2 = Q_2^2 \equiv Q^2$ behavior in similarity to the BL limit, see Eq. (1.50). At low energies, χ PT can be used to obtain the TFF series expansion at zero virtualities, leading to a clear prediction for $F_{P\gamma\gamma}$. A higher order calculation could be performed to obtain the single-virtual leading $Q_{1(2)}^2$ behavior, however, some unknown low-energy constants were required to regularize the theory, thus losing predictive power. The situation does not ameliorate for the double-virtual expansion, where an even higher order calculation is required to obtain the coefficients for $Q_{1(2)}^4$ and $Q_1^2 Q_2^2$ with the consequent proliferation of additional unknown low-energy constants.

The experimental situation for the double-virtual case is even more complicated. Whereas for the single-virtual case the theoretical ignorance was alleviated with a rich experimental knowledge of the TFF in a wide kinematical regime, there is at the moment not a single measurement for the double-virtual TFF. As a result, it is difficult to assess the different theoretical ideas. This situation is related to the particular kinematics of the processes in which the double-virtual TFF can be experimentally accessed.

In the space-like region, such measurement can be accessed at e^+e^- colliders in the $e^+e^- \rightarrow e^+e^-\gamma^*\gamma^* \rightarrow e^+e^-P$ reaction. Such cross section is two-fold suppressed. On the one hand, the photon emission from the e^\pm is suppressed for large photon virtualities. On the other hand, the TFF $F_{P\gamma^*\gamma^*}(Q_1^2, Q_2^2)$ receives an additional Q_2^2 suppression with respect to $F_{P\gamma^*\gamma^*}(Q_1^2, 0)$. Therefore, to obtain a significant amount of events, it is necessary to look at low virtualities, this is, at small e^\pm scattering angles. However, this kinematic regime is experimentally extremely challenging due to the detector geometry and Bhabha scattering background. Remarkably, there is an ongoing effort at BES III to measure this process at low energies [149], which will provide valuable information.

In the time-like region, the double-virtual TFF can be accessed at energies below the pseudoscalar mass in the double Dalitz decay process $P \rightarrow \gamma^*\gamma^* \rightarrow \ell^+\ell^-\ell^+\ell^-$. However, its large suppression due to the additional electromagnetic couplings with respect to the two photons and Dalitz decays, makes such process very challenging. In addition, even though its BR would provide valuable information, it is the differential decay width which gives direct access to the TFF, which measurement requires even higher statistics. Moreover, the presence of the photon propagators greatly enhances low energies relative to the high energies, hiding the double-virtual effects, of order $(\mathcal{O}(q_1^2 q_2^2))$, as compared to the single-virtual ones, of order $\mathcal{O}(q_{1(2)}^2)$, encoded in the slope parameter b_P and playing the main role in

	C_1^0	C_1^1	C_1^2	C_1^3	C_2^1	C_3^2	C_1^1	C_2^2	C_3^3	Exact
$F_{P\gamma\gamma}$	0.270	0.275	0.275	0.275	0.275	0.275	0.275	0.275	0.275	0.275
b_P	0.614	0.743	0.787	0.806	0.805	0.828	0.743	0.821	0.832	0.833
c_P	0.377	0.609	0.727	0.792	0.793	0.893	0.609	0.856	0.914	0.926
$a_{P;1,1}$	0.612	0.798	0.861	0.887	0.881	0.918	0.797	0.906	0.925	0.926
$a_{P;2,1}$	0.520	0.827	0.964	1.0319	1.019	1.124	0.827	1.087	1.150	1.157

Table 3.3: Convergence for the logarithmic model parameters. The parameters are defined according to Eq. (3.2) with $m_P = 1$ GeV.

this decay³.

3.4.1 Extracting the low-energy parameters from data

It is evident that a first measurement on the double-virtual TFF is required to improve our current knowledge, but is equally important to perform an appropriate and reliable theoretical analysis from these data. In this section we discuss, in analogy to Chapter 2, how CAs provide an excellent tool to perform such analysis and extract the relevant low- (and high-) energy parameters in Eq. (3.2) in a systematic and model-independent fashion, and assess on the precision which would be achieved.

For this purpose, we speculate about a possible measurement for the double-virtual TFF corresponding to 36 points in the $[(0, 5) \times (0, 5)]$ GeV² region⁴ and investigate what could be obtained for the double-virtual parameters from a fitting procedure similar to that in Chapter 2 for the single-virtual case. We emphasize that 11 of the 36 data points, corresponding to the single-virtual TFF, are already available at even finer gridding, and will be improved in the future thanks to BESIII [149], NA62 [150], A2 [148], KLOE-2 [151] and *GlueX* [152] collaborations. The purely double-virtual data-points are then reduced to 25. Moreover, only 15 of them are truly independent data points which need to be measured, as half of the square grid can be obtained by reflection from Bose symmetry.

To show the performance of the method, we employ the different sequences which have been revised in this chapter, $C_1^N(Q_1^2, Q_2^2)$, $C_N^N(Q_1^2, Q_2^2)$ and $C_{N+1}^N(Q_1^2, Q_2^2)$. We quote the extracted values for the different parameters of the series expansion, Eq. (3.2), in Tables 3.3 and 3.4 for the logarithmic and Regge model, respectively. The agreement and convergence obtained is excellent, meaning that we have the chance to have a decent extraction once the first measurement for the double-virtual TFF is performed. Naturally, the systematic accuracy that may be achieved depends on whether the quantity of data points is larger or smaller than that

³This handicap would be alleviated using the $\ell = \mu$ channel for the η and η' , which is insensitive to the very low-energy dynamics given the μ mass [137].

⁴We take a square grid with 1 GeV² spacing starting at (0, 0) GeV² and ending at (5, 5) GeV².

	C_1^0	C_1^1	C_1^2	C_1^3	C_2^1	C_2^2	C_1^1	C_2^2	C_3^3	Exact
$F_{P\gamma\gamma}$	0.273	0.275	0.275	0.275	0.275	0.275	0.275	0.275	0.275	0.275
b_P	1.085	1.246	1.295	1.315	1.316	1.334	1.246	1.330	1.335	1.336
c_P	1.186	1.632	1.813	1.900	1.911	2.005	1.632	1.978	2.009	2.016
$a_{P;1,1}$	1.824	2.038	2.050	2.042	2.627	2.017	2.034	2.020	2.017	2.016
$a_{P;2,1}$	2.690	3.239	3.267	3.238	3.177	3.124	3.239	3.141	3.122	3.119

Table 3.4: Convergence for the Regge model parameters. The parameters are defined according to Eq. (3.2) with $m_P = 1$ GeV.

c_1^{OPE}	C_1^0	C_2^1	C_3^2	C_1^1	C_2^2	C_3^3	Exact
Log	0.191	0.174	0.171	0.137	0.152	0.148	0.165
Regge	0.103	0.078	0.074	0.043	0.061	0.063	0.071

Table 3.5: The c_1^{OPE} coefficient in Eq. (3.30) extracted from different approximants for each model. The last column represents the exact value.

used here, but equally important is the measured energy range. On the one hand, if we would have enlarged the interval beyond 5 GeV², but keeping the same number of data points, the quality of the extraction would have deteriorated. On the other hand, taking a smaller interval —while keeping the number of data points— would improve the result and convergence of the sequence. Once more, we emphasize that the systematic error from the first element, the $C_1^0(Q_1^2, Q_2^2)$, is not negligible, which stress the necessity of using larger approximants. In particular, this means that, even if we employ the $C_1^0(Q_2^2, Q_2^2)$ approximant to describe the TFF in some calculation, we should not take the parameters which are obtained from a direct fit to this last, but those obtained for the highest approximants. This is a well-known feature in PAs and its oversight would result in a large systematic error.

3.4.2 Implementing and extracting the high-energy behavior

Given the large amount of unknowns in our approximants, it may be useful, specially regarding the real case in which data contain non-negligible statistical errors, to reduce the quantity of free parameters. One possibility is to implement the high-energy double-virtual behavior, which is dictated by pQCD as explained in Section 3.3.4. In this way, we do not only get rid of one parameter, but we can extract the high-energy expansion as well, see Section 3.3.4. We find that this approach results in an improved extraction of the low-energy parameters as compared to Tables 3.3 and 3.4, with the exception of the $C_1^0(Q_2^2, Q_2^2)$ approximant, which often involves a poor description. In addition, we extract the c_1^{OPE} parameter from the high-energy expansion Eq. (3.30), which result is shown in Table 3.5 for the logarithmic and Regge models for different approximants. In particular, we find that the diagonal (subdiagonal) sequence seems to provide a lower (upper) bound for

this value —in accordance with Section 3.3.4—, offering a powerful method to obtain an estimate for the systematic error.

The method presented here provides a powerful mathematical approach not only to reconstruct or extract the TFF, but for the experimentalists to analyze their data without any theoretical prejudice and to estimate reliable systematic errors in an easy way. This is actually not only of relevance for the double-virtual measurement projected at BESIII, but for those collaborations measuring the single-virtual TFF. In this sense, we have to recall that these experiments always involve a deeply virtual photon together with a quasi-real one; the virtuality from the latter is certainly small but does not need to vanish. As an example, for the Belle π^0 measurement [133] this is mainly less than 0.01 GeV^2 , whereas for *BABAR* it may be as large as 0.6 GeV^2 [76, 118]. To assess the corrections from the quasi-real photon effects, the experimental community requires then some model parametrizing the double-virtual TFF. The chosen parametrization is not unique, for instance, Belle uses a factorized approach, whereas *BABAR* takes a $1/(Q_1^2 + Q_2^2)$ parametrization. Our method would be of help for these experiments in order to improve in precision and systematics. In addition, this may allow to extract some information about the double-virtual TFF. Finally, there are ongoing lattice studies for the π^0 TFF [164]; such approaches do require as well some function to fit their results. Our approach would provide then a valuable tool for them as well.

3.5 Conclusions

In this chapter, we have introduced a generalization of PAs to the bivariate case. This generalization extends the previous ideas on Padé theory for the single-virtual to the most-general double-virtual TFF. For the case of symmetric functions, as the TFF, the use of Canterbury approximants is natural and straightforward, it guarantees the convergence to meromorphic functions (representing the large- N_c limit of QCD), respects factorization without imposing it (which may approximately holds at low-energies for the TFF), reproduces well-known properties from PAs and provides convergence to Stieltjes functions.

In addition, the performance of the approach has been illustrated through the use of two different models previously employed in the univariate case. We have found that the intuition from PAs when dealing with poles and cuts can be extrapolated to this case. Moreover, in similarity to PAs, the poles may be given in advance, though this implies again larger systematic errors. Once more, the method allows to implement not only the low-, but the high-energy information as well. As a final remark, we have shown that the underlying symmetries of the original function may help to improve on

convergence. Regretfully, there is no clear symmetry or relation among the low-energy expansion parameters for the TFF beyond that imposed from Bose symmetry, though a deeper study along this line would be of interest.

In analogy to PAs, our method allows then to extract the (theoretically unknown) low- and high-energy parameters entering the TFF from experimental data through a fitting procedure in a systematic and model-independent fashion. The ongoing experimental effort at BESIII to perform such a measurement would provide then the last required piece of information to reconstruct the double-virtual TFF. As an outcome, our method may be of interest for the experimental community (which often has to deal with the double-virtual TFF even if measuring the single-virtual one) and for the lattice community.

This chapter closes the theoretical framework which has been developed for describing the pseudoscalar TFFs. With all the required ingredients at hand, we proceed to discuss in the next chapters different applications in which these TFFs represent the main input in the calculation.

$\eta - \eta'$ mixing

Contents

4.1	Introduction	75
4.2	One-angle approximation	76
4.3	Two-angle mixing schemes	77
4.4	Determining the $\eta - \eta'$ mixing from the TFFs .	81
4.5	Applications	89
4.6	Conclusions and outlook	95

4.1 Introduction

The $\eta - \eta'$ mixing has been a subject of deep investigation since the advent of the quark model. Early attempts to describe the $\eta - \eta'$ structure through the use of $SU(3)_F$ symmetry and Gell-Mann-Okubo (GMO) mass formulas appeared in Refs. [165, 166], which obtained a mixing angle $\theta_P \approx -10^\circ$. Later on, as χ PT was established as the low-energy effective field theory of QCD and calculations at NLO became available, it was realized that corrections to the GMO mass formula shifted the mixing angle to $\theta_P \approx -20^\circ$, which was in better agreement with experimental results [167, 168]. However, in the years to come, different phenomenological analysis appeared, questioning such result and suggesting values from $\theta_P = -20^\circ$ to $\theta_P = -10^\circ$, depending on the observables taken into account and on the models assumptions [169–173]. This situation was understood after the development of large- N_c χ PT ($\ell N_c \chi$ PT), which provides a framework to bring the η' meson into χ PT. It was clear after the publication of [47, 174], and subsequent works [41, 175, 176], that the $\eta - \eta'$ mixing requires two angles to parametrize their decay constants as a consequence of $SU(3)_F$ breaking. This feature has

been incorporated in subsequent phenomenological analysis [119, 120, 177–181] resulting in different values depending on the modeling procedure.

In the following, we take our previous results from Chapter 2 in order to provide a new alternative determination for the $\eta - \eta'$ mixing parameters. As an advantage, this approach is free of the simplifying assumptions required in previous approaches. In Section 4.2, we provide a brief reminder of the mixing at LO in $\ell N_c \chi$ PT, whereas the necessity of a two-angle description at NLO is discussed in Section 4.3, where we introduce the octet-singlet and quark-flavor basis. Our novel approach for determining the mixing parameters is discussed in Section 4.4. As an innovation, we sequentially include the effects of OZI-violating parameters and, in general, the full NLO corrections in a comprehensive way. Applications concerning the mixing are discussed in Section 4.5. Finally, we present our conclusions in Section 4.6.

4.2 One-angle approximation

From the $\ell N_c \chi$ PT Lagrangian $\mathcal{L}^{(0)}$ Eq. (1.17), we extract the LO result for the kinetic and mass terms for the (bare) η_8 and η_0 fields, $\eta_B \equiv (\eta_8, \eta_0)^T$ [182, 183],

$$\mathcal{L}^{(0)} = \frac{1}{2} \partial_\mu \eta_B^T \mathcal{K} \partial^\mu \eta_B - \frac{1}{2} \eta_B^T \mathcal{M}^2 \eta_B, \quad (4.1)$$

$$\mathcal{K} = \mathbb{1}_{2 \times 2}, \quad \mathcal{M}^2 = \begin{pmatrix} M_8^2 & M_{80}^2 \\ M_{80}^2 & M_0^2 + M_\tau^2 \end{pmatrix}, \quad (4.2)$$

which entries can be expressed in terms of the LO π and K masses, Eqs. (1.20) and (1.21), as

$$M_8^2 = \frac{2B_0}{3}(\hat{m} + 2m_s) = \frac{1}{3}(4\dot{M}_K^2 - \dot{M}_\pi^2), \quad (4.3)$$

$$M_0^2 = \frac{2B_0}{3}(2\hat{m} + m_s) = \frac{1}{3}(2\dot{M}_K^2 + \dot{M}_\pi^2), \quad (4.4)$$

$$M_{80}^2 = \frac{2\sqrt{2}}{3}(\hat{m} - m_s) = -\frac{2\sqrt{2}}{3}(\dot{M}_K^2 - \dot{M}_\pi^2), \quad (4.5)$$

and $M_\tau^2 = \frac{6\tau}{F^2}$. It is clear then from $\hat{m} \neq m_s$ —equivalently, $\dot{M}_K^2 \neq \dot{M}_\pi^2$ —, that the η_8 and η_0 fields will mix among each other into the physical η and η' . At this order, Eq. (4.1) can be diagonalized through the rotation matrix

$$R(\theta_P) = \begin{pmatrix} \cos \theta_P & -\sin \theta_P \\ \sin \theta_P & \cos \theta_P \end{pmatrix}, \quad (4.6)$$

allowing to express the physical $\eta_P = (\eta, \eta')^T$ fields in terms of the bare ones in Eq. (4.1) as $\eta_P = R(\theta_P)\eta_B$, where [182, 183]

$$\sin(2\theta_P) = \frac{2M_{80}^2}{M_{\eta'}^2 - M_\eta^2}, \quad (4.7)$$

and $M_\eta^2, M_{\eta'}^2$ are the eigenvalues solving the previous system, this is, the prediction for the physical masses. The mixing introduced above when diagonalizing the mass term \mathcal{M} is referred to as the state-mixing and involves a single angle θ_P , not only at this order, but at any order. At LO in $\ell N_c \chi$ PT, one obtains the result $\theta_P = -19.6^\circ$ [183]. However, non-negligible corrections are found at higher orders in the systematic $\ell N_c \chi$ PT expansion [183, 184] shifting this value towards $\theta_P \approx -10^\circ$ [183].

Of special interest for our later discussions are the pseudoscalar decay constants. These are defined in terms of the QCD axial current as

$$\langle 0 | J_{5\mu}^a | P \rangle = i p_\mu F_P^a \quad J_{5\mu}^a = \bar{q} \gamma_\mu \gamma_5 \frac{\lambda^a}{2} q \quad \text{Tr}(\lambda^a \lambda^b) = 2\delta^{ab}, \quad (4.8)$$

where λ^a is a Gell-Mann matrix in flavor space and $\lambda^0 = \sqrt{2/3} \mathbb{1}_{3 \times 3}$. We remark that our normalization for the axial current yields $F_\pi = 92.21(14)$ MeV [10]. At LO in $\ell N_c \chi$ PT, one finds $F_\pi = F_K = F$. For the η and η' , due to the mixing, the decay constants are conveniently expressed, following Ref. [47] at LO as

$$F_P^{80} \equiv \begin{pmatrix} F_\eta^8 & F_\eta^0 \\ F_{\eta'}^8 & F_{\eta'}^0 \end{pmatrix} = F \begin{pmatrix} \cos \theta_P & -\sin \theta_P \\ \sin \theta_P & \cos \theta_P \end{pmatrix} = R(\theta_P) \begin{pmatrix} F & 0 \\ 0 & F \end{pmatrix} \equiv R(\theta_P) \hat{F}, \quad (4.9)$$

where $\hat{F} = \text{diag}(F_8, F_0)$ and $F_8 = F_0 = F$ at LO. Consequently, the η and η' couple both, to the octet and singlet axial currents. It follows then that, at LO, their couplings to these currents (F_P^{80}) can be expressed in terms of the octet and singlet \hat{F} decay constants using the same rotation matrix we used for the state mixing, this is, $F_P^{80} = R(\theta_P) \hat{F}$, cf. Eq. (4.6) and comments below. In the jargon of $\eta - \eta'$ mixing, the decay constants follow the state mixing. This situation is particular to the LO case. As we illustrate below, at higher orders, $SU(3)_F$ breaking effects destroy this simple picture, requiring a two-angle description to express the decay constants.

4.3 Two-angle mixing schemes

4.3.1 Octet-singlet scheme

When moving on to NLO, the $\eta - \eta'$ mixing becomes more involved as now the kinetic matrix \mathcal{K} in Eq. (4.1) becomes non-diagonal too [47, 120, 175, 178], a fact which was pointed out for the first time in [47, 175]. Actually, \mathcal{K} and \mathcal{M}^2 cannot be simultaneously diagonalized within a single rotation. The diagonalization is performed then, perturbatively, in two sequential steps [182, 183]. First, a field redefinition for the bare fields $\eta_B = Z^{1/2} \hat{\eta}$ allows to diagonalize the kinetic term \mathcal{K} . Then, the resulting mass matrix, $Z^{1/2} \mathcal{M} Z^{1/2}$, is diagonalized through a rotation $\eta_P = R(\theta_P) \hat{\eta}$, the required

angle in this rotation defines the state-mixing angle in analogy to Eq. (4.6). Note however that the overall transformation $\eta_P = R(\theta_P)(Z^{1/2}{}^T)^{-1}\eta_B$ includes the non-diagonal $Z^{1/2}$ matrix. For these reasons, the pseudoscalar decay constants cannot be expressed in a simple form analog to Eq. (4.9) as four parameters are now required. Instead, they are defined as

$$F_P^{80} \equiv \begin{pmatrix} F_\eta^8 & F_\eta^0 \\ F_{\eta'}^8 & F_{\eta'}^0 \end{pmatrix} \equiv \begin{pmatrix} F_8 \cos \theta_8 & -F_0 \sin \theta_0 \\ F_8 \sin \theta_8 & F_0 \cos \theta_0 \end{pmatrix} \neq R(\theta_P) \begin{pmatrix} F_8 & 0 \\ 0 & F_0 \end{pmatrix}. \quad (4.10)$$

We emphasize again that the state-mixing involves a single mixing angle, θ_P , at any order. It is the decay constants F_P^a description that requires two-angles or, alternatively, four independent quantities. $\ell N_c \chi$ PT provides then the appropriate framework to relate these decay constants to other quantities in the mesonic sector of QCD. Among others, the mixing-angle and additional decay constants F_π and F_K . Particularly, at NLO, the following relations hold [178, 182]¹

$$F_8^2 = \frac{4F_K^2 - F_\pi^2}{3}, \quad F_0^2 = \frac{2F_K^2 + F_\pi^2}{3} + F_\pi^2 \Lambda_1, \quad (4.11)$$

$$F_8 F_0 \sin(\theta_8 - \theta_0) = -\frac{2\sqrt{2}}{3} (F_K^2 - F_\pi^2), \quad (4.12)$$

$$\theta_8 + \theta_0 = 2\theta_P, \quad \theta_8 - \theta_0 = -\frac{4\sqrt{2}}{3} \left(\frac{F_K}{F_\pi} - 1 \right), \quad (4.13)$$

with Λ_1 an OZI-violating parameter. Eq. (4.10) defines the so-called octet-singlet mixing scheme and relations (4.11) to (4.13) hold up to NNLO corrections in the combined $\ell N_c \chi$ PT expansion. Given that $F_K/F_\pi = 1.198(5)$ [10], it follows from Eqs. (4.12) and (4.13) that $SU(3)_F$ breaking implies $\theta_8 \neq \theta_0$. It was the neglected $SU(3)_F$ breaking encoded in the GMO formula and F_8/F_π —not included up to [167, 168]— that lead to bad results in the earlier years [165, 166]. The same effect, this time encoded in $(\theta_8 - \theta_0) \neq 0$, lead to different extractions for the decay constants from different observables [169–173], which often require the decay constants rather than the state-mixing.

At this point, there is a further property which must be discussed. Given the anomalous dimension of the singlet axial current, the singlet decay constants defined via $\langle 0 | J_{5\mu}^0 | P \rangle = i p_\mu F_P^0$ will inherit the scale-dependency which is dictated from QCD [41, 47, 175]

$$\mu \frac{dF_0}{d\mu} = \gamma_A(\mu) F_0 = -\frac{3C_2(r)N_F\alpha_s^2}{8\pi^2} F_0 + \mathcal{O}(\alpha_s^3) = -N_F \left(\frac{\alpha_s(\mu)}{\pi} \right)^2 F_0. \quad (4.14)$$

¹To obtain these relations, the relevant LECs defining these quantities have been traded for F_π and F_K . Moreover, multiplicative factors such as $(F_K/F_\pi - 1)$ have been neglected as they can be understood as NNLO effects.

Here, μ is the renormalization scale, $\gamma_A(\mu)$ the axial current anomalous dimension [185] given in terms of the group invariant $C_2(r)$ —for the fundamental representation $C_2(r) = (N_c^2 - 1)/(2N_c)$ — and N_F is the number of active flavors (u, d, s, \dots) at that scale. The solution to this equation is given, at $\mathcal{O}(\alpha_s)$ as [47, 175, 185]

$$F_0(\mu) = F_0(\mu_0) \left(1 + \frac{2N_F}{\beta_0} \left(\frac{\alpha_s(\mu)}{\pi} - \frac{\alpha_s(\mu_0)}{\pi} \right) \right) \equiv F_0(\mu_0)(1 + \delta_{\text{RG}}(\mu)), \quad (4.15)$$

where μ_0 is some reference scale and we have used the LO result for the α_s running, involving at this order the beta function coefficient $\beta_0 = 11N_c/3 - 2N_F/3$. Of course, physical observables are scale independent, and $F_0(\mu)$ -dependent terms will be accompanied by additional terms in such a way that the scale-dependency is cancelled. In the $\ell N_c \chi\text{PT}$ Lagrangian, this is easy to see, as these (Λ_i OZI-violating) terms are explicitly included in order to make the (bare) Lagrangian scale-independent. As an example, the WZW part requires an additional term [47]²

$$\mathcal{L}_{\text{WZW}}^{(2)} \supset \frac{N_c \alpha \Lambda_3}{6\sqrt{6}\pi F} \epsilon^{\mu\nu\rho\sigma} F_{\mu\nu} F_{\rho\sigma} \eta_0, \quad (4.16)$$

where Λ_3 is a scale-dependent OZI-violating parameter with running $\Lambda_3(\mu) = \Lambda_3(\mu_0)(1 + \delta_{\text{RG}}(\mu))$ analogous to that in Eq. (4.15) and renders the two-photon decays in Eqs. (4.27) and (4.28) scale-independent. Alternatively, heavy processes involving $\eta(\eta')$ in final states are often expressed in terms of $\sum_i C_i(\mu) \langle 0 | \mathcal{O}_i | P \rangle$ matrix elements, where \mathcal{O}_i is a local operator —for instance, $\mathcal{O}_j = \bar{q} \gamma^\mu \gamma_5 q$ — and $C_i(\mu)$ is the so-called Wilson coefficient, which accounts for the operator evolution from the heavy ($\mu = M_H$) to the low ($\mu = \mu_0$) scale. The latter should match that of $F_0(\mu_0)$, implying that any shift $\mu_0 \rightarrow \mu'_0$ would not alter the result. This is the case for the TFF asymptotic behavior discussed in Section 4.4.

4.3.2 Quark-flavor basis

The features outlined above make the description of any physical process involving the singlet sector much involved. For this reason, later on, the quark-flavor mixing scheme was proposed in Ref. [119]. This scheme was motivated by the fact that vector and tensor singlet mesons —where the axial anomaly plays no role— can be pretty well described in terms of light and strange quark singlet components. Actually, we show below that such assumption agrees with NLO $\ell N_c \chi\text{PT}$ provided that OZI-violating effects are obviated. In such approximation, the physical states and decay constants follow the same mixing and can therefore be described in terms of one angle alone, which greatly simplifies our description. Defining the light and strange axial

²Note our $\epsilon^{0123} = 1$ convention and the replacement with respect to [47] $\psi \rightarrow (\sqrt{6}/F)\eta_0$.

currents $J_{5\mu}^{q,s} = \bar{q}\gamma_\mu\gamma_5\frac{\lambda^{q,s}}{2}q$, with $\lambda^q = \text{diag}(1, 1, 0)$ and $\lambda^s = \text{diag}(0, 0, \sqrt{2})$, the pseudoscalar decay constants $\langle 0 | J_{5\mu}^{q,s} | P(p) \rangle \equiv ip_\mu F_P^{q,s}$ read

$$(F_P^{qs}) \equiv \begin{pmatrix} F_\eta^q & F_\eta^s \\ F_{\eta'}^q & F_{\eta'}^s \end{pmatrix} \equiv \begin{pmatrix} F_q \cos \phi_q & -F_s \sin \phi_s \\ F_q \sin \phi_q & F_s \cos \phi_s \end{pmatrix}. \quad (4.17)$$

Relating the decay constants in both basis is rather simple as it only amounts to a rotation of our fundamental QCD currents. From the above definition, it is easy to check that the octet-singlet and quark-flavor basis are related via rotation matrix

$$\begin{pmatrix} J_{5\mu}^8 \\ J_{5\mu}^0 \end{pmatrix} = \frac{1}{\sqrt{3}} \begin{pmatrix} 1 & -\sqrt{2} \\ \sqrt{2} & 1 \end{pmatrix} \begin{pmatrix} J_{5\mu}^q \\ J_{5\mu}^s \end{pmatrix} \Rightarrow (J_{5\mu}^{80})_\alpha = U(\theta_{ideal})_{\alpha a} (J_{5\mu}^{qs})_a. \quad (4.18)$$

Here, the equation on the left-hand side has been expressed in matricial form in the right one with obvious identifications. The indices α and a denote octet-singlet and flavor indices, respectively (summation assumed if repeated indices). Then, the decay constants in Eqs. (4.10) and (4.17) can be related as

$$(F_P^{qs})_{Pa} = (F_P^{80})_{P\alpha} U(\theta_{ideal})_{\alpha a}, \quad (4.19)$$

where the index $P = \{\eta, \eta'\}$ and, again, summation over repeated indices is assumed. Relation (4.19) will be our dictionary when relating results in different basis. In this way, we can translate Eqs. (4.11) and (4.12) to their analogues in the quark-flavor basis obtaining [120, 178]

$$F_q^2 = F_\pi^2 + \frac{2}{3}F_\pi^2\Lambda_1, \quad F_s^2 = 2F_K^2 - F_\pi^2 + \frac{1}{3}F_\pi^2\Lambda_1, \quad (4.20)$$

$$F_q F_s \sin(\phi_q - \phi_s) = \frac{\sqrt{2}}{3} F_\pi^2 \Lambda_1. \quad (4.21)$$

It is clear, as anticipated, that neglecting the OZI-violating Λ_i parameters implies $\phi_q = \phi_s \equiv \phi$, achieving a simpler one-angle description for the decay constants, $F_P^{qs} = R(\phi)\text{diag}(F_q, F_s)$. Indeed, there is a strong phenomenological success supporting this idea [120, 178]. Under the assumption $\phi_q = \phi_s$ —that is commonly known as the FKS scheme [119, 177, 178]—, this basis has become a standard choice given its simplicity and the predictive power with respect to the octet-singlet one. This assumption is specially useful for studying the TFFs [67] within pQCD.

An alternative approach to understand this situation follows from the pQCD picture in Ref. [177] when considering the Fock state description of the η and η' . Given that $(m_u \simeq m_d) \ll m_s$, it seems reasonable that η and η' may be described in terms of light and strange quarks degrees of freedom

$$|\eta_q\rangle = \Psi_q \frac{1}{\sqrt{2}} |u\bar{u} + d\bar{d}\rangle + ..., \quad |\eta_s\rangle = \Psi_s |s\bar{s}\rangle + ..., \quad (4.22)$$

where the ellipses stand for additional Fock states including gluons and sea quarks, and Ψ_q and Ψ_s stand for the wave-functions, which are in general different from each other, i.e., $\Psi_q \neq \Psi_s$. Finally, $F_P^{q,s}$ is related to the $\Psi_{q,s}$ wave function normalization, cf. Eq. (1.46). Assuming further that

$$|\eta\rangle = \cos\phi|\eta_q\rangle - \sin\phi|\eta_s\rangle, \quad |\eta'\rangle = \sin\phi|\eta_q\rangle + \cos\phi|\eta_s\rangle, \quad (4.23)$$

implies that, when rotating back to the octet-singlet basis, an analogous $\eta - \eta'$ description along the lines of Eq. (4.23),

$$|\eta\rangle = \cos\theta_P|\eta_8\rangle - \sin\theta_P|\eta_0\rangle, \quad |\eta'\rangle = \sin\theta_P|\eta_8\rangle + \cos\theta_P|\eta_0\rangle, \quad (4.24)$$

would require defining the corresponding Fock states as

$$|\eta_8\rangle = \frac{\Psi_q + 2\Psi_s}{3} \frac{|u\bar{u} + d\bar{d} - 2s\bar{s}\rangle}{\sqrt{6}} + \frac{\sqrt{2}(\Psi_q - \Psi_s)}{3} \frac{|u\bar{u} + d\bar{d} + s\bar{s}\rangle}{\sqrt{3}}, \quad (4.25)$$

$$|\eta_0\rangle = \frac{\sqrt{2}(\Psi_q - \Psi_s)}{3} \frac{|u\bar{u} + d\bar{d} - 2s\bar{s}\rangle}{\sqrt{6}} + \frac{2\Psi_q + \Psi_s}{3} \frac{|u\bar{u} + d\bar{d} + s\bar{s}\rangle}{\sqrt{3}}, \quad (4.26)$$

so what has been defined as the octet(singlet) $|\eta_{8(0)}\rangle$ component is an admixture of the octet and singlet Fock states unless $SU(3)_F$ -symmetry represents a good approximation and $\Psi_q = \Psi_s$ holds. This represents a result analogous to that in Eq. (4.12). Conversely, in such $SU(3)_F$ -symmetric case, where $\theta_8 = \theta_0 = \theta_P$, we could start with an analogous single-octet description. Rotating back to the flavor basis, we would find an analogous result to that in Eq. (4.25), namely, that the light(strange) quark state is an admixture of light and strange quark Fock states unless $\Psi_8 = \Psi_0$. In this language, this is easy to see, as $|q\bar{q}\rangle$ -like states get mixed via the QCD anomaly, an OZI-violating effect analogous to the result in Eq. (4.21).

To summarize, the quark-flavor basis provides a simpler choice—in terms of a single angle— whenever the precision we aim for does not require to include OZI-violating effects in our framework and has become the most popular choice in phenomenological analyses [119, 120, 177, 178, 180, 181]. In the case where the required precision may become sensitive to OZI-violating effects, both basis involve the use of two-angles—alternatively, four independent decay constants— and the octet-singlet basis may become simpler for incorporating such effects.

4.4 Determining the $\eta - \eta'$ mixing from the TFFs

The different analyses used in the literature to extract the mixing parameters defined in the previous section— $F_8, F_0, \theta_8, \theta_0$ in the octet-singlet basis or, alternatively, F_q, F_s, ϕ_q, ϕ_s in the quark-flavor basis— find often non-compatible values among their extractions. As an illustration, we refer to

the approaches from Refs. [47, 119, 120, 179] which are depicted in Fig. 4.1. It would be desirable then to have an alternative approach which is defined in terms of $\ell N_c \chi$ PT quantities alone—the decay constants—and has control over the OZI-violating parameters. This requires avoiding, for instance, models for the $VP\gamma$ transitions—more comments on them in Section 4.5.1—which are widely used to extract the mixing parameters, or, eventually, the popular $J/\Psi \rightarrow \gamma\eta(\eta')$ decays—further comments on this point in Section 4.5.2. We suggest that this is possible using the available information on the η and η' TFFs from Chapter 2. Moreover, it is possible to account for the OZI-violating parameters, whose impact we discuss below. Actually our approach does not only allow to extract the above-mentioned mixing parameters but the additional OZI-violating parameter Λ_3 , cf. Eq. (4.16).

The starting point in our approach is the remarkable observation that, not only the low-energy behavior for the η and η' TFFs—related to their two photon decays—but their high-energy behavior $\lim_{Q^2 \rightarrow \infty} F_{P\gamma^*\gamma}(Q^2)$ dictated by pQCD Eq. (1.49) is given, essentially, in terms of the desired mixing parameters. Particularly, at NLO, the two-photon decays can be calculated from $\ell N_c \chi$ PT, obtaining [41, 138, 178]

$$F_{\eta\gamma\gamma} \equiv F_{\eta\gamma\gamma}(0) = \frac{1}{4\pi^2} \frac{\hat{c}_8(1+K_2^8)F_{\eta'}^0 - \hat{c}_0(1+K_2^0+\Lambda_3)F_{\eta'}^8}{F_{\eta'}^0 F_{\eta}^8 - F_{\eta'}^8 F_{\eta}^0}, \quad (4.27)$$

$$F_{\eta'\gamma\gamma} \equiv F_{\eta'\gamma\gamma}(0) = \frac{1}{4\pi^2} \frac{-\hat{c}_8(1+K_2^8)F_{\eta}^0 + \hat{c}_0(1+K_2^0+\Lambda_3)F_{\eta}^8}{F_{\eta'}^0 F_{\eta}^8 - F_{\eta'}^8 F_{\eta}^0}, \quad (4.28)$$

where $\hat{c}_8 = 1/\sqrt{3}$ and $\hat{c}_0 = 2\sqrt{2}/\sqrt{3}$ are charge factors. Besides, $K_2^8 \equiv K_2 \frac{7\dot{M}_\pi^2 - 4\dot{M}_K^2}{3}$ and $K_2^0 \equiv K_2 \frac{2\dot{M}_\pi^2 + \dot{M}_K^2}{3}$ are related to the LEC K_2 in the $\ell N_c \chi$ PT Lagrangian [41]³. The latter appear as well in the π^0 TFF via

$$F_{\pi\gamma\gamma} \equiv F_{\pi\gamma\gamma}(0) = \frac{1+K_2\dot{M}_\pi^2}{4\pi^2 F_\pi}. \quad (4.29)$$

From the experimental $\pi^0 \rightarrow \gamma\gamma$ result [10], we obtain $K_2 = -0.45(58)$, which is small and compatible with zero and has been often neglected in previous analyses.

It must be emphasized that, in Eqs. (4.27) and (4.28), the Λ_3 OZI-violating parameter from Eq. (4.16) must be included to render the result scale-independent. To see this, note that both F_P^0 and Λ_3 , unlike F_P^8 and K_2 , scale as $(1 + \delta_{\text{RG}}(\mu))$. This produces overall factors in the numerator and denominator canceling the scale-dependency. To obtain the expression for the high-energy behavior, we have first to take into account the running

³The K_2 LEC represents the $\ell N_c \chi$ PT version for the $SU(3)_F \chi$ PT $L_8^{6\epsilon}$ LEC, see Ref. [41]. Particularly, it compares to Eq. (1.51) via $K_2 \rightarrow -(1024\pi^2/3)L_8^{6\epsilon}$.

of the axial current, Eq. (4.14), which implies an additional running effect on top of that of the Gegenbauer coefficients, Eq. (1.47). From Eq. (4.15), and taking as the reference scale for the $(\eta)\eta' \rightarrow \gamma\gamma$ decays $\mu_0 = 1$ GeV, we obtain for F_P^0 at $Q^2 \rightarrow \infty$ the relation

$$F_P^0(\infty) = F_P^0 \left(1 - \frac{2N_F \alpha_s}{\beta_0 \pi} \right) = F_P^0(1 + \delta_{\text{RG}}(\infty)) \equiv F_P^0(1 + \delta), \quad (4.30)$$

where α_s is to be evaluated at 1 GeV and F_P^0 is the decay constant appearing in the $\eta(\eta') \rightarrow \gamma\gamma$ decays, to be taken at $\mu_0 = 1$ GeV. Taking into account corrections from higher orders by using the α_s -running to four-loops accuracy [186] as well as considering threshold effects, we obtain that $\delta = -0.17$. The high-energy behavior —assuming that asymptotic behavior is reached— then reads [67]

$$\eta_\infty \equiv \lim_{Q^2 \rightarrow \infty} Q^2 F_{\eta\gamma^*\gamma}(Q^2) = 2(\hat{c}_8 F_\eta^8 + \hat{c}_0(1 + \delta) F_\eta^0), \quad (4.31)$$

$$\eta'_\infty \equiv \lim_{Q^2 \rightarrow \infty} Q^2 F_{\eta'\gamma^*\gamma}(Q^2) = 2(\hat{c}_8 F_{\eta'}^8 + \hat{c}_0(1 + \delta) F_{\eta'}^0). \quad (4.32)$$

The resulting effect is by no means negligible and, to our best knowledge, was implemented for the first time in Ref. [67].

We have at this stage a set of four equations at our disposal (Eqs. (4.27), (4.28), (4.31) and (4.32)) to extract the four mixing parameters we are interested in. It seems then a straightforward task to determine the mixing parameters —at least, if we neglect the *a priori* small parameter Λ_3 and either neglect or take K_2 from the $\pi^0 \rightarrow \gamma\gamma$ decay. However, there is a subtle connection among the different equations which avoids for such an easy solution. As noted for the first time in our work in Refs. [114, 117], the system of equations is degenerate. To see this, we can obtain an expression for F_η^8 and $F_{\eta'}^8$ from Eqs. (4.31) and (4.32). Then, substituting in Eqs. (4.27) and (4.28), we can linearize the system, which may be expressed in matrix form as

$$A(F_\eta^8, F_{\eta'}^8, F_\eta^0, F_{\eta'}^0)^T = (\eta_\infty, \eta'_\infty, 0, 0)^T, \quad (4.33)$$

where the A matrix is defined as

$$A = \begin{pmatrix} 2\hat{c}_8 & 0 & 2\hat{c}_0(1 + \delta) & 0 \\ 0 & 2\hat{c}_8 & 0 & 2\hat{c}_0(1 + \delta) \\ 0 & \tilde{c}_0 & -\frac{2\pi^2}{\hat{c}_8} \eta'_\infty F_{\eta\gamma\gamma} & \frac{2\pi^2}{\hat{c}_8} \eta_\infty F_{\eta\gamma\gamma} - \tilde{c}_8 \\ -\tilde{c}_0 & 0 & \tilde{c}_8 - \frac{2\pi^2}{\hat{c}_8} \eta'_\infty F_{\eta'\gamma\gamma} & \frac{2\pi^2}{\hat{c}_8} \eta_\infty F_{\eta'\gamma\gamma} \end{pmatrix}, \quad (4.34)$$

where $\tilde{c}_8 = \hat{c}_8(1 + K_2^8)$ and $\tilde{c}_0 = \hat{c}_0(1 + K_2^0 + \Lambda_3)$. Then, the degeneracy is inferred from the determinant, which is proportional to

$$(\hat{c}_8^2(1 + K_2^8) + \hat{c}_0^2(1 + \delta)(1 + K_2^0 + \Lambda_3)) - 2\pi^2 (F_{\eta\gamma\gamma}\eta_\infty + F_{\eta'\gamma\gamma}\eta'_\infty). \quad (4.35)$$

It may look that Eq. (4.35) is in general non-vanishing. However, it turns out that

$$\begin{aligned} F_{\eta\gamma\gamma}\eta_\infty + F_{\eta'\gamma\gamma}\eta'_\infty &= \frac{\hat{c}_8^2(1+K_2^8) + \hat{c}_0^2(1+\delta)(1+K_2^0+\Lambda_3)}{2\pi^2} \\ &= \frac{3}{2\pi^2} \left(1 + \frac{1}{9} [K_2^8 + 8(\delta + (K_2^0 + \Lambda_3)(1+\delta))] \right), \end{aligned} \quad (4.36)$$

yields a vanishing value for Eq. (4.35), where in the last term we have replaced the charge factors \hat{c}_i . As an alternative approach, we can find that there is a null space for the system in Eq. (4.34),

$$(\hat{c}_0 F_{\eta'\gamma\gamma}(1+\delta), -\hat{c}_0(1+\delta)F_{\eta\gamma\gamma}, -\hat{c}_8 F_{\eta'\gamma\gamma}, \hat{c}_8 F_{\eta\gamma\gamma})^T. \quad (4.37)$$

All in all, we have to deal with a degenerate system, which may look like a dead-end for our approach. However, contrary to the expectations, it turns out that one can take advantage of Eq. (4.36) to solve all these problems. Curiously enough, the OZI-violating Λ_i parameters play a central role in this discussion. In order to illustrate their impact and conceptual relevance, we first set $K_2 = 0$ and sequentially include these parameters one by one. First, we set $\Lambda_1 = \Lambda_3 = 0$ and discuss the results. Second, we let $\Lambda_3 \neq 0$ but, still, $\Lambda_1 = 0$. Third, we let $\Lambda_1, \Lambda_3 \neq 0$ and obtain them through a fitting procedure. Finally, we include the parameter K_2 , which completes the full list of NLO LECs which are relevant to our study. The latter is the main result from this chapter and represents, to our best knowledge, the first result fully consistent with $\ell N_c \chi$ PT at NLO. Finally, we discuss our findings and compare to previous phenomenological approaches.

4.4.1 The $\eta - \eta'$ mixing: $K_2 = \Lambda_1 = \Lambda_3 = 0$

The simplest choice one can take to solve for the mixing parameters, see Ref. [117], is to set all the OZI-violating Λ_i parameters present in our equations to 0, this is $\Lambda_1 = \Lambda_3 = 0$ (as well as $K_2 = 0$). This choice implies, via Eq. (4.21), that $\phi_q = \phi_s \equiv \phi$. This does not only break the degeneracy of our system, but reduces the number of free parameters down to 3, which allows to solve the system using a set of three equations out of Eqs. (4.27), (4.28), (4.31) and (4.32). We call the attention however, that obtaining the same solution for any set is not guaranteed unless relation Eq. (4.36), $F_{\eta\gamma\gamma}\eta_\infty + F_{\eta'\gamma\gamma}\eta'_\infty = \frac{3}{2\pi^2}(1 + \frac{8}{9}\delta)$, is fulfilled. In our case, taking the input values from Table 2.14, we obtain $0.89(3)\frac{3}{2\pi^2}$ for the left hand side, whereas the right hand side yields $0.85\frac{3}{2\pi^2}$ for $\delta = -0.17$. Therefore, it seems that neglecting the OZI-violating parameters has not a tremendous impact. Note however that, to reach such agreement, we need to introduce the running parameter δ from Eq. (4.30), which in the FKS scheme should be zero.

In any case, since the condition Eq. (4.36) is not exactly fulfilled, every set of equations will yield only marginally-compatible solutions. In order to

solve the system, we decide to take the result which makes use of $F_{\eta\gamma\gamma}$, $F_{\eta'\gamma\gamma}$ and η_∞ alone. The reason is motivated in two-fold way. On the one hand, $F_{\eta\gamma\gamma}$ and $F_{\eta'\gamma\gamma}$ have been directly measured to an excellent precision. On the other hand, among the asymptotic values, η_∞ is the one with the most reliable extraction, see Chapter 2. Finally, we expect that the η parameters are theoretically cleaner, as they are less sensitive to the singlet effects we are neglecting at this stage. As a result, taking the $F_{\eta\gamma\gamma}$, $F_{\eta'\gamma\gamma}$ and η_∞ values from Table 2.14, we obtain [117]

$$\frac{F_q}{F_\pi} = 1.07(2), \quad \frac{F_s}{F_\pi} = 1.29(16), \quad \phi = 38.3(1.6)^\circ, \quad (4.38)$$

$$\frac{F_8}{F_\pi} = 1.22(11) \quad \frac{F_0}{F_\pi} = 1.15(5) \quad \theta_8 = -21.4(1.9)^\circ \quad \theta_0 = -11.2(5.0)^\circ, \quad (4.39)$$

where in the second line we have used Eq. (4.19) to translate the result into the octet-singlet basis. As an illustration, had we used η'_∞ instead of η_∞ , we would have obtained $F_q/F_\pi = 1.06(1)$, $F_s/F_\pi = 1.63(8)$, $\phi = 41.1(0.8)^\circ$. Had we obviated RG-effects, we would find some deviations in sets containing the η_∞ , while big deviations would be found for those containing η'_∞ , as the singlet content is more important for the η' , see Ref. [114]. Our result is in line with previous findings [47, 114, 119, 120, 179] and has competitive errors. For comparison, see Fig. 4.1, Option I.

4.4.2 The $\eta - \eta'$ mixing: $K_2 = \Lambda_1 = 0, \Lambda_3 \neq 0$

As illustrated before, the previous approach suffers from the fact that solutions from different sets yield different results which are only marginally compatible. This was easy to anticipate given that the degeneracy condition (4.36) was only marginally fulfilled for $\Lambda_3 = 0$. In this second approach, we assume that, still, $\Lambda_1 = 0$, but Λ_3 is a free parameter, which is fixed as to fulfill Eq. (4.36), obtaining [117] $\Lambda_3 = 0.06(4)$. Such value may be compared to the result $\Lambda_3 = -0.03(2)$ from Ref. [179] obtained from $VP\gamma$ decays. They differ in sign, but agree on its small magnitude, even beyond what is expected from the naive $1/N_c$ counting. Still, as $\Lambda_1 = 0$, we stick to the one-angle quark-flavor scheme, whereby any set of three equations can be used with the same result. Taking the same inputs as in previous section from Table 2.14, we obtain

$$\frac{F_q}{F_\pi} = 1.12(4), \quad \frac{F_s}{F_\pi} = 1.52(7), \quad \phi = 38.9(1.3)^\circ, \quad (4.40)$$

$$\frac{F_8}{F_\pi} = 1.40(5) \quad \frac{F_0}{F_\pi} = 1.27(3) \quad \theta_8 = -23.6(1.1)^\circ \quad \theta_0 = -7.3(3.2)^\circ. \quad (4.41)$$

As an advantage, choosing $\Lambda_3 \neq 0$, we can obtain analog results for any chosen set of equations, which improves with respect to the previous situation. Our results are displayed under the label Option II in Fig. 4.1 and show the impact of including the Λ_3 parameter.

4.4.3 The $\eta - \eta'$ mixing: $K_2 = 0, \Lambda_1, \Lambda_3 \neq 0$

The approaches adopted in Sections 4.4.1 and 4.4.2 present, at the formal level, some theoretical inconsistencies. Namely, we found that running effects—neglected in the common FKS scheme—encoded in δ , see Eq. (4.30), were important in our determination. However, these require, formally, the presence of the Λ_1 parameter if the scale-dependency for the asymptotic behavior is to be cancelled—see Eqs. (4.31) and (4.32). Similarly, including Λ_3 requires the presence of Λ_1 to cancel the scale-dependency in the two photon decays—see Eqs. (4.27) and (4.28). Besides, at the phenomenological level, there is further evidence pointing to $\Lambda_1 \neq 0$ effects. Particularly, our previous results—and basically every phenomenological estimate, see Fig. 4.1—indicate that $F_q > F_\pi$ with around 3σ significance. This, via Eq. (4.20), implies a non-vanishing positive value for Λ_1 , which in our simplified approach was taken to be zero. This in turn, would imply via Eq. (4.21) that $\phi_q \neq \phi_s$, invalidating then our previous assumptions and pointing out the necessity of using a general scheme with two different angles and non-zero $\Lambda_{1,3}$ parameters for describing the η and η' decay constants, an approach that we adopt in this section (but still retaining $K_2 = 0$).

In order to solve our system, and focusing on the octet-singlet basis, we have at disposal four equations—Eqs. (4.27), (4.28), (4.31) and (4.32)—and five unknowns— F_8 , F_0 , θ_8 , θ_0 and Λ_3 . In order to cure this situation, we can resort, as in the previous section, to the Eq. (4.36), which would provide the required constraint to fix Λ_3 , but we still have to face the fact that our system is linear dependent. In order to overcome this problem, we notice that NLO $\ell N_c \chi$ PT provides a clean prediction for both, F_8 and $F_8 F_0 \sin(\theta_8 - \theta_0)$ in terms of the well-known value for F_K/F_π [10]. Taking either of them as a constraint, one would add an additional equation to the previous system, which would provide a unique solution. Taking both, would lead to an overdetermined system, which in general has no solution. For this reason, we adopt a democratic procedure[138] in which we perform a fit including both F_8 and $F_8 F_0 \sin(\theta_8 - \theta_0)$ constraints⁴ together with Eqs. (4.27), (4.28), (4.31), (4.32) and (4.36). In addition, we ascribe a 3% theoretical uncertainty for the $\ell N_c \chi$ PT predictions by noticing that F_K/F_π typically receives 3% corrections from the NNLO⁵. Consequently, we add this error in quadrature on top of the one from [10] for our fitting procedure. As in the previous section, we take the inputs in Table 2.14. We obtain a

⁴We use preciser relations than those from Section 4.3.1: $(F_8/F_\pi)^2 = 1 + \frac{8}{3} \frac{F_K}{F_\pi} \left(\frac{F_K}{F_\pi} - 1 \right)$, and $F_8 F_0 \sin(\theta_8 - \theta_0) = -\frac{\sqrt{2}}{3} F_\pi^2 \left(\frac{F_K}{F_\pi} - 1 \right) \left(4 \frac{F_K}{F_\pi} + (\Lambda_1 \rightarrow 0) \right)$. See [120, 183].

⁵To see this, consider $F_K/F_\pi = 1.198 \simeq 1 + \epsilon + \epsilon^2$. This leads to the estimate for the NNLO correction $\epsilon^2 = 0.03$. Explicit results in Ref. [187] leads to similar values too.

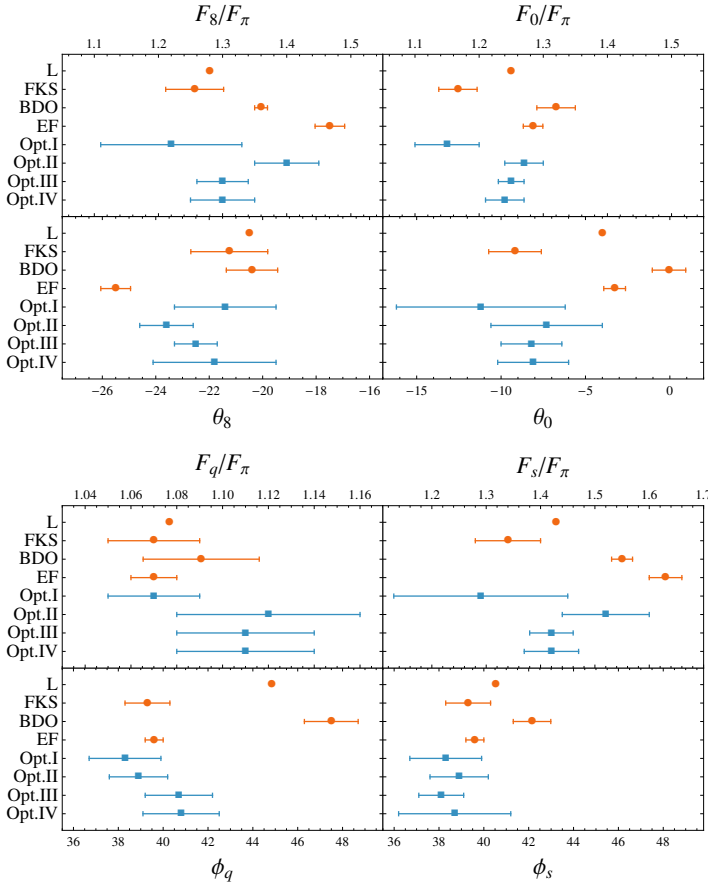


Figure 4.1: Our mixing parameters Eqs. (4.38) to (4.43) (blue squares) compared to different theoretical results (orange circles), see description in the text. The upper(lower) pannel displays our results in the octet-singlet(quark-flavor) basis. The references stand for L [47], FKS [119], BDO [179] EF [120].

fit with $\chi^2_\nu = 0.35$ and the following results for the mixing parameters [138]

$$\frac{F_8}{F_\pi} = 1.30(4), \quad \frac{F_0}{F_\pi} = 1.25(2), \quad \theta_8 = -22.5(0.8)^\circ, \quad \theta_0 = -8.2(1.8)^\circ, \quad (4.42)$$

$$\frac{F_q}{F_\pi} = 1.11(3), \quad \frac{F_s}{F_\pi} = 1.42(4), \quad \phi_q = 40.7(1.5)^\circ, \quad \phi_s = 38.1(1.0)^\circ. \quad (4.43)$$

These results are labelled as Option III in Fig. 4.1, where the impact of including $\Lambda_1 \neq 0$ can be appreciated. In addition, we obtain for the OZI-violating parameters and the state-mixing angle

$$\Lambda_3 = 0.05(3), \quad \Lambda_1 = 0.20(4), \quad \theta_P = -15.4(1.0)^\circ. \quad (4.44)$$

Here, Λ_1 and θ_P are not directly fitted parameters, but can be obtained by

means of Eq. (4.11)⁶ and Eq. (4.13), respectively.

4.4.4 The $\eta - \eta'$ mixing: $K_2, \Lambda_1, \Lambda_3 \neq 0$

Finally, to quantify the impact of a non-zero K_2 parameter and to have a fully consistent description at NLO in $\ell N_c \chi$ PT, we include the former in the last step. To do so, and given the poor extraction from $\pi^0 \rightarrow \gamma\gamma$ decays ($K_2 = -0.45(58)$), we incorporate this together with the experimental value for $F_{\pi\gamma\gamma}$ in our fitting procedure. We obtain a fit with $\chi^2_\nu = 0.54$ and the following values for the mixing parameters

$$\frac{F_8}{F_\pi} = 1.30(5), \quad \frac{F_0}{F_\pi} = 1.24(3), \quad \theta_8 = -21.8(2.3)^\circ, \quad \theta_0 = -8.1(2.1)^\circ, \quad (4.45)$$

$$\frac{F_q}{F_\pi} = 1.11(3), \quad \frac{F_s}{F_\pi} = 1.42(5), \quad \phi_q = 40.8(1.7)^\circ, \quad \phi_s = 38.7(2.5)^\circ. \quad (4.46)$$

In addition, we find

$$\Lambda_3 = 0.06(3), \quad K_2 = -0.15(50), \quad \Lambda_1 = 0.19(6), \quad \theta_P = -14.9(1.9)^\circ. \quad (4.47)$$

The results for the mixing parameters, Eqs. (4.45) to (4.47), represent the main result from this chapter. We remind that we have used in our procedure a renormalization scale $\mu_0 = 1$ GeV. Consequently, our values should be understood at such scale. This applies to the OZI-violating parameters $\Lambda_{1,3}$ and, in the octet-singlet basis, to the singlet decay constants F_P^0 . Whereas this may be adequate for pQCD studies such as those in Refs. [67, 188], the $\ell N_c \chi$ PT practitioner may find more helpful the scale-independent $\Lambda_1 - 2\Lambda_3 = 0.07(6)$ quantity. Our predictions can be compared in Fig. 4.1, Option IV, to our previous simplified approaches in order to appreciate the relevance of each parameter and to existing phenomenological determinations. Such determinations do not offer in general the values for the OZI-violating parameters, which are assumed to be zero. The exceptions are Ref. [179], $\Lambda_3 = -0.03(2)$, $\Lambda_1 = 0.20(4)$ and Ref. [47], $\Lambda_1 - 2\Lambda_3 = 0.25$.

In summary, we have performed a new determination for the $\eta - \eta'$ mixing parameters purely based on $\ell N_c \chi$ PT Lagrangian quantities —to this day, the only consistent framework to describe the $\eta - \eta'$ system. Our approach fully incorporates the required OZI-violating parameters (necessary to render scale-independent results) as well as the K_2 LEC, which are neglected in most of the previous phenomenological approaches [119, 120, 177, 178, 180, 181]. In addition, our approach does not rely on a phenomenological model involving further assumptions, as required for instance when using $V \rightarrow P\gamma$ transitions —find further details in Section 4.5.1. We note in this respect that previous approaches following the FKS scheme should have used

⁶Again, we use a preciser relation $(F_0/F_\pi)^2 = (1 + \frac{\Lambda_1}{2})^2 + \frac{4}{3}(\frac{F_K}{F_\pi} - 1)(\frac{F_K}{F_\pi} + \frac{\Lambda_1}{2})$ [183].

$F_q = F_\pi$ to be consistent. Finally, we emphasize that our approach makes use of 4 independent quantities alone to determine the mixing parameters. This contrasts with previous approaches requiring a larger amount of input in their fits and often with a large χ^2_ν value [120].

4.5 Applications

The extraction of the mixing parameters provides an important input to understand the structure of the $\eta - \eta'$, which is still a matter of debate and research nowadays due to its complexity —for the most recent studies, see [183, 184]. However, its interest lies beyond unravelling the structure of these pseudoscalars, as these parameters enter in a large variety of phenomenological applications. See for instance those in Refs. [67, 168, 178, 188–190], involving processes at low energies, such as $p\bar{p} \rightarrow \pi^0\eta^{(\prime)}$, mid-energies, such as $B^0 \rightarrow J/\Psi\eta^{(\prime)}$, or as energetic as $Z \rightarrow \eta^{(\prime)}\gamma$ decays. Consequently, our parameter extraction could be further tested using these processes. We do not pursue here such an ambitious programme, but merely describe two selected applications, namely, $V \rightarrow P\gamma$ and $P \rightarrow V\gamma$ transitions where $P = \eta^{(\prime)}$ and $V = \rho, \omega, \phi$, as well as $J/\Psi \rightarrow \eta^{(\prime)}\gamma$ decays.

4.5.1 Determining the $g_{VP\gamma}$ couplings

As a first application, we provide in this section the $g_{VP\gamma}$ couplings⁷ describing the interaction of the lowest-lying nonet of vector mesons with the pseudoscalar mesons and a photon. As such, they describe $\rho, \omega, \phi \rightarrow \eta\gamma$, $\eta' \rightarrow \rho(\omega)\gamma$ and $\phi \rightarrow \eta'\gamma$ decays, from which they can be experimentally extracted. Alternatively, these parameters can be theoretically related to the QCD-anomalous Green function $\langle P | T \{ J_\mu^{EM}(x), J_\nu^a(0) \} | 0 \rangle$ which, for vanishing virtualities, is given in terms of the triangle anomaly. The $g_{VP\gamma}$ couplings appear then when a dispersive representation saturated with the lowest-lying vector resonances is adopted [120, 170, 178]. The resulting expressions are given in Appendix B.1, which include the OZI violating parameter Λ_3 as appearing in Ref. [178] and K_2 as an additional novelty. Our results found for the $g_{VP\gamma}$ couplings are displayed in Tab. 4.1 together with the experimental values; the different outcomes for the methods employed in Sections 4.4.1 to 4.4.4 are labelled as Option I, II, III and IV, respectively. Though the agreement is not excellent, it has to be taken into account that higher resonances and continuum has been neglected in the employed dispersive representation, which implies non-negligible modeling associated errors, to some extent common both to the η and η' [170]. Therefore, it may be more adequate to take the ratio $g_{V\eta\gamma}/g_{V\eta'\gamma}$ instead [178], which is displayed in Table 4.1 as well. Actually, the agreement among our predictions and the

⁷The coupling is defined as $\langle P | J_\mu^{EM} | V_\nu \rangle |_{(p_P - p_V)^2=0} = -g_{VP\gamma} \epsilon_{\mu\nu\rho\sigma} p_P^\rho p_V^\sigma$ [170].

	Option I	Option II	Option III	Option IV	Experiment
$g_{\rho\eta\gamma}$	1.50(4)	1.45(2)	1.48(3)	1.47(5)	1.58(5)
$g_{\rho\eta'\gamma}$	1.18(5)	1.22(3)	1.21(3)	1.23(8)	1.32(3)
$g_{\omega\eta\gamma}$	0.57(2)	0.56(1)	0.57(1)	0.56(2)	0.45(2)
$g_{\omega\eta'\gamma}$	0.55(2)	0.56(1)	0.56(1)	0.56(4)	0.43(2)
$g_{\phi\eta\gamma}$	-0.83(11)	-0.70(4)	-0.78(5)	-0.72(5)	-0.69(1)
$g_{\phi\eta'\gamma}$	0.98(14)	0.86(7)	0.89(4)	0.84(5)	0.72(1)
$g_{\rho\eta\gamma}/g_{\rho\eta'\gamma}$	1.27(8)	1.22(3)	1.22(4)	1.19(12)	1.20(5)
$g_{\omega\eta\gamma}/g_{\omega\eta'\gamma}$	1.04(4)	1.00(2)	1.02(2)	1.00(10)	1.05(7)
$g_{\phi\eta\gamma}/g_{\phi\eta'\gamma}$	-0.85(6)	-0.81(8)	-0.87(7)	-0.87(7)	-0.96(4)
$R_{J/\psi}$	4.74(55)	4.94(46)	5.57(64)	5.66(69)	4.67(20)

Table 4.1: Summary of $g_{V\eta\gamma}$ couplings together with $R_{J/\psi}$, see description in the text. Experimental determinations are from Ref. [10].

experiment in these ratios is excellent for the ρ and ω cases and reasonable for the ϕ . The predictive power for these decays, which are used as inputs in traditional approaches instead, should be considered as an advantage from our approach.

4.5.2 Charmonium decays: $R_{J/\psi}$

It has been argued in Refs. [189, 190] that the $\eta - \eta'$ mixing parameters could be used as well to calculate decays in the charmonium region. Note that all these processes need to change flavor, which—neglecting electromagnetic effects—necessarily happens through OZI violating mechanisms, where the singlet sector plays a central role. Specially popular, and widely used in phenomenological analyses [119, 120, 170] are the $J/\Psi \rightarrow \eta^{(\prime)}\gamma$ decays, in particular its ratio $R_{J/\Psi}$ defined in Eq. (4.48) below. It is thought that the dominant mechanism underlying these decays is given by an intermediate two gluon state as depicted in Fig. 4.2 (see Ref. [191]) which allows to express the ratio as

$$R_{J/\psi} = \frac{BR(J/\psi \rightarrow \eta'\gamma)}{BR(J/\psi \rightarrow \eta\gamma)} = \left| \frac{\langle \eta' | G^{\mu\nu,c} \tilde{G}_{\mu\nu}^c | 0 \rangle}{\langle \eta | G^{\mu\nu,c} \tilde{G}_{\mu\nu}^c | 0 \rangle} \right|^2 \left(\frac{m_{J/\psi}^2 - m_{\eta'}^2}{m_{J/\psi}^2 - m_\eta^2} \right)^3, \quad (4.48)$$

where the first factor is the matrix element required from the process as outlined in Ref. [170] and the second factor is pure phase space. Note that a factorization formalism is implicit, assuming as well that everything else but the above matrix elements cancels out in the ratio.

Remarkably, even though $\ell N_c \chi$ PT does not incorporate gluons as explicit degrees of freedom, it allows to calculate Green's functions involving them. This possibility is brought by Ward identities, which in this case via Eq. (1.7) relate the purely gluonic current in Eq. (4.48) to quark currents and their divergencies. Particularly, for each individual flavor $q = u, d, s, \dots$, Eq. (1.7),

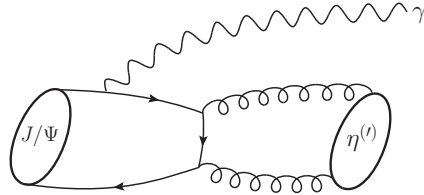


Figure 4.2: Expected main contribution to $J/\Psi \rightarrow \gamma\eta^{(\prime)}$ processes.

reads

$$\partial_\mu(\bar{q}\gamma^\mu\gamma_5 q) = 2m_q\bar{q}i\gamma_5 q - \frac{g_s^2}{32\pi^2}\epsilon^{\alpha\beta\mu\nu}G_{\alpha\beta}^cG_{\mu\nu}^c \equiv 2m_q\bar{q}i\gamma_5 q + \omega. \quad (4.49)$$

As an interesting academic exercise, we can further explore this relation, which under certain simplifying assumptions, allows to calculate the required $\langle P | G^{\mu\nu,c} \tilde{G}_{\mu\nu}^c | 0 \rangle$ matrix elements in terms of the mixing parameters [119, 120, 170]. To show this, note that the divergence of the singlet axial current⁸ in the limit in which $m_{u,d} \rightarrow 0$ reads

$$-\frac{3\alpha_s}{4\pi}G^{\mu\nu,c}\tilde{G}_{\mu\nu}^c \stackrel{m_{u,d} \rightarrow 0}{=} \sqrt{3}\left(\sqrt{2}\partial^\mu J_{5\mu}^0 - (2/\sqrt{3})m_s\bar{s}i\gamma_5 s\right). \quad (4.50)$$

Fortunately, for $m_{u,d} \rightarrow 0$, the pseudoscalar strange quark current appearing above can be connected to the divergence of the octet axial current which, *in such limit*, reads $\partial^\mu J_{5\mu}^8 = -(2/\sqrt{3})m_s\bar{s}i\gamma_5 s$. As a consequence, the following expression has been obtained in the literature [119, 120, 170]

$$-\frac{3\alpha_s}{4\pi}G^{\mu\nu,c}\tilde{G}_{\mu\nu}^c \stackrel{m_{u,d} \ll m_s}{\simeq} \sqrt{3}\left(\sqrt{2}\partial^\mu J_{5\mu}^0 + \partial^\mu J_{5\mu}^8\right) \quad (4.51)$$

which holds up to light quark mass corrections or, equivalently, m_π^2/m_K^2 effects [178]. The relation above allows to express the $R_{J/\Psi}$ ratio in terms of the axial currents matrix elements as defined in Eqs. (4.8) and (4.10):

$$R_{J/\Psi} \simeq \left| \frac{m_{\eta'}^2(F_8 \sin \theta_8 + \sqrt{2}F_0 \cos \theta_0)}{m_\eta^2(F_8 \cos \theta_8 - \sqrt{2}F_0 \sin \theta_0)} \right|^2 \left(\frac{m_{J/\Psi}^2 - m_{\eta'}^2}{m_{J/\Psi}^2 - m_\eta^2} \right)^3 \quad (4.52)$$

where \simeq stands for $m_{u,d} \neq 0$ effects, which will be estimated below. To check what is expected in different regimes of the theory as well as the accuracy of the approximation in Eq. (4.51), we take the LO results in $\ell N_c \chi$ PT. For the $\hat{m} \rightarrow 0$ case (i.e. $m_\pi^2 \rightarrow 0$) the equality in Eq. (4.51) holds exactly, and the gluonic matrix elements read, at LO,

$$\sqrt{3}m_P^2(F_P^8 - \sqrt{2}F_P^0) \stackrel{\hat{m} \rightarrow 0}{=} \langle P | \omega | 0 \rangle = \sqrt{6}F_P^0 M_\tau^2, \quad (4.53)$$

⁸The singlet axial current reads $J_{5\mu}^0 = (1/\sqrt{6})(\bar{u}\gamma_\mu\gamma_5 u + \bar{d}\gamma_\mu\gamma_5 d + \bar{s}\gamma_\mu\gamma_5 s)$; for completeness, $J_{5\mu}^8 = (1/2\sqrt{3})(\bar{u}\gamma_\mu\gamma_5 u + \bar{d}\gamma_\mu\gamma_5 d - 2\bar{s}\gamma_\mu\gamma_5 s)$.

whereas the ratio itself reads, again at LO,

$$\left| \frac{\langle \eta' | \omega | 0 \rangle}{\langle \eta | \omega | 0 \rangle} \right|^2 = \left| \frac{\cos \theta_P}{-\sin \theta_P} \right|^2. \quad (4.54)$$

For the special case where m_s effects are negligible as compared to the topological ones, this is, $m_K^2 \ll M_\tau^2$, the η and η' would become purely octet and singlet, respectively, with masses and mixing angle at LO

$$m_\eta^2 = \frac{4}{3} m_K^2 \left(1 - \frac{2}{3} \epsilon \right), \quad m_{\eta'}^2 = M_\tau^2 \left(1 + \frac{2}{3} \epsilon \right), \quad \theta_P = -\frac{2\sqrt{2}}{3} \epsilon, \quad (4.55)$$

with $\epsilon = m_K^2/M_\tau^2$. As a consequence, the η would not receive a singlet admixture and would not couple to the gluons, with the ratio in Eq. (4.54) diverging as $| -3/(2\sqrt{2})\epsilon^{-1} |^2$.

An opposite scenario would be that in which the large- N_c limit represents an excellent approximation, whereby $M_\tau^2 \rightarrow 0$ and $FM_\tau^2 = 6\tau/F \sim 1/\sqrt{N_c} \rightarrow 0$, but $m_s > 0$ (i.e. $M_\tau^2 \ll m_K^2$). In such a case, the η would be become a massive η_s meson, whereas the η' would become a massless η_q , with masses and mixing angle at LO

$$m_\eta^2 = 2m_K^2 \left(1 + \frac{1}{6} \tilde{\epsilon} \right), \quad m_{\eta'}^2 = \frac{2}{3} M_\tau^2 \left(1 - \frac{1}{6} \tilde{\epsilon} \right), \quad \theta_P = \pi - \theta_{ideal} + \frac{1}{3\sqrt{2}} \tilde{\epsilon}, \quad (4.56)$$

with now $\tilde{\epsilon} = M_\tau^2/m_K^2$. In this case, both matrix elements would vanish as $M_\tau^2 \rightarrow 0$, but its ratio in Eq. (4.54) would be kept fixed at $| -\sqrt{2}(1 - (1/2)\tilde{\epsilon}) |^2$, with 2 its limiting value. Consequently, as far as LO results are concerned, a result $R_{J/\Psi} > 2$ would directly point towards $M_\tau > m_s$.

Finally, but still at LO, we discuss the accuracy of the approximation of neglecting the light quark masses in Eq. (4.51). From the LO results in Ref. [183], for which $M_\tau = 0.82$ GeV and $\theta_P = -19.6^\circ$, we obtain for the left hand side of Eq. (4.53) 0.60 and 1.58 for the η and η' . For the right hand side, the results read 0.55 and 1.55, respectively. As a consequence, we obtain that the equality Eq. (4.51) holds at around 5% precision for the matrix elements, implying a 10% systematic uncertainty for the $R_{J/\Psi}$ result.

After this discussion, we proceed to our determination. From Eq. (4.52) and our mixing parameters determination from Sections 4.4.1 to 4.4.4, we obtain the results quoted in the last row from Table 4.1. We find a difference of 1.4σ among our final result for the mixing parameters prediction (Option IV) and experiment. Yet this is not large, it would be interesting to have a preciser theoretical and experimental prediction, as this process could be sensitive to non-standard phenomena such as gluonium admixtures or $c\bar{c}$ content in the η' . However, to confirm such eventual discrepancy may require a more detailed analysis, including the light-quark mass effects neglected above, that could be around a 10% effect and would involve additional Λ_i OZI-violating parameters. In addition, it would be interesting to retain

additional OZI-suppressed contributions to the hard process non considered in Fig. 4.2 and which may be non-negligible in the light of $\psi(2S)$ decays —see discussions in [192]. Finally, it has to be mentioned that previous analysis did not include the RG effects which would appear in such process, necessary to render the amplitude scale-independent. A similar argument to that above Eq. (4.30) would imply $(1 - \delta_{\text{RG}}(m_{J/\Psi}^2)) = (1 - 0.05)$. Re-evaluating then Eq. (4.52) including such factor in the F_0 terms, we obtain $R_{J/\Psi} = 4.99(61)$, a non-negligible effect that shifts our value closer to the experimental one, and suggests the relevance of a more refined analysis.

4.5.3 Light- and strange-quark transition form factors

As explained in Sec. 4.3.2, under the assumption that large- N_c OZI-violating effects are negligible, the η and η' Fock states may be described through the use of a single angle in terms of the light and strange quarks wave functions Ψ_q, Ψ_s , common to the η and η' . These define the meson distribution amplitudes $\phi_\eta^q = \phi_{\eta'}^q \equiv \phi_q$ and $\phi_\eta^s = \phi_{\eta'}^s \equiv \phi_s$, Eq. (1.46), which are used to calculate the η and η' TFFs. Such distribution amplitudes can be used to obtain the unphysical —i.e., non measurable— light- and strange-quark TFF, $F_{q\gamma^*\gamma}(Q^2)$ and $F_{s\gamma^*\gamma}(Q^2)$, respectively, in terms of which the physical η and η' TFF can be expressed as

$$F_{\eta\gamma^*\gamma}(Q^2) = \cos \phi F_{q\gamma^*\gamma}(Q^2) - \sin \phi F_{s\gamma^*\gamma}(Q^2), \quad (4.57)$$

$$F_{\eta'\gamma^*\gamma}(Q^2) = \sin \phi F_{q\gamma^*\gamma}(Q^2) + \cos \phi F_{s\gamma^*\gamma}(Q^2). \quad (4.58)$$

The light- and strange-quark TFFs are related to the physical ones via rotation

$$F_{q\gamma^*\gamma}(Q^2) = \cos \phi F_{\eta\gamma^*\gamma}(Q^2) + \sin \phi F_{\eta'\gamma^*\gamma}(Q^2), \quad (4.59)$$

$$F_{s\gamma^*\gamma}(Q^2) = -\sin \phi F_{\eta\gamma^*\gamma}(Q^2) + \cos \phi F_{\eta'\gamma^*\gamma}(Q^2). \quad (4.60)$$

Our mixing parameters extraction would allow to find such a decomposition, which represents an interesting theoretical result. In order to reconstruct them, we take our averaged result $\phi \equiv (\phi_q + \phi_s)/2 = 39.5(1.1)^\circ$ from the mixing angles obtained in Section 4.4.3⁹ together with our fits from the TFFs in Chapter 2. In addition, as a consequence of assuming a mild large- N_c OZI violating effects, which seems a reasonable estimation according to our results, it is theoretically expected that the π^0 distribution amplitude ϕ_π should be the same as that from the light-quarks ϕ_q . This is easy to understand as, in this limit, the $U(3)_F$ symmetry would be recovered, guaranteeing then the equality of all distribution amplitudes —symmetry breaking effects should be accounted though for the strange quark, which does not represent a problem for the arguments above. Consequently, the resulting TFF should be,

⁹This should not be a bad approximation given our results in the previous section; we note however that $\Lambda_1 \neq 0$ implies that this is not a strict result but an approximate one.

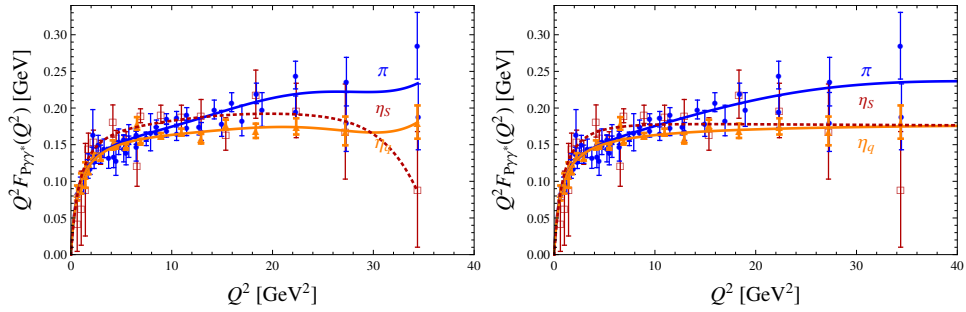


Figure 4.3: The light(strange)-quark TFF in orange(dotted-red) together with the π^0 TFF (blue). The left plot shows the P_N^N -based description, whereas the right one represents the P_1^N one. The former TFFs have been multiplied by a charge factor $3/5$ and $3/\sqrt{2}$, respectively (see details in the text). When possible, the η and η' TFF data points have been combined to extract what would be the light- and strange-quark TFF data as orange triangles and open-red squares, respectively. The data for the π^0 appears as blue points.

up to a charge factor $5/3$, equivalent $(F_{q\gamma^*\gamma}(Q^2) = (5/3)F_{\pi\gamma^*\gamma}(Q^2))$. For this reason, we plot in Fig. 4.3, the results for the π^0, η_q and η_s TFF obtained from Eqs. (4.59) and (4.60) and normalized to the π^0 charge. This amounts to multiply the light- and strange-quark TFF by the charge factors $3/5$ and $3/\sqrt{2}$, respectively. We find that actually the light-quark and the π^0 TFFs match each other up to the $Q^2 \sim 6$ GeV^2 scale, where the controversial Belle-BABAR discrepancy manifests [76, 133]. Provided $\phi_q \simeq \phi_\pi$, our approach supports Belle data against BABAR and strongly calls for a new preciser measurement at Belle II. In addition, the results above show a behavior beyond the simplest VMD (P_1^0 approximant) approach and should warn therefore against oversimplified descriptions. Finally, we give the resulting (dimensionful, i.e. $m_P = 1$ in Eq. (2.1)) slope for these TFFs

$$b_{\eta_q} = 1.67(3) \text{ GeV}^{-2} = (0.774(6) \text{ GeV})^{-2}, \quad (4.61)$$

$$b_{\eta_s} = 0.57^{(+0.17)}_{(-0.19)} \text{ GeV}^{-2} = (1.43^{(+0.37)}_{(-0.20)} \text{ GeV})^{-2}, \quad (4.62)$$

which has been obtained from our values in Table 2.14. These could be compared with the results for the π^0, η , and η' results from Chapter 2¹⁰,

$$b_\pi = 1.78(12) \text{ GeV}^{-2} = (0.750(26) \text{ GeV})^{-2}, \quad (4.63)$$

$$b_\eta = 1.916(39) \text{ GeV}^{-2} = (0.722(7) \text{ GeV})^{-2}, \quad (4.64)$$

$$b_{\eta'} = 1.42(3) \text{ GeV}^{-2} = (0.874(13) \text{ GeV})^{-2}, \quad (4.65)$$

which shows again the expected similarity among the π^0 and the light-quark quantities.

¹⁰To obtain them, the results from Table 2.14 should be multiplied by m_P^{-2} .

4.6 Conclusions and outlook

In this chapter, we have presented a new and alternative determination for the $\eta - \eta'$ mixing parameters using information on the TFFs exclusively. As an advantage, our formulation allows for a straightforward connection to the quantities arising in the $\ell N_c \chi$ PT Lagrangian —up to day, the only consistent framework to describe the $\eta - \eta'$ system—and avoids thereby the use of models and approximations as those taken in studies using $V \rightarrow P\gamma$ and $P \rightarrow V\gamma$ processes or J/Ψ decays. Moreover, besides implementing the full NLO $\ell N_c \chi$ PT expressions including the relevant OZI-violating parameters, we have been able to provide a determination for them. Even if we find small values for them, their role is not negligible and plays a crucial role in the TFFs asymptotic behavior—the role of the LEC K_2 is by contrast negligible. We remark that including them is necessary to achieve formally a consistent picture. This is a disadvantage from previous approaches, in which these parameters were kept finite for some quantities and vanishing in others. To illustrate their impact, we used a sequential approach in which the different OZI-violating effects and finally K_2 were sequentially included one by one. Remarkably, we achieve a competitive prediction with respect to existing approaches, that required a large amount of inputs in their fits and usually obtained a large χ^2_ν value, highlighting possible model-dependencies. This put us in a perfect position to test the mixing-scheme in different observables.

Possible venues to improve and extend our work would be a thorough and detailed calculation of the RG-equation for the singlet axial current, including higher orders. In addition, it would be interesting to see if ongoing studies of the $\eta - \eta'$ provide additional insights which may help in extracting the mixing parameters [183, 184, 193]. Lattice studies such as [194] would help in this point as well—note however that they obtain the pseudoscalar, rather than the axial current matrix element. A final point of interest would be the application of our results to the calculation of additional charmonium and weak decays in lines of Refs. [189, 190] with a proper account of OZI-violating effects.

Chapter 5

Pseudoscalar to lepton pair decays

Contents

5.1	Introduction	97
5.2	The process: basic properties and concepts . .	98
5.3	A rational description for $F_{P\gamma^*\gamma^*}(Q_1^2, Q_2^2)$. . .	105
5.4	Final results	112
5.5	Implications for χ PT	116
5.6	Implications for new physics contributions . . .	120
5.7	Conclusions and outlook	127

5.1 Introduction

The pseudoscalar decays into lepton pairs, $P \rightarrow \ell\bar{\ell}$, are a beautiful place to keep track of the evolution of our understanding of QCD, which is behind the mechanism driving these processes. Its pioneering study was initiated by Drell [195] back in 1959, well before the time where the pseudoscalar decays into photons were properly understood on basis of the Adler [42]-Bell-Jackiw [43] (ABJ) anomaly. Still, he was able to set a lower bound for the $\pi^0 \rightarrow e^+e^-$ decay. Further studies (some of them rather qualitative) appeared in the 60's with the advent of VMD ideas [196–200] which were just being developed at that time. Later on, the development of perturbative QCD stimulated different approaches in the 80's. Among them, quark loop models based on duality ideas [112, 201–205] and phenomenological models based on the novel understanding of exclusive reactions in pQCD [206] —which were improved through the use of data [207–209]. More recently, the development of χ PT, the low-energy effective field theory of QCD, provided an alternative approach to study these decays [210, 211], which in addition may be complemented with large- N_c and resonant ideas [99, 212].

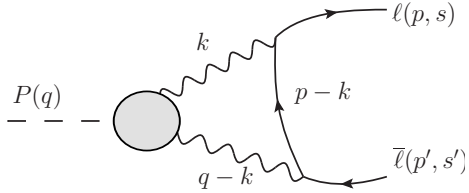


Figure 5.1: The leading order contribution to $P \rightarrow \bar{\ell}\ell$ processes. The shadowed blob stands for the QCD dynamics in the $P \rightarrow \gamma^*\gamma^*$ transition encoded in $F_{P\gamma^*\gamma^*}(k^2, (q-k)^2)$.

The motivation for this continuous study has been undoubtedly bound to the different experimental anomalies appearing in these processes along the years, stimulating a continuous revision and speculation about new-physics effects [213–217].

In this chapter, we apply all the machinery developed for reconstructing the TFFs and benefit from our novel ideas, gaining on precision and obtaining, for the first time, a reliable systematic error estimation, taking special care of the η and η' cases. In this way, we want to update the status of these decays to the standards of precision met nowadays—required for testing the low-energy frontier of the SM [218, 219]. The calculation details of these processes together with their relevant features are outlined in Section 5.2. The systematic error assessment is described in Section 5.3, including a careful description of some particular features—previously overlooked—present for the η and η' but not for the π^0 . Our results, discussed in Section 5.4, show interesting features when compared to χ PT as we describe in Section 5.5. Finally, we discuss new physics implications in Section 5.6.

5.2 The process: basic properties and concepts

The leading order¹ QED contribution to $P \rightarrow \bar{\ell}\ell$ decays is mediated through an intermediate two-photon state as sketched in Fig. 5.1. The gray blob appearing there stands for the hadronic effects encoded in the $P \rightarrow \gamma^*\gamma^*$ transition. For real photons, such process is theoretically well known in terms of the ABJ anomaly, and can be obtained as well in the odd-parity sector of χ PT, see Section 1.6.2. For deeply virtual photons, the limits $\lim_{Q^2 \rightarrow \infty} F_{P\gamma^*\gamma}(Q^2)$ [102] and $\lim_{Q^2 \rightarrow \infty} F_{P\gamma^*\gamma^*}(Q^2, Q^2)$ [191] (see Section 1.6.1) are known as well. However, the interpolation in between these two regimes is a theoretically unknown territory, what has been amended through wise and different modeling procedures, explaining the large amount of studies on these processes. Parametrizing such interaction in terms of the

¹An additional but subleading tree-level Z^0 boson electroweak contribution exists too, cf. Section 5.6.

most general TFF, $F_{P\gamma^*\gamma^*}(q_1^2, q_2^2)$, we obtain for the matrix element

$$\begin{aligned} i\mathcal{M} &= \int \frac{d^4k}{(2\pi)^4} (-ie^2 F_{P\gamma^*\gamma^*}(k^2, (k-q)^2)) \epsilon^{\mu\nu\rho\sigma} k_\mu (q-k)_\rho \frac{-ig_{\nu\nu'}}{k^2} \frac{-ig_{\sigma\sigma'}}{(q-k)^2} \\ &\quad \times \bar{u}_{p,s} (-ie\gamma^{\nu'}) i \frac{(\not{p} - \not{k}) + m_\ell}{(p-k)^2 - m_\ell^2} (-ie\gamma^{\sigma'}) v_{p's'} \\ &= \int \frac{d^4k}{(2\pi)^4} e^4 \epsilon^{\mu\nu\rho\sigma} k_\mu q_\rho \frac{[\bar{u}_{p,s} \gamma_\nu ((\not{p} - \not{k}) + m_\ell) \gamma_\sigma v_{p's'}]}{k^2 (q-k)^2 ((p-k)^2 - m_\ell^2)} F_{P\gamma^*\gamma^*}(k^2, (k-q)^2), \end{aligned} \quad (5.1)$$

where k is the momentum running through the loop and must be integrated over all energies. The definitions for the different elements follow the conventions² in [1] and can be found in Appendix A. At this stage of the calculation, it is convenient to evaluate the spinor contractions. This can be done using the pseudoscalar projector defined in Eq. (A16) from Ref. [220]. We recall it here adapted to our conventions—which amounts to shift the antisymmetric tensor sign with respect to [220]—for completeness,

$$v_{p',s'} \bar{u}_{p,s} |_{\text{out}, \mathcal{P}} = \frac{1}{2\sqrt{2}q^2} \left[-2m_\ell \not{q} \gamma_5 - i\epsilon_{\alpha\beta\gamma\delta} \gamma^\alpha \gamma^\beta \not{p}^\gamma \not{p}^\delta + q^2 \gamma_5 \right]. \quad (5.2)$$

The subindex out means that such equality holds for the final state particles, while subindex \mathcal{P} means that it is in a pseudoscalar state. Using standard trace techniques together with Eq. (5.2), we find that the spinorial part in square brackets from Eq. (5.1) yields $-i(2\sqrt{2}m_\ell/m_P)\epsilon_{\nu\sigma\alpha\beta}q^\alpha k^\beta$. Inserting back into Eq. (5.1) and using $\epsilon^{\nu\sigma\mu\rho}\epsilon_{\nu\sigma\alpha\beta} = -2(\delta_\alpha^\mu\delta_\beta^\rho - \delta_\beta^\mu\delta_\alpha^\rho)$, we obtain the final result

$$i\mathcal{M} = 2\sqrt{2}m_\ell m_P \alpha^2 F_{P\gamma\gamma} \frac{2i}{\pi^2 q^2} \int d^4k \frac{[k^2 q^2 - (k \cdot q)^2] \tilde{F}_{P\gamma^*\gamma^*}(k^2, (k-q)^2)}{k^2 (q-k)^2 ((p-k)^2 - m_\ell^2)}, \quad (5.3)$$

where the $\sqrt{2}m_P$ term can be traced back to the effective pseudoscalar $\bar{u}\gamma_5 v$ interaction³ and m_ℓ to the helicity flip. $F_{P\gamma\gamma} \equiv F_{P\gamma\gamma}(0,0)$ and so $\tilde{F}_{P\gamma^*\gamma^*}(k^2, (k-q)^2)$ is the normalized TFF, $\tilde{F}_{P\gamma^*\gamma^*}(0,0) = 1$. The decay width reads then (see Appendix A.3)

$$\Gamma(P \rightarrow \bar{\ell}\ell) = \frac{1}{16\pi m_P} \beta_\ell |\mathcal{M}|^2, \quad (5.4)$$

with $\beta_\ell = \sqrt{1 - 4m_\ell^2/m_P^2}$ the lepton velocity. It is customary in the literature to express Eq. (5.4) in terms of the $\Gamma(P \rightarrow \gamma\gamma)$ ⁴ result, so the

²Here it may worth to stress that in our convention $\epsilon^{0123} = +1$.

³To see this, note that, from Eq. (5.2), $\text{Tr}(\bar{u}\gamma_5 v) = \sqrt{2}m_P$. In addition, this allows to effectively express $i\mathcal{M} = -i(\bar{u}i\gamma_5 v)2m_\ell \alpha^2 F_{P\gamma\gamma} \mathcal{A}(q^2)$, with $\mathcal{A}(q^2)$ defined in Eq. (5.6)

⁴The two photon decay-width reads $\Gamma(P \rightarrow \gamma\gamma) = \frac{e^4 m_P^3}{64\pi} |\mathcal{M}|^2$.

normalization for the TFF dependency disappears, which is the reason that it was factored out in Eq. (5.3). In such a way, the final result reads

$$\frac{\text{BR}(P \rightarrow \bar{\ell}\ell)}{\text{BR}(P \rightarrow \gamma\gamma)} = 2 \left(\frac{\alpha m_\ell}{\pi m_P} \right)^2 \beta_\ell |\mathcal{A}(q^2)|^2. \quad (5.5)$$

The prefactor⁵ in Eq. (5.5) already predicts tiny BRs for these processes, which are known as rare decays. This is due to the electromagnetic α^2 and the helicity flip suppression m_ℓ^2/m_P^2 factors with respect to the $P \rightarrow \gamma\gamma$ decay. The last parameter, $\mathcal{A}(q^2)$, is related to the loop amplitude and encode the QCD dynamics encapsulated in the TFF,

$$\mathcal{A}(q^2) = \frac{2i}{\pi^2 q^2} \int d^4 k \frac{(k^2 q^2 - (k \cdot q)^2) \tilde{F}_{P\gamma^*\gamma^*}(k^2, (q-k)^2)}{k^2 (q-k)^2 ((p-k)^2 - m_\ell^2)}. \quad (5.6)$$

The formulae in Eqs. (5.5) and (5.6) represent the main standard results necessary to calculate the BRs. At this point, it may seem hopeless to say anything about Eq. (5.6) without any information on the TFF, which is actually required to render the—otherwise divergent—loop integral finite. However, it is still possible to derive some important general results. Among them, the unitary bound obtained by Drell [195], the result for a constant TFF (of relevance for χ PT) and the relevant regimes in which a precise TFF determination is required. The latter is an essential prerequisite for any proper discussion on systematic errors and how to reconstruct the TFF.

5.2.1 The unitary bound

To derive the imaginary part associated to these processes, we use the Cutcosky rules, relating the imaginary part of the diagram to its discontinuities [1]. The latter are computed replacing the propagators which can be put on-shell as $\frac{1}{p^2 - m^2 + i\epsilon} \rightarrow -2\pi i \delta(p^2 - m^2) \theta(p^0)$. For the π^0 —being the lightest hadronic particle—the only possible intermediate state appearing in the loop is the two photon one. Following Cutcosky and replacing the photon propagators in Eq. (5.6), one obtains⁶

$$\begin{aligned} \text{Im } \mathcal{A}_{\gamma\gamma} &= \frac{(-2\pi i)^2}{\pi^2 q^2} \int d^4 k \frac{(q^2 k^2 - (q \cdot k)^2) \tilde{F}_{P\gamma\gamma}(k^2, (q-k)^2)}{((p-k)^2 - m^2)} \delta(k^2) \delta((q-k)^2), \\ &= \frac{-2}{m_P^2} \int d\Omega_3 dk^0 \frac{m_P^2 (k^0)^3 \tilde{F}_{P\gamma\gamma}(0,0)}{m_P k^0 (1 - \beta_\ell \cos \theta)} \frac{1}{2m_P} \delta(k^0 - \frac{m_P}{2}), \\ &= \frac{\pi}{4} \int d\Omega_3 \frac{1}{\beta_\ell \cos \theta - 1} = \frac{\pi}{2\beta_\ell} \ln \left(\frac{1 - \beta_\ell}{1 + \beta_\ell} \right). \end{aligned} \quad (5.7)$$

⁵ The prefactor in Eq. (5.5) is $\mathcal{O}(10^{-10})$ for the $\pi^0 \rightarrow e^+ e^-$, $\mathcal{O}(10^{-11}(10^{-7}))$ for the $\eta \rightarrow e^+ e^- (\mu^+ \mu^-)$ and $\mathcal{O}(10^{-12}(10^{-7}))$ for the $\eta' \rightarrow e^+ e^- (\mu^+ \mu^-)$.

⁶ We use polar coordinates $dk^4 = d\Omega_3 dk^0 \frac{1}{2} \mathbf{k} d\mathbf{k}^2$ and specialize to the pseudoscalar rest frame, where $\vec{q} = (m_P, \vec{0})$ and $\vec{p} = m_P/2(1, \vec{\beta}_\ell)$. To perform integration over $d\mathbf{k}^2$ we use $\delta(k^2 - m_i^2) = \delta((k^0)^2 - \mathbf{k}^2 - m_i^2)$.

Remarkably, this observation allowed Drell [195] to put already a lower bound in 1959, which is known as the unitary bound,

$$|\mathcal{A}(m_\pi^2)|^2 \geq (\text{Im } \mathcal{A}_{\gamma\gamma}(m_\pi^2))^2 = \left(\frac{\pi}{2\beta_\ell} \ln \left(\frac{1-\beta_\ell}{1+\beta_\ell} \right) \right)^2 = (-17.52)^2. \quad (5.8)$$

Quite often, this bound has been extended to the heavier η, η' and K_L pseudoscalar states. This generalization is however incorrect, as all of these particles will have intermediate $\pi^+\pi^-\gamma$ states in addition, cf. Fig. 5.3. This is specially important for the η' , where such $\pi^+\pi^-$ state becomes resonant at the ρ peak, besides the additional ω resonance. This feature is carefully illustrated for the η and η' in Section 5.3.3 in order to assess the systematic error. We find small corrections for the η , but large deviations for the η' . As a further illustration, we derive in Appendix B.2 the additional contributions to the imaginary part that a narrow-width vector meson would produce.

Repeatedly, this result has been used in the literature for estimating the whole amplitude using Cauchy's integral formula, which is often referred to as a dispersion relation. This consists in reconstructing the original function Eq. (5.6) from its $\gamma\gamma$ discontinuity above $q^2 = 0$. As the imaginary part, Eq. (5.7), does not fall rapidly enough at infinity —which is related to the divergent character of Eq. (5.6) for a constant TFF—a subtraction is required, so the final result reads [201, 207, 221]

$$\text{Re } \mathcal{A}(q^2) = \mathcal{A}(0) + \frac{q^2}{\pi} \int_0^\infty ds \frac{\text{Im } \mathcal{A}_{\gamma\gamma}(s)}{s(s-q^2)}. \quad (5.9)$$

Still, the value for $\mathcal{A}(0)$ must be calculated from Eq. (5.6), which represents though a simpler calculation. The result from the dispersive integral leads exactly to the terms in brackets in Eq. (5.12). We note here that such calculations are approximate. For a general pseudoscalar mass the additional contributions to the imaginary part coming from the TFF must be specified —actually these would allow to write an unsubtracted dispersion relation, cf. Appendix B.2. Consequently, such calculations are approximate as they would neglect all kinds of $m_{P,\ell}/\Lambda$ corrections, where Λ is some TFF characteristic scale [201, 209, 221].

5.2.2 Results for a constant form factor

Before continuing, it will be useful in view of the next discussion and Section 5.5, to estimate the result which is obtained when taking a constant (WZW) TFF. Obviously, the result will include some divergent term —to be cancelled once the TFF is switched on— which needs regularization. Taking $\tilde{F}_{P\gamma^*\gamma^*}(k^2, (k-q)^2) = 1$, the loop integral Eq. (5.6) can be expressed using

dimensional regularization in terms of known scalar integrals

$$\begin{aligned}\mathcal{A}^{\text{WZW}}(q^2) &= 2 \frac{q^\mu q^\nu}{q^2} C_{\mu\nu}(q^2, m_\ell^2, m_\ell^2; 0, 0, m_\ell^2) - 2B_0(m_\ell^2; 0, m_\ell^2) \\ &= \frac{1}{2} (q^2 C_0(q^2, m_\ell^2, m_\ell^2; 0, 0, m_\ell^2) - 3B_0(m_\ell^2; 0, m_\ell^2) + 1).\end{aligned}\quad (5.10)$$

Note here that if we were to use some cut-off in our integrals for the regularization procedure—which is particularly useful for deriving the approximate formula—the peculiarities of dimensional regularization must be accounted for carefully. As an example, from the first line in Eq. (5.10), the divergent part arises from

$$2 \frac{4}{d} \text{Div}[C_{00}] - 2 \text{Div}[B_0] = \frac{2}{d} \Delta_\epsilon - 2 \Delta_\epsilon = -\frac{3}{2} \Delta_\epsilon + \frac{1}{4}, \quad (5.11)$$

where we have used $d = 4 - \epsilon$ and $\Delta_\epsilon = \frac{2}{\epsilon} - \gamma_E + \ln 4\pi$. The additional finite extra-term which is found should be subtracted from Eq. (5.10) if not using dimensional regularization. Performing the calculation for the scalar functions C_0 and B_0 , we find, in dimensional regularization,

$$\mathcal{A}^{\text{WZW}}(q^2) = \frac{i\pi}{2\beta_\ell} L + \frac{1}{\beta_\ell} \left[\frac{1}{4} L^2 + \frac{\pi^2}{12} + \text{Li}_2\left(\frac{\beta_\ell - 1}{1 + \beta_\ell}\right) \right] - \frac{5}{2} + \frac{3}{2} \ln\left(\frac{m_\ell^2}{\mu^2}\right), \quad (5.12)$$

where $L = \ln\left(\frac{1 - \beta_\ell}{1 + \beta_\ell}\right)$, $\beta_\ell = \sqrt{1 - \frac{4m_\ell^2}{q^2}}$ is the lepton velocity and $\text{Li}_2(x)$ is the dilogarithm function⁷. If we were using a cut-off regularization $\mu^2 \rightarrow \infty$, from Eq. (5.10), and accounting for the last piece in Eq. (5.11), we would find similar results but replacing the last terms in Eq. (5.12) by $-\frac{5}{4} - \frac{3}{2} \ln(1 + \frac{\mu^2}{m_\ell^2})$.

5.2.3 Approximate results and main properties

Before providing any input for the TFF, it is very convenient to analyze the loop-integral. This allows to identify the relevant scales involved in the problem, which is extremely important in order to achieve the most appropriate TFF description. For this task, it is very convenient to carry out an approximate calculation in terms of $m_{P,\ell}^2/\Lambda^2$, where Λ is some characteristic scale encoded in the form factor. Following [212], we take

$$\mathcal{A}(q^2) = \mathcal{A}^{\text{WZW}}(q^2) + \frac{2i}{\pi^2 q^2} \int d^4 k \frac{(k^2 q^2 - (k \cdot q)^2) (F_{P\gamma^*\gamma^*}(k^2, (q - k)^2) - 1)}{k^2 (q - k)^2 ((p - k)^2 - m_\ell^2)}, \quad (5.13)$$

where we have added and subtracted a constant term—precisely, that in Eq. (5.12). The remaining integral is essentially zero at scales $k^2 \sim m_P^2, m_\ell^2$

⁷The dilogarithm or Spence's function is defined as $\text{Li}_2(x) = - \int_0^x dt \frac{\ln(1-t)}{t}$.

below Λ^2 , as the TFF remains constant. Above, all the terms $\mathcal{O}(p^2, q^2, m_\ell^2)$ can be neglected. At such scales, the leading term from the tensor $k^\mu k^\nu q_\mu q_\nu$ part is given by $k^\mu k^\nu \sim (1/d)k^2 g^{\mu\nu}$, as additional terms are m_P^2/Λ^2 suppressed. We are left then with

$$\begin{aligned}\mathcal{A}(q^2) &\simeq \mathcal{A}^{\text{WZW}}(q^2) + \frac{2i}{\pi^2} \left(1 - \frac{1}{d}\right) \int d^4 k \frac{F_{P\gamma^*\gamma^*}(k^2, k^2) - 1}{(k^2)^2}, \\ &= \mathcal{A}^{\text{WZW}}(q^2) - 3 \int_0^\mu dQ \frac{F_{P\gamma^*\gamma^*}(Q^2, Q^2) - 1}{Q}.\end{aligned}\quad (5.14)$$

The first line corresponds, essentially, to the result Eq. (12) in [212], whereas in the second one, we have Wick-rotated and introduced a cut-off regularization. The obtained integral is still divergent for $\mu \rightarrow \infty$, which is expected as it must cancel the divergency in $\mathcal{A}^{\text{WZW}}(q^2)$, see Eq. (5.12). In order to remove it, we identify the origin of the UV divergent term in Eq. (5.12), subtract⁸ there, and plug into Eq. (5.14), obtaining

$$\begin{aligned}\mathcal{A}^{\text{app}}(q^2) &= \frac{i\pi}{2\beta_\ell} L + \frac{1}{\beta_\ell} \left[\frac{1}{4} L^2 + \frac{\pi^2}{12} + \text{Li}_2 \left(\frac{\beta_\ell - 1}{1 + \beta_\ell} \right) \right] - \frac{5}{4} \\ &\quad + \int_0^\infty dQ \frac{3}{Q} \left(\frac{m_\ell^2}{Q^2 + m_\ell^2} - F_{P\gamma^*\gamma^*}(Q^2, Q^2) \right).\end{aligned}\quad (5.15)$$

This kind of approximation, obtained in many different ways, has been widely used in the literature, see explicitly in Refs. [207, 212] and implicit in most of the quoted references. Exceptions are the full calculation in Ref. [222], and those including partial corrections in Refs. [206, 208, 209]. While these are relevant to the precision we are aiming, specially for the η and η' cases, the approximation in Eq. (5.15) is enough, at least for the π^0 , to understand the relevant dynamics in this process. To illustrate this, we plot in Fig. 5.2 the integrand of Eq. (5.15), $\mathcal{K}(Q^2)$, for the electron case. As one can see, it involves the space-like symmetric ($Q_1^2 = Q_2^2$) kinematics. In addition, the integrand is peaked at very low-energies close to the lepton mass, where the TFF essentially remains constant. The TFF effects become visible and specially relevant in the (0.1 – 0.4) GeV region, where the slope parameter is roughly enough to describe the TFF; the effects from additional parameters appear roughly above this region —where the two black lines in Fig. 5.2 separate—and represent a minor contribution to the integral. The high-energy tail plays though a non-negligible role too. Given the sensitivity to the double virtual regime, this challenging process would represent the first experimental probe to the TFF double-virtual kinematics. From the features enumerated above, any serious approach developed to deal with this process should implement:

⁸That amounts to remove the $-\frac{3}{2} \ln(1 + \mu^2/m_\ell^2)$ term from $\mathcal{A}^{\text{WZW}}(q^2)$. Note that we are using a cut-off regularization, so the comments below Eq. (5.12) apply.

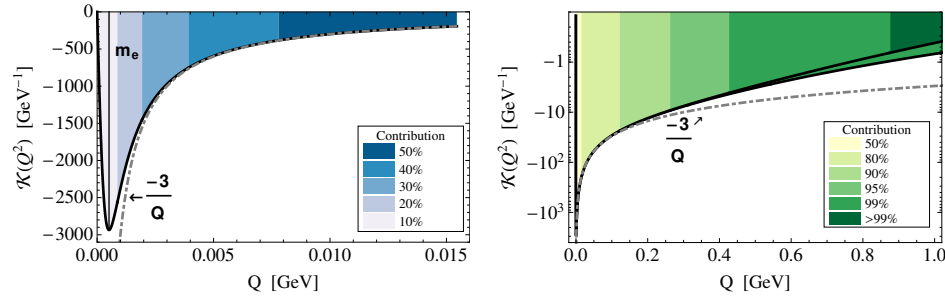


Figure 5.2: The integrand in Eq. (5.15), $\mathcal{K}(Q^2)$, for $\ell = e$ and partial contributions to the integral. The left figure stands for the low-energies, whereas the right one, in logarithmic-scale, stands for the high-energies. The upper(lower) black line stand from our factorization(OPE) models (see Section 5.3.1) and the dot-dashed gray line for a constant TFF.

- The appropriate space-like low-energy behavior. Particularly, the slope parameter should be described as precise as possible to obtain the most accurate description below 1 GeV.
- A proper implementation (not modeling) of the doubly-virtual behavior.
- A minimum implementation for the high-energy behavior (i.e. the correct Q^2 behavior discussed in Section 1.6.1).

However, previous approaches have often adopted either quark models [112, 201–205] or simplified VMD models saturated with the lowest-lying resonance [200, 201, 206, 209, 223]. As such models cannot properly reproduce the data, one may doubt about the accuracy of their results, this is, their non-assessed systematic errors. To supply this, some approaches have adopted a VMD-like approach where the effective mass is obtained from a fitting procedure to high-energy (mostly above 2 GeV²) space-like data [208, 209]. We have seen in Chapter 2 that this can be understood as the first element of a PA, which systematic error is certainly large. Besides, these approaches face the problem that no double-virtual data is available so far, for which some model must be assumed⁹ [207, 208]. The associated error of this procedure or how the data would be incorporated into their descriptions is not clear. A possible alternative to circumvent these problems is provided by χ PT [210]. In such framework, every pseudoscalar decay depends, at LO, on the same common counterterm (see Section 5.5). Obtaining this from a particular channel, one may predict the others. We only note for the moment that the NLO effects cannot be neglected as will be discussed in Section 5.5. Therefore, this approach is not feasible at the

⁹Note that those parameterizations using a factorized form, such as Ref. [209], imply an important unaccounted error, as such model violates the OPE expansion.

required precision. Last but not least, (as explained) most of the calculations employed so far rely on numerical approximations for the calculation in Eq. (5.6). If this is not a bad approximation for the $\pi^0 \rightarrow e^+e^-$ decay given the strong $m_e \ll m_\pi \ll \Lambda$ hierarchy (Λ represents the TFF scale), these approximations, which would simplify the loop calculation, are not appropriate for the heavier η and η' cases, where the induced error may become larger than the statistic and systematic ones.

5.3 A rational description for $F_{P\gamma^*\gamma^*}(Q_1^2, Q_2^2)$

In view of the problems raised in the preceding section, CAs seem an ideal and robust framework to deal with these shortcomings. First, they are able to systematically incorporate the appropriate low-energy expansion, not only for the single- but for the double-virtual case. Second, they are able to accommodate what is known from the high-energies. Third, they provide a method to obtain a systematic error. We analyze therefore the $P \rightarrow \bar{\ell}\ell$ processes in the light of CAs with the idea of achieving a preciser and more accurate prediction for these decays, including a systematic error and performing a precise numerical evaluation. This, together with the most recent evaluation for the radiative corrections in Refs. [224–226], would promote their SM prediction to the standards of precision met nowadays, and would provide a reliable quantity to compare with the available or upcoming experimental results.

5.3.1 Reconstructing the transition from factor

The reconstruction of a general function from CAs was discussed in great detail in Chapter 3. The lowest approximant at our disposal corresponds to the $C_1^0(Q_1^2, Q_2^2)$, which, given the low-energy TFF expansion,

$$\tilde{F}_{P\gamma^*\gamma^*}(Q_1^2, Q_2^2) = 1 - \frac{b_P(Q_1^2 + Q_2^2)}{m_P^2} + \frac{a_{P;1,1}Q_1^2Q_2^2}{m_P^4} + \frac{c_P(Q_1^4 + Q_2^4)}{m_P^4} + \dots, \quad (5.16)$$

can be reconstructed, fully-based on its low-energy expansion, as

$$C_1^0(Q_1^2, Q_2^2) = \frac{1}{1 + \frac{b_P}{m_P^2}(Q_1^2 + Q_2^2) + \frac{2b_P^2 - a_{P;1,1}}{m_P^4}Q_1^2Q_2^2}, \quad (5.17)$$

where all the single virtual parameters have already been determined in Chapter 2 (see Table 2.14). It remains then to assign a numerical value to the double-virtual parameter $a_{P;1,1}$ —not determined so far due to the absence of double virtual experimental data. In order to make a well-educated guess for this parameter, we consider the two extreme regimes relevant for our calculation. On the one hand, at the very low-energies involved in our calculation,

χ PT should provide a reliable estimate for the TFF behavior. It turns out that, according to the study in Ref. [91], the chiral leading logs suggest that a factorization approach ($F_{P\gamma^*\gamma^*}(Q_1^2, Q_2^2) \simeq F_{P\gamma^*\gamma}(Q_1^2) \times F_{P\gamma^*\gamma}(Q_2^2)$) should provide a good approximation¹⁰, implying that $a_{P;1,1} \simeq b_P^2$ — corrections appearing an order higher (even two in the chiral limit) than expected. On the other hand, at the very high-energies relevant for the integrand tail, the OPE expansion (i.e., that $F_{P\gamma^*\gamma^*}(Q^2, Q^2) \sim Q^{-2}$) requires $a_{P;1,1} = 2b_P^2$ if a two-point approximation is employed (see Section 3.3.4), suggesting that corrections to the chiral leading logs should push the factorized value upwards. For these reasons, we choose to take the $b_P^2 < a_{P;1,1} < 2b_P^2$ ¹¹ band as a compromise between the low energies and the appropriate high-energy behavior [218, 219]. If the real value — to be extracted from the experiment or lattice results — is eventually observed to lie within this band, success is guaranteed.

In order to improve this description, we should move on along the C_{N+1}^N sequence and construct larger approximants. This would allow then to implement both, the low- and the high-energy behavior at the same time, and would make the preceding discussion unnecessary. However, the next approximant, the C_2^1 , already contains too many double-virtual parameters, further complicating its reconstruction and numerical evaluation, for which we omit its discussion here¹².

5.3.2 Systematic error I: the π^0

Given the short length of our sequence, including only a single element, it is extremely important to check on the systematics. For these reasons, we come back once more to our recurrent logarithmic and Regge models defined in Chapter 3 for the most general double-virtual case,

$$F_{\pi^0\gamma^*\gamma^*}^{\text{Regge}}(Q_1^2, Q_2^2) = \frac{a F_{P\gamma\gamma}}{Q_1^2 - Q_2^2} \frac{\left[\psi^{(0)}\left(\frac{M^2 + Q_1^2}{a}\right) - \psi^{(0)}\left(\frac{M^2 + Q_2^2}{a}\right) \right]}{\psi^{(1)}\left(\frac{M^2}{a}\right)}, \quad (5.18)$$

$$F_{\pi^0\gamma^*\gamma^*}^{\log}(Q_1^2, Q_2^2) = \frac{F_{P\gamma\gamma} M^2}{Q_1^2 - Q_2^2} \ln\left(\frac{M^2 + Q_1^2}{M^2 + Q_2^2}\right). \quad (5.19)$$

We note that for the Regge and logarithmic models the condition $b_P^2 < a_{P;1,1} < 2b_P^2$ is satisfied. In particular, for the Regge model, $a_{P;1,1} = [2\psi^{(1)}(\frac{M^2}{a})\psi^{(3)}(\frac{M^2}{a})]/[3(\psi^{(2)}(\frac{M^2}{a})^2)b_P^2] = 1.13b_P^2$, whereas for the logarithmic one $a_{P;1,1} = (4/3)b_P^2$. Performing the numerical integration in Eq. (5.6), we

¹⁰Actually, this approximation is supported as well from the dispersive study in [96].

¹¹Note that values above $2b_P^2$ would imply in addition a pole in the SL region.

¹²For an extended discussion for the C_2^1 approximant we refer to Chapter 6.

obtain¹³

$$\mathcal{A}(m_\pi^2) = 9.73 - 17.52i \quad \text{BR}(\pi^0 \rightarrow e^+ e^-) = 6.14 \times 10^{-8}, \quad (5.20)$$

$$\mathcal{A}(m_\pi^2) = 8.78 - 17.52i \quad \text{BR}(\pi^0 \rightarrow e^+ e^-) = 5.87 \times 10^{-8}, \quad (5.21)$$

for the Regge and logarithmic models respectively. This is to be compared with their corresponding C_1^0 reconstruction, which for the chosen $b_P^2 < a_{P;1,1} < 2b_P^2$ band yields,

$$\mathcal{A}(m_\pi^2) = (9.63 \div 10.09) - 17.52i \quad \text{BR}(\pi^0 \rightarrow e^+ e^-) = (6.08 \div 6.22) \times 10^{-8}, \quad (5.22)$$

$$\mathcal{A}(m_\pi^2) = (8.78 \div 9.24) - 17.52i \quad \text{BR}(\pi^0 \rightarrow e^+ e^-) = (5.87 \div 6.00) \times 10^{-8}, \quad (5.23)$$

where the first(second) value corresponds to $a_{P;1,1} = 2b_P^2(b_P^2)$, i.e., the value implied by OPE(factorization). As a curiosity, we find that, for the logarithmic model, constraining the OPE ($a_{P;1,1} = 2b_P^2$) seems to be the better choice. This is just an accident which can be understood from the fact that, for $Q_1^2 = Q_2^2$, that model is parametrically equivalent to such approximant¹⁴, see Eq. (3.17). Indeed, this observation does not apply to the Regge model. In general, whether the result is closer to the OPE or the factorization choice will depend on the pseudoscalar masses, the double-virtual low-energy behavior and how the TFF approaches the asymptotic regime. It seems hard to us to judge on a better choice with a single approximant at hand. Consequently, we take the given band as the best (more conservative) error estimation one can do at this point. As a further comment, we find that additional sources of error beyond the double-virtual reconstruction are masked within this band.

In principle, it seems that these results would apply for the η and η' cases. However, such extrapolation cannot be strictly performed. For the η and η' , the approximation in Eq. (5.15) is not appropriate anymore; it is easy to see that the loop-integral in Eq. (5.6) does not involve space-like arguments for the TFF alone, but time-like ones in the $-m_P^2 \leq Q^2 \leq 0$ region too. Whereas this does not represent a problem for the π^0 , it poses a problem for the η and η' cases, as such region includes the $\pi\pi$ threshold for the η and reaches the ρ and ω resonances for the η' . It has yet to be seen if our approximants have the ability to reproduce the corresponding real and imaginary parts required in these processes. In the following section, we discuss that this is actually possible provided that we deal with Stieltjes functions, a unique feature which cannot be reproduced in traditional approaches.

¹³We use $F_{P\gamma^*\gamma^*}(Q_1^2, Q_2^2) = \frac{1}{\psi^{(1)}(M^2/a)} \sum_{m=0}^{\infty} \frac{\Lambda^4}{(Q_1^2 + (M^2 + na))(Q_2^2 + (M^2 + na))}$ [97] for the Regge model; for the logarithmic model, we use Eq. (3.16).

¹⁴This would not be the case for the heavier η and η' , as the behavior for $Q_1^2 \neq Q_2^2$ becomes relevant too.

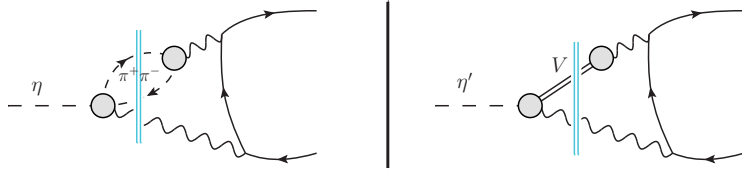


Figure 5.3: Intermediate hadronic states invalidating the unitary bound for the $\eta, (\eta')$, left(right).

5.3.3 Systematic error II: the η and η'

The η and η' masses are large enough to yield intermediate hadronic states in the $P \rightarrow \bar{\ell}\ell$ processes as sketched in Fig. 5.3, which implies an additional imaginary part beyond that of the $\gamma\gamma$ contribution. As we will show, this diminishes the imaginary part, invalidating then the unitary bound. This effect has never been considered before when calculating these decays and must be taken into account when evaluating the systematic error. Indeed, when the intermediate state becomes resonant, this effect becomes the dominant source of error.

To quantitatively study this effect, we take a toy-model for the TFF that includes both, a two-pion production threshold and a vector resonance. The model is conceived in such a way that the time-like region contains all the required features of the physical TFF up to the η' mass. The first ingredient in our toy-model is factorization, which as explained before seems a reasonable choice at low-energies and does not spoil our discussion. The second ingredient is the use of vector meson dominance ideas [116] allowing to express the (normalized) single-virtual TFF as

$$\tilde{F}_{P\gamma^*\gamma}(s) = c_{P\rho}G_\rho(s) + c_{P\omega}G_\omega(s) + c_{P\phi}G_\phi(s), \quad (5.24)$$

where $G_V(s)$ are the different resonance contributions weighted by the dimensionless couplings c_{PV} obtained from a quark-model, $c_{\eta(\eta')\rho} = 9/8(9/14)$, $c_{\eta(\eta')\omega} = 1/8(1/14)$, $c_{\eta(\eta')\phi} = -2/8(4/14)$ [95], and $G_V(0) = 1$. In order to incorporate the $\pi\pi$ intermediate branch cut in Fig. 5.3, fulfilling unitarity and analyticity, we take for the ρ contribution, $G_\rho(s)$, a model based on Refs. [227, 228]

$$G_\rho(s) = \frac{M_\rho^2}{M_\rho^2 - s + \frac{sM_\rho^2}{96\pi^2 F_\pi^2} \left(\ln\left(\frac{m_\pi^2}{\mu^2}\right) + \frac{8m_\pi^2}{s} - \frac{5}{3} - \sigma(s)^3 \ln\left(\frac{\sigma(s)-1}{\sigma(s)+1}\right) \right)} \quad (5.25)$$

with $\sigma(s) = \sqrt{1 - 4m_\pi^2/s}$, and the parameters $M_\rho = 0.815$ GeV, $F_\pi = 0.115$ GeV, $\mu = 0.775$ GeV, and $m_\pi = 0.139$ GeV, chosen to reproduce the pole position $s_\rho = (M - i\Gamma/2)^2$ with $M = 0.764$ GeV and $\Gamma = 0.144$ GeV

from [123], while for the (narrow-width) ω, ϕ resonances, we take¹⁵

$$G_{\omega,\phi} = \frac{M_{\omega,\phi}^2 + M_{\omega,\phi}\Gamma_{\omega,\phi}(s_{th}/M_{\omega,\phi}^2)^{3/2}}{M_{\omega,\phi}^2 - s + M_{\omega,\phi}\Gamma_{\omega,\phi}((s_{th} - s)/M_{\omega,\phi}^2)^{3/2}}, \quad (5.26)$$

with parameters fixed from PDG masses and widths [10]. This choice makes our model very similar to the dispersive approach formulated in [95].

To evaluate the BR, we calculate the loop amplitude in Eq. (5.6) with the TFF from Eq. (5.24) as an input —this parametrization already implements the desired threshold and resonance effects displayed in Fig. 5.3. It is convenient for the integration procedure to employ a Cauchy integral representation for the TFF,

$$\tilde{F}_{P\gamma^*\gamma^*}(q_1^2, q_2^2) = \int_{s_{th}}^{\infty} dM_1^2 \int_{s_{th}}^{\infty} dM_2^2 \frac{\text{Im } \tilde{F}_{P\gamma^*\gamma}(M_1^2)}{q_1^2 - M_1^2 - i\epsilon} \frac{\text{Im } \tilde{F}_{P\gamma^*\gamma}(M_2^2)}{q_2^2 - M_2^2 - i\epsilon}. \quad (5.27)$$

The loop integral in Eq. (5.6) can be expressed then, after changing the integration order, as

$$\begin{aligned} \mathcal{A}(q^2) &= \frac{1}{\pi^2} \int_{s_{th}}^{\infty} dM_1^2 \int_{s_{th}}^{\infty} dM_2^2 \text{Im } \tilde{F}_{P\gamma^*\gamma}(M_1^2) \text{Im } \tilde{F}_{P\gamma^*\gamma}(M_2^2) \\ &\quad \times \left(2i \int \frac{d^4 k}{\pi^2} \frac{(q^2 k^2 - (qk)^2)}{q^2 k^2 (q - k)^2 ((p - k)^2 - m_\ell^2)} \frac{1}{k^2 - M_1^2} \frac{1}{(q - k)^2 - M_2^2} \right) \\ &\equiv \frac{2}{\pi^2} \int_{s_{th}}^{\infty} dM_1^2 \int_{s_{th}}^{M_1^2} dM_2^2 \text{Im } \tilde{F}_{P\gamma^*\gamma}(M_1^2) \text{Im } \tilde{F}_{P\gamma^*\gamma}(M_2^2) \times K(M_1^2, M_2^2). \end{aligned} \quad (5.28)$$

This procedure results in an easy evaluation of the loop amplitude, denoted as $K(M_1^2, M_2^2)$, through standard one-loop techniques [229] or a numerical evaluation using **FeynCalc** [230] and **LoopTools** [231]. Now, the threshold effects are clear and easier to handle. To illustrate them, we plot the imaginary part of the integrand in Eq. (5.28) in terms of $\text{Im } \tilde{F}_{P\gamma^*\gamma}(M_V^2)$ and $\text{Im } K(M_V^2)$ —containing both $\gamma\gamma$ and vector contributions— when dispersing only one virtuality in Eq. (5.28) for simplicity (i.e., we consider a q^2 -independent narrow width approximation for the second virtuality). The resulting plot is shown in Fig. 5.4 as a solid-black (dashed-purple) line for the $\eta(\eta')$ in terms of the dispersive variable M_V once the $\int d^4 k$ integration has been performed to give $K(M_V^2)$ in the last line of Eq. (5.28). These lines have to be convoluted with $\text{Im } \tilde{F}_{P\gamma^*\gamma}(M_V^2)$ (bluish area in Fig. 5.4) in order to obtain $\text{Im } \mathcal{A}(q^2)$. For $M_V > m_P$, the imaginary part corresponds to

¹⁵We explored further refined models with an improved threshold behavior for the ω and ϕ resonances. Given their narrow width they led to very similar results and we decided to take the ones in Eq. (5.26) for not obscuring our study and deviating the attention from our main concern, an estimation of a systematic error.

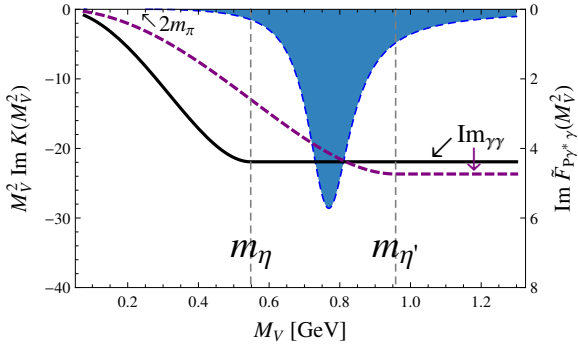


Figure 5.4: The imaginary part for integrand Eq. (5.28) expressed in terms of $M_V^2 \text{Im } K(M_V^2)$ (black and dashed-purple lines for the η and η' , respectively) which has then to be convoluted with $\text{Im } \tilde{F}_{P\gamma^*\gamma}(M_V^2)$; in the figure $\text{Im } \tilde{F}_{P\gamma^*\gamma}(M_V^2) = \text{Im } G_\rho(M_V^2)$ is shown —the ω and ϕ resonances would produce sharp peaks on top.

		$\gamma\gamma$	Total
$\text{Im } \mathcal{A}_{\eta \rightarrow \ell\ell}(m_\eta^2)$	ee	-21.920	-21.805
	$\mu\mu$	-5.468	-5.441
$\text{Im } \mathcal{A}_{\eta' \rightarrow \ell\ell}(m_{\eta'}^2)$	ee	-23.675	-19.251
	$\mu\mu$	-7.060	-5.733

Table 5.1: Imaginary part of $\mathcal{A}(q^2)$ (Total) compared to the imaginary part calculated from the $\gamma\gamma$ channel alone. The hadronic contributions lower the total value of the imaginary part with respect to the $\gamma\gamma$ contribution, invalidating the unitary bound.

the $\gamma\gamma$ contribution, which diminishes as soon as $M_V < m_P$. Consequently, for resonances heavier than the pseudoscalar mass, there will be a slight modification whenever the resonance tail (in our case at $2m_\pi$) appears below m_P . On the other hand, for resonances lighter than the pseudoscalar mass, the shift will be considerable. All in all, as unitarity implies, the imaginary part will be shifted whenever an intermediate hadronic channel appears below m_P . For completeness, we illustrate in Table 5.1 the numerical shift in the imaginary part with respect to the $\gamma\gamma$ contribution in our toy-model Eq. (5.24), showing the break of the unitary bound.

Given that our model is a Stieltjes function, it is well known that the $C_{N+1}^N(Q_1^2, Q_2^2)$ sequence is guaranteed to converge in the whole complex plane, except along the cut [56], where zeros and poles of our CA will clutter to reproduce the discontinuity [56, 58], see Fig. 1.6. Such poles will be responsible for effectively generating an imaginary part in our integral mimicking the cut contribution due to Cauchy's integral theorem —even if the approximation for $\tilde{F}_{P\gamma^*\gamma^*}(q_1^2, q_2^2)$ does not converge above the cut. As an illustration, we collect the results for both, BR and $\mathcal{A}(m_P^2)$, from our simplest approximant, the $C_1^0(Q_1^2, Q_2^2)$, in Table 5.2 and compare its results with the toy model. The comparison of the BRs reveals a systematic error

BR($P \rightarrow \ell\ell$)	Toy-model	C_1^0	Error (%)	$\mathcal{A}(m_P^2)$	Toy-model	C_1^0
$(\eta \rightarrow ee) \times 10^{-9}$	5.4095	5.4179	0.16	$(\eta \rightarrow ee)$	$31.4 - 21.8i$	$31.4 - 21.9i$
$(\eta \rightarrow \mu\mu) \times 10^{-6}$	4.49361	4.52701	0.74	$(\eta \rightarrow \mu\mu)$	$-1.09 - 5.44i$	$-1.05 - 5.47i$
$(\eta' \rightarrow ee) \times 10^{-10}$	1.70507	1.88331	9	$(\eta' \rightarrow ee)$	$46.4 - 19.2i$	$48.7 - 20.5i$
$(\eta' \rightarrow \mu\mu) \times 10^{-7}$	1.1953	1.46089	18	$(\eta' \rightarrow \mu\mu)$	$3.09 - 5.73i$	$3.82 - 6.10i$

Table 5.2: Comparison between our toy-model result and the simplest $C_1^0(Q_1^2, Q_2^2)$ approximation for each channel. The Error column represents the relative deviation between the model and the approximation. Left part collects the BR, whereas the right part contains the loop amplitude $\mathcal{A}(m_P^2)$.

induced by the fact that we have truncated the CA sequence. For the η , such error is almost negligible (the role of the vector resonances is very mild there), whereas for the η' it goes almost up to 20%. These percentages will be used as an estimate of our systematic error in our final results for the $C_1^0(Q_1^2, Q_2^2)$ element.

We would like to remark at this point that using a VMD model with the ρ mass—which was standard in the past for performing this calculation—instead of the more sophisticated model in Eq. (5.24), we would have found $\text{BR}(\eta \rightarrow ee) = 5.30 \times 10^{-9}$, which implies a larger systematic uncertainty compared to our result in Table 5.2. A VMD fit to generated space-like data in the $(0 - 15)$ GeV 2 does not improve on the result either. In such case, we would have obtained $\text{BR}(\eta \rightarrow ee) = 5.26 \times 10^{-9}$. These numbers illustrate the potential large systematic error coming from the usage of VMD data-fitting procedures from high-energies for processes which are low-energy dominated, even if the quality of the fit is good enough.

As we have said, the convergence of the CA sequence to our toy model is guaranteed [56, 58, 160], and we show it by constructing the higher elements of the $C_M^N(Q_1^2, Q_2^2)$ sequence, calculating with them the amplitude in Eq. (5.6), $\mathcal{A}(m_P^2)^{\text{CA}}$ for short, and studying the relative distance in the complex plane, defined as $|1 - \mathcal{A}(m_P^2)^{\text{CA}} / \mathcal{A}(m_P^2)|$. The results are shown in Fig. 5.5, where, for simplicity, we employ only the G_ρ contribution in Eq. (5.24) (without ω, ϕ contributions).

The results in Fig. 5.5 show the ability of our approximants to systematically account for the TFF to arbitrary precision since the relative distance decreases when the order of the CA increases, even in the presence of the non trivial behavior of the branch cut from the intermediate hadronic states. Note the *a priori* irregular convergence for the η case in Fig. 5.5 (top panel). This is just an accident due to the appearance of effective poles for the particular chosen TFF close to the η mass; whenever some pole is located close to the η mass, it leads to a bad determination. This is compensated in higher approximants with a nearby zero to this pole, alleviating this effect and making it negligible as $N \rightarrow \infty$ as shown in Fig. 5.5 (bottom right

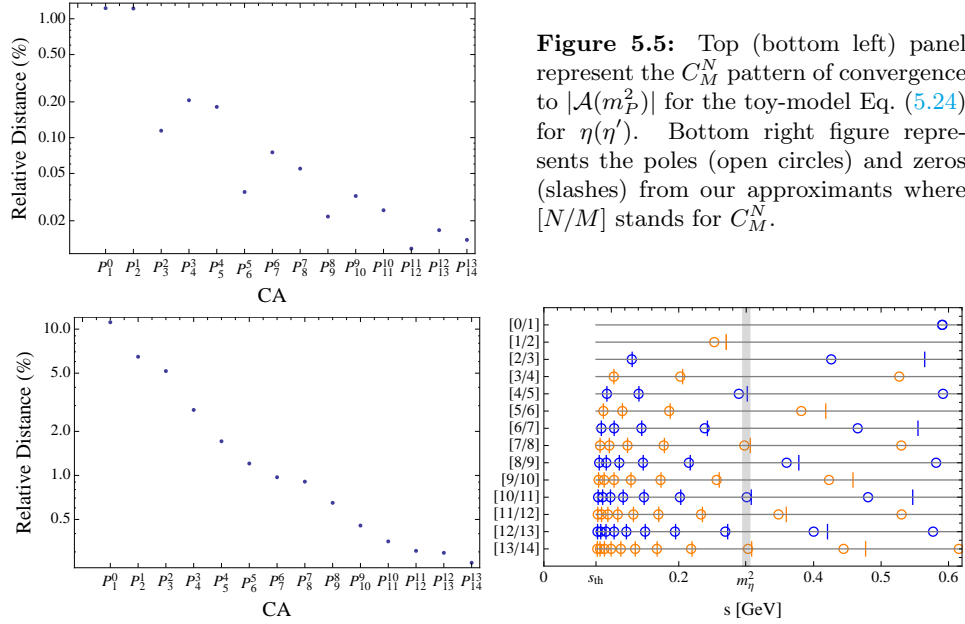


Figure 5.5: Top (bottom left) panel represent the C_M^N pattern of convergence to $|\mathcal{A}(m_P^2)|$ for the toy-model Eq. (5.24) for $\eta(\eta')$. Bottom right figure represents the poles (open circles) and zeros (slashes) from our approximants where $[N/M]$ stands for C_M^N .

panel), where the poles and zeros for different approximants are plotted.

We find then that, for the $C_{N+1}^N(Q_1^2, Q_2^2)$ element, the systematic error can be accounted for by the difference in the BR with respect to the $C_N^{N-1}(Q_1^2, Q_2^2)$ result. As in our case study, we only reach the $C_1^0(Q_1^2, Q_2^2)$ approximant, this procedure does not apply and we take as the systematic error for the BR the one which is displayed in the fourth column in Table 5.2. This possibly overestimates the systematic error, see comments in Section 5.4, but we opt for this to remain on the conservative side. As soon as experimental data on the doubly virtual TFF becomes available, we will be able to extend our CA sequence and reduce the systematic error.

5.4 Final results

Having carefully revised all the systematic errors which must be accounted for the π^0 , η and η' , we are finally in the position to give our final results for these decays. As it has been explained, given the uncertainty on the TFF double-virtual behavior, we restrict ourselves to the lowest approximant (C_1^0) and take the double-virtual parameter, $a_{P;1,1}$, in the $b_P^2 \leq a_{P;1,1} \leq 2b_P^2$ range. This choice represents a compromise between the low- and high-energy regimes. Particularly, we showed in Section 5.3.2 that this range provides a band wide enough to cover the full systematic error for the C_1^0 for the π^0 case. Regrettably, this did not apply to the η and η' , as they feature additional intermediate states implying a slower convergence. For this reason, we evaluated in Table 5.2 an additional systematic error that should

Process	$\mathcal{A}(m_P^2)$	$\mathcal{A}^{Z^0}(m_P^2)$	$\mathcal{A}^{\text{app}}(m_P^2)$
$\pi^0 \rightarrow e^+ e^-$	$(10.00 \div 10.46)(12) - 17.52i$	-0.05	$(9.84 \div 10.30) - 17.52i$
$\eta \rightarrow e^+ e^-$	$(30.95 \div 31.51)(11) - 21.92(0)i$	-0.03	$(27.53 \div 28.00) - 21.92i$
$\eta \rightarrow \mu^+ \mu^-$	$-(1.52 \div 0.99) (5) - 5.47(0)i$	-0.03	$-(2.33 \div 1.87) - 5.47i$
$\eta' \rightarrow e^+ e^-$	$(47.4 \div 48.2) (5) - 21.0(5)i$	0.03	$(35.20 \div 35.66) - 23.68i$
$\eta' \rightarrow \mu^+ \mu^-$	$(2.95 \div 3.65) (19) - 6.3(17)i$	0.03	$-(0.66 \div 0.20) - 7.06i$

Table 5.3: Our results for $a_{P;11} \in (2b_P^2 \div b_P^2) \equiv (\text{OPE} \div \text{Factorization})$. The error is statistical alone. We quote the Z^0 boson contribution $\mathcal{A}^{Z^0}(m_P^2)$ separately and show the approximated $\mathcal{A}^{\text{app}}(m_P^2)$ result, Eq. (5.15), for comparison.

be included on top of the previous band (see Table 5.2). Our final results are obtained through a precise numerical evaluation of Eq. (5.6) —involving no approximations— using `FeynCalc` [230]¹⁶ and `LoopTools` [231]¹⁷.

The results for the $\mathcal{A}(m_P^2)$ amplitude in Eq. (5.6) are displayed in Table 5.3 in form of a range associated to $a_{P;1,1} = (2b_P^2 \div b_P^2) \equiv (\text{OPE} \div \text{Fact})$. We include the statistical and systematic error associated to the b_P parameter determination obtained in Chapter 2, Table 2.14 —required for the TFF reconstruction. In addition, we include the Z^0 boson contribution separately (see details in Section 5.6) and the result that would have been obtained from the approximate formula Eq. (5.15) in the third and fourth columns, respectively. We note that employing the approximate result implies non-negligible errors, especially for the η' , as can be seen from the last row in Table 5.3 —the agreement observed for the last row in Table 5.4, which does not involve $\mathcal{A}(m_P^2)$ but $|\mathcal{A}(m_P^2)|$, is just accidental.

The results for the BR, including the —often neglected— Z^0 boson contribution, are given in Table 5.4. There, we include three different sources of errors on top of the $a_{P;1,1}$ range. The first one is associated to the experimental measurement for $\text{BR}(P \rightarrow \gamma\gamma)$ and has been frequently ignored; the second is that arising from the b_P parameter; the third one, which applies for the η and η' alone, corresponds to the additional systematic error associated to the resonant region, see Section 5.3.3. In addition, we show in the third and fourth columns the result that would have been obtained if not including the Z^0 boson and using the approximated formula Eq. (5.15), respectively.

¹⁶For the factorization limit, this is possible using partial fraction decomposition and involves one, two and three point scalar functions. For the OPE limit, the TFF $\sim (k^2 + (q - k)^2 - M^2)^{-1}$ can be expressed as $\sim ((k - q/2)^2 - (M^2/2 - q^2/4))^{-1}/2$ and its integration involves one, two, three and four point functions.

¹⁷In addition, we checked the results by performing an analytical calculation for the relevant scalar integrals using the techniques in Ref. [229].

Process	BR	BR w/ Z^0	BR app
$\pi^0 \rightarrow e^+ e^-$	$(6.20 \div 6.35)(0)(4)(0) \times 10^{-8}$	$(6.22 \div 6.36) \times 10^{-8}$	$(6.17 \div 6.31) \times 10^{-8}$
$\eta \rightarrow e^+ e^-$	$(5.31 \div 5.44)(3)(2)(1) \times 10^{-9}$	$(5.32 \div 5.45) \times 10^{-9}$	$(4.58 \div 4.68) \times 10^{-9}$
$\eta \rightarrow \mu^+ \mu^-$	$(4.72 \div 4.52)(2)(3)(4) \times 10^{-6}$	$(4.70 \div 4.51) \times 10^{-6}$	$(5.16 \div 4.88) \times 10^{-6}$
$\eta' \rightarrow e^+ e^-$	$(1.82 \div 1.87)(7)(2)(16) \times 10^{-10}$	$(1.82 \div 1.87) \times 10^{-10}$	$(1.22 \div 1.24) \times 10^{-10}$
$\eta' \rightarrow \mu^+ \mu^-$	$(1.36 \div 1.49)(5)(3)(25) \times 10^{-7}$	$(1.35 \div 1.48) \times 10^{-7}$	$(1.42 \div 1.41) \times 10^{-7}$

Table 5.4: Our results for $a_{P;11} \in (2b_P^2 \div b_P^2) \equiv (\text{OPE} \div \text{Factorization})$. The errors refer respectively to those from $\text{BR}(P \rightarrow \gamma\gamma)$, b_P and the systematic one. We compare to the results either neglecting the Z^0 boson contribution (BR w/ Z^0) or using the approximation in Eq. (5.15). See details in the text.

Tables 5.3 and 5.4 represent the main results from this chapter [218, 219]. They provide an updated calculation of the SM values for $P \rightarrow \ell\ell$ decays. As a novelty, they are the first ones making full use of the available data for the relevant TFFs. Moreover, we are the first ones implementing an appropriate low-energy description, which is crucial for these processes, as well as an appropriate double-virtual description accounting for the low- and high-energy effects, reflected in the given band. Furthermore, we are able to estimate, for the first time, a systematic error, which is by no means negligible for the η and, specially, the η' , and has been previously overlooked. In addition, our calculation does not involve numerical approximations when calculating the loop integral, which for the η and η' becomes a large effect as can be inferred from Tables 5.3 and 5.4. As a result, we find that the lepton mass corrections neglected in [209] are by no means negligible for the muonic channels at the precision we are aiming.

From the quoted results, we find that the main source of error for the π^0 and η is the double-virtual description, which could be dramatically improved by constructing the C_2^1 approximant. This would be possible if having double-virtual experimental data or some additional constraints. Still, we emphasize that the current value is already below the experimental uncertainties and improves previous estimates, see Table 5.5. Concerning the η' , the major source of errors comes from the systematic uncertainty associated to threshold and resonance effects (we note though that this error is likely to be overestimated, as the model employed does not provide a realistic SL description) that could be partially improved, again, if reaching the C_2^1 approximant. Investigations in this respect are undergoing¹⁸. Still it would be desirable to have an alternative approach to systematically implement not only the low- and high-energy behaviors, but the information about the time-like region, such as physical resonances and threshold discontinuities.

¹⁸For further details on the C_2^1 , see Chapter 6.

BR	This Work	Exp.	Previous SM [232]
$\text{BR}(\pi^0 \rightarrow e^+ e^-) \times 10^8$	6.28(7)(4)[8]	7.48(38) [233]	6.23(12) \rightarrow 6.26
$\text{BR}(\eta \rightarrow e^+ e^-) \times 10^9$	5.38(6)(4)[7]	$\leq 2.3 \times 10^3$ [234]	4.53(9) \rightarrow 5.19
$\text{BR}(\eta \rightarrow \mu^+ \mu^-) \times 10^6$	4.62(10)(5)[11]	5.8(8) [10, 235]	5.35(27) \rightarrow 4.76
$\text{BR}(\eta' \rightarrow e^+ e^-) \times 10^{10}$	1.85(2)(18)[18]	≤ 56 [236, 237]	1.182(14) \rightarrow 1.83
$\text{BR}(\eta' \rightarrow \mu^+ \mu^-) \times 10^7$	1.42(7)(26)[27]	—	1.364(10) \rightarrow 1.24

Table 5.5: Our final results for the BRs as compared to the available experimental measurements. The first error gives the chosen (OPE÷Fact) band; the second one is the combined error from Table 5.4; the third error, in brackets, is the combination of them. For completeness, we give the commonly quoted as SM values: the first value with the error uses an approximate calculation, whereas the second one implements certain corrections.

Finally, we compare to the experimental available results in Table 5.5. For the ease of comparison, we take the middle value from Table 5.4 and include the (OPE÷Fact) range as an additional source of error (see comments in Table 5.5).

- For $\pi^0 \rightarrow e^+ e^-$, the most recent result —dominating the current PDG [10] value— comes from KTeV Collaboration [233] and implies a 3σ deviation from our theoretical result. Such value is extracted from $\text{BR}(\pi^0 \rightarrow e^+ e^-, x_D > 0.95) = 6.44(25)(22) \times 10^{-8}$ [233], where $x_D = m_{e^+ e^-}^2 / m_\pi^2$ and the first(second) error is statistical(systematic). Accounting for the radiative corrections (RC) in [238] and extrapolating to $x_D = 1$, they obtain $\text{BR}(\pi^0 \rightarrow e^+ e^-) = 7.48(29)(25) \times 10^{-8}$. As a result of the discrepancy, the authors in Ref. [224] have performed a full two-loop evaluation of the RC with the Bremsstrahlung diagrams evaluated in the soft-photon approximation. There, the authors noticed that the previous estimate [238] neglected a class of subleading diagrams, which due to partial cancelations among the leading ones, turned out to be dominant and reduced the size of the RC from 14% [238] down to 6% [224]. Finally, the authors in [225] have performed the exact calculation for the Bremsstrahlung diagrams, confirming the goodness of the soft photon approximation and closing the exact full two-loop evaluation of the RC. The work from Refs. [224, 225] suggest then $\text{BR}(\pi^0 \rightarrow e^+ e^-) = 6.87(36) \times 10^{-8}$, 1.5σ away from our result. Still, this discrepancy is hard to be explained within QCD, as it would require an extremely damped TFF at very low-energies, implying an unexpected TFF behavior as well as a slow convergence for the OPE expansion¹⁹. In light of this result, it is tempting to discuss about new physics scenarios, a debate to which we come back in Section 5.6.

¹⁹More details in Chapter 6.

- For the $\eta \rightarrow \mu^+ \mu^-$, we observe an interesting discrepancy with respect to the experimental result, which corresponds to a 2σ deviation —note that this discrepancy would disappear if we would have used the approximated result Eq. (5.15) instead. Still, the experimental accuracy prevents us from drawing any conclusion. For this, a new preciser experiment would be desired. In this respect, there exists the possibility that such decay could be measured at the LHCb [239] Collaboration. Amusingly, if the discrepancy were to be explained on QCD grounds, this time we would require a flatter TFF, contrary to the π^0 case, which represents an intriguing situation. A similar situation is found when looking at possible new physics scenarios, a discussion to which we come back in Section 5.6.
- Finally, we turn our attention to the η' decays. At present, only a recent upper bound exists for the $\eta' \rightarrow e^+ e^-$ channel from VEPP-2000 at Novosibirsk [236, 237], which improves the previous one by two orders of magnitude [10], but is still two orders of magnitude above our prediction. In the future, it may be possible as well to find the first signal for the $\eta' \rightarrow \mu^+ \mu^-$ channel at LHCb [239].

5.5 Implications for χ PT

At LO, the χ PT prediction involves two different contributions. The first one is obtained when replacing the LO χ PT result for the TFF, this is, the constant WZW term (left diagram in Fig. 5.6). The second one is the counterterm required to regularize the divergent integral and is obtained from the following lagrangian [210–212]

$$\frac{3i\alpha^2}{32\pi^2} \bar{\ell} \gamma^\mu \gamma_5 \ell \left[\chi_1 \text{tr} \left(\mathcal{Q}^2 \left\{ U^\dagger, \partial_\mu U \right\} \right) + \chi_2 \text{tr} \left(\mathcal{Q} U^\dagger \mathcal{Q} \partial_\mu U - \mathcal{Q} \partial_\mu U^\dagger \mathcal{Q} U \right) \right], \quad (5.29)$$

where \mathcal{Q} stands for the charge matrix. Following the definitions in Appendix A, the leading term, depicted in the right diagram from Fig. 5.6, yields

$$i\mathcal{M} = 2\sqrt{2}m_\ell m_P \alpha^2 F_{P\gamma\gamma} \chi(\mu), \quad (5.30)$$

where $\chi(\mu) \equiv -(\chi_1(\mu) + \chi_2(\mu))/4$ is the (scale-dependent) counterterm and the TFF result is to be taken from the LO piece in Section 1.6.2. Recalling our result for a constant TFF, Eq. (5.12), the LO χ PT prediction reads

$$\mathcal{A}^{\text{LO}}(q^2) = \frac{i\pi}{2\beta_\ell} L + \frac{1}{\beta_\ell} \left[\frac{1}{4} L^2 + \frac{\pi^2}{12} + \text{Li}_2 \left(\frac{\beta_\ell - 1}{1 + \beta_\ell} \right) \right] - \frac{5}{2} + \frac{3}{2} \ln \left(\frac{m_\ell^2}{\mu^2} \right) + \chi(\mu). \quad (5.31)$$

As we see, there exists at this order a single available term, $\chi(\mu)$, to determine all the $P \rightarrow \bar{\ell}\ell$ processes, including π^0, η, η' as well as $\ell = e, \mu$ final



Figure 5.6: The LO contributions to the $P \rightarrow \bar{\ell}\ell$ process in χ PT. The diagram on the left stands for the WZW (constant) TFF. The one on the right is the required counterterm.

	$\pi^0 \rightarrow e^+e^-$	$\eta \rightarrow e^+e^-$	$\eta \rightarrow \mu^+\mu^-$	$\eta' \rightarrow e^+e^-$	$\eta' \rightarrow \mu^+\mu^-$
$\chi(\mu)$	(2.53 \div 2.99)	(5.90 \div 6.46)	(3.29 \div 3.82)	(14.2 \div 14.9) + 2.52 <i>i</i>	(5.61 \div 6.31) + 0.75 <i>i</i>
$\chi(\mu)_{m_\pi}$	(2.53 \div 2.99)	(2.66 \div 3.12)	—	(2.16 \div 2.62)	—
$\chi(\mu)_{UV}$	(2.53 \div 2.99)	(5.50 \div 6.05)	(3.11 \div 3.64)	(16.8 \div 17.7) + 7.09 <i>i</i>	(6.56 \div 7.35) + 2.12 <i>i</i>

Table 5.6: Our equivalent χ PT counter-term $\chi(\mu)$ together with its equal-mass version, $\chi(\mu)_{m_\pi}$, and the $U(3)_F$ -symmetric TFFs version, $\chi(\mu)_{UV}$. Results for $\mu = 0.77$ GeV.

states. This approach benefits from being rigorous, model-independent and very predictive at the leading order. Regretfully, we find that large corrections are expected to arise at higher orders, requiring a NLO calculation with its consequent loss of predictiveness as the number of counterterms increases.

To illustrate this, we obtain for each particular decay the associated counterterm $\chi(\mu)$ which is required to reproduce our results from Table 5.3. This is, we subtract Eq. (5.31) from our results. The obtained values are shown in the first row from Table 5.6. The large $\chi(\mu)$ variations which arise when comparing different channels indicates the relevance of NLO corrections and the danger of fixing some counterterm from a particular channel to predict the others.

In the following, we investigate the sources of these differences and identify which are the most relevant effects. On the one hand, there is a clear difference among each of the pseudoscalars which should arise from $U(3)_F$ -breaking effects. As a first step, we take all the masses to be equal to the π^0 and calculate again the results from Table 5.3. Subtracting Eq. (5.31), we obtain the results in the $\chi(\mu)_{m_\pi}$ row from Table 5.6, which represent a large effect. All the remaining differences in this row arise from $U(3)$ -breaking effects in the TFFs alone (i.e., $b_\pi \neq b_\eta \neq b_{\eta'}$). These are less pronounced as may be inferred from the $\chi(\mu)_{UV}$ row in Table 5.6, where we recalculate $\chi(\mu)$ for the case in which all the TFFs are equal to that of the π^0 , but the pseudoscalar masses are the physical ones. On the other hand, there is a notorious impact among the different leptonic channels, which is clear when comparing the η and η' electronic channels against the muonic ones.

All these effects will be generated at higher orders in χ PT as one obtains a q^2 -dependent TFF introducing some hadronic scale. This will generate

additional $m_{P,\ell}^2/\Lambda^2$ corrections explaining the observed differences, which will be further commented in Section 5.5.2. As an illustration, this is the only way to generate an imaginary part for the η' , to be associated with the pion loop in Fig. 5.3, left.

5.5.1 The π^0 -exchange contribution to the $2S$ hyperfine-splitting in the muonic hydrogen

The results collected in Table 5.6, first row, are also relevant for calculating the π^0 pole-contribution to the $2S$ hyperfine-splitting in the muonic hydrogen [240–242] ($\Delta E_{\text{HFS}}^\pi$). Such calculation can be performed within χ PT, which involves again Eq. (5.31). However, the kinematics of the process involves a vanishingly small Q^2 space-like momentum for the π^0 , since its contribution to the $2S$ hyperfine-splitting appears in the t -channel. As such, it is $\mathcal{A}(Q^2 \simeq 0)$ instead of $\mathcal{A}(m_\pi^2)$ which is relevant now [240], shifting the values obtained in Table 5.6. To illustrate this, we recalculate $\mathcal{A}(0)$ from Eq. (5.6) taking the limit $Q^2 \rightarrow 0$, and obtain the new subtraction constant which should be used in Eq. (5.31) to reproduce our results. We obtain

$$\chi_{\pi^0}^{ee}(\mu) = (2.37 \div 2.83) \quad (5.32)$$

for $\ell = e$, which is smaller than its counterpart collected in Table 5.6. However, for the $2S$ hyperfine-splitting in muonic hydrogen what is needed is the coupling to muons ($\ell = \mu$). In that case, we obtain

$$\chi_{\pi^0}^{\mu\mu}(\mu) = (2.18 \div 2.63), \quad (5.33)$$

which is even lower than Eq. (5.32). Note that the shift is of the order of the uncertainties quoted in Table 5.6 and arises again from the full q^2 and m_ℓ^2 dependence in Eq. (5.6), which is not accounted for at LO in χ PT. To close the discussion, we note that it was pointed out for the first time in Ref. [241] that, to obtain the π^0 contribution to $\Delta E_{\text{HFS}}^\pi$, it was necessary to account for the full q^2 -dependency of $\mathcal{A}(q^2)$ given its non-analytic behavior at $q^2 = 0$. Consequently, and for the sake of completeness, we quote what would be obtained in such case using our exact $\mathcal{A}(q^2)$ numerical result. This can be calculated through Eq. (37) and Eq. (39) in Ref. [240] and leads²⁰

$$\Delta E_{\text{HFS}}^\pi = -(0.13 \div 0.12) \text{ } \mu\text{eV}, \quad (5.34)$$

where the uncertainties from the slope and TFF normalization can be neglected against the dominating one, that arises from the chosen (OPE \div Fact) range chosen for the double-virtual parameter. We note that the connection between the $\chi_{\pi^0}^{ee}(\mu)$ in Eq. (5.32) and $\chi_{\pi^0}^{\mu\mu}(\mu)$ in Eq. (5.33) and that extracted from the experimental results is non-trivial as it is TFF dependent.

²⁰In our approach, we take the $\Lambda_\pi \rightarrow \infty$ limit in Ref. [240], which corresponds with the treatment in [241] and corresponds to the π^0 -pole.

In quoting our results, we implicitly assume that there is no new-physics contribution. However, if the current discrepancies among theory and experiment persists, indicating new physics contribution—which we will discuss in Section 5.6—the connection between the experimental $\chi(\mu)$ and that in Eqs. (5.32) and (5.33) will depend on the particular new-physics scenario and will have to be reanalyzed.

The results above are illustrative as well regarding $(g-2)_\mu$ hadronic contributions, which in χ PT involve $\chi(\mu)$ together with an additional counterterm, $C(\mu)$, as an input [243]. If we were able to determine $C(\mu)$ somehow, from $(g-2)_e$ for example, and $\chi(\mu)$ would be taken from the experimental $\pi^0 \rightarrow e^+e^-$ result, extrapolating up to the μ case may imply a non-negligible error as illustrated above; similar effects may arise for $C(\mu)$ itself too.

5.5.2 Corrections

As discussed above, the precision which is reached at the LO in χ PT for processes involving a $P\bar{\ell}\ell$ vertex may not be enough—a feature which manifests when comparing the same process for a different $\ell = e, \mu$ channel. This suggests to look at the next to leading order. In this respect, χ PT would yield a power series expansion for the TFF²¹

$$\tilde{F}_{P\gamma^*\gamma^*}(q_1^2, q_2^2) = \underbrace{1}_{\text{LO}} + \underbrace{\frac{1}{\Lambda^2}(q_1^2 + q_2^2)}_{\text{NLO}} + \underbrace{\frac{1}{\Lambda^4}(q_1^4 + q_2^4)}_{\text{NNLO}} + \underbrace{\frac{1}{\Lambda^4}(q_1^2 q_2^2)}_{\text{NNLO}} + \mathcal{O}\left(\frac{q^6}{\Lambda^6}\right). \quad (5.35)$$

Then, we could calculate the result of Eq. (5.6) for the TFF in Eq. (5.35),

$$\begin{aligned} \mathcal{A}(q^2, m_\ell^2) &= \frac{2i}{\pi^2 q^2} \int d^4 k \frac{(k^2 q^2 - (k \cdot q)^2)}{k^2 (q - k)^2 ((p - k)^2 - m_\ell^2)} \left[1 + \frac{(\dots)}{\Lambda^2} + \frac{(\dots)}{\Lambda^4} + \dots \right] \\ &\equiv \mathcal{A}^{\text{LO}}(q^2, m_\ell^2) + \mathcal{A}^{\text{NLO}}(q^2, m_\ell^2) + \mathcal{A}^{\text{NNLO}}(q^2, m_\ell^2) + \dots, \end{aligned} \quad (5.36)$$

where $\mathcal{A}^{\text{LO}}(q^2)$ has been given in Eq. (5.31) and

$$\mathcal{A}^{\text{NLO}}(q^2, m_\ell^2) = \frac{1}{3\Lambda^2}(q^2 - 10m_\ell^2)(1 - L_\ell) + \frac{1}{9\Lambda^2}(4m_\ell^2 - q^2), \quad (5.37)$$

$$\mathcal{A}^{\text{NNLO}}(q^2, m_\ell^2) = \left[\frac{126m_\ell^4 - q^4 - 8m_\ell^2 q^2}{12\Lambda^4} L_\ell + \frac{26m_\ell^2 q^2 + 7q^4 - 702m_\ell^4}{72\Lambda^4} \right]. \quad (5.38)$$

where $L_\ell = \ln(m_\ell^2/\Lambda^2)$. We notice that the LO leading logs L_ℓ correspond—not surprisingly as they arise from a power-like expansion as well—to the corrections found in [208, 209] if Λ is taken as the VMD scale. We

²¹For simplicity, we have assumed a single scale for the TFF inspired in typical VMD models. Note that logarithmic terms coming from loops are of course present too. However, they are subleading as compared to the power expansion and may be Taylor expanded for the π^0 and η cases.

adopt then a more modest approach and retain the leading logs alone, which represents a good approximation. This would produce a straightforward generalization to higher orders as well as a tool to estimate the convergence of the chiral expansion. Of particular relevance is the difference $\mathcal{A}(q^2, m_\mu^2) - \mathcal{A}(q^2, m_e^2)$, where one expects a better convergence for Eq. (5.36) due to partial cancellations. Taking into account the smallness of the lepton masses, we find that such a shift is given, to a reasonable accuracy, as

$$\begin{aligned} \mathcal{A}(q^2, m_e^2) - \mathcal{A}(q^2, m_\mu^2) &= \mathcal{A}^{\text{LO}}(q^2, m_e^2) - \mathcal{A}^{\text{LO}}(q^2, m_\mu^2) \\ &+ \frac{q^2}{3\Lambda^2} \left(1 + \frac{q^2}{4\Lambda^2} \right) \ln \left(\frac{m_\mu^2}{m_e^2} \right) + \frac{10m_\mu^2}{3\Lambda^2} \ln \left(\frac{\Lambda^2}{m_\mu^2} \right). \end{aligned} \quad (5.39)$$

Whereas our theoretical results for the leptonic and muonic channels in Table 5.3 could not be reproduced at LO with an unique counterterm, the observed differences in Table 5.6 Section 5.5.1 can be easily accounted for, to a good approximation, taking into account the additional terms in Eq. (5.39) —an exception is the η' case, for which the pion loops cannot be neglected in order to extract an imaginary part. The expansion above, Eq. (5.39), proves extremely useful to relate different leptonic channels, which is not only relevant in the cases discussed above but for χ PT studies on lepton flavor violation in $K_L \rightarrow \bar{\ell}\ell$ decays [244].

5.6 Implications for new physics contributions

5.6.1 Generic new physics scenarios

Given the current puzzles existing in the low-energy precision frontier of particle physics—specifically, the long standing discrepancy among the electron and muon anomalous magnetic moments [10, 20], and the most recent proton radius puzzle coming from the different values obtained from electronic- and muonic-hydrogen experiments [245], together with \mathcal{R}_K and $\mathcal{R}_{D^{(*)}}$ [246] from B -decays—where lepton universality seems to fail contrary to what is expected in the standard model, it would be very interesting to study whether similar puzzles appear in the processes discussed here as well. Having updated the SM values for $P \rightarrow \bar{\ell}\ell$ decays with careful account of systematic errors, we discuss possible new physics (NP) contributions, specially given the current discrepancies in the two existing measured decays. As it is explained in Appendix B.3, any additional contribution—such as leptoquark-like—will always manifest, after Fierz-rearrangement, only through effective pseudoscalar (\mathcal{P}) and axial (A) contributions which, given the existing well-motivated models [217, 247, 248], are conveniently expressed using the effective Lagrangian

$$\mathcal{L} = \frac{g}{4m_W} \sum_f m_A c_f^A (\bar{f} \not{A} \gamma_5 f) + 2m_f c_f^{\mathcal{P}} (\bar{f} i \gamma_5 f) \mathcal{P},$$

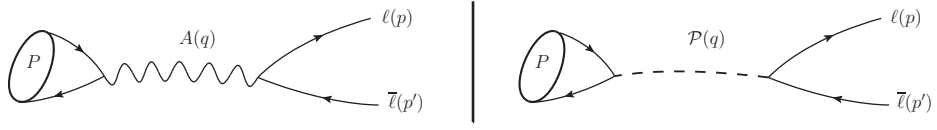


Figure 5.7: Left(right): additional tree level contributions from an axial(pseudoscalar) field. The P stands for the pseudoscalar meson; $A(\mathcal{P})$ stands for the axial(pseudoscalar) field with momentum q ; $\ell(\bar{\ell})$ for the (anti)lepton with momentum $p(p')$.

where g, m_W are the standard electroweak parameters, and $c_f^{A,\mathcal{P}}$ are dimensionless couplings to the fermions $f = \{u, d, s, e, \mu\}$. These interactions yield additional tree-level contributions as shown in Fig. 5.7. Their corresponding amplitudes (see Appendix A) read

$$i\mathcal{M} = \frac{igc_\ell^A m_A}{4m_W} [\bar{u}_{p,s} \gamma_\mu \gamma_5 v_{p',s'}] \frac{-i \left(g_{\mu\nu} - \frac{q_\mu q_\nu}{m_A^2} \right)}{m_P^2 - m_A^2} \frac{igm_A}{4m_W} \sum_q \overbrace{\langle 0 | J_{\mu 5}^{\text{NP}} | P(q) \rangle}^{\langle 0 | J_{\mu 5}^{\text{NP}} | P(q) \rangle}, \quad (5.40)$$

$$i\mathcal{M} = \frac{igc_\ell^{\mathcal{P}}}{2m_W} m_\ell [\bar{u}_{p,s} i\gamma_5 v_{p',s'}] \frac{i}{m_P^2 - m_{\mathcal{P}}^2} \frac{ig}{2m_W} \sum_q \overbrace{\langle 0 | c_q^{\mathcal{P}} m_q \bar{q} i\gamma_5 q | P(q) \rangle}^{\langle 0 | \mathcal{P}^{\text{NP}} | P(q) \rangle}, \quad (5.41)$$

for the axial and pseudoscalar contribution, respectively. In order to relate the hadronic matrix element $\langle 0 | J_{\mu 5}^{\text{NP}} | P(q) \rangle$ in Eq. (5.40) to the pseudoscalar decay constants

$$\langle 0 | J_{\mu 5}^a | P(q) \rangle \equiv iq_\mu F_P^a, \quad J_{\mu 5}^a = \bar{q} \gamma_\mu \gamma_5 \frac{\lambda^a}{2} q, \quad q = (u, d, s)^T, \quad (5.42)$$

we re-express $J_{\mu 5}^{\text{NP}}$ —as defined in Eq. (5.40)— in terms of the $U(3)_F$ axial current in Eq. (5.42)²². For that, we use the relation $\text{Tr}(\lambda^a \lambda^b) = 2\delta^{ab}$, whereby we obtain

$$\begin{aligned} \langle 0 | J_{\mu 5}^{\text{NP}} | P \rangle &= \langle 0 | \sum_a \text{Tr}(J_{\mu 5}^{\text{NP}} \lambda^a) J_{\mu 5}^a | P \rangle \\ &= \sum_a \text{Tr}(\text{diag}(c_u^A, c_d^A, c_s^A) \lambda^a) \langle 0 | J_{\mu 5}^a | P \rangle. \end{aligned} \quad (5.43)$$

²²In the flavor basis λ^8 and λ^0 can be traded for $\lambda^q = \text{diag}(1, 1, 0)$ and $\lambda^s = \text{diag}(0, 0, \sqrt{2})$, see Chapter 4. An analogous procedure applies then.

Then, from Eqs. (5.42) to (5.43) and the equations of motion²³, Eq. (5.40) can be expressed as

$$\begin{aligned} i\mathcal{M} &= -ic_\ell^A \frac{g^2}{16m_W^2} 2m_\ell (\bar{u}_{p,s} i\gamma_5 v_{p',s'}) \sum_a \text{Tr}(J_{\mu 5}^{\text{NP}} \lambda^a) F_P^a \\ &= -ic_\ell^A \frac{G_F}{\sqrt{2}} m_\ell (\bar{u}_{p,s} i\gamma_5 v_{p',s'}) \sum_a \text{Tr}(J_{\mu 5}^{\text{NP}} \lambda^a) F_P^a \\ &= c_\ell^A m_\ell m_P G_F \sum_a \text{Tr}(J_{\mu 5}^{\text{NP}} \lambda^a) F_P^a, \end{aligned} \quad (5.44)$$

where in the second and third lines we have used $G_F = g^2/(4\sqrt{2}m_W^2)$ and the projector in Eq. (5.2), respectively. This produces an effective additional contribution to the $\mathcal{A}(q^2)$ loop amplitude in Eq. (5.6),

$$\mathcal{A}(q^2) \rightarrow \mathcal{A}(q^2) + \frac{\sqrt{2}G_F}{4\alpha^2 F_{P\gamma\gamma}} c_\ell^A \sum_a \text{Tr}(J_{\mu 5}^{\text{NP}} \lambda^a) F_P^a. \quad (5.45)$$

As an example, the Z^0 boson contribution is obtained after taking $c_u^Z = -c_{d,s,e,\mu}^Z = 1$, leading for $P = \{\pi^0, \eta, \eta'\}$

$$\mathcal{A}(q^2) \rightarrow \mathcal{A}(q^2) - \frac{2\sqrt{2}G_F F_\pi}{4\alpha^2 F_{P\gamma\gamma}} \left\{ 1, \frac{F_\eta^8}{\sqrt{3}F_\pi} - \frac{F_\eta^0}{\sqrt{6}F_\pi}, \frac{F_{\eta'}^8}{\sqrt{3}F_\pi} - \frac{F_{\eta'}^0}{\sqrt{6}F_\pi} \right\}.$$

Alternatively, we could have used the flavor basis instead, then

$$\mathcal{A}(q^2) \rightarrow \mathcal{A}(q^2) - \frac{2\sqrt{2}G_F F_\pi}{4\alpha^2 F_{P\gamma\gamma}} \left\{ 1, -\frac{F_\eta^s}{\sqrt{2}F_\pi}, -\frac{F_{\eta'}^s}{\sqrt{2}F_\pi} \right\}.$$

For the pseudoscalar contribution, the $\langle 0 | \mathcal{P}^{\text{NP}} | P(q) \rangle$ hadronic matrix element determination in Eq. (5.41) is more involved whenever the singlet component appears, which is the case for the η and η' . To illustrate this, we outline its LO calculation in χ PT, which amounts to retain the leading term from the LO lagrangian²⁴ arising from the interaction between the pseudoscalar field P and the pseudoscalar current \mathcal{P} defined in χ PT from the building block $\chi \equiv 2Bi\mathcal{P}$. Then, in the presence of new physics of pseudoscalar type, $\chi \rightarrow 2Bi\mathcal{P}^{\text{NP}}$. For the π^0 such term corresponds to

$$FB\hat{m}(c_u^{\mathcal{P}} - c_d^{\mathcal{P}})\mathcal{P}^{\text{NP}}\pi^0,$$

from which the matrix element reads ($2B\hat{m} = m_\pi^2$)

$$\langle 0 | \mathcal{P}^{\text{NP}} | \pi^0 \rangle = FB\hat{m}(c_u^{\mathcal{P}} - c_d^{\mathcal{P}}) = \frac{F_\pi}{2} m_\pi^2 (c_u^{\mathcal{P}} - c_d^{\mathcal{P}}).$$

²³For the spinors, these imply $\bar{u}_{p,s}\not{p} = -\not{p}' v_{p',s'} = m_\ell$, see see Appendix A.

²⁴This is, $\frac{F^2}{4}(\chi^\dagger U + U^\dagger \chi)$.

where the LO results $F_\pi = F$ and $m_\pi = 2B\hat{m}$ have been used, see Eq. (1.20). For the η and η' , it gets more involved. The analogous LO term in the effective lagrangian contributing to the matrix element reads now

$$FB\mathcal{P}^{\text{NP}} \left(\frac{1}{\sqrt{3}} (\hat{m}(c_u^P + c_d^P) - 2c_s^P m_s) \eta_8 + \sqrt{\frac{2}{3}} (\hat{m}(c_u^P + c_d^P) + c_s^P m_s) \eta_1 \right). \quad (5.46)$$

After relabeling, introducing $g_8 \equiv (c_u^P + c_d^P - 2c_s^P)/\sqrt{3}$ and $g_0 \equiv \sqrt{2}(c_u^P + c_d^P + c_s^P)/\sqrt{3}$, together with the definitions in Chapter 4, Eq. (5.46) reads

$$\frac{F_0}{2} (\eta_8(g_8 M_8^2 + g_0 M_{80}^2) + \eta_1(g_8 M_{80}^2 + g_0 M_0^2)) \mathcal{P}^{\text{NP}},$$

Finally, using the $\eta - \eta'$ masses, mixing and decay constants at LO²⁵, we obtain for the matrix element

$$\langle 0 | \mathcal{P}^{\text{NP}} | \eta(\eta') \rangle = \sum_a \frac{1}{2} F_{\eta(\eta')}^a g_a m_{\eta(\eta')}^2 \left(1 - \delta^{a0} \frac{M_\tau^2}{M_{\eta(\eta')}^2} \right), \quad (5.47)$$

where g_a has been defined above and $M_\tau^2 = 6\tau/F^2$ is the topological mass term—see Chapter 4. After some algebra, we have obtained a relation which is very similar to the π^0 result—except for the singlet $a = 0$ term—and resembling that of the axial current matrix element. The natural question is how to find a general result valid at all orders in an easy way, for which is convenient to recall the Ward identity Eq. (1.7)

$$\partial_\mu (\bar{q} \gamma^\mu \gamma_5 q) = 2m_q \bar{q} i \gamma_5 q - \frac{g_s^2}{32\pi^2} \epsilon^{\alpha\beta\mu\nu} G_{\alpha\beta}^c G_{\mu\nu}^c \equiv 2m_q \bar{q} i \gamma_5 q + \omega, \quad (5.48)$$

which for the $U(3)_F$ axial current, Eq. (5.42), reads

$$\partial^\mu J_{\mu 5}^a = \{\mathcal{P}^a, \mathcal{M}\} + \delta^{a0} \sqrt{N_F/2} \omega; \quad \mathcal{P}^a = \bar{q} i \gamma_5 \frac{\lambda^a}{2} q, \quad q = (u, d, s)^T,$$

where $\mathcal{M} = \text{diag}(\hat{m}, \hat{m}, m_s)$ is the quark mass matrix. In such a way, the pseudoscalar current can be expressed in terms of the axial current and the winding number density ω . Then, using the same algebra as previously, the matrix element can be expressed as

$$\begin{aligned} \langle 0 | \mathcal{P}^{\text{NP}} | P(p) \rangle &= \frac{1}{2} \sum_a \text{Tr}(\mathcal{P}^{\text{NP}} \lambda^a) \langle 0 | \partial^\mu J_{5\mu}^a - \delta^{a0} \sqrt{3/2} \omega | P(p) \rangle \\ &= \frac{m_P^2}{2} \sum_a \text{Tr}(\text{diag}(c_u^P, c_d^P, c_s^P) \lambda^a) F_P^a (1 - \Delta \delta^{0a}) \end{aligned} \quad (5.49)$$

²⁵At LO, $\eta_{8(0)} = \eta(\eta') \cos \theta_P \pm \eta'(\eta) \sin \theta_P$, $\theta_P = -19.6^\circ$ and the decay constants read $F_\eta^8 = F_0 \cos \theta_P$, $F_{\eta'}^8 = F_0 \sin \theta_P$, $F_\eta^0 = -F_0 \sin \theta_P$, $F_{\eta'}^0 = F_0 \cos \theta_P$. In addition $\tan \theta_P = M_{80}^2 (M_0^2 + M_\tau^2 - M_\eta^2)^{-1} = M_{80}^2 (M_{\eta'}^2 - M_8^2)^{-1} = (M_8^2 - M_\eta^2)/M_{80}^2 = (M_{\eta'}^2 - M_0^2 - M_\tau^2)/M_{80}^2$.

where $\Delta = \langle 0 | \sqrt{6}\omega | P \rangle / m_P^2 F_P^0$. Still, Δ needs to be determined. A nice solution can be borrowed from [120]. Neglecting the u and d quark masses \hat{m} —which roughly amounts to take $m_\pi^2/m_{K,\eta,\eta'}^2 \rightarrow 0$ —we obtain from the octet and singlet Ward identities,

$$\sqrt{3/2} \omega = \partial^\mu J_{\mu 5}^0 + \frac{1}{\sqrt{2}} \partial^\mu J_{\mu 5}^8.$$

Plugging this relation into Eq. (5.49), we obtain $\Delta = 1 + F_P^8/(\sqrt{2}F_P^0)$, so the pseudoscalar contribution to $P \rightarrow \bar{\ell}\ell$ can be finally expressed as

$$\begin{aligned} i\mathcal{M} &= -i[\bar{u}_{p,s} i\gamma_5 v_{p',s'}] \frac{g^2}{8m_W^2} \frac{m_P^2 m_\ell c_\ell^P}{m_P^2 - m_\mathcal{P}^2} \sum_a \text{Tr}(\mathcal{P}^{\text{NP}} \lambda^a) F_P^a (1 - \delta^{0a} - \frac{\delta^{0a} F_P^8}{F_P^0 \sqrt{2}}), \\ &= -i[\bar{u}_{p,s} i\gamma_5 v_{p',s'}] \frac{G_F}{\sqrt{2}} \frac{m_P^2 m_\ell c_\ell^P}{m_P^2 - m_\mathcal{P}^2} \sum_a \text{Tr}(\mathcal{P}^{\text{NP}} \lambda^a) F_P^a (1 - \delta^{0a} (1 + \frac{F_P^8}{F_P^0 \sqrt{2}})), \\ &= G_F \frac{m_P^3 m_\ell c_\ell^P}{m_P^2 - m_\mathcal{P}^2} \sum_a \text{Tr}(\mathcal{P}^{\text{NP}} \lambda^a) F_P^a (1 - \delta^{0a} (1 + \frac{F_P^8}{F_P^0 \sqrt{2}})). \end{aligned} \quad (5.50)$$

This induces an additional contribution to the $\mathcal{A}(q^2)$ loop amplitude in Eq. (5.6),

$$\mathcal{A}(q^2) \rightarrow \mathcal{A}(q^2) + \frac{\sqrt{2}G_F m_P^2 c_\ell^{\text{NP}}}{4\alpha^2 F_{P\gamma\gamma} (m_P^2 - m_\mathcal{P}^2)} \sum_a \text{Tr}(\mathcal{P}^{\text{NP}} \lambda^a) F_P^a (1 - \delta^{0a} (1 + \frac{F_P^8}{F_P^0 \sqrt{2}})). \quad (5.51)$$

We note that the approximation taken for calculating the $\langle 0 | \omega | P \rangle$ matrix element has been used with great success in $J/\Psi \rightarrow \gamma\eta(\eta')$ decays [120] and has been checked in Section 4.5.2. Actually, at LO in χPT ²⁶, the difference between Eq. (5.47) and Eq. (5.49) is of 8%(1%) for the $\eta(\eta')$, enough for our study.

In the flavor basis, neglecting the u and d quark masses, only the strange part contributes. Using an analogous procedure, we find

$$\mathcal{A}(q^2) \rightarrow \mathcal{A}(q^2) + \frac{\sqrt{2}G_F m_P^2 c_\ell^{\text{NP}}}{4\alpha^2 F_{P\gamma\gamma} (m_P^2 - m_\mathcal{P}^2)} \sum_a \text{Tr}(\mathcal{P}^{\text{NP}} \lambda^a) F_P^a (1 - \frac{F_P^q}{\sqrt{2}F_P^s}) (1 - \delta^{aq}). \quad (5.52)$$

5.6.2 Implications for new physics

All in all, both contributions may be summarized to yield an additional term modifying Eq. (5.6) as

$$\mathcal{A}(q^2) \rightarrow \mathcal{A}(q^2) + \frac{\sqrt{2}G_F F_\pi}{4\alpha_{em}^2 F_{P\gamma\gamma}} (\lambda_P^A + \lambda_P^P), \quad (5.53)$$

²⁶At this order, the η and η' masses are [183] $M_\eta^2 = 0.244\text{GeV}^2$ $M_{\eta'}^2 = 0.917\text{GeV}^2$ and $M_0^2 = 0.673\text{GeV}^2$.

where G_F is the Fermi coupling constant, and $F_\pi \simeq 92$ MeV is the pion decay constant. The λ -terms depend on the pseudoscalar meson structure, which for the η and η' involve the mixing parameters. In the flavor-mixing scheme, they read²⁷

$$\lambda_P^A = c_\ell^A \left[\frac{F_P^3}{F_\pi} (c_u^A - c_d^A) + \frac{F_P^q}{F_\pi} (c_u^A + c_d^A) + \frac{F_P^s}{F_\pi} \sqrt{2} c_s^A \right], \quad (5.54)$$

$$\lambda_P^P = \frac{c_\ell^P}{1 - \frac{m_P^2}{m_P^2}} \left[\frac{F_P^3}{F_\pi} (c_u^P - c_d^P) + \frac{F_P^q}{F_\pi} (-c_s^P) + \frac{F_P^s}{F_\pi} \sqrt{2} c_s^P \right]. \quad (5.55)$$

Taking the result from the mixing parameters in Chapter 4 to numerically calculate Eqs. (5.54) and (5.55) Eq. (5.53) yields

$$\begin{aligned} \mathcal{A}(m_{\pi^0}^2) &+ 0.026 (c_\ell^A (c_u^A - c_d^A) + c_\ell^P (c_u^P - c_d^P) (1 - m_P^2/m_P^2)^{-1}), \\ \mathcal{A}(m_\eta^2) &+ 0.026 (0.84 c_\ell^A (c_u^A + c_d^A) - 1.27 c_\ell^A c_s^A - 2.11 c_\ell^P c_s^P (1 - m_P^2/m_P^2)^{-1}), \\ \mathcal{A}(m_{\eta'}^2) &+ 0.021 (0.72 c_\ell^A (c_u^A + c_d^A) + 1.61 c_\ell^A c_s^A + 0.89 c_\ell^P c_s^P (1 - m_P^2/m_P^2)^{-1}). \end{aligned}$$

To discuss the sensitivity of each particular channel to NP, it is convenient to cast a very approximate result for $\mathcal{A}(m_P^2)$, namely

$$\mathcal{A}(m_P^2) \simeq i\pi \left[\ln \left(\frac{m_\ell}{m_P} \right) \right] + \left[\ln^2 \left(\frac{m_\ell}{m_P} \right) - 3 \ln \left(\frac{\Lambda}{m_\ell} \right) + \delta_{\text{NP}} \right], \quad (5.56)$$

where Λ is some effective hadronic scale characterizing the TFF and δ_{NP} is the NP contribution in Eq. (5.53). From Eq. (5.56), we see that, as the lepton mass gets lighter, the amplitude will be dominated by the $\ln(m_\ell/m_P)$ terms, which become large and make the NP contribution harder to see. Indeed, for $\ell = e$, the relative NP contribution to the BR is approximately given by $2\delta_{\text{NP}}(\ln^2(\frac{m_e}{m_P}) + \pi^2)^{-1}$. If we are aiming to find contributions from NP, it is therefore much easier to look for the $\ell = \mu$ channel as the NP part is insensitive to m_ℓ (see Eq. (5.53)).

With respect to m_P , from the logarithmic scaling, we infer that there is no big difference in the SM in choosing either π^0 , η , or η' as their masses are of same order. Furthermore, the NP axial contribution does not depend on m_P , see Eq. (5.54), meaning that is equally likely to appear in any case. This contrasts with the pseudoscalar NP contribution, which strongly depends on m_P (cf. Eq. (5.55)) and gets bigger as m_P and m_ℓ (the mass of the new pseudoscalar particle) approach each other. Still, this is *a priori* irrelevant unless there is a well-motivated NP scale which is close to either the π^0 , η , or η' masses.

From this discussion, we conclude that $\eta(\eta') \rightarrow \mu^+ \mu^-$ decays are the best candidates to look for NP effects (as the π^0 cannot decay into muons). For

²⁷By definition, $F_{\pi^0}^8 = F_{\pi^0}^0 \equiv 0$ and $F_{\pi^0}^3 \equiv F_\pi$. From Chapter 4, $F_{\eta(\eta')}^q = 0.84(0.72)F_\pi$, $F_{\eta(\eta')}^s = -0.90(1.14)F_\pi$ and $F_{\eta(\eta')}^3 \equiv 0$.

illustrating the statements above, we give the approximate NP contribution to the branching ratio for each particular process,

$$\begin{aligned} BR(\pi^0 \rightarrow e^+ e^-) & \left(1 + 0.001 \left[c_\ell^A (c_u^A - c_d^A) + c_\ell^P \frac{c_u^P - c_d^P}{1 - m_\mathcal{P}^2/m_P^2} \right] \right), \\ BR(\eta \rightarrow \mu^+ \mu^-) & \left(1 + (-0.002) \left[0.84 c_\ell^A (c_u^A + c_d^A) - 1.27 c_\ell^A c_s^A - \frac{2.11 c_\ell^P c_s^P}{1 - m_\mathcal{P}^2/m_P^2} \right] \right), \\ BR(\eta' \rightarrow \mu^+ \mu^-) & \left(1 + (+0.003) \left[0.72 c_\ell^A (c_u^A + c_d^A) + 1.61 c_\ell^A c_s^A + \frac{0.89 c_\ell^P c_s^P}{1 - m_\mathcal{P}^2/m_P^2} \right] \right). \end{aligned}$$

We see that, as stated above, the $\ell = e$ channel has the same sensitivity for every pseudoscalar. For $\ell = \mu$, we find it two(three) times more sensitive than the $\ell = e$ channel for the $\eta(\eta')$. These numbers imply, together with the experimental precision reached for the $\pi^0(\eta)$ decay (we do not consider the central value, but the obtained precision), bounds for the c^A parameters of the order of 7(8). As an example, for the Z^0 boson ($c_\ell^A = c_{d,s}^A = -c_u^A \equiv 1$), the c_f^A combination is $-2(-1.27)[1.61]$ for $\pi^0(\eta)[\eta']$.

Interesting enough, a typical Z^0 -like contribution has opposite sign for $\pi^0 \rightarrow e^+ e^-$ than for $\eta \rightarrow \mu^+ \mu^-$, contrary to experimental implications. This would suggest either different couplings (necessarily $SU(2)_F$ breaking), or lepton flavor violating (LFV) models, which would couple different to distinct generation of quarks, leptons, or both. Moreover, in order to avoid $(g-2)_\mu$ problems, we would need, either some balance from an additional vector-like contribution²⁸ or, again, LFV models in which the coupling to the muon is suppressed.

For a pseudoscalar contribution, as in Ref. [217], the effective couplings may become even larger as the new particle mass approaches the π^0, η, η' masses, meaning that would be visible for one of the pseudoscalars alone. Finally, we comment on the existing correlations given the pseudoscalar structure. We see for instance that $\pi^0 \rightarrow e^+ e^-$ and $\eta \rightarrow \mu^+ \mu^-$ are, in general, anti-correlated unless there is a pseudoscalar particle \mathcal{P} with $m_{\pi^0} < m_\mathcal{P} < m_\eta$ (or a different structure for distinct generations). Again, $(g-2)_\mu$ would play an important constraint for the pseudoscalar case as well.

To conclude, there is still the chance to look for NP contributions, specially in the $\ell = \mu$ channel, and a variety of phenomenology is possible depending on which kind of interaction is chosen. Still, our study suggests to go beyond simple scenarios; this seems nevertheless the standard in high energy physics nowadays, and scenarios of this kind have been and are still studied at present. In this discussion, we have omitted a detailed discussion of available physical constraints for these scenarios. This constitutes a field

²⁸The dominant Schwinger-like contribution for a vector(scalar)-like coupling has positive sign whereas the axial(pseudoscalar) one has opposite sign, providing a fine tuning cancelation.

of study by itself. To mention some constraints, $(g - 2)_\mu$ and low-energy parity violating would provide tight bounds. For additional discussion along these lines, see Refs. [217, 247–250].

5.7 Conclusions and outlook

In this chapter, we have reviewed as a first application of CAs the status of pseudoscalar decays into lepton pair $P \rightarrow \bar{\ell}\ell$ processes. We have shown that the main problem in these processes is to obtain a precise and reliable determination for the TFFs, not only at the high energies, but —especially—at the low-energies. This feature, which has been known since long, has been ignored due to the lack of ability to incorporate these two regimes at once in a single theory, systematically, precisely and model independently —the perfect scenario to test and apply our acquired knowledge.

Thanks to our method we have been able, for the first time, to provide a systematic error for these processes. This was specially important regarding the η and η' , where previously unaccounted systematic errors associated to the existence of threshold production lead to unrealistic underestimated errors. Still, thanks to the precise achieved description, we have been able to improve on the precision in most of results, even after the inclusion of previously unaccounted errors. In addition, we have carried out a precise numerical evaluation and avoided approximations commonly employed in the literature. Such an error cannot be neglected at all when dealing with the η and η' , which would induce a very large systematic error. For completeness, we have included the Z^0 boson contribution as well.

From our results, we have confirmed the present experimental discrepancies in the $\pi^0 \rightarrow e^+e^-$ and $\eta \rightarrow \mu^+\mu^-$ decays —the latter often obviated in the literature because of the approximations employed in the loop integral among others. In light of this situation we have discussed the possible implications of new physics. We find that that appropriate scenarios to describe the discrepancy most likely require light new-physics degrees of freedom of lepton-flavor violating nature. Finally, we have shown that previous χ PT-based calculations at LO imply non-negligible errors and should be avoided. For this reason, we have provided a simple formula which provides, in a simple way, the required corrections.

For the moment, we have only employed the simplest C_1^0 approximant due to the absence of double-virtual data. Reaching the C_2^1 approximant would greatly reduce the obtained uncertainty and evidence the performance of the method. This is an ongoing effort which we will briefly discuss in the next chapter. An additional line of thought to be followed is developing a modified approach for the η' in which the time-like features could be easily implemented too.

The muon $(g - 2)$: pseudoscalar-pole contribution

Contents

6.1	Introduction	129
6.2	Standard Model contributions to a_μ	130
6.3	Generic HLbL contribution to a_μ	136
6.4	The pseudoscalar-pole contribution	138
6.5	Beyond pole approximation	154
6.6	Final results for a_μ^{HLbL}	161
6.7	Conclusions and outlook	162

6.1 Introduction

The anomalous magnetic moment of fermions, proportional to $(g - 2)$ ¹, has been a path of effort and triumphs in theoretical and experimental particle physics. First, back in 1928, the new relativistic Dirac theory for *elementary* spin-1/2 fermions ℓ predicted $g_\ell = 2$, in contrast to the classical expectation $g_\ell = 1$ [251]. The g_e measurement in 1934 [252] confirmed the Dirac theory of electrons. Nevertheless, subsequent preciser measurements were performed [253–256] finding slight deviations from $g_e = 2$. This could be soon explained after the great effort from Tomonaga, Feynmann, Schwinger and Dyson in the development of the renormalization of Quantum Field Theories (QFT), culminating with the Schwinger prediction of g_ℓ at NLO [257],

$$a_\ell \equiv \frac{g_\ell - 2}{2} = \frac{\alpha}{2\pi}, \quad (6.1)$$

¹In particular, given a fermion ℓ , $\mu_m = g_\ell \frac{e\mathcal{Q}}{2m_\ell} S$, whereby $\mu_{\text{anom}} = (g_\ell - 2) \frac{e\mathcal{Q}}{2m_\ell} S$.

which established QED —the very first QFT— as a serious microscopic theory of the electromagnetic interactions. Since then, experiments and theory have evolved, and still, $(g - 2)$ continues to be one of the finest tests of our understanding of particle physics. At present, both e and μ anomalous magnetic moments have been measured; their most recent results read

$$a_e^{\text{exp}} = 115965218.073(28) \times 10^{-11}, \quad (6.2)$$

$$a_\mu^{\text{exp}} = 116592091(63) \times 10^{-11}. \quad (6.3)$$

The first one is the result from [258], whereas the second one is the updated value [259] from [21], after the new muon-to-proton magnetic ratio determination [260]. Regardless the precise determination for a_e , it is a_μ on which we focus from now on. This is due to its higher sensitivity to new physics in the naive scaling $\delta a_\ell = \mathcal{C} m_\ell^2 / \Lambda_{NP}^2$ with $\mathcal{C} \sim \mathcal{O}(\frac{\alpha}{\pi})$ [20], which make heavy leptons more interesting (unfortunately, precise experiments are not yet accessible for the heavier τ lepton). Given the current precision, $a_{\mu(e)}$ is sensitive to $\mathcal{O}(200(50) \text{ GeV})$ physics², which is complementary to the LHC. As an example, it could help in distinguishing among SUSY models [262]. Alternatively, for models with extra-dimensions, it would be sensitive to Kaluza-Klein gravitons [263] despite of constraints from electroweak precision observables [264]. This contrasts with Littlest Higgs models which have little influence on $(g_\mu - 2)$ [265]. Finally, it is well suited for testing Dark Photons [266, 267] scenarios. However, before searching for new physics, it is necessary to provide a robust theoretical prediction within the SM at the same level of precision as the experimental one. This is very pressing given the expected precision in the forthcoming muon $(g - 2)$ experiments at Fermilab [22] and J-PARC [23] around 16×10^{-11} . Below, we review the current status and motivate the needs for improving the current estimation for the hadronic light-by-light pseudoscalar pole contribution, to which this chapter is devoted.

6.2 Standard Model contributions to a_μ

6.2.1 QED

In the SM, the major contribution to a_μ arises from QED corrections including e, μ and τ leptons alone. At one loop, the only diagram is the Schwinger term, Fig. 6.1 left, which was calculated by Schwinger in 1948 [257]. Then, at two loops, there are 9 diagrams contributing to a_μ , among which we find the so-called vacuum polarization, see Fig. 6.1 center —the full calculation was carried out by Petermann and Sommerfield in 1957 [268–270]. At three-loops, there are 72 diagrams, including the light-by-light one, Fig. 6.1 right,

²There are however some exceptions violating this scaling [261] and would make a_e very interesting as well for testing new physics scenarios [223, 261].

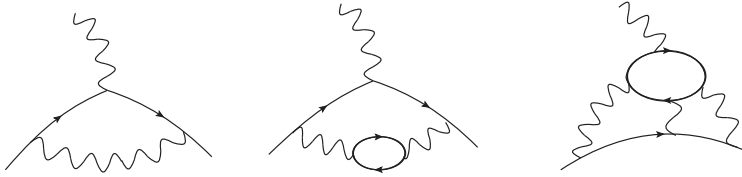


Figure 6.1: Representatives contribution to a_ℓ . First, the one-loop Schwinger contribution. Second, one of the two-loops contributions: the vacuum polarization. Third, one of the three-loops contribution: the light-by-light. In all these diagrams the loops contain charged leptons alone, i.e., $\ell = e, \mu, \tau$.

and their calculation required a huge effort taking almost 40 years [271–276]. Up to this order, analytic calculations are tractable, whereas at higher orders the number of diagrams as well as the calculational complexity increases. Nonetheless, a great effort has been done from the group of Kinoshita and collaborators to numerically compute the four- and five-loop contributions [277]. The up-to-date result is

$$\begin{aligned} a_\mu^{\text{QED}} &= \frac{1}{2} \left(\frac{\alpha}{\pi} \right) + 0.765857425(17) \left(\frac{\alpha}{\pi} \right)^2 + 24.05050996(32) \left(\frac{\alpha}{\pi} \right)^3 \\ &\quad + 130.8796(63) \left(\frac{\alpha}{\pi} \right)^4 + 753.29(1.04) \left(\frac{\alpha}{\pi} \right)^5 \\ &= 116\,584\,718.951(80) \times 10^{-11}. \end{aligned} \quad (6.4)$$

In the calculation we used the most precise determination from $\alpha^{-1} = 137.035\,999\,049(90)$ [259, 277] from Rb-atom [278] combined with the Rydberg constant and m_{Rb}/m_e in [260]. The errors are dominated from the α determination in the Schwinger term and, to a lesser extent, the computational error at four-loops. Likewise, for the electron [279] $a_e^{\text{QED}} = 115\,965\,218.007(77) \times 10^{-11}$.

6.2.2 Electroweak

The next sizable contributions to a_μ are the hadronic ones, and part of them are indeed one of the main objects of study in this thesis. However, due to their complexity, we leave their discussion for the last part of this section. Then, the last piece remaining in the SM are the electroweak contributions —find the one-loop contributions in Fig. 6.2. They have been analytically computed at one- and two-loops, in Ref. [280] and Refs. [281–283], respectively. Remarkably, such calculation was the first at two-loop that was performed within the electroweak sector of the SM. The last full re-evaluation after the Higgs discovery obtained [284]

$$a_\mu^{\text{EW}} = (194.80(1) - 41.23(1.0)) \times 10^{-11} = 153.6(1) \times 10^{-11}, \quad (6.5)$$

where the first and second terms represent the one- and two-loop contributions. The error is dominated in this case by hadronic uncertainties.

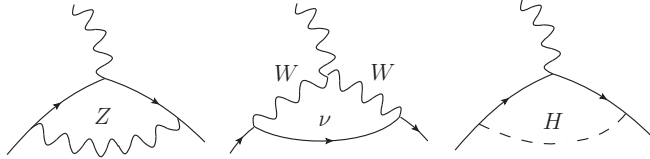


Figure 6.2: Electroweak contributions to a_ℓ at one loop.

Similarly, for the electron $a_e^{\text{EW}} = 0.00297(5) \times 10^{-11}$ [223].

6.2.3 QCD

As anticipated, we finally discuss the QCD or hadronic contributions. In contrast to the previous cases, these cannot be perturbatively calculated in a combined α and α_s expansion, as the latter becomes non-perturbative at low-energies, which turns out to be the most relevant region in a_μ calculations. Therefore, we must relegate to a perturbative expansion in α together with some machinery dealing with the hadronic interactions in its non-perturbative regime.

HVP

At order $\mathcal{O}(\alpha^2)$, the only hadronic contribution is the hadronic vacuum polarization (HVP), which is shown in Fig. 6.3 left. Fortunately for this case, data comes to our rescue. The reason being that the HVP is an analytic function of which the imaginary part is related to the process $e^+e^- \rightarrow$ hadrons by virtue of the optical theorem. Then, a dispersive representation allows to express such contribution as an integral over the mentioned cross-section [20]. This procedure allows to include all the hadronic effects in a data-driven approach using the available exclusive processes at low-energies and a matching to the pQCD prediction at the high-energies, obtaining [285]

$$a_\mu^{\text{HVP-LO};e^+e^-} = 6923(42) \times 10^{-11}. \quad (6.6)$$

Alternatively, it is possible to use $\tau \rightarrow \nu + \text{hadrons}$ data after correcting for isospin effects, which yields [285] $7015(47) \times 10^{-11}$ instead and shows some tension with the e^+e^- -based calculation at the level of 1.5σ . At higher orders $\mathcal{O}(\alpha^3, \alpha^4)$, there appear corrections to the HVP —see the second and third diagrams in Fig. 6.3. Again, all the hadronic information can be obtained from data. From the update [286] of Ref. [287],

$$a_\mu^{\text{HVP-NLO}} = -98.4(7) \times 10^{-11}. \quad (6.7)$$

Finally, the very recent result of Ref. [288] obtains

$$a_\mu^{\text{HVP-NNLO}} = 12.4(1) \times 10^{-11}. \quad (6.8)$$

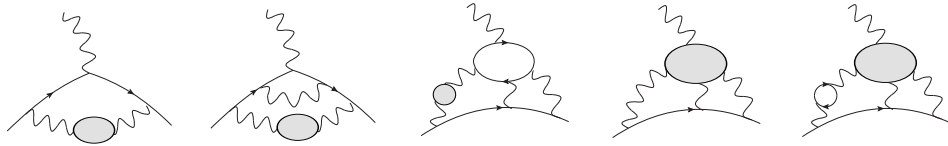


Figure 6.3: Hadronic contributions to a_μ : The first, second and third stand for the LO and representative NLO and NNLO hadronic vacuum polarization. Fourth and fifth represent the LO and representative NLO hadronic light-by-light contribution. The blobs represents hadronic physics whereas loops represent the leptons.

Putting together the information from Eqs. (6.6) to (6.8), we obtain for the HVP contributions

$$a_\mu^{\text{HVP-}e^+e^-} = 6837(42) \times 10^{-11}, \quad (6.9)$$

of which the error is dominated by the $\sigma(e^+e^- \rightarrow \pi^+\pi^-)$ experimental data uncertainty. The present accuracy is of the order of the current ($g_\mu - 2$) experiment, but three times larger than the projected ones. This situation is planned to be solved with a more precise and more extensive experimental programme. It is important to remark at this point that there are alternative determinations obtaining slightly different results [20, 289, 290]. Moreover, some experimental discrepancies exist —see Ref. [291]— which illustrates that a closer work among the theoretical and experimental community to agree on a common procedure and database is required. In addition, there are alternative ideas to attack this problem, such the space-like approach in Ref. [292] or the effort from the lattice community: MILC Collaboration [293], RBC-UKQCD [294], Mainz [295] and ETM Collaboration [296]. While their results are promising, additional work is required in order to reduce the error. Hopefully, in the near future the different approaches may converge to a very precise and robust determination for the HVP. Similarly, for the electron [288, 297]

$$a_e^{\text{HVP}} = (0.1866(11) - 0.02234(14) + 0.0028(1)) \times 10^{-11} = 0.16706(11) \times 10^{-11}. \quad (6.10)$$

HLbL

The last relevant hadronic contribution, starting at $\mathcal{O}(\alpha^3)$, is the hadronic light-by-light (HLbL), —fourth diagram in Fig. 6.3. Regretfully, this process cannot be directly related to a measurable cross section. Being a function of the four incoming-momenta —though the external one may be set to zero for our purposes— the underlying hadronic function depends on many invariants and is much more complicated than the HVP, which depends on a single quantity. This implies that mixed regions involving low- and high-energies at the same time appear, involving both non-perturbative and perturbative

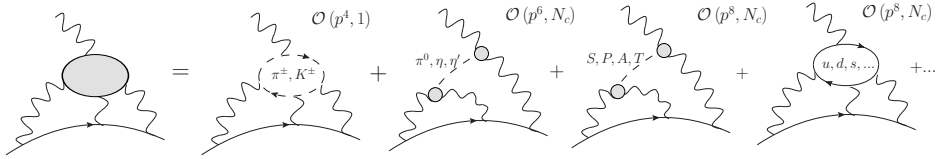


Figure 6.4: Chiral and large- N_c decomposition of the HLbL, see Ref. [298].

input.

With no data at rescue, one needs some theoretical expansion parameter. Given the size of α_s , the only perturbative parameters at hand are the chiral expansion in terms of small momenta (anticipating the impact of low energies in this quantity), and the large number of colors, N_c . This observation allowed to a first decomposition of the leading terms in Ref. [298], which are shown in Fig. 6.4. In such expansion, the leading contributions are the charged pion and kaon loops, and the pseudo-Goldstone bosons π^0 , η and η' exchanges. Numerically however, it is the latter that dominates.

Still, the diagrams in Fig. 6.4 cannot be calculated from first principles in QCD. Therefore, different approaches have been used. As an example, there exist Extended Nambu-Jona-Lasinio models, effective theories such as Hidden Gauge Symmetry, or large- N_c models where the minimum amount of resonances required to fulfill the high-energy behavior are included (see Refs. in [299]). The fact that all these approaches do not actually calculate the same quantities as shown in Fig. 6.4 and the ambiguities when including the known constraints explain the range of different results and the lack of agreement within the community. An attempt to reconcile all these approaches lead to the estimate $a_\mu^{\text{HLbL-LO}} = 105(26) \times 10^{-11}$ [299]. A more recent evaluation for this quantity appeared in Ref. [20], which most recent update [300] reads

$$a_\mu^{\text{HLbL-LO}} = 102(39) \times 10^{-11}, \quad (6.11)$$

Nevertheless, this result may neglect important theoretical uncertainties from the models. Therefore, its error should not be taken on the same foot as in the HVP case, where this is associated to the data uncertainties alone. Similarly, for the electron $a_e^{\text{HLbL-LO}} = 3.9(1.3) \times 10^{-14}$ [20]. Data-based approaches would help in solving this situation, and such is the concern of this thesis chapter. As an example, dispersive approaches have been proposed both in Mainz [301] and Bern [302, 303], though they are limited in the energy range of applicability [304]. Note at this respect that the pseudo-Goldstone boson exchanges were already calculated as an euclidean two-loop integral in Ref. [305]. In addition, there are ongoing promising proposals in the Lattice community aiming for this calculation [306–308] as well as approaches from Dyson-Schwinger equations [309]. Finally, NLO corrections

have been estimated [310],

$$a_\mu^{\text{HLbL-NLO}} = 3(2) \times 10^{-11}. \quad (6.12)$$

Putting all the pieces —Eqs. (6.4), (6.5), (6.9), (6.11) and (6.12)— together, we obtain the full SM contribution

$$a_e^{\text{th}} = 115965218.181(77) \times 10^{-11}, \quad (6.13)$$

$$a_\mu^{\text{th}} = 116591815(57) \times 10^{-11}, \quad (6.14)$$

where the errors are totally dominated from the α determination for the first, and from QCD errors for the second. Comparison to experiment gives

$$a_e^{\text{exp}} - a_e^{\text{th}} = -0.108(82) \times 10^{-11}, \quad (6.15)$$

$$a_\mu^{\text{exp}} - a_\mu^{\text{th}} = 276(85) \times 10^{-11}. \quad (6.16)$$

For the electron, there is a nice agreement between theory and experiment and the current α determination is the limiting factor when aiming for precision. By contrast, for the muon, there is a significant 3.2σ discrepancy, which suggests the possibility that NP effects are present in this quantity [20]. In order to establish whether the discrepancy is here to stay or if it is a statistical fluctuation, two experiments have been proposed at Fermilab [22] and J-PARC [23] with a precision around 16×10^{-11} for a_μ . However, this would not be significant if the theoretical uncertainty, fully dominated by the LO HVP and HLbL contributions, is not improved accordingly. Whereas the first contribution is expected to be improved with the forthcoming new data, such as those from $e^+e^- \rightarrow \pi^+\pi^-$ cross section measurements, more work is required to improve the error on the LO HLbL contribution.

It is the subject of this work to improve on the current precision of the HLbL. In particular, we focus on the dominant contribution among those depicted in Fig. 6.4: the pseudoscalar-pole, which is required at the 10% accuracy level according to future experiments. At this level of precision, one needs to carefully account for all possible source of errors, specially the systematic ones, and avoid model dependencies. This contrasts to previous determinations, for which the current experimental error did not require such standards of precision and had different concerns, such as the sign problem [305] or the full-HLbL tensor high-energy behavior [20, 311, 312]. In Section 6.3, the formalism to calculate the most general HLbL contribution is introduced. Then, we focus on the pseudoscalar pole contribution in Section 6.4, where the meaning of the former—not to be confused with alternative “off-shell” approaches—is carefully outlined. Such contribution requires a precise model-independent description for the pseudoscalar TFFs, which we implement once more through the techniques of CAs. These are

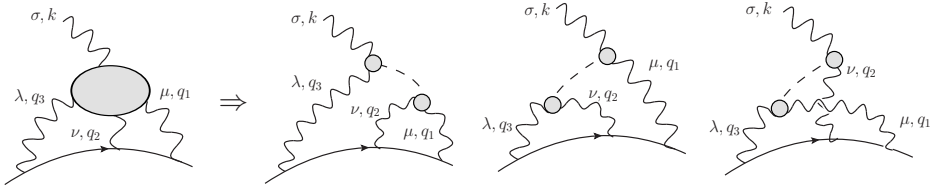


Figure 6.5: The pseudoscalar-exchange contribution to $(g - 2)$. All the momenta, except for the external photon (k), are outgoing from the TFF vertex. We take q_1, q_2, k independent, then $q_3 = (k - q_1 - q_2)$.

introduced—and their systematic error carefully discussed—and successfully employed for extracting a precise determination for the pseudoscalar pole contribution in Section 6.4.3. In Section 6.5, we outline how our description can be implemented into previous approaches. Finally, we combine our value with the additional contributions to give an estimate for the full HLbL in Section 6.6 and give the conclusions and outlook in Section 6.7.

6.3 Generic HLbL contribution to a_μ

The most general vertex describing the fermion-photon interaction

$$\langle \ell^-(p') | (ie) j^\mu(0) | \ell^-(p) \rangle \equiv -ie \bar{u}(p') \Gamma^\mu(p', p) u(p) \quad (6.17)$$

can be parametrized relying on C , P , and T invariance as [1]

$$\Gamma^\mu(p', p) = \gamma^\mu F_1(k^2) + i \frac{\sigma^{\mu\nu} k_\nu}{2m_\ell} F_2(k^2), \quad (6.18)$$

where $k = p' - p$ and $F_{1,2}(k^2)$ are the Dirac and Pauli form factors. The former is fixed by gauge-invariance at $k^2 = 0$, which via Ward-identities constrains $F_1(0) = 1$. The latter, which vanishes at tree-level, is not constrained by any symmetry. From this parametrization, it is possible to calculate the electromagnetic interactions at the classical level. A comparison to classical equations allows then to identify the gyromagnetic ratio $g_\ell = 2(F_1(0) + F_2(0)) = 2 + 2F_2(0)$ [1], thus $a_\ell = F_2(0)$, which is our object of study.

In our case of study, following Ref. [305], the HLbL diagram (left diagram

in Fig. 6.5), gives the following contribution to the electromagnetic vertex

$$\begin{aligned} -ie\Gamma_\rho(p', p) = & \int \frac{d^4 q_1}{(2\pi)^4} \int \frac{d^4 q_2}{(2\pi)^4} \frac{(-i)^3}{q_1^2 q_2^2 (k - q_1 - q_2)^2} \\ & \times \frac{i}{(p' - q_1)^2 - m_\ell^2} \frac{i}{(p' - q_1 - q_2)^2 - m_\ell^2} \\ & \times (-ie)^3 \gamma^\mu (\not{p}' - \not{q}_1 + m_\ell) \gamma^\nu (\not{p}' - \not{q}_1 - \not{q}_2 + m_\ell) \gamma^\lambda \\ & \times (ie)^4 \Pi_{\mu\nu\lambda\rho}(q_1, q_2, k - q_1 - q_2), \end{aligned} \quad (6.19)$$

where $\Pi_{\mu\nu\lambda\rho}(q_1, q_2, k - q_1 - q_2)$ denotes the HLbL tensor for light quarks $q = u, d, s$, defined in terms of the QCD Green's function

$$\begin{aligned} \Pi_{\mu\nu\lambda\rho}(q_1, q_2, q_3) = & \int d^4 x_1 \int d^4 x_2 \int d^4 x_3 e^{i(q_1 \cdot x_1 + q_2 \cdot x_2 + q_3 \cdot x_3)} \\ & \times \langle 0 | T j_\mu(x_1) j_\nu(x_2) j_\lambda(x_3) j_\rho(0) | 0 \rangle, \end{aligned} \quad (6.20)$$

in which $j_\mu = \frac{2}{3}\bar{u}\gamma_\mu u - \frac{1}{3}\bar{d}\gamma_\mu d - \frac{1}{3}\bar{s}\gamma_\mu s$ stands for the electromagnetic current and $|0\rangle$ represents the QCD vacuum. In addition, the Ward identities $\{q_1^\mu; q_2^\nu; q_3^\lambda; k^\rho\} \Pi_{\mu\nu\lambda\rho}(q_1, q_2, q_3) = 0$ allow to rewrite the HLbL tensor as³

$$\Pi_{\mu\nu\lambda\rho}(q_1, q_2, q_3) = -k^\sigma (\partial/\partial k^\rho) \Pi_{\mu\nu\lambda\sigma}(q_1, q_2, q_3). \quad (6.21)$$

Inserting this back into Eq. (6.19) results in an expression of the kind $\Gamma_\rho(p', p) = k^\sigma \int \dots (\partial/\partial k^\rho) \Pi_{\mu\nu\lambda\sigma}(q_1, q_2, q_3) \equiv k^\sigma \Gamma_{\rho\sigma}$, that allows to use the trace technique described in Ref. [305],

$$F_2(0) = \frac{1}{48m_\ell} \text{tr} ((\not{p} + m_\ell)[\gamma^\rho, \gamma^\sigma](\not{p} + m_\ell) \Gamma_{\rho\sigma}(p, p)), \quad (6.22)$$

which allows to take the limit $k \rightarrow 0$ afterwards without introducing any kinematical singularity. Then, our desired a_μ^{HLbL} contribution is given as

$$\begin{aligned} a_\mu^{\text{HLbL}} = & -ie^6 \int \frac{d^4 q_1}{(2\pi)^4} \int \frac{d^4 q_2}{(2\pi)^4} \frac{1}{q_1^2 q_2^2 (q_1 + q_2)^2} \frac{1}{(p - q_1 - q_2)^2 - m_\ell^2} \frac{1}{48m_\ell} \\ & \times \frac{1}{(p - q_1)^2 - m_\ell^2} \text{tr} \left((\not{p} + m_\ell)[\gamma^\rho, \gamma^\sigma](\not{p} + m_\ell) \gamma^\mu (\not{p} - \not{q}_1 + m_\ell) \right. \\ & \left. \gamma^\nu (\not{p} - \not{q}_1 - \not{q}_2 + m_\ell) \gamma^\lambda \right) \frac{\partial}{\partial k^\rho} \Pi_{\mu\nu\lambda\sigma}(q_1, q_2, k - q_1 - q_2) \Big|_{k \rightarrow 0}. \end{aligned} \quad (6.23)$$

At this point, an input for the HLbL tensor $\Pi_{\mu\nu\lambda\rho}(q_1, q_2, q_3)$ is required. As previously stated, the most relevant features for this quantity can be classified according to a combined chiral and large- N_c counting. In the following,

³To see this, take $0 = \partial/\partial k^\rho (k^\sigma \Pi_{\mu\nu\lambda\sigma}(q_1, q_2, q_3)) = \delta_\rho^\sigma \Pi_{\mu\nu\lambda\sigma}(q_1, q_2, q_3) + k^\sigma (\partial/\partial k^\rho) \Pi_{\mu\nu\lambda\sigma}(q_1, q_2, q_3)$, from which previous identity follows.

we extract from the HLbL tensor expression, Eq. (6.20), what has been phenomenologically found to be the dominant contribution, the pseudoscalar-pole. We stress that such a piece can be model-independently defined in contrast to other approaches [20, 311, 312] in terms of the pseudoscalar TFFs, which is essential in avoiding additional sources of systematic uncertainties. Then, we use the framework of CAs in order to describe the TFFs, providing a critical revision of systematic errors. We remark that the chiral large- N_c counting is used to identify the most relevant contributions alone —our pseudoscalar-pole description involves however no chiral, large- N_c , or any other approximation, and aspires to give a full theoretical description for this quantity, which can serve as well as an input in dispersive approaches that evaluate further contributions beyond the pseudoscalar-pole.

6.4 The pseudoscalar-pole contribution

6.4.1 The pole approximation to the HLbL

As quoted by Weinberg [313] (see chapter 10.2), “often the S -matrix for a physical process can be well approximated by the construction of a single-pole”. To understand this, we follow Weinberg and discuss the particular case of the HLbL tensor Green’s function⁴

$$\Pi^{\mu\nu\rho\sigma}(p_1, p_2, p_3, p_4) = \left(\prod_i^4 \int d^4 x_i \right) e^{ip_1 \cdot x_1} e^{ip_2 \cdot x_2} e^{-ip_3 \cdot x_3} e^{-ip_4 \cdot x_4} \times \langle 0 | T\{j^\mu(x_1)j^\nu(x_2)j^\rho(x_3)j^\sigma(x_4)\} | 0 \rangle. \quad (6.24)$$

Inserting intermediate particle states in Eq. (6.24), we obtain

$$\begin{aligned} \Pi^{\mu\nu\rho\sigma}(p_1, p_2, p_3, p_4) &= \int d^4 x_2 d^4 x_4 e^{ip_2 \cdot x_2} e^{-ip_4 \cdot x_4} \frac{i}{q^2 - m_P^2 + i\epsilon} \\ &\times \langle 0 | T\{j^\mu(0)j^\nu(x_2)\} | P(q) \rangle \langle P(q) | T\{j^\rho(0)j^\sigma(x_4)\} | 0 \rangle \\ &\times (2\pi)^4 \delta^{(4)}(p_1 + p_2 - p_3 - p_4) + \text{OT}, \end{aligned} \quad (6.25)$$

where $q = p_1 + p_2 = p_3 + p_4$, P refers to intermediate (on-shell) pseudoscalar states, in our case, $P = \pi^0, \eta$ and η' and OT refers to crossed channels (i.e. different time-orderings) and additional (multi)particle states not necessarily of pseudoscalar nature. Identifying the above matrix elements with the S -matrix for a pseudoscalar to electromagnetic current transition⁵,

$$\int d^4 x e^{iq \cdot x} \langle 0 | T\{j^\mu(x)j^\nu(0)\} | P \rangle = i \mathcal{M}_{P \rightarrow \gamma^* \gamma^*}^{\mu\nu}, \quad (6.26)$$

⁴Usually $x_4 = 0$ is taken together with four-momentum conservation. By retaining this, we explicitly obtain the momentum conservation, $(2\pi)^4 \delta^{(4)}(\sum_i p_i)$ function, in Eq. (6.24).

⁵Note that coupling then to the photons would require an additional $(ie)^2$ factor, which has actually been accounted for in Eq. (6.19).

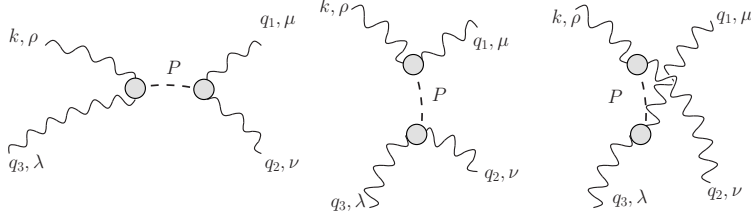


Figure 6.6: The s, t and u channel pseudoscalar-pole contribution to the HLbL tensor.

allows to express the behavior around the pseudoscalar poles for the HLbL Green's function (momentum conservation is now implied) as

$$\Pi^{\mu\nu\rho\sigma}(p_1, p_2, p_3) = i\mathcal{M}_{P \rightarrow \gamma^* \gamma^*}^{\mu\nu} \frac{i}{(p_1 + p_2)^2 - m_P^2} i\mathcal{M}_{\gamma^* \gamma^* \rightarrow P}^{\rho\sigma} + \text{crossed}. \quad (6.27)$$

Accounting for the additional crossed channels, we find what is known as the pseudoscalar-pole contribution to the HLbL tensor. For the kinematics⁶ described in Fig. 6.5 [305], this is given as

$$\begin{aligned} \Pi_{\mu\nu\lambda\rho}^{P\text{-pole}}(q_1, q_2, q_3) = & i \frac{F_{P\gamma^*\gamma^*}(q_1^2, q_2^2) F_{P\gamma^*\gamma^*}(q_3^2, k^2)}{(q_1 + q_2)^2 - m_P^2} \epsilon_{\mu\nu\alpha\beta} q_1^\alpha q_2^\beta \epsilon_{\lambda\rho\sigma\tau} q_3^\sigma k^\tau \\ & + i \frac{F_{P\gamma^*\gamma^*}(q_1^2, k^2) F_{P\gamma^*\gamma^*}(q_2^2, q_3^2)}{(q_2 + q_3)^2 - m_P^2} \epsilon_{\mu\rho\alpha\beta} q_1^\alpha k^\beta \epsilon_{\nu\lambda\sigma\tau} q_2^\sigma q_3^\tau \\ & + i \frac{F_{P\gamma^*\gamma^*}(q_1^2, q_3^2) F_{P\gamma^*\gamma^*}(k^2, q_2^2)}{(q_1 + q_3)^2 - m_P^2} \epsilon_{\mu\lambda\alpha\beta} q_1^\alpha q_3^\beta \epsilon_{\nu\rho\sigma\tau} q_2^\sigma k^\tau, \end{aligned} \quad (6.28)$$

where the different terms correspond to the s, t and u channels depicted in Fig. 6.6. The procedure outlined above allows then to extract a contribution to the HLbL tensor which is defined in terms of a physical measurable quantity, the pseudoscalar TFFs.

In the preceding discussion we have retained a particular (exclusive) contribution among all the intermediate states. At present, there is an ongoing effort to improve the charged pion loop [302, 303] contribution, which should be the most relevant multiparticle contribution to a_μ^{HLbL} ; the relevance of pQCD may be estimated, in a model-dependent way, from the OPE expansion, a discussion which we postpone to Section 6.5. Still, as we have outlined, the pseudoscalar-pole contribution is a model-independent and properly defined contribution in QFT, associated to an isolated pole in the S matrix, which we proceed to discuss.

⁶Remember that the vector currents are defined to have $q_1, q_2, q_3, -k$ outgoing momenta ($k = q_1 + q_2 + q_3$).

6.4.2 Master formula and main properties

In this section, we provide the calculation details following Refs. [20, 305]. Moreover, we discuss the relevant kinematical regions of the integral in view of the obtained kernel functions. Plugging the pole-contribution, Eq. (6.28), into the master formula Eq. (6.23), one obtains the result, see Ref. [305]

$$a_\mu^{\text{HLbL};P} = -e^6 \int \frac{d^4 q_1}{(2\pi)^4} \frac{d^4 q_2}{(2\pi)^4} \frac{1}{q_1^2 q_2^2 (q_1 + q_2)^2 [(p + q_1)^2 - m_\ell^2][(p - q_2)^2 - m_\ell^2]} \left[\frac{F_{P\gamma^*\gamma^*}(q_1^2, (q_1 + q_2)^2) F_{P\gamma^*\gamma^*}(q_2^2, 0)}{q_2^2 - m_\pi^2} T_1(q_1, q_2; p) + \frac{F_{P\gamma^*\gamma^*}(q_1^2, q_2^2) F_{P\gamma^*\gamma^*}((q_1 + q_2)^2, 0)}{(q_1 + q_2)^2 - m_\pi^2} T_2(q_1, q_2; p) \right], \quad (6.29)$$

where

$$T_1(q_1, q_2; p) = \frac{16}{3}(p \cdot q_1)(p \cdot q_2)(q_1 \cdot q_2) - \frac{16}{3}(p \cdot q_2)^2 q_1^2 - \frac{8}{3}(p \cdot q_1)(q_1 \cdot q_2)q_2^2 + 8(p \cdot q_2)q_1^2 q_2^2 - \frac{16}{3}(p \cdot q_2)(q_1 \cdot q_2)^2 + \frac{16}{3}m_\ell^2 q_1^2 q_2^2 - \frac{16}{3}m_\ell^2 (q_1 \cdot q_2)^2, \quad (6.30)$$

$$T_2(q_1, q_2; p) = \frac{16}{3}(p \cdot q_1)(p \cdot q_2)(q_1 \cdot q_2) - \frac{16}{3}(p \cdot q_1)^2 q_2^2 + \frac{8}{3}(p \cdot q_1)(q_1 \cdot q_2)q_2^2 + \frac{8}{3}(p \cdot q_1)q_1^2 q_2^2 + \frac{8}{3}m_\ell^2 q_1^2 q_2^2 - \frac{8}{3}m_\ell^2 (q_1 \cdot q_2)^2. \quad (6.31)$$

In deriving Eqs. (6.29) to (6.31), the change of variables $q_2 \rightarrow q_2 - q_1$, then $q_1 \rightarrow -q_1$ has been used. The second and third graphs in Fig. 6.5 give the same contribution proportional to $T_1(q_1, q_2; p)$, whereas the fourth diagram in Fig. 6.5 provides the term proportional to $T_2(q_1, q_2; p)$. In the last, the symmetry property $q_1 \leftrightarrow -q_2$ has been used. To further simplify the integral Eq. (6.29), we use the Wick rotation and employ the techniques of Gegenbauer polynomials [20, 305]. Following the approach in Ref. [20],

$$a_\ell^{\text{HLbL};P} = \frac{-2\pi}{3} \left(\frac{\alpha}{\pi} \right)^3 \int_0^\infty dQ_1 dQ_2 \int_{-1}^{+1} dt \sqrt{1 - t^2} Q_1^3 Q_2^3 \times \left[\frac{F_1 I_1(Q_1, Q_2, t)}{Q_2^2 + m_P^2} + \frac{F_2 I_2(Q_1, Q_2, t)}{Q_3^2 + m_P^2} \right], \quad (6.32)$$

where $Q_3^2 = Q_1^2 + Q_2^2 + 2Q_1 Q_2 t$ and

$$F_1 = F_{P\gamma^*\gamma^*}(Q_1^2, Q_3^2) F_{P\gamma^*\gamma^*}(Q_2^2, 0), \quad (6.33)$$

$$F_2 = F_{P\gamma^*\gamma^*}(Q_1^2, Q_2^2) F_{P\gamma^*\gamma^*}(Q_3^2, 0), \quad (6.34)$$

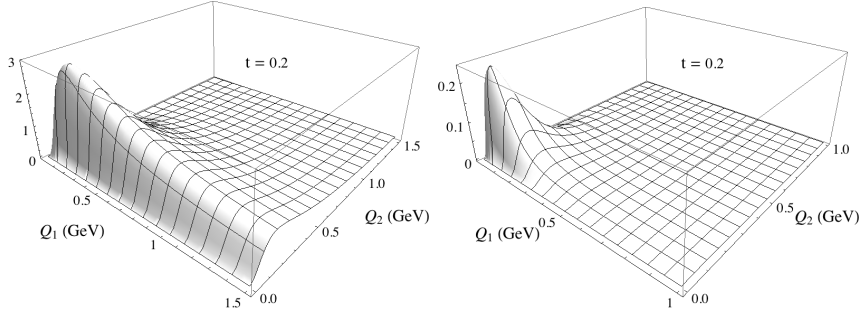


Figure 6.7: Integrands in Eq. (6.32) for $P = \pi^0$ and a constant TFF and $t = 0.2$ (we omit the overall $(\alpha/\pi)^3$ factor). Left and right stand for the first ($\sim F_1$) and second ($\sim F_2$) terms in the integrand in Eq. (6.32), respectively.

and

$$I_1(Q_1, Q_2, t) = \frac{1}{m_\ell^2 Q_3^2} \left[-\frac{4m_\ell^2 t}{Q_1 Q_2} - (1 - R_{m_1}) \left(\frac{2Q_1 t}{Q_2} - 4(1 - t^2) \right) + (1 - R_{m_1})^2 \frac{Q_1 t}{Q_2} + 8X(Q_1, Q_2, t) (Q_2^2 - 2m_\ell^2)(1 - t^2) \right], \quad (6.35)$$

$$I_2(Q_1, Q_2, t) = \frac{1}{m_\ell^2 Q_3^2} \left[-2(1 - R_{m_1}) \left(\frac{Q_1 t}{Q_2} + 1 \right) - 2(1 - R_{m_2}) \left(\frac{Q_2 t}{Q_1} + 1 \right) - 4X(Q_1, Q_2, t) (Q_3^2 + 2m_\ell^2(1 - t^2)) \right]. \quad (6.36)$$

In the last term, the $Q_1 \leftrightarrow -Q_2$ invariance has been used again to make $I_2(Q_1, Q_2, t)$ symmetric. The above expressions employ the functions arising from angular integration,

$$X(Q_1, Q_2, t) = \frac{1}{Q_1 Q_2 \sqrt{1 - t^2}} \arctan \left(\frac{z \sqrt{1 - t^2}}{1 - zt} \right), \quad (6.37)$$

$$z = \frac{Q_1 Q_2}{4m_\ell^2} (1 - R_{m_1})(1 - R_{m_2}), \quad (6.38)$$

$$R_{m_i} = \sqrt{1 + 4m_\ell^2/Q_i^2}. \quad (6.39)$$

Having defined all the required equations, it is interesting before embarking on the TFF description and performing the numerical calculation, to discuss the main aspects of the integrand in Eq. (6.32) and study the main features which are required in order to provide a very precise estimation of this quantity —for a thorough study see Ref. [314]. First we plot, up to an overall $(\alpha/\pi)^3$ factor, the two terms in Eq. (6.32) for $P = \pi^0$ and a constant TFF in Fig. 6.7. For plotting, we choose $t = 0.2$, though a similar shape appears for different t values. As one can see, both integrands peak at very low-energies and the first one features a non-negligible tail extending up

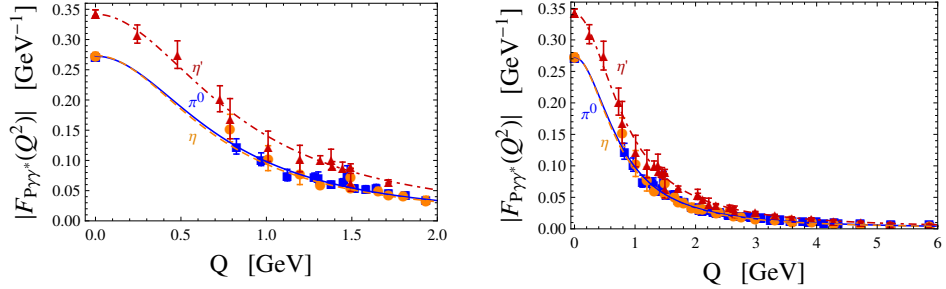


Figure 6.8: The single virtual π^0 , η and η' TFF description from PAs from Chapter 2 as blue, dashed orange and red dash-dotted lines, together with the available space-like data at low-energies from CELLO [107], CLEO [108], L3 [105] and the normalization extracted from [10] in blue squares, orange circles and red triangles for the π^0 , η and η' , respectively.

to moderate energies. From this observation it is clear that any approach aiming for a precise determination must provide an extremely precise description for the TFF below 1 GeV [315]. Unfortunately, there is no data available in this region for the single virtual TFF, see Fig. 6.8 —there is the notorious exception of the η' data from L3, which however has never been included in previous analyses. In practice, this means that previous calculations have required a model for the TFF together with an extrapolation down to $Q^2 \sim 0$. The error that such extrapolation may induce was a systematic source of error not accounted for. However, a precise low-energy description—which in principle would be provided from χ PT—is not enough. At high energies, the mentioned tail for the first integral cannot be neglected; the behavior of such is given (after angular t integration) for large Q_1 in Eq. (6.40), for large Q_2 in Eq. (6.41) and for large $Q_1 = Q_2 \equiv Q$ in Eq. (6.40) below [305, 314]

$$\frac{8\pi^2 Q_2^3 (1-t^2)^{3/2}}{3m_\mu^2(m_P^2+Q_2^2)} \frac{1}{Q_1} (R_{m_2}(2m_\mu^2 - Q_2^2) + Q_2^2) + \mathcal{O}(Q_1^{-2}), \quad (6.40)$$

$$\frac{8\pi Q_1^2 t (1-t^2)^{3/2}}{3m_\mu^2 Q_2^2} (Q_1^2(R_{m_1} - 1) - 2m_\mu^2) + \mathcal{O}(Q_2^{-3}), \quad (6.41)$$

$$\frac{8\pi m_\mu^2 \sqrt{1-t^2} (3-t)(1-t)}{3Q^2} + \mathcal{O}(Q^{-4}). \quad (6.42)$$

As one can see, the resulting integral diverges for a constant TFF. Consequently, any parametrization for the TFF must incorporate, beyond a precise TFF description at low-energies, the appropriate high-energy behavior which is necessary to render the integral finite. On turn, the second (subleading) term falls much faster. Its high-energy behavior is given for large $Q_{1,2}$ values in Eq. (6.43) and for large $Q_1 = Q_2 \equiv Q$ in Eq. (6.44)

below [305, 314]

$$\frac{8\pi Q_{2,1}^3(1-t^2)^{3/2}}{9m_\mu^2 Q_{1,2}^3} \left((R_{m_{2,1}} - 1)(m_\mu^2 + Q_{2,1}^2) - 2m_\mu^2 \right) + \mathcal{O}(Q_{1,2}^{-4}), \quad (6.43)$$

$$\frac{4m_\mu^4 \pi (1-t)^{3/2} (2-t)}{9\sqrt{1+t} Q^4}. \quad (6.44)$$

From the equations above, it can be observed that such an integral yields a finite result even for a constant TFF.

6.4.3 A rational description for $F_{P\gamma^*\gamma^*}(Q_1^2, Q_2^2)$

In the previous subsection, we found that any description for $F_{P\gamma^*\gamma^*}(Q_1^2, Q_2^2)$ aiming to obtain a precise determination for the pseudoscalar-pole contribution $a_\mu^{\text{HLbL};P}$ requires:

- A full-energy description in the whole space-like region; the time-like features do not directly play a role in this calculation, as one has performed a Wick rotation to Euclidean space.
- An extremely precise description at energies below 1 GeV, with special emphasis on the region $Q^2 \sim 0$.
- An appropriate high-energy behavior providing a convergent integral. Actually, given the non-negligible tail from the integrand, implementing the correct Q^2 power-like behavior becomes relevant.

This means that any phenomenological approach should:

- Reproduce the available data in the space-like region. In addition, having a finite-data set, the approach should guarantee that the extrapolation down to $Q^2 = 0$ and $Q^2 = \infty$ converges to the original function; in this sense, the method should provide an error estimation for the extrapolation procedure.
- Have the ability to be systematically improved to meet the eventual required precision.

For the moment, we can distinguish three different approaches calculating the pseudoscalar-pole contribution. First, there are those which provide a theoretical model for the TFF [316, 317]. These may entail large systematic uncertainties inherent to the models, which do not correspond to the full QCD theory and are hard to estimate. Second, there are those phenomenological data-based parametrizations, typically inspired on large- N_c and VMD ideas, see for instance [100, 305, 318]. Whereas these kind of models may reproduce the fitted data, it is unclear how precise their extrapolations to $Q^2 = 0$ and $Q^2 = \infty$ are and their associated errors —the reason

for which very precise low-energy data is highly desired in these approaches. In addition, strictly speaking, they should include the whole family of vector resonances; their truncation, arbitrary choice of resonances, the connection among the required large- N_c inputs with the real world, and the unavoidable large- N_c corrections must play a role, of which the systematic error is missing and hard to account for. Finally, we find the (recently proposed) dispersive reconstruction of the TFFs [302, 303]. Whereas this approach would provide in principle an exact numerical calculation, in the real world some approximations must be taken. As an example, only the lowest-lying thresholds are employed and the dispersive integrals must be cut at some value. A serious disadvantage arising from this feature is the inability to extend up to arbitrary large Q^2 values. Estimating the (Q^2 -dependent) systematic error and eventually improving their result—if the available experimental data eventually requires it—is a weakness of the method, while they may profit from a large amount of time-like data as compared to other approaches.

To amend for these shortcomings and determine this calculation to the required precision nowadays—which is beyond the reach of previous studies—we propose to use a rational approach description based on Canterbury approximants. As we have seen, our approach provides a corpus to extract and implement not only the relevant low-energy behavior but the high-energy one as well from a data-based procedure. The uniqueness of the method resides in the convergence checks and provides a tool to safely extrapolate to the regions where no data is available. On top, its sequential implementation allows to account for a systematic error in an easy way. Given the available limited information—specially on the doubly-virtual TFF—we restrict our studies to the $C_1^0(Q_1^2, Q_2^2)$ and $C_2^1(Q_1^2, Q_2^2)$ elements of the $C_{N+1}^N(Q_1^2, Q_2^2)$ sequence; different sequences turn out not to obey the high-energy behavior, for which they are not considered.

The first element: $C_1^0(Q_1^2, Q_2^2)$

Given the low-energy expansion for the TFF

$$F_{P\gamma^*\gamma^*}(Q_1^2, Q_2^2) = F_{P\gamma\gamma}(1 - \frac{b_P(Q_1^2 + Q_2^2)}{m_P^2} + \frac{a_{P;1,1}Q_1^2Q_2^2}{m_P^4} + \frac{c_P(Q_1^4 + Q_2^4)}{m_P^4} + \dots), \quad (6.45)$$

the lowest CA we can construct in terms of its low-energy parameters defined above is given as

$$C_1^0(Q_1^2, Q_2^2) = \frac{F_{P\gamma\gamma}}{1 + \frac{b_P}{m_P^2}(Q_1^2 + Q_2^2) + \frac{2b_P^2 - a_{P;1,1}}{m_P^4}Q_1^2Q_2^2}. \quad (6.46)$$

All the necessary single-virtual parameters— $F_{P\gamma\gamma}$ and b_P —have been determined so far in Chapter 2 and summarized Table 2.14. It remains however

the determination for the double-virtual parameter $a_{P;1,1}$. Even if this is not available at the moment, the possibility of having access to the doubly-virtual TFF in the near future would allow for such an extraction (efforts are being made in BESIII). Still, for the moment, we are compelled to judge on a theoretical reasonable estimate. On one side, given the low-energy dominance of the process we are looking for, we may find guidance in χ PT. From the work in Ref. [91], it seems that χ PT favors a factorized behavior, namely, that $F_{P\gamma^*\gamma^*}(Q_1^2, Q_2^2) \sim F_{P\gamma^*\gamma}(Q_1^2)F_{P\gamma^*\gamma}(Q_2^2)$, implying $a_{P;1,1} = b_P^2$. Actually, such behavior was obtained as well for the η case in a dispersive analysis [96]. On the other side, we may find help from the high energies, where the two point approximant with the OPE behavior (see Eq. (1.50)) built-in⁷ implies, as a first approximation, that $a_{P;1,1} = 2b_P^2$ —moreover, this upper value avoids for poles in the SL region. This suggests that the high-energy corrections should drive the value which is obtained from the low-energies in some region in between $b_P^2 \leq a_{P;1,1} \leq 2b_P^2$. Then, we will take this range as a theoretical estimate where the real value —to be determined from data— is likely to be found. Of course, experimental data will have the last word on this choice.

Second element: $C_2^1(Q_1^2, Q_2^2)$

The next CA within the chosen sequence is parametrically given as

$$C_2^1(Q_1^2, Q_2^2) = \frac{F_{P\gamma\gamma}(1+\alpha_1(Q_1^2+Q_2^2)+\alpha_{1,1}Q_1^2Q_2^2)}{1+\beta_1(Q_1^2+Q_2^2)+\beta_2(Q_1^4+Q_2^4)+\beta_{1,1}Q_1^2Q_2^2+\beta_{2,1}Q_1^2Q_2^2(Q_1^2+Q_2^2)+\beta_{2,2}Q_1^4Q_2^4}. \quad (6.47)$$

The single virtual parameters can be related to the low-energy expansion of the TFF, see Eq. (2.1), as

$$\alpha_1 = \frac{-b_P^3 + 2b_P c_P - d_P}{m_P^2(b_P^2 - c_P)}, \beta_1 = \frac{b_P c_P - d_P}{m_P^2(b_P^2 - c_P)}, \beta_2 = \frac{c_P^2 - b_P d_P}{m_P^4(b_P^2 - c_P)}. \quad (6.48)$$

Alternatively, we could have employed a combined low- and high-energy expansion (see Section 1.5.2) which enforces the BL behavior ($F_{P\gamma^*\gamma}(Q^2) \sim P_\infty Q^{-2}$). Sacrificing d_P in favor of P_∞ , we would obtain

$$\alpha_1 = \frac{P_\infty(b_P^2 - c_P)}{F_{P\gamma\gamma} - b_P P_\infty}, \beta_1 = \frac{b_P F_{P\gamma\gamma} - c_P P_\infty}{F_{P\gamma\gamma} - b_P P_\infty}, \beta_2 = \frac{F_{P\gamma\gamma}(b_P^2 - c_P)}{F_{P\gamma\gamma} - b_P P_\infty}. \quad (6.49)$$

The additional $\alpha_{i,j}$ and $\beta_{i,j}$ parameters are connected to the double virtual series expansion, see Chapter 3. Given our lack of experimental or theoretical information for the doubly-virtual TFF, it is hard to express them in terms of the low-energy expansion. As a first start, we proceed analogous to the previous section and fix the value from $\beta_{1,1}$ from the low-energy parameter $a_{P;1,1}$, which leads to the constraint

$$\beta_{1,1} = -a_{P;1,1} + \alpha_{1,1} - 2\alpha_1\beta_1 + 2\beta_1^2 \quad (6.50)$$

⁷With the OPE behavior we mean that $F_{P\gamma^*\gamma^*}(Q^2, Q^2)$ behaves as Q^{-2} as $Q^2 \rightarrow \infty$.

To fix the additional remaining parameters we are doomed to use some high-energy constraints, even though this may come at cost of the low-energy description. Nicely, the OPE behavior allows to set $\beta_{2,2} = 0$. Moreover, if we do not only fix the power-like behavior as for the $C_1^0(Q_1^2, Q_2^2)$ case, but constrain its leading coefficient from Eq. (1.50), we find

$$\alpha_{1,1} = (2/3)\beta_{2,1}P_\infty/F_{P\gamma\gamma}, \quad (6.51)$$

where P_∞ is the BL TFF asymptotic behavior. For the π^0 , $\pi_\infty^0 = 2F_\pi$, whereas for the η and η' this depends on the mixing parameters and was determined in Chapter 2. Still, there is an additional undetermined parameter, $\beta_{2,1}$. Therefore, we make use of the higher order terms in the OPE expansion, which for the π^0 reads [20, 69]

$$F_{\pi\gamma^*\gamma^*}(Q^2, Q^2) = (2/3)F_\pi \left(\frac{1}{Q^2} - \frac{8}{9} \frac{\delta^2}{Q^4} + \dots \right). \quad (6.52)$$

The δ parameter has been estimated using sum rules, obtaining $\delta^2 = 0.20(2)$ [20, 69]. To extend this value to the η and η' cases, we replace $2F_\pi \rightarrow \eta_\infty^{(\prime)}$ and apply an additional 30% uncertainty due to $SU(3)_F$ breaking and large- N_c corrections (note that this is enough for all the low- and high-energy parameters analyzed so far). This provides the remaining constraint

$$\beta_{2,1} = \frac{9F_{P\gamma\gamma}(a_{1,PP}P_\infty + 2\alpha_1(3F_{P\gamma\gamma} + P_\infty\beta_1) - 2P_\infty(\beta_1^2 + \beta_2))}{2P_\infty(3P_\infty - 8F_{P\gamma\gamma}\delta^2)}. \quad (6.53)$$

Finally, we could employ our previous estimation $b_P^2 \leq a_{P;1,1} \leq 2b_P^2$. However, the appearance of poles for certain $a_{P;1,1}$ values restrict the chosen range. To see this, take $a_{P;1,1} = \lambda b_P^2$ and the phenomenological observation that $c_p \sim b_P^2$ and $d_P \sim b_P^3$; avoiding the appearance of poles requires then

$$\frac{9(-3b_P F_{P\gamma\gamma}^2 + b_P^2 F_{P\gamma\gamma} P_\infty \lambda)}{2P_\infty(3P_\infty - 8F_{P\gamma\gamma}\delta^2)} + \mathcal{O}(\epsilon) > 0 \longrightarrow \lambda > \frac{3F_{P\gamma\gamma}}{b_P P_\infty} + \mathcal{O}(\epsilon), \quad (6.54)$$

where we used that, phenomenologically, $(3P_\infty - 8F_{P\gamma\gamma}\delta^2) > 0$. It turns out that $\lambda \sim 2$ in our cases, supporting our assumption that high-energy QCD properties should drive up the factorization value closer to the OPE choice, $a_{P;1,1} = 2b_P^2$ and naturally providing an $a_{P;1,1}$ lower bound. In addition, from Padé theory, it is not expected to find complex-conjugated poles⁸ in the SL region; this provides in practice an upper bound for $a_{P;1,1}$ above $2b_P^2$ and a (more generous) band for $a_{P;1,1}$ solely based in Padé theory criteria.

⁸The PA reality condition forces the approximant to have either real or pair of complex-conjugated poles.

Systematic errors

Before we present our final results, it is necessary to set up some procedure allowing to determine the systematic error to be associated to a certain element within our chosen C_{N+1}^N sequence. Actually, given the length of our sequence, consisting of two elements alone, it is extremely important to check on the expected convergence. For this purpose, we come back again to two models which have been widely-employed along this work. These are the Regge [97, 110] and the proposed doubly-virtual logarithmic models defined in Section 3.3,

$$F_{P\gamma^*\gamma^*}^{\text{Regge}}(Q_1^2, Q_2^2) = \frac{a F_{P\gamma\gamma}}{Q_1^2 - Q_2^2} \frac{\left[\psi^{(0)}\left(\frac{M^2+Q_1^2}{a}\right) - \psi^{(0)}\left(\frac{M^2+Q_2^2}{a}\right) \right]}{\psi^{(1)}\left(\frac{M^2}{a}\right)}, \quad (6.55)$$

$$F_{P\gamma^*\gamma^*}^{\log}(Q_1^2, Q_2^2) = \frac{F_{P\gamma\gamma} M^2}{Q_1^2 - Q_2^2} \ln\left(\frac{1 + Q_1^2/M^2}{1 + Q_2^2/M^2}\right). \quad (6.56)$$

Recall that such models incorporate a well-defined high-energy behavior for the doubly-virtual TFF, whereas the single-virtual one behave as $\ln(Q^2)Q^{-2}$, not fulfilling the BL behavior, but convergent enough in order to perform the integral Eq. (6.32). The relevance of these models is that an infinite sequence of CAs is required to describe the underlying function, which makes them an ideal laboratory to test convergence properties.

To test the performance of our approximants, we calculate the HLbL contribution, Eq. (6.32), for the specific (dominant) case of the π^0 . We show our results together with the exact outcome from the model in Table 6.1. To test the accuracy of different assumptions, we show the result from different strategies: matching all the doubly-virtual low-energy parameters (LE), setting the OPE Q^{-2} power-like behavior as well as including its leading c/Q^2 coefficient⁹ and, finally, using a factorized form (Fact), which has been a common approach. We find that, whereas the factorization result does not converge to the model value —a feature to be expected as the original models do not factorize— the LE approach approximates the exact value even if the proper doubly-virtual high-energy behavior is not built-in. This requires however the use of a large sequence and may not be the best choice in our case. Certainly, any of the OPE choices seems to provide the best convergence pattern, which can be understood as the OPE becomes relevant already at a low scale; still, the first element could involve a large systematic error. Finally, we observe that the difference among the C_{N+1}^N and C_N^{N-1} elements is enough to give the size of the systematic error. Summarizing, we

⁹Note that, for the logarithmic model Eq. (6.56), the C_{N+1}^N approximants with the OPE behavior built-in already reproduce the whole $Q_1^2 = Q_2^2$ regime, see Eq. (3.17), so the entries OPE: Q^{-2} and OPE: c/Q^2 in Table 6.1 are equivalent.

	Regge model				Logarithmic model			
	C_1^0	C_2^1	C_3^2	C_4^3	C_1^0	C_2^1	C_3^2	C_4^3
LE	66.0	71.9	72.8	73.1	87.9	97.6	99.7	100.5
OPE: $\sim Q^{-2}$	77.4	73.4	73.3	73.3	99.5	101.2	101.4	101.5
OPE: c/Q^2	-	73.1	73.3	73.3				
Fact	65.1	68.8	69.0	69.1	85.2	92.4	93.6	94.0
Fit ^{OPE}	80.2	75.1	73.7	73.4	113.1	104.0	102.2	101.8
Exact	73.3				101.5			

Table 6.1: Result for $a_\mu^{\text{HLbL};\pi}$, Eq. (6.32), for different approximants compared to the exact result. The first columns stand for the Regge model, whereas the last four columns stand for the logarithmic one. See details in the text.

conclude from this study that CAs provide a reliable systematic approach to perform the desired calculation, which systematic error estimation can be accounted for from the difference of a given element with the previous one and convergence rate is improved when implementing the OPE even if this is not necessary. In our discussion above, it cannot be overemphasized the relevance of having employed the low-energy TFF expansion in Eq. (6.45) when reconstructing the approximants—as the framework requires—rather than fitting the rational functions to data themselves. As an illustration, we show in the Fit^{OPE} row of Table 6.1 what would have been obtained if fitting the $C_{N+1}^N(Q_1^2, Q_2^2)$ rational functions, with the OPE power-like behavior implemented, to a 16×16 grid of equally-spaced double-virtual data ranging from $0 \leq Q_{1,2}^2 \leq 35 \text{ GeV}^2$. The convergence obtained is slower, and illustrates the difference and the power of CAs with respect to standard fitting approaches—we stress in addition that, in these fits, no assumption of factorization either in numerator or denominator has been employed, which differs from traditional rational approaches, for which we foresee a yet slower convergence.

6.4.4 Results for the pseudoscalar-pole contribution

Having discussed the construction of the approximants and the associated systematic errors, we are in the position to give our final results for the pseudoscalar-pole contribution to a_μ^{HLbL} . For this, we take our results from Table 2.14 for $F_{P\gamma\gamma}, b_P, c_P, d_P$ and P_∞ , which are required for reconstructing the CAs. The pseudoscalar and lepton masses are taken from [10]. For the η and η' cases, we reconstruct the single-virtual parameters using the low-energy constraints, see Eq. (6.48). For the π^0 case, there is no reliable extraction for the d_π parameter so far. Consequently, we use the BL behavior in order to determine the $C_2^1(Q_1^2, Q_2^2)$ approximant single-virtual parameters, cf. Eq. (6.49).

$a_\mu^{\text{HLbL};P}$	Fact ($a_{P;1,1} = b_P^2$)	OPE ($a_{P;1,1} = 2b_P^2$)
π^0	$54.0(1.1)_F(2.5)_{b_\pi}[2.7]_t$	$64.9(1.4)_F(2.8)_{b_\pi}[3.1]_t$
η	$13.0(0.4)_F(0.4)_{b_\eta}[0.6]_t$	$17.0(0.6)_F(0.4)_{b_\eta}[0.7]_t$
η'	$12.0(0.4)_F(0.3)_{b_{\eta'}}[0.5]_t$	$16.0(0.5)_F(0.3)_{b_{\eta'}}[0.6]_t$
Total	$79.0[2.8]_t$	$97.9[3.2]_t$

Table 6.2: Result for $a_\mu^{\text{HLbL};P}$, Eq. (6.32), for the C_1^0 approximants for different $a_{P;1,1}$ values in units of 10^{-11} . See description in the text.

$a_\mu^{\text{HLbL};P}$	$a_{P;1,1}^{\min}$	$a_{P;1,1}^{\max}$
π^0	$63.9(1.3)_L(0)_\delta[1.3]_t$	$62.9(1.2)_L(0.3)_\delta[1.2]_t$
η	$16.6(0.8)_L(0)_\delta[1.0]_t$	$16.2(0.8)_L(0.5)_\delta[0.9]_t$
η'	$14.7(0.7)_L(0)_\delta[0.7]_t$	$14.3(0.5)_L(0.5)_\delta[0.7]_t$
Total	$95.2[1.7]_t$	$93.4[1.7]_t$

Table 6.3: Result for $a_\mu^{\text{HLbL};P}$, Eq. (6.32), for the $C_2^1(Q_1^2, Q_2^2)$ approximants for different $a_{P;1,1}$ values in units of 10^{-11} . See description in the text.

We show the results from the $C_1^0(Q_1^2, Q_2^2)$ approximant for the different pseudoscalars in Table 6.2 [315]. There, we display the results for the double-virtual parameter $b_P^2 \leq a_{P;1,1} \leq 2b_P^2$, labelled as Fact and OPE, respectively. The errors are separated into those arising from the TFF normalization, $(\cdot)_F$ and those coming from the slope, $(\cdot)_{b_P}$ and are symmetrized. The total error, $[\cdot]_t$, is the combination in quadrature of both of them. The sum of the π^0 , η and η' contributions from our $C_1^0(Q_1^2, Q_2^2)$ approximant considering our $a_{P;1,1}$ range and adding errors in quadrature reads

$$a_\mu^{\text{HLbL};P;C_1^0} = (79.0 \div 97.9)(3.2) \times 10^{-11}. \quad (6.57)$$

For the $C_2^1(Q_1^2, Q_2^2)$ approximation, we estimate our results for the chosen $a_{P;1,1}$ range in which no space-like poles appear, $a_{P;1,1}^{\min} \leq a_{P;1,1} \leq a_{P;1,1}^{\max}$, as previously explained¹⁰. For the OPE parameter δ , see Eq. (6.52), we take $\delta^2 = 0.20(2)$ from Refs. [20, 69], and apply the mentioned 30% correction to the η and η' to account for the symmetry breaking effects. Again, we decompose the different sources of errors into the single-virtual terms, $(\cdot)_L$, the uncertainty on δ , $(\cdot)_\delta$, and add them in quadrature to obtain the total error, which is given as $[\cdot]_t$ and symmetrized. The numerical values are given in Table 6.3. The sum of the different pseudoscalars $C_2^1(Q_1^2, Q_2^2)$ results for the given band reads

$$a_\mu^{\text{HLbL};P;C_2^1} = (93.4 \div 95.2)(1.7) \times 10^{-11}. \quad (6.58)$$

¹⁰This leads, for the minimum, $a_{\pi;1,1}^{\min} = 1.92b_\pi^2$, $a_{\eta;1,1}^{\min} = 1.84b_\eta^2$ and $a_{\eta';1,1}^{\min} = 1.32b_{\eta'}^2$, whereas for the maximum $a_{\pi;1,1}^{\max} = 2.07b_\pi^2$, $a_{\eta;1,1}^{\max} = 2.33b_\eta^2$ and $a_{\eta';1,1}^{\max} = 3.41b_{\eta'}^2$.

Comparing with the OPE result from the previous element in Eq. (6.57), $97.9(3.2) \times 10^{-11}$, we obtain the systematic error, leading to the final result for the π^0 , η and η' pseudoscalar-pole contributions to the HLbL

$$a_\mu^{\text{HLbL};P} = (93.4 \div 95.2)(1.7)_{\text{stat}}(4.5)_{\text{sys}}[4.8]_t \times 10^{-11}, \quad (6.59)$$

where the first error includes both statistic and systematic errors from the CA reconstruction, the second one is the systematic error associated with the C_2^1 element, and the last one is a combination in quadrature of the formers and is dominated by systematics. Our result may be compared to that in Ref. [305], $a_\mu^{\text{HLbL};P} = (58(10) + 13(1) + 12(1) = 83(12)) \times 10^{-11}$, and the more recent result from Ref. [100], $a_\mu^{\text{HLbL};P} = (57.5(6) + 14.4(2.6) + 10.8(0.9) = 82.7(2.8)) \times 10^{-11}$ —note that the latter does not use any data to parameterize the η and η' TFFs beyond the information which is included in the mixing parameters and represents a major drawback at the required precision. Our approach represents a clear improvement over previous estimates since

- It is the only one making full use of data for the η and η' , which must be carefully described given the required 10% precision. As an example, Ref. [305] did use the CLEO slope [108] only, whereas Ref. [100] did not directly use any data, but a prediction from their framework based on the π^0 TFF, suffering from (unaccounted) $SU(3)_F$ -breaking and large- N_c corrections. Both of these approaches *cannot* reproduce the experimental data accounted for in our approach, which reflects a relevant systematic source of error. Furthermore, it is the only one which is fully-data driven.
- It incorporates the appropriate low-energy behavior encoded in the low-energy parameters (which previous approaches cannot guarantee and is crucial for this calculation) together with the high energies. This comes out naturally by construction in our framework. Note that incorporating the high-energy behavior for the η and η' mesons is required at the desired 10% precision, as it can be observed when comparing the two columns in Table 6.2, which contrasts with the —commonly employed— factorization approached.
- Finally, we are the first to provide a systematic error, which is by no means negligible. If the approaches in Refs. [100, 305] were reconstructed in the spirit of Padé type approximants, see Sections 1.5.2 and 3.3.3, one would expect a systematic error larger than our.

Last, we comment on the error sources. We find that the statistical error in each channel is similar regarding the single-virtual parameters, the δ parameter and our ignorance on the $a_{P;1,1}$ parameter, which are required to improve if a better precision is desired. A first measurement of the double

virtuality would drastically improve on the $a_{P;1,1}$ -induced error and would represent an important milestone. Such measurements would be possible in the future, at least for the π^0 , at BESIII [149]. Actually, this would possibly allow to trade δ for a low-energy parameter, which would be very interesting. To improve the single-virtual parameters errors for the π^0 would require, looking at Tables 6.2 and 6.3, an improved determination for the b_π , c_π and —given the relevance of the low energies— to eventually employ d_π instead of the asymptotic value. This would be possible with new low-energy data which are expected in the near future from the BESIII [149] experiment in the SL region, and from the NA62 [150] and A2 [148] collaborations in the low-energy TL region. In addition, it is expected that further low-energy SL data in the $(0.01 - 0.4)$ GeV² range would be provided by the KLOE-2 [151] and *GlueX* [152] collaborations. For the η and η' , this would require new precise measurements from their two-photons decays, which would be possible at the *GlueX* experiment [145]. Regarding the systematic error, we find that this is similar to the statistical one for the π^0 and η cases and larger for the η' , which points out the relevance of the high-energies for the latter due to its mass. In this respect, it would be very interesting to have precise high-energy data for the η' , which would be possible in Belle II experiment. Still, to pin down the systematic errors would be possible only if higher approximants could be constructed, demanding the determination of additional parameters, where double-virtual measurements cannot be avoided. Actually, it is the systematic error which dominates the final number as this source is taken to be fully correlated among the pseudoscalars. This is natural to expect if one assumes a similar convergence pattern for the different channels.

6.4.5 Cross-checks I: The light-quark transition form factor

Given the precision we are aiming for in our calculation, every possible cross-check poses a valuable result, which is specially important for the dominant π^0 contribution. Actually, much has been discussed given the differences between *BABAR* [76] and *Belle* [133] results regarding the π^0 TFF. We note in this respect that the disagreement¹¹ arises mainly from the region at $(8 - 13)$ GeV²¹²; it was checked in Ref. [111] that still, removing either *Belle* or *BABAR* from the data sets produced compatible results for the LEPs extraction, clearing up any possible inconsistency or additional errors. Nevertheless, given such disagreement at intermediate energies, a second test would be welcome. In this respect, we mentioned in Section 4.5.3 that, to a reasonable accuracy and up to an overall charge factor, the light quark and the π^0 TFFs should be very similar (see Fig. 4.3 at this respect). This offers

¹¹Actually, the global difference is not statistically significant —around 0.8σ .

¹²The apparent rising from *BABAR* data at high-energies is much less important and we checked this to be irrelevant for $(g_\mu - 2)$ —see Ref. [319] as well.

$a_\mu^{\text{HLbL};P}$	Fact ($a_{P;1,1} = b_P^2$)	OPE ($a_{P;1,1} = 2b_P^2$)
LQ I	$50.4(1.3)_F(0.5)b_\pi[1.4]_t$	$60.4(1.5)_F(0.6)b_\pi[1.6]_t$
LQ II	$56.2(1.5)_F(0.6)b_\pi[1.6]_t$	$67.4(1.7)_F(0.7)b_\pi[1.8]_t$

Table 6.4: Result for $a_\mu^{\text{HLbL};\pi^0}$ from C_1^0 using the light quark TFF in 10^{-11} units. See details in the text.

$a_\mu^{\text{HLbL};P}$	$a_{P;1,1}^{\text{min}}$	$a_{P;1,1}^{\text{max}}$
LQ I	$57.1(1.6)_L(0)_\delta[1.6]_t$	$57.1(2.0)_L(1.1)_\delta[2.3]_t$
LQ II	$63.7(1.8)_L(0)_\delta[1.8]_t$	$63.7(2.2)_L(1.2)_\delta[2.5]_t$

Table 6.5: Result for $a_\mu^{\text{HLbL};\pi^0}$ from C_2^1 using the light quark TFF in 10^{-11} units. See details in the text.

the opportunity to calculate again the $a_\mu^{\text{HLbL};\pi^0}$ contribution employing the light-quark TFF instead of the π^0 one. The obtained results are labelled as LQ I and shown in Tables 6.4 and 6.5 for the $C_1^0(Q_1^2, Q_2^2)$ and $C_2^1(Q_1^2, Q_2^2)$ approximants. The results are close, but are not compatible with those from Tables 6.2 and 6.3. However, as we said, such equivalence cannot be exact as $\Lambda_1 > 0$ was found, which particularly implies $F_q > F_\pi$. At large energies, the BL behavior enhancement is roughly compensated through the singlet axial current running effects, see Eq. (4.30); at low-energies however, there exist no compensation, producing a lower value for the TFF normalization, which in turn is the most relevant parameter. This effect can be corrected by normalizing the light quark TFF to the π^0 one. In this way, the results labelled as LQ II in Tables 6.4 and 6.5 are obtained, which agreement to the π^0 TFF results is embarrassingly good. We conclude therefore that new data, like that expected from BESIII can improve in precision but is unlikely to shift much the obtained central results in the previous section. This closes the discussion regarding the single-virtual part, but leaves the double-virtual part unanswered, to which we proceed below.

6.4.6 Cross-checks II: $\pi^0 \rightarrow e^+e^-$ implications on $(g_\mu - 2)$

As it has been discussed, the lack of experimental double-virtual data for the TFFs represents one of the major problems for reconstructing our approximants, which requires then some additional theoretical inputs often motivated from the high-energy regime —where we have better control on QCD. Still, we discussed in Chapter 5 that $P \rightarrow \bar{\ell}\ell$ decays may provide indirect experimental evidence of this behavior, as they involve an integral —with similar weights to that in a_μ^{HLbL} — over the double-virtual TFF. Consequently, one may constrain some parameter of the approximant requiring this to reproduce the observed BRs.

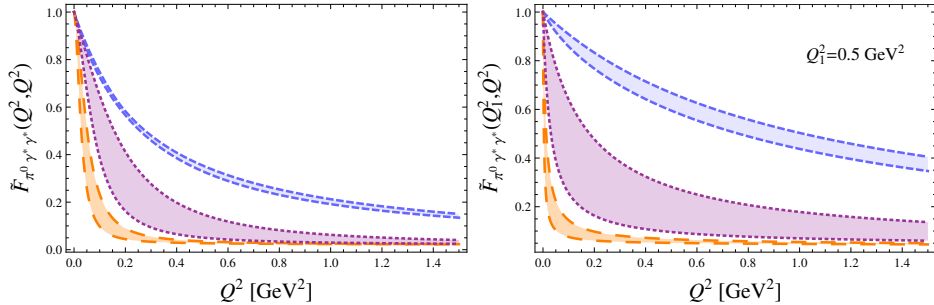


Figure 6.9: Left pannel: normalized TFF assuming $Q_1^2 = Q_2^2 \equiv Q^2$. Right pannel: normalized TFF assuming $Q_1^2 = 0.5 \text{ GeV}^2$. Upper (blue) band shows our $C_2^1(Q_1^2, Q_2^2)$ estimation with $1.92b_\pi^2 \leq a_{\pi;1,1} \leq 2b_\pi^2$. Middle (purple) band reproduces KTeV within 1σ when latest RC are included . Lower (orange) band reproduces KTeV measurement within 1σ when the latest RC are not included. See details in the text.

As we pointed out in Chapter 5, there is an interesting discrepancy in the $\pi^0 \rightarrow e^+e^-$ channel measured by KTeV Collaboration [233] —though this is reduced when taking into account the latest RC [224, 225]. We discuss in this section the impact that such measurement has in the a_μ^{HLLbL} contribution to $(g_\mu - 2)$. For this purpose, we require our C_1^0 and C_2^1 approximants to reproduce the RC-corrected value $\text{BR}(\pi^0 \rightarrow e^+e^-) = 6.87(36) \times 10^{-8}$.

For the lowest $C_1^0(Q_1^2, Q_2^2)$ approximant, there is only one parameter to be tuned, this is $a_{\pi;1,1}$. We find that reproducing KTeV value requires then $a_{\pi;1,1} = -(32 \div 4)b_\pi^2$, where the first number stands for reproducing the central value and the second that which is 1σ below¹³. One may argue that this approximant does not obey the OPE and should not be trusted then. However, we emphasize once more at this point that it is the low-energy behavior of the approximant the one which is responsible for reproducing the experimental value, well before the OPE comes into play. Consequently, this should not greatly change the conclusions with respect to those obtained with higher elements implementing the OPE.

For the next approximant, the $C_2^1(Q_1^2, Q_2^2)$, we have two free parameters, that associated to $a_{\pi;1,1}$, and, in addition, that we associated to δ^2 , see Eq. (6.52). We notice that reproducing KTeV results requires that $\delta^2 \gtrsim 10 \text{ GeV}^2$ together with $a_{\pi;1,1} = -(39 \div 4)b_\pi^2$ —very similar to the C_1^0 results as we anticipated.

All in all, we find that a strongly decreasing TFF is required. In addition, from the δ^2 value obtained for the C_2^1 approximant, the OPE convergence should be rather slow (cf. Eq. (6.52)), a feature not observed so far. These results are shown as a purple band in Fig. 6.9. While the very low-energy

¹³This calculation and the one below have been preformed employing the approximate methods in Ref. [209], which are accurate enough for the $\pi^0 \rightarrow e^+e^-$ decay

behavior is not extremely different from the approximant in our previous section (blue band), it is clear that an experimental measurement above 0.2 GeV^2 would clearly distinguish both scenarios without requiring a high precision (around $(30 - 50)\%$).

Translating the previous numbers into the the π^0 -pole contribution, we obtain, for the C_2^1 approximant, $a_\mu^{\text{HLbL};\pi^0-\text{KTeV}} = 36(7) \times 10^{-11}$. Not surprisingly, the same result would have been obtained for the C_1^0 approximant, which shows the potentiality of CAs to investigate the role of data in $(g_\mu - 2)$. The present result represents a large deviation when comparing to Table 6.3 and is larger than the projected experimental uncertainties. In this respect, it would be very interesting to have an experimental analysis on double-virtual data. As it is shown in Fig. 6.9, this would not require a tremendous precision. Moreover, it does not necessarily involve a measurement for $Q_1^2 = Q_2^2$. Keeping a photon virtuality finite, but different from zero, would provide an interesting result, see Fig. 6.9 right. Had we use the KTeV experimental result without the latest RC would accentuate the differences indicated above. As an example, we show in Fig. 6.9 the TFF that such value would imply as an orange band.

6.5 Beyond pole approximation

So far, we have calculated the π^0 , η , and η' pole contributions to a_μ^{HLbL} . However, it is clear that such contributions cannot account for all the QCD properties alone, and particularly the high-energy behavior, which can be described in terms of quarks and gluons. Indeed, when deriving the pole-contribution from Eq. (6.24), we dismissed any multiparticle state $(3\pi, \dots)$, resonances $(\pi(1300), \dots)$, and $q\bar{q}$ continuum. In order to effectively account for these additional QCD effects in the overall a_μ^{HLbL} calculation, it has been customary to analyze the high-energy behavior of QCD, which is given by the OPE. In this line, it was pointed out for the first time by Melnikov and Vainshtein [311], that the pion-pole contribution cannot account for the HLbL high-energy QCD behavior which is obtained from the OPE in some particular kinematical limit, a feature which should be fixed. We refer to this approach as MV. Later on, the author(s) in [20, 312] pointed to similar features arising when studying the $\langle VVP \rangle$ Green's function high-energy behavior [98]. Their approach to solve this is referred to as JN from now on. These approaches are the ones employed when calculating the current values for a_μ^{HLbL} . In the following sections, we briefly describe these approaches, what they may physically stand for, their pros and cons. We note that taking these approaches one is providing a model with no clear connection to physical observables. The separation of the different contributions is hard to perform and one incurs in potential double-counting problems.

6.5.1 a_μ^{HLbL} à la Melnikov-Vainshtein

To obtain the relevant kinematics for the HLbL tensor in the a_μ^{HLbL} scattering, we need to take the case for which one of the vector currents attaches to a real photon. This means, shifting from our previous general HLbL tensor, Eq. (6.20), to the following Green's function

$$\int d^4x d^4y e^{-iq_1x} e^{-iq_2y} \langle 0 | T\{j_{\mu_1}(x)j_{\mu_2}(y)j_{\mu_3}(0)\} | \gamma \rangle, \quad (6.60)$$

where, for the calculation, we can take the limit of vanishing photon momenta, then $q_1 + q_2 + q_3 = 0$. In the space-like region, this allows for two relevant different regimes. The first, is that in which $Q_1^2 \sim Q_2^2 \sim Q_3^2$. The second, is that for which one of the photon momenta is much smaller, as an example $Q_1^2 \sim Q_2^2 \gg Q_3^2$. In this particular kinematic regime, the OPE for these two highly virtual photons can be easily performed. Following Ref. [311], Eq. (6.60) reduces to¹⁴

$$\int d^4z e^{-i(q_1+q_2)z} \frac{(q_1 - q_2)\delta}{(q_1 - q_2)^2} \epsilon^{\rho\delta}_{\mu_1\mu_2} \langle 0 | T\{j_{5\rho}(z)j_{\mu_3}(0)\} | \gamma \rangle. \quad (6.61)$$

The required matrix element, connected to the famous triangle-amplitude, is well-known [311] and is related to the Adler [42]-Bell-Jackiw [43] anomaly for non-singlet currents. Thanks to this and non-renormalizability theorems for the anomaly, the authors claim that they are able to relate the behavior at $Q_3^2 \sim 0$ with that at $Q_3^2 \rightarrow \infty$, obtaining that no suppression —beyond that of the pseudoscalar propagator— is required for the vertex involving the external photon. This observation leads them to the conclusion that no TFF should be employed at the external vertex, since otherwise this would introduce an additional suppression. As the authors point out, constraining such behavior is a modelization for the required HLbL function, including effects beyond the pseudo-Goldstone bosons poles; labeling this contribution as the “pion-pole” is just an abuse of language then. Somehow, in analogy to PAs, they are modeling some general QCD Green's function using some low- and high-energy constraints. After this, all different contributions get entangled and cannot be separated, which makes hard to tell what is included in their model and what is not. We only emphasize here that such derivation was obtained in a particular kinematical limit for the HLbL function and its implementation is certainly model-dependent. This point will be better understood in the next section when dealing with the JN approach.

Implementing then our approach into their method is straightforward; it reduces to set the vertex with the external photon to $F_{P\gamma\gamma}$. Following the same procedure as in Section 6.4, we quote our results for the C_1^0 and C_2^1 approximants in Tables 6.6 and 6.7, respectively. Accounting for the errors

¹⁴In Ref. [311], $j_5^\rho(z)$ is defined as $\bar{q}(z)Q^2\gamma^\rho\gamma_5q(z)$, where q stands for the light quarks and Q and for the charge operator.

$a_\mu^{\text{HLbL};P}$	Fact	OPE
π^0	$66.3(1.4)_F(2.6)_{b_\pi}[3.0]_t$	$84.5(1.8)_F(2.9)_{b_\pi}[3.4]_t$
η	$19.6(7)_F(5)_{b_\eta}[8]_t$	$28.9(1.0)_F(0.6)_{b_\eta}[1.1]_t$
η'	$19.4(6)_F(4)_{b_{\eta'}}[7]_t$	$30.4(1.0)_F(0.5)_{b_{\eta'}}[1.1]_t$
Total	$105.3[3.2]_t$	$143.8[3.7]_t$

Table 6.6: Result for $a_\mu^{\text{HLbL};P}$, Eq. (6.32), for the C_1^0 approximants for different $a_{P;1,1}$ values in units of 10^{-11} . See description in the text.

$a_\mu^{\text{HLbL};P}$	$a_{P;1,1}^{\min}$	$a_{P;1,1}^{\max}$
π^0	$82.7(1.7)_L(0)_\delta[1.7]_t$	$80.8(1.3)_L(0.5)_\delta[1.4]_t$
η	$27.8(1.3)_L(0)_\delta[1.3]_t$	$27.0(1.4)_L(0.8)_\delta[1.6]_t$
η'	$26.8(1.1)_L(0)_\delta[1.1]_t$	$25.8(0.7)_L(0.9)_\delta[1.1]_t$
Total	$137.3[2.4]_t$	$133.6[2.4]_t$

Table 6.7: Result for $a_\mu^{\text{HLbL};P}$, Eq. (6.32), for the C_2^1 approximants for different $a_{P;1,1}$ values in units of 10^{-11} . See description in the text.

in exactly the same way as in Section 6.4, we obtain

$$a_\mu^{\text{HLbL};P-\text{MV}} = (134 \div 137)(2)_{\text{sys}}(10)_{\text{stat}}[10]_t \times 10^{-11}. \quad (6.62)$$

Again, it is the systematic error (specially relevant for the η') which dominates the full error. Our value can be compared to the original one in [311], $a_\mu^{\text{HLbL};P-\text{MV}} = (76.5 + 18 + 18) \times 10^{-11} \rightarrow 114(10) \times 10^{-11}$. We find that including the η and η' high-energy behavior is once more very important to the precision we are aiming for, whereas this was not implemented in Ref. [311]. Moreover, it must be emphasized again that our approach allows for the proper implementation of the low-energies at the same time. Finally, our method allows to estimate for a systematic error concerning the pseudoscalars TFF description. The question still remains on the systematic error in the modellization which has been done when taking the external vertex as constant and possible corrections particular to the singlet component. Actually, this procedure to calculate a_μ^{HLbL} has been criticized in Ref. [20], see Sections 5.1.1, 5.2.1 and 6.2 therein, a debate which is left to the authors.

6.5.2 a_μ^{HLbL} à la Jegerlehner Nyffeler

A relevant quantity for the a_μ^{HLbL} calculation, but simpler than the HLbL Green's function, Eq. (6.24), is the $\langle VVP \rangle$ Green's function discussed in

[98]¹⁵

$$\begin{aligned} (\Pi_{VVP})_c^{\mu\nu} &\equiv \int d^4x \int d^4y e^{i(px+qy)} \langle 0 | T\{j^\mu(x)j^\nu(y)\} \mathcal{P}^c(0) | 0 \rangle \\ &\equiv -2 \text{tr}(\mathcal{Q}^2 \lambda^c) \epsilon^{\mu\nu\alpha\beta} p_\alpha q_\beta \mathcal{H}_V(p^2, q^2; (p+q)^2). \end{aligned} \quad (6.63)$$

Note that we have already specialized to the electromagnetic current as compared to [98]; $\mathcal{P}^c = \bar{q}i\gamma_5 \frac{\lambda^c}{2} q$ stands for the pseudoscalar source and \mathcal{Q} is the charge operator. The OPE expansion for $\langle VVP \rangle$ was obtained in [98] and reads¹⁶

$$\lim_{\lambda \rightarrow \infty} \mathcal{H}_V((\lambda p)^2, (\lambda q)^2; (\lambda q + \lambda p)^2) = -\frac{\langle \bar{\psi}\psi \rangle_0}{2\lambda^4} \frac{p^2 + q^2 + (p+q)^2}{p^2 q^2 (p+q)^2}, \quad (6.64)$$

$$\lim_{\lambda \rightarrow \infty} \mathcal{H}_V((\lambda p)^2, (q - \lambda p)^2; q^2) = \frac{-1}{\lambda^2} \langle \bar{\psi}\psi \rangle_0 \frac{1}{p^2 q^2}, \quad (6.65)$$

$$\lim_{\lambda \rightarrow \infty} \mathcal{H}_V((\lambda p)^2, q^2; (q + \lambda p)^2) = \frac{1}{\lambda^2} \frac{1}{p^2} \Pi_{VT}(q^2). \quad (6.66)$$

The limiting behaviors for the $\Pi_{VT}(q^2)$ function read [20, 98]

$$\lim_{\lambda \rightarrow \infty} \Pi_{VT}((\lambda q)^2) = -\frac{1}{\lambda^2} \frac{\langle \bar{\psi}\psi \rangle_0}{q^2} + \mathcal{O}(\lambda^{-4}), \quad \Pi_{VT}(0) = -\frac{\langle \bar{\psi}\psi \rangle_0}{2} \chi, \quad (6.67)$$

where χ is the quark condensate magnetic susceptibility [20]. It is relevant at this point to note the connection (in the chiral and large- N_c limit) to the Goldstone bosons (π^0, η, η') pole contributions. From the LSZ-reduction formalism, see Ref. [1], we know that such function behaves as

$$(\Pi_{VVP})_c^{\mu\nu} = \frac{i\sqrt{Z_P}}{(p+q)^2} \int d^4x e^{iqx} \langle 0 | T\{j^\mu(x)j^\nu(0)\} | P(p+q) \rangle + \dots \quad (6.68)$$

where the ellipses refer to terms which are non-singular at $(p+q)^2 = 0$ and the residue stands for the matrix element $\sqrt{Z_P^c} = \langle 0 | \mathcal{P}^c(0) | P \rangle = -\frac{\langle \bar{\psi}\psi \rangle_0}{F} = FB$ ¹⁷. This allows to connect with the pseudoscalar-pole contribution

$$\begin{aligned} \lim_{(p+q)^2 \rightarrow 0} (p+q)^2 (\Pi_{VVP})_c^{\mu\nu} &\equiv -2 \text{tr}(\mathcal{Q}^2 \lambda^c) \epsilon^{\mu\nu\alpha\beta} p_\alpha q_\beta \mathcal{H}_V^P(p^2, q^2) \\ &= i\sqrt{Z_P^c} \int d^4x e^{iqx} \langle 0 | T\{j^\mu(x)j^\nu(0)\} | P(p+q) \rangle. \end{aligned} \quad (6.69)$$

¹⁵Note the relative minus sign with respect to [98] arising from our antisymmetric tensor conventions.

¹⁶ $\langle \bar{\psi}\psi \rangle_0$ refers to the quark condensate in the chiral limit [40].

¹⁷ F is the decay constant in the chiral limit [40]; see Section 1.3 for the origin of B , which is to be taken in the chiral limit too.

Taking the last line in terms of the matrix element for the pseudoscalar to photons transition, Eq. (6.26), and using the TFF definition, see Eq. (1.42), we obtain the desired connection¹⁸

$$F_{P\gamma^*\gamma^*}(p^2, q^2) = -\frac{F}{\langle\bar{\psi}\psi\rangle_0} 2 \text{tr}(\mathcal{Q}^2 \lambda^c) \mathcal{H}_V^P(p^2, q^2). \quad (6.70)$$

The previous analysis could have been performed analogous to the procedure in Section 6.4.1. It is tempting at this point to follow Weinberg again, as we did to calculate the pseudoscalar-pole contributions, and create a general off-shell pseudoscalar function which we approximate with the Goldstone boson (P) pole. Up to some irrelevant factors in Eq. (6.70),

$$\mathcal{H}_V(p^2, q^2, (p+q)^2) \simeq \frac{F_{P^*\gamma^*\gamma^*}(p^2, q^2; (p+q)^2)}{(p+q)^2} \rightarrow \frac{F_{P\gamma^*\gamma^*}(p^2, q^2)}{(p+q)^2}. \quad (6.71)$$

an approximation to the pole-contribution —expected to dominate at low-energies— to such function. The first term has been named the off-shell pseudoscalar form factor. Care must be taken in not to associate this to any physical TFF, a connection which is only possible in the on-shell case via the LSZ-formalism [1].

The relevant point here is that $F_{P^*\gamma^*\gamma^*}(p^2, q^2)/(p+q)^2$ should obey then the OPE expansion Eqs. (6.64) to (6.66), this is [20, 312],

$$\lim_{\lambda \rightarrow \infty} F_{P^*\gamma^*\gamma^*}((\lambda p)^2, (\lambda q)^2; (\lambda q + \lambda p)^2) = \text{tr}(\mathcal{Q}^2 \lambda^c) \frac{F}{\lambda^2} \frac{p^2 + q^2 + (p+q)^2}{p^2 q^2}, \quad (6.72)$$

$$\lim_{\lambda \rightarrow \infty} F_{P^*\gamma^*\gamma^*}((\lambda p)^2, (q - \lambda p)^2; q^2) = 2 \text{tr}(\mathcal{Q}^2 \lambda^c) \frac{F}{\lambda^2} \frac{1}{p^2}, \quad (6.73)$$

$$\lim_{\lambda \rightarrow \infty} F_{P^*\gamma^*\gamma^*}((\lambda p)^2, 0; (\lambda p)^2) = \text{tr}(\mathcal{Q}^2 \lambda^c) F \chi. \quad (6.74)$$

Identifying $F_{P^*\gamma^*\gamma^*}(p^2, q^2)$ with $F_{P\gamma^*\gamma^*}(p^2, q^2)$, we find that the first condition, Eq. (6.72), is accounted from $F_{P\gamma^*\gamma^*}(p^2, q^2)$ up to an overall constant, the second, Eq. (6.73), is trivially satisfied from $F_{P\gamma^*\gamma^*}(p^2, q^2)$ as well. However, the last one, Eq. (6.74), is not satisfied as it would contradict the BL limit. Consequently, the pseudoscalar pole approximation cannot be accurate at high-energies, as it contradicts the $\langle VVP \rangle$ OPE behavior. This feature took the authors in [20, 312] to redefine an off-shell TFF for the π^0 which effectively accounts for Eq. (6.74). We emphasize again that this is a modelization which goes beyond the pion-pole, including then additional QCD contributions —implying similar problems to that in previous section. In the following, we describe how these high-energy constraints may be accounted for in our formalism in a similar but systematic manner.

¹⁸Note that here we omit the $(ie)^2$ coupling arising from the photons. Therefore, the TFF here defined has a relative minus sign with respect to those in previous chapters.

$C_1^0(Q_1^2, Q_2^2)$ implementation

First, we start from the lowest element, the C_1^0 , and construct the approximant for what has been defined as the pseudoscalar off-shell form factor, Eq. (6.71), based on the constraints in Eqs. (6.72) to (6.74). As said, the conditions in Eqs. (6.72) and (6.73) were already satisfied within the pole approximation $F_{P\gamma^*\gamma^*}(p^2, q^2)$, but not the condition in Eq. (6.74). This is possible to achieve if we would modify the C_1^0 approximant by adding some polynomial depending on the pseudoscalar virtuality in the numerator. However, such a piece would spoil the first condition, Eq. (6.72). It seems hopeless then to obtain this with the lowest approximant. However, we can work instead the piece appearing in the loop integral arising from the external vertex and reverse the relation in Eq. (6.71)

$$\frac{F_{P\gamma^*\gamma^*}(Q^2, 0)}{Q^2 + m_P^2} \rightarrow \frac{F_{P^*\gamma^*\gamma}(Q^2, 0; Q^2)}{Q^2 + m_P^2} \simeq \mathcal{H}_V(Q^2, 0, Q^2), \quad (6.75)$$

where we have switched off the chiral limit ($m_P \neq 0$). We could think of this as a C_1^0 -type approximant

$$\mathcal{H}_V(p^2, q^2, (p+q)^2) \simeq \frac{F_{P\gamma\gamma}}{1 - \frac{b_P}{m_P^2}(p^2 + q^2)} \frac{1}{(p+q)^2 - m_P^2}. \quad (6.76)$$

If we insist in constraining the third condition Eq. (6.74), we are forced to remove then the term in the denominator proportional to $(p+q)^2(p^2 + q^2)$

$$\mathcal{H}_V(p^2, q^2, (p+q)^2) \simeq -\frac{F_{P\gamma\gamma}}{m_P^2 - b_P(p^2 + q^2) - (p+q)^2}, \quad (6.77)$$

a valid procedure from our approach which does not require preserving the pole structure. In this way, we are able to implement the power-like behavior in Eqs. (6.72) to (6.74). If we would use Eq. (6.77) to predict the value for χ upon comparing to Eq. (6.66), we would find $\chi = -F_{P\gamma\gamma}/(F_0(1 + b_P) \text{tr}(Q^2 \lambda^c)) = -8.9$ for the π^0 case. The $a_\mu^{\text{HLbL}; P}$ results using Eq. (6.77) for the external vertex and our previous C_1^0 description in Eq. (6.46) with the OPE built-in ($a_{P;1,1} = 2b_P^2$) are given in Table 6.8.

$C_2^1(Q_1^2, Q_2^2)$ implementation

In this second element, there is more freedom to implement the high-energy conditions, Eqs. (6.72) to (6.74). Once more, we proceed *à la* Padé type and fix the pion pole for the denominator. However, in contrast to the previous element, we can incorporate in general additional $(Q_1 + Q_2)^2$ and $(Q_1 + Q_2)^2(Q_1^2 + Q_2^2)$ terms (in accordance with our systematic expansion) in the numerator of Eq. (6.47) which do not spoil the high-energy behavior. The second of these terms can be related to Eq. (6.74), whereas the

$a_\mu^{\text{HLbL};P-\text{JN}}$	
π^0	$82.5(1.8)_F(3.1)_{b_\pi}[3.5]_t$
η	$22.8(0.8)_F(0.6)_{b_\eta}[1.0]_t$
η'	$20.6(0.7)_F(0.5)_{b_{\eta'}}[0.8]_t$
Total	$125.9[3.7]_t$

Table 6.8: Result for $a_\mu^{\text{HLbL};P-\text{JN}}$, Eq. (6.32), using the C_1^0 approximant defined in Eq. (6.77) at the external vertex in units of 10^{-11} . See description in the text.

first one can be related, after taking $Q_1^2 = Q_2^2 = 0$, to the low-energy chiral expansion for the $\langle VVP \rangle$ function, see Eq. (5) in Ref. [320] (very similar results would be obtained from [100]). This is very important as the low-energies play a major role in the a_μ^{HLbL} integrand, Eq. (6.32). Fulfilling Eq. (6.74) requires adding to the numerator $\sim (Q_1^2 + Q_2^2)((Q_1 + Q_2)^2 + m_P^2)(-F_0\chi \text{tr}(Q^2\lambda^c))$, whereas fulfilling the low-energy chiral expansion requires —note that Ref. [320] works in the chiral limit—

$$\mathcal{H}_V(0, 0, Q^2) = \text{Tr}(\hat{Q}^2\lambda^c) \frac{N_c}{8\pi^2 F} \frac{1}{-Q^2} \left(1 + \underbrace{-\frac{(16\pi)^2}{N_c} t_1}_{0.32 \pm 0.10 \pm 0.12} Q^2 \right) \quad (6.78)$$

where t_1 is a LEC. The numerical value $0.32(10)(12)$ has been obtained from the estimate in [320], i.e., $t_1 \simeq -F^2/(64M_V^4)$, where $M_V = 0.77$ GeV and $F = F_\pi$ is used. The ± 0.10 error has been obtained taking the difference among F and F_π [321] and the half-width rule for M_ρ [322]. This should account for the π^0 given its small mass. For extending to the η and, —given its singlet nature— specially the η' , we assume an additional 30% correction for symmetry breaking effects, which should be enough for describing the differences. This leads the ± 0.12 error in Eq. (6.78). All in all, we require adding to the numerator in Eq. (6.47)

$$0.32((Q_1 + Q_2)^2 + m_P^2) - \beta_2(Q_1^2 + Q_2^2)((Q_1 + Q_2)^2 + m_P^2)F_\pi\chi \text{tr}(Q^2\lambda^c). \quad (6.79)$$

Note that additional m_P^2 terms have been included in order to recover the pole contribution as $(Q_1 + Q_2)^2 \rightarrow -m_P^2$. In addition, we take from [20] $\chi = -3.3(1.1)$ together with an additional 30% error for the η and η' accounting for symmetry breaking effects. The obtained results are given in Table 6.9. We note that the large difference among the values in the “min” and “OPE” columns are due to the fact that the first one does not obey the OPE constraint Eq. (6.74)¹⁹. Consequently, this value should be thought as a limiting value, and shows the necessity of having a determination for the doubly-virtual coefficients. The displayed errors are those which have been

¹⁹For $a_{P;1,1} = a_{P;1,1}^{\text{min}}$, the $\alpha_{1,1}$ and $\beta_{2,1}$ parameters in Eq. (6.47) go to 0.

$a_\mu^{\text{HLbL};P-\text{JN}}$	$a_{P;1,1}^{\min}$	$a_{P;1,1}^{\max}$
π^0	78.7	$69.4(1.5)_L(0.6)_\delta(0.4)_\chi(1.8)_{\text{Low}}[2.5]_t$
η	32.9	$22.2(2.7)_L(1.7)_\delta(0.8)_\chi(2.2)_{\text{Low}}[3.9]_t$
η'	41.2	$25.6(0.9)_L(2.1)_\delta(1.8)_\chi(4.0)_{\text{Low}}[5.0]_t$
Total	152.8	$120.6[6.8]_t$

Table 6.9: Result for $a_\mu^{\text{HLbL};P-\text{JN}}$ for the C_2^1 approximants modified as in Eq. (6.79) for different $a_{P;1,1}$ values in units of 10^{-11} . See description in the text.

already defined in Section 6.4.4 together with that from the magnetic susceptibility χ parameter, $(\cdot)_\chi$, and the low-energy behavior in Eq. (6.78), $(\cdot)_{\text{Low}}$. We find again non-negligible differences with respect to the pole contributions. Note however that these effects come mainly from the low-energies. Actually, if we would have retained the OPE condition but switching off the low-energy constraint (i.e., $t_1 = 0$), we would have found for the $a_{P;1,1}^{\max}$ column in Table 6.9, 64.1, 18.2, 18.5 for the π^0 , η and η' , respectively, in units of 10^{-11} .

Furthermore, if we would have applied the modified form factor Eq. (6.71) at the external vertex alone, similar to the previous section, we would have found for the ‘‘OPE’’ column in Table 6.9, 67.0, 20.3, 18.1 for the π^0 , η , η' , respectively, in units of 10^{-11} and a weak dependence on χ . Our result should be compared with that in [20], $a_\mu^{\text{HLbL};P-\text{JN}} = (72(12) + 14.5(4.8) + 12.5(4.2) = 99(16)) \times 10^{-11}$ and points out the necessity to implement the high-energy behavior not only for the π^0 but for the η and η' mesons as well.

In the light of previous results, we think that implementing our framework in this approach would require a minimal information on the double-virtual TFF in order to narrow down the errors. Similarly, a comparison between the C_2^1 and C_1^0 approximation is difficult given the slight different procedures. Estimating a reliable systematic error would require thus reproducing a higher element, say C_3^2 , which requires again, among others, double-virtual information. For all these reasons, we do not consider this number for updating the full a_μ^{HLbL} contribution.

We remark that the difference in errors with respect to Ref. [20] is related to their approximation style, which resembles a CA-type approximation which avoids some of the problems encountered here. The additional error that this may induce is unknown. Still, the systematic errors pointed out above, signal a potentially large unaccounted systematic error.

6.6 Final results for a_μ^{HLbL}

Having discussed the results for the pseudoscalar-pole contribution, we give the final results for the total a_μ^{HLbL} . For this, we need to incorporate, in

addition to the former, the additional contributions outlined in Fig. 6.4. These are, the charged pseudoscalar loops [20, 316, 317], higher resonances exchanges (we consider the axials [300, 323], but not the scalars [20, 299] and tensors [323] as they are partially accounted for by the $\pi^+\pi^-$ loop and we may incur in a double-counting problem) and the quark loop [20, 316, 317, 324], which seems necessary in this approach to account for the high-energy behavior. Taking the central value from Eq. (6.59) leads to

$$\begin{aligned} a_\mu^{\text{HLbL}} &= (94.4(4.8) - 19(13)_{\text{Ploop}} + 6.4(2.0)_{\text{axial}} + 21(3)_{\text{Qloop}}) \times 10^{-11} \\ &= 102.8(14) \times 10^{-11}, \end{aligned} \quad (6.80)$$

where errors have been added in quadrature as they are taken independent from each other. The total error is fully dominated by the charged pseudoscalar loop contribution. In this respect, it is pressing to improve such error as well as to determine a reliable systematic error for it, which would be possible in dispersive analysis for the $\pi^+\pi^-$ contribution. From our point of view, this would set up the foundations to have a reliable precise determination for the a_μ^{HLbL} .

Finally, we address the impact of our study to existing alternative approaches. First, respecting the MV approach [311] from Section 6.5.1, the authors argue that only pseudoscalar and axial contributions should be accounted. Taking our result from Section 6.5.1 and updating the axial contribution [300, 323], we obtain

$$\begin{aligned} a_\mu^{\text{HLbL}} &= (136(9) - 0(10)_{\text{Ploop}} + 6.4(2.0)_{\text{axial}}) \times 10^{-11} \\ &= 142(21) \times 10^{-11}, \end{aligned} \quad (6.81)$$

where the second number is a theoretical error they estimate for the pseudoscalar loop contribution. In order to compare with their result, $136(25) \times 10^{-11}$, errors have been added linearly as well. In addition, previous estimation was used in the Glasgow consensus [299] to obtain the a_μ^{HLbL} . Substituting for this new value and updating the axial vector contribution as well [300, 323], we obtain

$$\begin{aligned} a_\mu^{\text{HLbL}} &= (136(11) - 19(19)_{\text{Ploop}} + 6.4(2.0)_{\text{axial}} - 7(7)_{\text{scalar}} + 2.3_c) \times 10^{-11} \\ &= 119(23) \times 10^{-11}, \end{aligned} \quad (6.82)$$

where the last contribution is from the c quark. In the result above, errors have been combined in quadrature; the result should be compared against $105(26) \times 10^{-11}$ [299].

6.7 Conclusions and outlook

In this chapter, we have updated the pseudoscalar pole contribution to the $(g_\mu - 2)$ hadronic light-by-light, where the key quantities are, once more, the

pseudoscalar TFFs. Such calculation requires a precise error in order to meet future experiments criteria —at the order of 10%— which cannot be easily obtained using model approximations to QCD. Moreover, the phenomenological approaches employed so far, in which experimental data is used to reduce the model-dependence, lack the presence of experimental data at low energies. Unfortunately, this turns out to be the most relevant region in the present calculation and their accuracy relies therefore on extrapolations. Moreover, their choices and particular ansatz for the fitting functions may incur in additional theoretical errors which are, so far, unquantified.

For these reasons, we advocate the use of Canterbury approximants in order to reconstruct the pseudoscalar TFFs, which have been introduced and worked out in previous chapters. These allow to implement both, the low energies and the high ones, which play a relevant role as well in the calculation and have been often disregarded for the η and η' . To demonstrate their performance, we have made use of two different theoretical models for the TFF which have proven useful before. This has allowed to illustrate the convergence of the approach and how the systematic error can be obtained. The reconstruction of the first two elements of the chosen CA sequence has been illustrated then, requiring full use of the available information on pseudoscalar TFFs. This has allowed to obtain a precise determination meeting the future experimental criteria for the pseudoscalar pole contribution to a_μ^{HLbL} , including a precise determination for the systematic error which, globally, turns out to dominate the full calculation and represents one of the main advances with respect to previous approaches.

We have been very careful in order to illustrate what the pseudoscalar pole contribution means and why we advocate such calculation. Still, our approach can be incorporated into alternative approaches including a pion pole, such as the MV or JN approaches.

Finally, we have employed the existing determinations for the additional contributions to the a_μ^{HLbL} in order to estimate the full number. We find that the dominating error at the moment is the pseudoscalar loop contribution, which is expected to be improved in the near future from ongoing dispersive approaches, and would set up the foundations to achieve a precise and model-independent calculation for the a_μ^{HLbL} .

In addition, we have shown that our results could be improved in the near future given the intensive experimental activity regarding $\gamma\gamma$ physics, which has received a strong incentive from the future ($g_\mu - 2$) experiments. In particular, BESIII, NA62 and A2 future results regarding the π^0 TFF are relevant —also future experiments at KLOE-2 and *GlueX* collaborations are expected to provide valuable information on this. For the η and η' , the *GlueX* Collaboration is likely to improve the two-photon decays and TFFs. More important, it is possible that, in the future, the BESIII Collaboration provides the first measurement on the double-virtual π^0 TFF, which is specially relevant for this calculation.

Chapter 7

Conclusions and outlook

In the present thesis, I have studied the lightest pseudoscalars, π^0 , η and η' , transition form factors (TFFs). The objective was to achieve a precise space-like low-energy description and simultaneously to incorporate the high energies with a realistic estimate of the the systematic error. These features are crucial to provide a precise determination for the hadronic light-by-light (HLbL) contribution to the muon anomalous magnetic moment, $(g_\mu - 2)$, and have proven useful for further applications. For this purpose, we used the theory of Padé approximants to describe the single-virtual TFFs. The relevant feature of the approach was to provide a mathematical well-defined framework where the previous requirements can in principle be systematically implemented to arbitrary precision. One of the main features was the systematic implementation. The resulting pattern allowed to check the performance and the systematic errors.

The central quantities required in our approach were the low-energy parameters appearing in the TFFs series expansion, guaranteeing the appropriate description at low-energies. Determining such parameters without any theoretical prejudice was achieved through a data-fitting procedure to the existing space-like data from e^+e^- colliders using Padé approximants. Remarkably, the high-energy data was fundamental in order to achieve a precise description free of large systematic errors. As an outcome, we anticipated that the resulting parameterization would provide an excellent description for the low-energy time-like data —unlike previous vector meson dominance descriptions— at least, below production thresholds. This hypothesis was checked for the time-like data for the η meson at the A2 Collaboration at MAMI. Our parameterization was found to provide an excellent description of data, including those above threshold. Furthermore, our results were corroborated in dispersive approaches, all in all, confirming the power and reliability of the method. The success of the method in the low-energy

time-like region could have been anticipated given the P -wave nature of the discontinuity, which softens out the non-analiticities and allows to understand the latest results for the η' as well. For these reasons, we included in a second stage these data-sets into our approach, obtaining the most precise determination for the η and η' low-energy parameters. In the near future, the upcoming experimental results will provide valuable information and will help to improve our results. Most importantly, there is an ongoing analysis of the π^0 TFF at low space-like energies at BESIII —further in the future, even lower energies will be accessed at KLOE-2 and *GlueX* collaborations. In addition, low-energy time-like data from the Dalitz decay are expected to appear from NA62 and A2 collaborations, which will definitely improve our low-energy parameters determination. Additional data is expected for the η and η' too.

Beyond the single-virtual TFF studies, we discussed how to implement the most general double-virtual case, which is a prerequisite for the calculations developed in this thesis. This required to introduce, for the first time in this context, the notion of Canterbury approximants, which serve as a generalization of Padé approximants to the bivariate case. The current lack of any data did not allow to extract the required low-energy parameters belonging to the double-virtual TFF series expansion. Nonetheless, we provided a careful analysis based on pseudo-data showing the potential of future double-virtual measurements to extract the required parameters. At present, there is an ongoing effort at BESIII to measure the π^0 double-virtual TFF. The framework provided in this work would serve as an important analysis tool for the experimentalists at BESIII as well as in extracting the required parameters. A further opportunity would be the investigation of the existing $V \rightarrow P\gamma^*$ processes, in which the approximants are constructed *à la* Padé type, for narrow vector mesons V .

The phenomenology related to the physics of TFFs is very rich and is not restricted to $(g_\mu - 2)$ physics. To start with, the connection of the low- and high-energy behaviors of the η and η' TFFs made possible to study the $\eta - \eta'$ mixing. For this purpose, we carefully discussed the relevance of using a two-angle formalism for describing the decay constants as well as accounting for the peculiarities of the singlet content, which, even if N_c -suppressed, produce non-negligible effects in the asymptotic behaviors. As an advantage with respect to traditional approaches, the adopted formalism benefits from using inputs which are well-defined in large- N_c chiral perturbation theory —our best tool so far to describe the η and η' . The equations involved in our approach resulted in a degenerate system of equations. Remarkably, this could be used to obtain an additional OZI-violating parameter often ignored. As a result, our framework consistently incorporated all the chiral corrections and OZI-violating parameters involved at NLO in large- N_c

chiral perturbation theory, which have been commonly neglected in most of the phenomenological studies. The obtained results were competitive in comparison to existing determinations despite the small amount of required input and are of relevance for the study of exclusive processes involving the η and η' , which require an accurate input for the mixing parameters.

As a first test of the double-virtual implementation, we discussed the application of our approach to the rare $P \rightarrow \bar{\ell}\ell$ decays. The involved calculation not only required a precise TFF description at low space-like energies, but a reasonable description of the high-energies, providing an excellent ground to test our description. As a further advantage of our approach, we showed that its application could be safely extended to the η and η' cases, which may not be the case for existing calculations. Besides, we performed an exact numerical calculation, which is crucial for the η and η' cases. In contrast, most of the previous approaches used approximations, suffering from large systematics. The current lack of any direct experimental constraint on the double-virtual transition form factor was supplied with a very generous estimate based on very general principles in order to avoid as much as possible a strong model-dependence. Nonetheless, the introduced uncertainty is well below the experimental one. The achieved predictions represent the most updated results and include, for the first time, a systematic error. We confirmed the existing deviation for the $\pi^0 \rightarrow e^+e^-$ result and a slight deviation for the $\eta \rightarrow \mu^+\mu^-$, which provides a strong motivation for a future measurement, e.g. there are plans to measure the former at NA62, whereas the latter could be measured at LHCb. As a result, we studied the new physics scenarios which could provide a reason for such discrepancies; these seem to require new light degrees of freedom and some fine-tuning in order to avoid constraints and explain, at the same time, both deviations. In addition, we discussed the implications of our results for chiral perturbation theory. This is very important as it is the used framework to test analogous K_L decays, which provide stringent tests on lepton universality among others. Besides, this is of interest for calculations regarding the hyperfine splitting in muonic hydrogen. In the future, it would be interesting to perform a similar analysis for the K_L given the available time-like data from single and double Dalitz decays. Achieving a precise description, including a careful numerical evaluation, and a reliable systematic error is very important, as $K_L \rightarrow \bar{\ell}\ell$ decays can place strong constraints on certain new-physics scenarios.

Finally, we calculated the pseudoscalar-pole of the HLbL contribution to $(g_\mu - 2)$, which was our primary goal in this work. Given the current discrepancy among the experimental $(g_\mu - 2)$ extraction and theoretical calculations, planned experiments will measure this quantity with improved precision, which urges the theoretical community to improve on the preci-

sion of hadronic contributions to this observable. Among others, this requires an error around 10% for the HLbL pseudoscalar pole contribution, challenging current theoretical estimates. Such calculation demands, again, a precise description of the double-virtual TFFs at low space-like energies, but requires as well an appropriate implementation of higher energies, in the region around 1 GeV. Furthermore, the double-virtual behavior is essential, which may be the bottleneck of future dispersive descriptions for the TFF. Again, our approach is almost tailor-made for such calculation. The sensitivity of the calculation to intermediate energies and the requested precision required the construction of two elements. As an important novelty, our approach incorporated, for the first time, an accurate η and η' description which cannot be neglected anymore given the required precision. The obtained results provide, for the first time, a systematic error which is actually the dominant one and provides a step forward towards a precise model-independent calculation of the HLbL contribution to $(g_\mu - 2)$. The future TFF measurements, specially those regarding double-virtual measurements, will undoubtedly provide very interesting results not only for the TFFs but for the $(g_\mu - 2)$ evaluation as well. Furthermore, the possibility of lattice techniques to access the TFFs and the hadronic light-by-light tensor will provide valuable inputs for this calculation.

Appendix A

Definitions and conventions

A.1 Conventions

We follow the conventions from Peskin and Schroeder's book [1]. This means, among others, to use units in which $\hbar = c = 1$ and the following conventions for the (diagonal) metric $g^{\mu\nu}$ and antisymmetric tensor $\epsilon^{\mu\nu\rho\sigma}$

$$g^{\mu\nu} = \text{diag}(+1, -1, -1, -1), \quad \epsilon^{0123} = -\epsilon_{0123} = +1. \quad (\text{A.1})$$

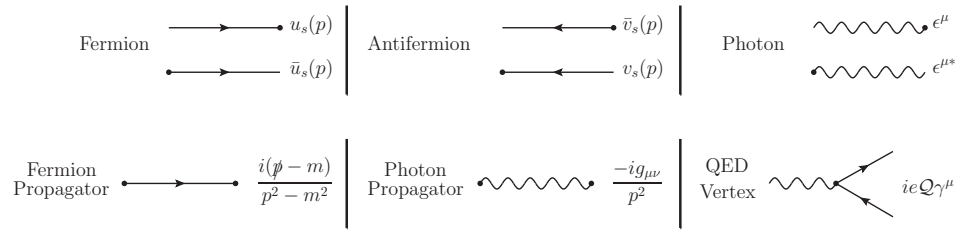
Consequently, for time-like quantities $q^2 > 0$, whereas for space-like quantities, $q^2 < 0$, which is often noted in capital letters as $Q^2 \equiv -q^2 > 0$. Four vectors are often noted as $q = (q^0, \mathbf{q})$, with \mathbf{q} denoting a space-component. The slashed notation, $\gamma^\mu k^\nu g_{\mu\nu} \equiv \not{k}$ with γ^μ a Dirac matrix is employed.

A.2 Feynman rules and spinors

We make use of the Feynman rules following from the QED lagrangian

$$\mathcal{L}_{\text{QED}} = \bar{\psi}(i\not{D} - m)\psi - \frac{1}{4}(F_{\mu\nu})^2, \quad D_\mu = \partial_\mu - i\mathcal{Q}A_\mu, \quad (\text{A.2})$$

which can be read from the diagrams below. The figures are to be read from left to right; momentum p flows from left to right; the dot denotes the vertex to which the lines attach; the fermion arrow gives the fermion number flow;



$u_s(p)$ and $v_s(p)$ are Dirac spinors fulfilling Dirac equation

$$\bar{u}_s(p)(\not{p} - m) = (\not{p} - m)u_s(p) = 0, \quad \bar{v}_s(p)(\not{p} + m) = (\not{p} + m)v_s(p) = 0. \quad (\text{A.3})$$

For convenience, we also employ along this work the (shorter) notation $u_{p,s} \equiv u_s(p)$ and similar for $v_s(p)$. The γ^μ and $\gamma_5 \equiv i\gamma^0\gamma^1\gamma^2\gamma^3$ matrices are defined in the Weyl or chiral basis

$$\gamma^\mu = \begin{pmatrix} 0 & \sigma^\mu \\ \bar{\sigma}^\mu & 0 \end{pmatrix}, \quad \gamma_5 = \begin{pmatrix} -\mathbb{1} & 0 \\ 0 & \mathbb{1} \end{pmatrix}, \quad \sigma^\mu = (\mathbb{1}, \boldsymbol{\sigma}), \quad \bar{\sigma}^\mu = (\mathbb{1}, -\boldsymbol{\sigma}) \quad (\text{A.4})$$

with $\boldsymbol{\sigma}$ referring to the Pauli matrices

$$\sigma^1 = \begin{pmatrix} 0 & 1 \\ 1 & 0 \end{pmatrix}, \quad \sigma^2 = \begin{pmatrix} 0 & -i \\ i & 0 \end{pmatrix}, \quad \sigma^3 = \begin{pmatrix} 1 & 0 \\ 0 & -1 \end{pmatrix}. \quad (\text{A.5})$$

A.3 S-matrix, cross sections and decay rates

The amplitude for some particular process is given in terms of the S -matrix element,

$$\langle p_1, p_2, \dots | S | p_{\mathcal{A}} p_{\mathcal{B}} \rangle \equiv i\mathcal{M}(p_{\mathcal{A}} p_{\mathcal{B}} \rightarrow \{p_f\})(2\pi)^4 \delta^{(4)}(p_{\mathcal{A}} + p_{\mathcal{B}} - \sum p_f) \quad (\text{A.6})$$

where the amplitude for the process, \mathcal{M} for short, is calculated from the Feynman rules. $|p_{\mathcal{A},\mathcal{B}}\rangle$ denotes the initial asymptotic states whereas p_f denote the final ones. Cross sections can be obtained then as

$$d\sigma = \frac{1}{2E_{\mathcal{A}}2E_{\mathcal{B}}|v_{\mathcal{A}} - v_{\mathcal{B}}|} \left(\prod_f \frac{d^3 p_f}{(2\pi)^3} \frac{1}{2E_f} \right) |\mathcal{M}(p_{\mathcal{A}} p_{\mathcal{B}} \rightarrow \{p_f\})|^2 \times (2\pi)^4 \delta^{(4)}(p_{\mathcal{A}} + p_{\mathcal{B}} - \sum p_f), \quad (\text{A.7})$$

with $v_{\mathcal{A},\mathcal{B}}$ the initial particles velocity. Decay rates are expressed as

$$d\Gamma = \frac{1}{2m_{\mathcal{A}}} \left(\prod_f \frac{d^3 p_f}{(2\pi)^3} \frac{1}{2E_f} \right) |\mathcal{M}(m_{\mathcal{A}} \rightarrow \{p_f\})|^2 (2\pi)^4 \delta^{(4)}(p_{\mathcal{A}} - \sum p_f), \quad (\text{A.8})$$

with $m_{\mathcal{A}}$ the initial particle mass. For the particular case of two-body decays with equal masses, m_f , reads

$$d\Gamma = d\Omega \frac{\beta}{64\pi^2 m_{\mathcal{A}}} |\mathcal{M}(m_{\mathcal{A}} \rightarrow \{p_f\})|^2, \quad \beta = \sqrt{1 - 4m_f^2/m_{\mathcal{A}}^2}. \quad (\text{A.9})$$

Note that for indistinguishable particles in the final state (i.e. $\gamma\gamma$) an extra $1/2$ factor appears.

Appendix **B**

Supplementary material

B.1 Formulae for the $g_{VP\gamma}$ couplings

Proceeding in the lines of [120, 170] and including the OZI-violating term Λ_3 appearing in the anomalous QCD sector [178], and K_2 we obtain that

$$\frac{g_{\rho\eta\gamma}}{m_\rho} = \frac{\sqrt{6}}{8\pi^2 f_\rho} \frac{1}{c_{\theta_8-\theta_0}} \left(\frac{c_{\theta_0}}{F_8} (1+K_2 \dot{M}_\pi^2) - \frac{\sqrt{2} s_{\theta_8}}{F_0} (1+K_2 \dot{M}_\pi^2 + \Lambda_3) \right), \quad (\text{B.1})$$

$$\frac{g_{\rho\eta'\gamma}}{m_\rho} = \frac{\sqrt{6}}{8\pi^2 f_\rho} \frac{1}{c_{\theta_8-\theta_0}} \left(\frac{s_{\theta_0}}{F_8} (1+K_2 M_\pi^2) + \frac{\sqrt{2} c_{\theta_8}}{F_0} (1+K_2 M_\pi^2 + \Lambda_3) \right), \quad (\text{B.2})$$

$$\frac{g_{\omega\eta\gamma}}{m_\omega} = \left(\frac{c_{\theta_0} \left[c_{\theta_V} (1+\delta_a^8) - \frac{s_{\theta_V}}{\sqrt{2}} (1+\delta_b^8) \right]}{4\pi^2 f_\omega F_8 c_{\theta_8-\theta_0}} - \frac{s_{\theta_8} \left[s_{\theta_V} (1+\delta_a^0) + c_{\theta_V} \delta_b^0 \right]}{4\pi^2 f_\omega F_0 c_{\theta_8-\theta_0}} \right), \quad (\text{B.3})$$

$$\frac{g_{\omega\eta'\gamma}}{m_\omega} = \left(\frac{s_{\theta_0} \left[c_{\theta_V} (1+\delta_a^8) - \frac{s_{\theta_V}}{\sqrt{2}} (1+\delta_b^8) \right]}{4\pi^2 f_\omega F_8 c_{\theta_8-\theta_0}} + \frac{c_{\theta_8} \left[s_{\theta_V} (1+\delta_a^0) + c_{\theta_V} \delta_b^0 \right]}{4\pi^2 f_\omega F_0 c_{\theta_8-\theta_0}} \right), \quad (\text{B.4})$$

$$\frac{g_{\phi\eta\gamma}}{m_\phi} = - \left(\frac{c_{\theta_0} \left[s_{\theta_V} (1+\delta_a^8) + \frac{c_{\theta_V}}{\sqrt{2}} (1+\delta_b^8) \right]}{4\pi^2 f_\phi F_8 c_{\theta_8-\theta_0}} + \frac{s_{\theta_8} \left[c_{\theta_V} (1+\delta_a^0) - s_{\theta_V} \delta_b^0 \right]}{4\pi^2 f_\phi F_0 c_{\theta_8-\theta_0}} \right), \quad (\text{B.5})$$

$$\frac{g_{\phi\eta'\gamma}}{m_\phi} = - \left(\frac{s_{\theta_0} \left[s_{\theta_V} (1+\delta_a^8) + \frac{c_{\theta_V}}{\sqrt{2}} (1+\delta_b^8) \right]}{4\pi^2 f_\phi F_8 c_{\theta_8-\theta_0}} - \frac{c_{\theta_8} \left[c_{\theta_V} (1+\delta_a^0) - s_{\theta_V} \delta_b^0 \right]}{4\pi^2 f_\phi F_0 c_{\theta_8-\theta_0}} \right), \quad (\text{B.6})$$

where $s_\theta \equiv \sin \theta$ and $c_\theta \equiv \cos \theta$ abbreviations have been employed. In the definitions above, $F_{8,0}$ are the decay constants defined in Eq. (4.10). Besides, the additional $\ell N_c \chi$ PT NLO corrections are fully introduced in Chapter 4,

and are encoded in the δ parameters defined as

$$\delta_a^8 = K_2 M_8^2 \quad \delta_b^8 = K_2 (3M_8^2 - M_0^2), \quad (\text{B.7})$$

$$\delta_a^0 = K_2 M_8^2 + \Lambda_3 \quad \delta_b^0 = K_2 M_{80}^2, \quad (\text{B.8})$$

where the mass parameters above have been introduced in Eqs. (4.3) to (4.5) and can be defined in terms of the LO π and K masses, $\dot{M}_\pi^2, \dot{M}_K^2$, that we associate to the physical ones. f_V is the vector meson decay constant defined in terms of the matrix element $\langle 0 | J_\mu^V | V \rangle = m_V f_V \varepsilon_\mu$ [120, 170]¹ with θ_V the $\omega - \phi$ mixing angle that we take from Ref. [120], $\theta_V = 38.7(2)^\circ$ and m_V is the vector meson mass. Experimentally, f_V can be related to the vector meson leptonic decay-width,

$$\Gamma_{V \rightarrow e^+ e^-} = \frac{4\pi}{3} \alpha^2 \frac{f_V^2}{m_V} c_V, \quad (\text{B.9})$$

where c_V is a charge factor, $c_{\rho, \omega, \phi} = (\frac{1}{\sqrt{2}}, \frac{s_{\theta_V}}{\sqrt{6}}, \frac{c_{\theta_V}}{\sqrt{6}})$. Taking the values from [10], we find [120]

$$f_\rho = 0.221(1) \text{ MeV}, \quad f_\omega = 0.180(3) \text{ MeV}, \quad f_\phi = 0.239(4) \text{ MeV}. \quad (\text{B.10})$$

The experimental $g_{VP\gamma}$ couplings can be obtained from $V \rightarrow P\gamma$ and $P \rightarrow V\gamma$ processes, which decay-width is given as

$$\Gamma(P \rightarrow V\gamma) = \frac{\alpha}{8} g_{VP\gamma}^2 \left(1 - \frac{m_V^2}{m_P^2}\right)^3, \quad (\text{B.11})$$

$$\Gamma(V \rightarrow P\gamma) = \frac{\alpha}{24} g_{VP\gamma}^2 \left(1 - \frac{m_P^2}{m_V^2}\right)^3. \quad (\text{B.12})$$

B.2 Cutcosky rules for additional vector states in $P \rightarrow \bar{\ell}\ell$

As it was explained in Section 5.2.1, for heavier pseudoscalar states there are additional contributions to the imaginary part beyond the $\gamma\gamma$ one. Whereas the $\pi^+\pi^-\gamma$ state, including the resonant contribution, was illustrated in Section 5.3.3 with the aid of a model, the narrow-width vector meson contributions can be easily calculated. For this, we only need to note that such contributions are related to a pole in the TFF, corresponding for the γV and $V V$ intermediate channels to

$$\lim_{k^2 \rightarrow m_V^2} (k^2 - m_V^2) F_{P\gamma^*\gamma}(k^2, 0) = \text{Res}_{\gamma V}, \quad (\text{B.13})$$

$$\lim_{k_{1,2}^2 \rightarrow m_V^2} (k_1^2 - m_V^2)(k_2^2 - m_V^2) F_{P\gamma^*\gamma}(k_1^2, k_2^2) = \text{Res}_{V V}. \quad (\text{B.14})$$

¹ $J_\mu^\rho \equiv J_\mu^3$, $J_\mu^\omega \equiv \frac{1}{\sqrt{2}}(J_\mu^8 s_{\theta_V} + J_\mu^0 c_{\theta_V})$ and $J_\mu^\phi \equiv \frac{1}{\sqrt{2}}(J_\mu^8 c_{\theta_V} - J_\mu^0 s_{\theta_V})$, where J_μ^a are isospin currents as defined in Eq. (1.6). As an illustration, $\theta_V = \pi - \theta_{ideal} = 35.3^\circ$ would correspond to $J_\mu^\omega = \frac{1}{\sqrt{2}}(\bar{u}\gamma_\mu u + \bar{d}\gamma_\mu d)$ and $J_\mu^\phi = -\bar{s}\gamma_\mu s$.

The generalization to additional possible VV' intermediate states is obvious. Accounting for the residues introduced above and following Cutcosky rules, we obtain, for the γV intermediate states

$$\begin{aligned} \text{Im } \mathcal{A} &= \frac{(-2\pi i)^2}{\pi^2 q^2} \int d^4 k \frac{(q^2 k^2 - (q \cdot k)^2) \text{Res}_{\gamma V}}{k^2((p - k)^2 - m^2)} \delta(k^2 - m_V^2) \delta((q - k)^2) \\ &= \frac{\text{Res}_{\gamma V}}{m_P} \frac{1}{m_V^2} \int d\Omega_3 dk^0 \frac{\mathbf{k}^3 \delta(k^0 - (m_P^2 + m_V^2)/(2m_P))}{m_V^2 - m_P(k^0 - \beta_\ell \mathbf{k} \cos \theta)} \\ &= \frac{\text{Res}_{\gamma V}}{4m_V} \left(1 - \frac{m_V^2}{m_P^2}\right)^2 \int d\Omega_3 \frac{1}{\beta_\ell \cos \theta - 1} \\ &= \frac{\text{Res}_{\gamma V}}{m_V^2} \frac{\pi}{2\beta_\ell} \left(1 - \frac{m_V^2}{m_P^2}\right)^2 \ln \left(\frac{1 - \beta_\ell}{1 + \beta_\ell} \right) \theta(m_P - m_V). \end{aligned} \quad (\text{B.15})$$

There exist an additional (identical contribution) for the symmetric channel, call it $V\gamma$. Similarly, for the VV intermediate states, and defining β_V as β_ℓ when $m_\ell \rightarrow m_V$ is replaced, we find

$$\begin{aligned} \text{Im } \mathcal{A} &= \frac{(-2\pi i)^2}{\pi^2 q^2} \int d^4 k \frac{(q^2 k^2 - (q \cdot k)^2) \delta(k^2 - m_V^2) \text{Res}_{VV}}{k^2(q - k)^2((p - k)^2 - m^2)} \delta((q - k)^2 - m_V^2) \\ &= \frac{1}{m_P} \frac{\text{Res}_{VV}}{m_V^4} \int d\Omega_3 dk^0 \frac{\mathbf{k}^3 \delta(k^0 - (m_P^2 + m_V^2)/(2m_P))}{m_V^2 - m_P(k^0 - \beta_\ell \mathbf{k} \cos \theta)} \\ &= \frac{\beta_V^3 \text{Res}_{VV}}{4m_V^4} \int d\Omega_3 \frac{1}{\beta_\ell \beta_V \cos \theta - \frac{1}{2}(1 + \beta_V^2)} \\ &= \frac{\text{Res}_{VV}}{m_V^4} \frac{\pi}{2\beta_\ell} \beta_V^2 \ln \left(\frac{1 + \beta_V^2 - 2\beta_\ell \beta_V}{1 + \beta_V^2 + 2\beta_\ell \beta_V} \right) \theta(m_P - 2m_V). \end{aligned} \quad (\text{B.16})$$

As a particular example, we take a simplified VMD approach where

$$F_{P\gamma^*\gamma^*}(q_1^2, q_2^2) = \frac{m_V^4}{(q_1^2 - m_V^2)(q_2^2 - m_V^2)}, \quad \text{Res}_{\gamma V} = m_V^2, \quad \text{Res}_{VV} = m_V^4. \quad (\text{B.17})$$

Taking into account all the channels, we obtain for the imaginary part

$$\begin{aligned} \text{Im } \mathcal{A}(q^2) &= \frac{\pi}{2\beta_\ell} \ln \left(\frac{1 - \beta_\ell}{1 + \beta_\ell} \right) - \frac{\pi}{\beta_\ell} \left(1 - \frac{m_V^2}{q^2} \right)^2 \ln \left(\frac{1 - \beta_\ell}{1 + \beta_\ell} \right) \theta(q^2 - m_V^2) \\ &\quad + \frac{\pi}{2\beta_\ell} \beta_V^2 \ln \left(\frac{1 + \beta_V^2 - 2\beta_\ell \beta_V}{1 + \beta_V^2 + 2\beta_\ell \beta_V} \right) \theta(q^2 - 4m_V^2). \end{aligned} \quad (\text{B.18})$$

The shape for the imaginary part is illustrated in Fig. B.1 as a function of the pseudoscalar mass for the individual and total contributions using $m_V = 0.77$ GeV. The resulting function approaches 0 asymptotically as it should, since the vector channels provide a finite result for the loop integral Eq. (5.6).

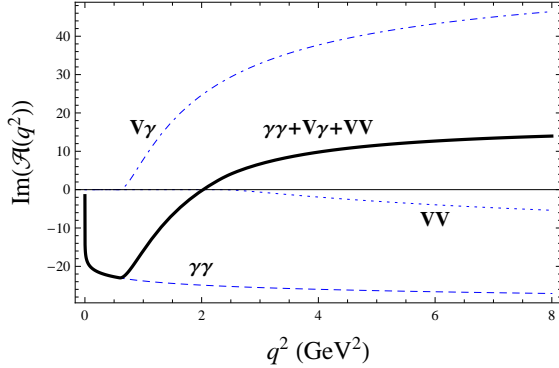


Figure B.1: Eq. (B.18) is shown for $m_V = 0.77$ GeV. The different channels open at the threshold values $q^2 = 0, m_V^2, 4m_V^2$, respectively. There is a smooth cancellation as $q^2 \rightarrow \infty$.

B.3 Fierz transformations

Given the quantum numbers of the system, $J^{PC} = 0^{-+}$, any new contribution to $P \rightarrow \bar{\ell}\ell$ decays necessarily results from an effective $(\bar{q}\Gamma q)(\bar{\ell}\Gamma\ell)$ interaction where $\Gamma = \Gamma_{P,A} \equiv i\gamma_5, \gamma^\mu\gamma_5$ and, again, $q = u, d, s$ and $\ell = e, \mu$. Note that this does not necessarily implies that such term arises from an UV completion featuring an intermediate axial or pseudoscalar field as calculated in Section 5.6; it could arise as well from an effective leptoquark-like interaction $(\bar{q}\tilde{\Gamma}\ell)(\bar{\ell}\tilde{\Gamma}q)$ where $\tilde{\Gamma} \neq \Gamma_{P,V}$. Still, such term can be Fierz rearranged, this means, expressed as [214, 325]

$$(\bar{q}\tilde{\Gamma}_i\ell)(\bar{\ell}\tilde{\Gamma}_iq) = \sum_j \lambda_{ij}(\bar{q}\Gamma_i q)(\bar{\ell}\Gamma_j\ell), \quad (\text{B.19})$$

$$\Gamma_S = 1 \quad \Gamma_P = i\gamma_5 \quad \Gamma_V = \gamma^\mu \quad \Gamma_A = \gamma_5\gamma^\mu \quad \Gamma_T = \sigma^{\mu\nu}. \quad (\text{B.20})$$

Then, only the relevant effective pseudoscalar and axial interactions do contribute to the process, which can be obtained using²

$$\lambda_{SA} = \frac{1}{4} \quad \lambda_{VA} = \frac{1}{2} \quad \lambda_{TA} = 0 \quad \lambda_{AA} = \frac{1}{2} \quad \lambda_{PA} = \frac{1}{4}, \quad (\text{B.21})$$

$$\lambda_{SP} = \frac{1}{4} \quad \lambda_{VP} = -1 \quad \lambda_{TP} = 3 \quad \lambda_{AP} = 1 \quad \lambda_{PP} = -\frac{1}{4}. \quad (\text{B.22})$$

Consequently, any leptoquark contribution can be obtained from the results given in Eqs. (5.53) to (5.55) using Eqs. (B.19) to (B.22).

²Note an extra sign arising from the anticommuting nature of the spinor fields q, ℓ . This should be removed if dealing with numeric quantities such as the spinors $u(v)_{s,p}$

Bibliography

- [1] M. E. Peskin and D. V. Schroeder, (1995).
- [2] J. F. Donoghue, E. Golowich, and B. R. Holstein, *Dynamics of the Standard Model*, 1st ed., Cambridge monographs on mathematical physics (Cambridge University Press, 1992).
- [3] G. Aad *et al.* (ATLAS), [Phys. Lett. B716, 1 \(2012\)](#), [arXiv:1207.7214 \[hep-ex\]](#) .
- [4] S. Chatrchyan *et al.* (CMS), [Phys. Lett. B716, 30 \(2012\)](#), [arXiv:1207.7235 \[hep-ex\]](#) .
- [5] N. Arkani-Hamed, D. P. Finkbeiner, T. R. Slatyer, and N. Weiner, [Phys. Rev. D79, 015014 \(2009\)](#), [arXiv:0810.0713 \[hep-ph\]](#) .
- [6] R. Adam *et al.* (Planck), (2015), [arXiv:1502.01582 \[astro-ph.CO\]](#) .
- [7] P. A. R. Ade *et al.* (Planck), (2015), [arXiv:1502.01589 \[astro-ph.CO\]](#) .
- [8] M. Li, X.-D. Li, S. Wang, and Y. Wang, [Commun. Theor. Phys. 56, 525 \(2011\)](#), [arXiv:1103.5870 \[astro-ph.CO\]](#) .
- [9] S. P. Martin, [\(1997\)](#), [10.1142/9789814307505_0001](#).
- [10] K. A. Olive *et al.* (Particle Data Group), [Chin. Phys. C38, 090001 \(2014\)](#).
- [11] S. Weinberg, [Phys. Rev. D19, 1277 \(1979\)](#).
- [12] L. Susskind, [Phys. Rev. D20, 2619 \(1979\)](#).
- [13] N. Arkani-Hamed, A. G. Cohen, T. Gregoire, and J. G. Wacker, [JHEP 08, 020 \(2002\)](#), [arXiv:hep-ph/0202089 \[hep-ph\]](#) .

- [14] N. Arkani-Hamed, A. G. Cohen, E. Katz, and A. E. Nelson, *JHEP* **07**, 034 (2002), [arXiv:hep-ph/0206021 \[hep-ph\]](https://arxiv.org/abs/hep-ph/0206021) .
- [15] N. Arkani-Hamed, S. Dimopoulos, and G. R. Dvali, *Phys. Lett.* **B429**, 263 (1998), [arXiv:hep-ph/9803315 \[hep-ph\]](https://arxiv.org/abs/hep-ph/9803315) .
- [16] M. K. Gaillard and B. W. Lee, *Phys. Rev.* **D10**, 897 (1974).
- [17] J. R. Ellis, M. K. Gaillard, D. V. Nanopoulos, and S. Rudaz, *Nucl. Phys.* **B131**, 285 (1977), [Erratum: Nucl. Phys.B132,541(1978)].
- [18] H. Albrecht *et al.* (ARGUS), *HADRONS, QUARKS AND GLUONS. PROCEEDINGS, HADRONIC SESSION OF THE 22ND RENCONTRE DE MORIOND, LES ARCS, FRANCE, MARCH 15-21, 1987*, *Phys. Lett.* **B192**, 245 (1987), [,51(1987)].
- [19] S. Schael *et al.* (SLD Electroweak Group, DELPHI, ALEPH, SLD, SLD Heavy Flavour Group, OPAL, LEP Electroweak Working Group, L3), *Phys. Rept.* **427**, 257 (2006), [arXiv:hep-ex/0509008 \[hep-ex\]](https://arxiv.org/abs/hep-ex/0509008) .
- [20] F. Jegerlehner and A. Nyffeler, *Phys. Rept.* **477**, 1 (2009), [arXiv:0902.3360 \[hep-ph\]](https://arxiv.org/abs/0902.3360) .
- [21] G. W. Bennett *et al.* (Muon g-2), *Phys. Rev.* **D73**, 072003 (2006), [arXiv:hep-ex/0602035 \[hep-ex\]](https://arxiv.org/abs/hep-ex/0602035) .
- [22] B. Lee Roberts (Fermilab P989), *Tau lepton physics. Proceedings, 11th International Workshop, TAU 2010, Manchester, UK, September 13-17, 2010*, *Nucl. Phys. Proc. Suppl.* **218**, 237 (2011).
- [23] T. Mibe (J-PARC g-2), *Proceedings, 6th International Workshop on e+e- Collisions from Phi to Psi (PHIPSI09)*, *Chin. Phys.* **C34**, 745 (2010).
- [24] R. L. Jaffe, *Proceedings, 6th International Conference on Hyperons, charm and beauty hadrons (BEACH 2004)*, *Phys. Rept.* **409**, 1 (2005), [arXiv:hep-ph/0409065 \[hep-ph\]](https://arxiv.org/abs/hep-ph/0409065) .
- [25] S. Godfrey and S. L. Olsen, *Ann. Rev. Nucl. Part. Sci.* **58**, 51 (2008), [arXiv:0801.3867 \[hep-ph\]](https://arxiv.org/abs/0801.3867) .
- [26] R. Aaij *et al.* (LHCb), *Phys. Rev. Lett.* **115**, 072001 (2015), [arXiv:1507.03414 \[hep-ex\]](https://arxiv.org/abs/1507.03414) .
- [27] K. A. Olive *et al.* (Particle Data Group), *Chin. Phys.* **C38**, 090001 (2014), see the review “Quantum chromodynamics —S. Bethke, G. Dissertori and G.P. Salam”, pp. 122-138.

[28] P. A. Baikov, K. G. Chetyrkin, and J. H. Kühn, (2016), [arXiv:1606.08659 \[hep-ph\]](https://arxiv.org/abs/1606.08659) .

[29] A. Jaffe and E. Witten, “Yang-Mills and Mass Gap,” (2000), <http://www.claymath.org/millennium-problems>.

[30] K. A. Olive *et al.* (Particle Data Group), *Chin. Phys. C***38**, 090001 (2014), see the review “Lattice quantum chromodynamics — S. Hashimoto, J. Laiho and S.R. Sharpe”, pp. 286-295.

[31] K. G. Wilson, *Phys. Rev. D***10**, 2445 (1974), [,45(1974)].

[32] S. Scherer and M. R. Schindler, *Lect.Notes Phys.* **830**, pp.1 (2012).

[33] G. ’t Hooft, *Nucl. Phys.* **B72**, 461 (1974).

[34] E. Witten, *Nucl. Phys.* **B156**, 269 (1979).

[35] S. Weinberg, *Phys. Rev. Lett.* **18**, 188 (1967).

[36] S. R. Coleman, J. Wess, and B. Zumino, *Phys. Rev.* **177**, 2239 (1969).

[37] C. G. Callan, Jr., S. R. Coleman, J. Wess, and B. Zumino, *Phys. Rev.* **177**, 2247 (1969).

[38] S. Weinberg, *Physica* **A96**, 327 (1979).

[39] J. Gasser and H. Leutwyler, *Annals Phys.* **158**, 142 (1984).

[40] J. Gasser and H. Leutwyler, *Nucl. Phys.* **B250**, 465 (1985).

[41] R. Kaiser and H. Leutwyler, *Eur. Phys. J.* **C17**, 623 (2000), [arXiv:hep-ph/0007101 \[hep-ph\]](https://arxiv.org/abs/hep-ph/0007101) .

[42] S. L. Adler, *Phys. Rev.* **177**, 2426 (1969).

[43] J. S. Bell and R. Jackiw, *Nuovo Cim.* **A60**, 47 (1969).

[44] J. L. Goity, A. M. Bernstein, and B. R. Holstein, *Phys. Rev. D***66**, 076014 (2002), [arXiv:hep-ph/0206007 \[hep-ph\]](https://arxiv.org/abs/hep-ph/0206007) .

[45] J. Wess and B. Zumino, *Phys. Lett.* **B37**, 95 (1971).

[46] E. Witten, *Nucl. Phys.* **B223**, 422 (1983).

[47] H. Leutwyler, *Quantum chromodynamics. Proceedings, Conference, QCD’97, Montpellier, France, July 3-9, 1997*, *Nucl. Phys. Proc. Suppl.* **64**, 223 (1998), [arXiv:hep-ph/9709408 \[hep-ph\]](https://arxiv.org/abs/hep-ph/9709408) .

[48] E. Witten, *Nucl. Phys.* **B160**, 57 (1979).

[49] R. F. Lebed, *Mesons and light nuclei. Proceedings, 11th Indian-Summer School on Intermediate-Energy Physics, Prague, Czech Republic, September 7-11, 1998*, *Czech. J. Phys.* **49**, 1273 (1999), [arXiv:nucl-th/9810080](https://arxiv.org/abs/nucl-th/9810080) [nucl-th].

[50] A. V. Manohar, in *Probing the standard model of particle interactions. Proceedings, Summer School in Theoretical Physics, NATO Advanced Study Institute, 68th session, Les Houches, France, July 28-September 5, 1997. Pt. 1, 2* (1998) pp. 1091–1169, [arXiv:hep-ph/9802419](https://arxiv.org/abs/hep-ph/9802419) [hep-ph].

[51] G. 't Hooft, *Nucl. Phys.* **B75**, 461 (1974).

[52] S. Peris, in *Phenomenology of large $N(c)$ QCD. Proceedings, Tempe, USA, January 9-11, 2002* (2002) pp. 259–269, [arXiv:hep-ph/0204181](https://arxiv.org/abs/hep-ph/0204181) [hep-ph].

[53] S. Peris, *Phys. Rev.* **D74**, 054013 (2006), [arXiv:hep-ph/0603190](https://arxiv.org/abs/hep-ph/0603190) [hep-ph].

[54] P. Masjuan and S. Peris, *JHEP* **05**, 040 (2007), [arXiv:0704.1247](https://arxiv.org/abs/0704.1247) [hep-ph].

[55] P. Masjuan Queralt, *Rational Approximations in Quantum Chromodynamics*, Ph.D. thesis, Barcelona, IFAE (2010), [arXiv:1005.5683](https://arxiv.org/abs/1005.5683) [hep-ph].

[56] G. A. Baker, *Essentials of Padé Approximants*, 1st ed. (Academic Press, New York, 1975).

[57] G. A. Baker and P. Graves-Morris, *Padé Approximants*, 2nd ed., Encyclopedia of Mathematics and its Applications No. 59 (Cambridge University Press, New York, 1996).

[58] P. Masjuan and S. Peris, *Phys. Lett.* **B686**, 307 (2010), [arXiv:0903.0294](https://arxiv.org/abs/0903.0294) [hep-ph].

[59] P. Masjuan and S. Peris, *Phys. Lett.* **B663**, 61 (2008), [arXiv:0801.3558](https://arxiv.org/abs/0801.3558) [hep-ph].

[60] X. Feng, S. Aoki, H. Fukaya, S. Hashimoto, T. Kaneko, J.-i. Noaki, and E. Shintani, *Phys. Rev. Lett.* **109**, 182001 (2012), [arXiv:1206.1375](https://arxiv.org/abs/1206.1375) [hep-lat].

[61] S. D. Cohen, H.-W. Lin, J. Dudek, and R. G. Edwards, *Proceedings, 26th International Symposium on Lattice field theory (Lattice 2008)*, PoS **LATTICE2008**, 159 (2008), [arXiv:0810.5550](https://arxiv.org/abs/0810.5550) [hep-lat].

[62] H.-W. Lin and S. D. Cohen, *Proceedings, 10th Conference on Quark Confinement and the Hadron Spectrum (Confinement X)*, (2013), [PoSConfinementX,113(2012)], [arXiv:1302.0874 \[hep-lat\]](https://arxiv.org/abs/1302.0874) .

[63] G. P. Lepage and S. J. Brodsky, *Phys. Rev.* **D22**, 2157 (1980).

[64] F. del Aguila and M. K. Chase, *Nucl. Phys.* **B193**, 517 (1981).

[65] E. Braaten, *Phys. Rev.* **D28**, 524 (1983).

[66] S. S. Agaev, V. M. Braun, N. Offen, and F. A. Porkert, *Phys. Rev.* **D83**, 054020 (2011), [arXiv:1012.4671 \[hep-ph\]](https://arxiv.org/abs/1012.4671) .

[67] S. Agaev, V. Braun, N. Offen, F. Porkert, and A. Schäfer, *Phys. Rev.* **D90**, 074019 (2014), [arXiv:1409.4311 \[hep-ph\]](https://arxiv.org/abs/1409.4311) .

[68] A. V. Efremov and A. V. Radyushkin, *Theor. Math. Phys.* **42**, 97 (1980), [Teor. Mat. Fiz.42,147(1980)].

[69] V. A. Novikov, M. A. Shifman, A. I. Vainshtein, M. B. Voloshin, and V. I. Zakharov, *Nucl. Phys.* **B237**, 525 (1984).

[70] V. M. Braun *et al.*, *Phys. Rev.* **D74**, 074501 (2006), [arXiv:hep-lat/0606012 \[hep-lat\]](https://arxiv.org/abs/hep-lat/0606012) .

[71] R. Arthur, P. A. Boyle, D. Brommel, M. A. Donnellan, J. M. Flynn, A. Juttner, T. D. Rae, and C. T. C. Sachrajda, *Phys. Rev.* **D83**, 074505 (2011), [arXiv:1011.5906 \[hep-lat\]](https://arxiv.org/abs/1011.5906) .

[72] V. M. Braun, S. Collins, M. Göckeler, P. Pérez-Rubio, A. Schäfer, R. W. Schiel, and A. Sternbeck, in *Proceedings, QCD Evolution Workshop (QCD 2015)* (2015) [arXiv:1510.07429 \[hep-lat\]](https://arxiv.org/abs/1510.07429) .

[73] T. Huang, T. Zhong, and X.-G. Wu, *Phys. Rev.* **D88**, 034013 (2013), [arXiv:1305.7391 \[hep-ph\]](https://arxiv.org/abs/1305.7391) .

[74] N. G. Stefanis, A. P. Bakulev, S. V. Mikhailov, and A. V. Pimikov, *Phys. Rev.* **D87**, 094025 (2013), [arXiv:1202.1781 \[hep-ph\]](https://arxiv.org/abs/1202.1781) .

[75] S. S. Agaev, V. M. Braun, N. Offen, and F. A. Porkert, *Phys. Rev.* **D86**, 077504 (2012), [arXiv:1206.3968 \[hep-ph\]](https://arxiv.org/abs/1206.3968) .

[76] B. Aubert *et al.* (BaBar Collaboration), *Phys. Rev.* **D80**, 052002 (2009), [arXiv:0905.4778 \[hep-ex\]](https://arxiv.org/abs/0905.4778) .

[77] A. V. Radyushkin, *Phys. Rev.* **D80**, 094009 (2009), [arXiv:0906.0323 \[hep-ph\]](https://arxiv.org/abs/0906.0323) .

[78] S. Noguera and V. Vento, *Eur. Phys. J.* **A46**, 197 (2010), [arXiv:1001.3075 \[hep-ph\]](https://arxiv.org/abs/1001.3075) .

[79] S. Noguera and V. Vento, *Eur. Phys. J.* **A48**, 143 (2012), [arXiv:1205.4598 \[hep-ph\]](https://arxiv.org/abs/1205.4598) .

[80] S. Noguera and S. Scopetta, *Phys. Rev.* **D85**, 054004 (2012), [arXiv:1110.6402 \[hep-ph\]](https://arxiv.org/abs/1110.6402) .

[81] P. Kroll, *Eur. Phys. J.* **C71**, 1623 (2011), [arXiv:1012.3542 \[hep-ph\]](https://arxiv.org/abs/1012.3542) .

[82] A. V. Radyushkin, *Phys. Lett.* **B735**, 417 (2014), [arXiv:1404.7032 \[hep-ph\]](https://arxiv.org/abs/1404.7032) .

[83] I. C. Cloët, L. Chang, C. D. Roberts, S. M. Schmidt, and P. C. Tandy, *Phys. Rev. Lett.* **111**, 092001 (2013), [arXiv:1306.2645 \[nucl-th\]](https://arxiv.org/abs/1306.2645) .

[84] S. J. Brodsky, F.-G. Cao, and G. F. de Teramond, *Phys. Rev.* **D84**, 075012 (2011), [arXiv:1105.3999 \[hep-ph\]](https://arxiv.org/abs/1105.3999) .

[85] Y. Klopot, A. Oganesian, and O. Teryaev, *Phys. Rev.* **D87**, 036013 (2013), [Erratum: *Phys. Rev.* D88,no.5,059902(2013)], [arXiv:1211.0874 \[hep-ph\]](https://arxiv.org/abs/1211.0874) .

[86] Y. Klopot, A. Oganesian, and O. Teryaev, *JETP Lett.* **99**, 679 (2014), [arXiv:1312.1226 \[hep-ph\]](https://arxiv.org/abs/1312.1226) .

[87] J. Bijnens, A. Bramon, and F. Cornet, *Z. Phys.* **C46**, 599 (1990).

[88] L. Ametller, J. Bijnens, A. Bramon, and F. Cornet, *Phys. Rev.* **D45**, 986 (1992).

[89] B. Borasoy and R. Nissler, *Eur. Phys. J.* **A19**, 367 (2004), [arXiv:hep-ph/0309011 \[hep-ph\]](https://arxiv.org/abs/hep-ph/0309011) .

[90] T. Ebertshauser, H. W. Fearing, and S. Scherer, *Phys. Rev.* **D65**, 054033 (2002), [arXiv:hep-ph/0110261 \[hep-ph\]](https://arxiv.org/abs/hep-ph/0110261) .

[91] J. Bijnens, K. Kampf, and S. Lanz, *Nucl. Phys.* **B860**, 245 (2012), [arXiv:1201.2608 \[hep-ph\]](https://arxiv.org/abs/1201.2608) .

[92] K. Kampf, *Proceedings, 16th International Conference on Quantum Chromodynamics (QCD 12)*, 10.1016/j.nuclphysbps.2012.12.036, [Nucl. Phys. Proc. Suppl. 234, 299 (2013)], [arXiv:1209.2902 \[hep-ph\]](https://arxiv.org/abs/1209.2902) .

[93] M. Gorchtein, P. Guo, and A. P. Szczepaniak, *Phys. Rev.* **C86**, 015205 (2012), [arXiv:1102.5558 \[nucl-th\]](https://arxiv.org/abs/1102.5558) .

[94] M. Hoferichter, B. Kubis, S. Leupold, F. Niecknig, and S. P. Schneider, *Eur. Phys. J.* **C74**, 3180 (2014), [arXiv:1410.4691 \[hep-ph\]](https://arxiv.org/abs/1410.4691) .

[95] C. Hanhart, A. Kupśc, U. G. Meißner, F. Stollenwerk, and A. Wirzba, *Eur. Phys. J.* **C73**, 2668 (2013), [Erratum: *Eur. Phys. J.* C75,no.6,242(2015)], [arXiv:1307.5654 \[hep-ph\]](https://arxiv.org/abs/1307.5654) .

[96] C. W. Xiao, T. Dato, C. Hanhart, B. Kubis, U. G. Meißner, and A. Wirzba, (2015), [arXiv:1509.02194 \[hep-ph\]](https://arxiv.org/abs/1509.02194) .

[97] E. Ruiz Arriola and W. Broniowski, *Phys. Rev.* **D74**, 034008 (2006), [arXiv:hep-ph/0605318 \[hep-ph\]](https://arxiv.org/abs/hep-ph/0605318) .

[98] M. Knecht and A. Nyffeler, *Eur. Phys. J.* **C21**, 659 (2001), [arXiv:hep-ph/0106034 \[hep-ph\]](https://arxiv.org/abs/hep-ph/0106034) .

[99] T. Husek and S. Leupold, *Eur. Phys. J.* **C75**, 586 (2015), [arXiv:1507.00478 \[hep-ph\]](https://arxiv.org/abs/1507.00478) .

[100] P. Roig, A. Guevara, and G. López Castro, *Phys. Rev.* **D89**, 073016 (2014), [arXiv:1401.4099 \[hep-ph\]](https://arxiv.org/abs/1401.4099) .

[101] H. Czyz, S. Ivashyn, A. Korchin, and O. Shekhovtsova, *Phys. Rev.* **D85**, 094010 (2012), [arXiv:1202.1171 \[hep-ph\]](https://arxiv.org/abs/1202.1171) .

[102] S. J. Brodsky and G. P. Lepage, *Conference on Nuclear Structure and Particle Physics Oxford, England, April 6-8, 1981*, *Phys. Rev.* **D24**, 1808 (1981).

[103] I. Larin *et al.* (PrimEx), *Phys. Rev. Lett.* **106**, 162303 (2011), [arXiv:1009.1681 \[nucl-ex\]](https://arxiv.org/abs/1009.1681) .

[104] D. Babusci *et al.* (KLOE-2), *JHEP* **01**, 119 (2013), [arXiv:1211.1845 \[hep-ex\]](https://arxiv.org/abs/1211.1845) .

[105] M. Acciarri *et al.* (L3), *Phys. Lett.* **B418**, 399 (1998).

[106] J. Bijnens, A. Bramon, and F. Cornet, *Phys. Rev. Lett.* **61**, 1453 (1988).

[107] H. Behrend *et al.* (CELLO Collaboration), *Z.Phys.* **C49**, 401 (1991).

[108] J. Gronberg *et al.* (CLEO Collaboration), *Phys.Rev.* **D57**, 33 (1998), [arXiv:hep-ex/9707031 \[hep-ex\]](https://arxiv.org/abs/hep-ex/9707031) .

[109] P. Masjuan, S. Peris, and J. J. Sanz-Cillero, *Phys. Rev.* **D78**, 074028 (2008), [arXiv:0807.4893 \[hep-ph\]](https://arxiv.org/abs/0807.4893) .

[110] E. Ruiz Arriola and W. Broniowski, *Phys. Rev.* **D81**, 094021 (2010), [arXiv:1004.0837 \[hep-ph\]](https://arxiv.org/abs/1004.0837) .

[111] P. Masjuan, *Phys.Rev.* **D86**, 094021 (2012), [arXiv:1206.2549 \[hep-ph\]](https://arxiv.org/abs/1206.2549)

[112] L. Ametller, L. Bergstrom, A. Bramon, and E. Masso, *Nucl.Phys.* **B228**, 301 (1983).

[113] S. J. Brodsky, F.-G. Cao, and G. F. de Teramond, *Phys. Rev.* **D84**, 033001 (2011), arXiv:1104.3364 [hep-ph] .

[114] R. Escribano, P. Masjuan, and P. Sanchez-Puertas, *Phys.Rev.* **D89**, 034014 (2014), arXiv:1307.2061 [hep-ph] .

[115] P. Masjuan, E. Ruiz Arriola, and W. Broniowski, *Phys. Rev.* **D85**, 094006 (2012), arXiv:1203.4782 [hep-ph] .

[116] L. G. Landsberg, *Phys. Rept.* **128**, 301 (1985).

[117] R. Escribano, P. Masjuan, and P. Sanchez-Puertas, *Eur. Phys. J.* **C75**, 414 (2015), arXiv:1504.07742 [hep-ph] .

[118] P. del Amo Sanchez *et al.* (BaBar Collaboration), *Phys.Rev.* **D84**, 052001 (2011), arXiv:1101.1142 [hep-ex] .

[119] T. Feldmann, P. Kroll, and B. Stech, *Phys. Rev.* **D58**, 114006 (1998), arXiv:hep-ph/9802409 [hep-ph] .

[120] R. Escribano and J.-M. Frere, *JHEP* **06**, 029 (2005), arXiv:hep-ph/0501072 [hep-ph] .

[121] P. Masjuan, E. Ruiz Arriola, and W. Broniowski, *Phys. Rev.* **D87**, 014005 (2013), arXiv:1210.0760 [hep-ph] .

[122] P. Masjuan, E. Ruiz Arriola, and W. Broniowski, *Phys. Rev.* **D87**, 118502 (2013), arXiv:1305.3493 [hep-ph] .

[123] P. Masjuan and J. J. Sanz-Cillero, *Eur.Phys.J.* **C73**, 2594 (2013), arXiv:1306.6308 [hep-ph] .

[124] P. Masjuan, J. Ruiz de Elvira, and J. J. Sanz-Cillero, *Phys. Rev.* **D90**, 097901 (2014), arXiv:1410.2397 [hep-ph] .

[125] R. I. Dzhelyadin *et al.*, *Phys. Lett.* **B94**, 548 (1980), [Yad. Fiz.32,998(1980)].

[126] R. Arnaldi *et al.* (NA60), *Phys. Lett.* **B677**, 260 (2009), arXiv:0902.2547 [hep-ph] .

[127] H. Berghauser *et al.*, *Phys. Lett.* **B701**, 562 (2011).

[128] M. Hodana and P. Moskal (WASA-at-COSY), *Proceedings, 12th International Workshop on Production, properties and interaction of mesons (MESON 2012)*, *EPJ Web Conf.* **37**, 09017 (2012), arXiv:1210.3156 [nucl-ex] .

[129] P. Aguar-Bartolome *et al.* (A2), *Phys. Rev.* **C89**, 044608 (2014), [arXiv:1309.5648 \[hep-ex\]](https://arxiv.org/abs/1309.5648) .

[130] M. Ablikim *et al.* (BESIII), *Phys. Rev.* **D92**, 012001 (2015), [arXiv:1504.06016 \[hep-ex\]](https://arxiv.org/abs/1504.06016) .

[131] B. Kubis and J. Plenter, *Eur. Phys. J.* **C75**, 283 (2015), [arXiv:1504.02588 \[hep-ph\]](https://arxiv.org/abs/1504.02588) .

[132] B. Aubert *et al.* (BaBar Collaboration), *Phys. Rev.* **D74**, 012002 (2006), [arXiv:hep-ex/0605018 \[hep-ex\]](https://arxiv.org/abs/hep-ex/0605018) .

[133] S. Uehara *et al.* (Belle), *Phys. Rev.* **D86**, 092007 (2012), [arXiv:1205.3249 \[hep-ex\]](https://arxiv.org/abs/1205.3249) .

[134] C. Terschlüsen, “diploma thesis,” (2010).

[135] R. I. Dzhelyadin *et al.*, *Phys. Lett.* **B88**, 379 (1979), [JETP Lett.30,359(1979)].

[136] R. I. Dzhelyadin *et al.*, *Sov. J. Nucl. Phys.* **32**, 520 (1980), [Yad. Fiz.32,1005(1980)].

[137] R. Escribano and S. Gonzalez-Solis, (2015), [arXiv:1511.04916 \[hep-ph\]](https://arxiv.org/abs/1511.04916) .

[138] R. Escribano, S. Gonzalez-Solis, P. Masjuan, and P. Sanchez-Puertas, (2015), [arXiv:1512.07520 \[hep-ph\]](https://arxiv.org/abs/1512.07520) .

[139] A. Uras, *Proceedings, International Conference on Strangeness in Quark Matter (SQM 2011)*, *Acta Phys. Polon. Supp.* **5**, 465 (2012), [arXiv:1201.0270 \[hep-ex\]](https://arxiv.org/abs/1201.0270) .

[140] M. N. Achasov *et al.*, *Eur. Phys. J.* **C12**, 25 (2000).

[141] R. R. Akhmetshin *et al.* (CMD-2), *Phys. Lett.* **B605**, 26 (2005), [arXiv:hep-ex/0409030 \[hep-ex\]](https://arxiv.org/abs/hep-ex/0409030) .

[142] M. N. Achasov *et al.*, *Phys. Rev.* **D74**, 014016 (2006), [arXiv:hep-ex/0605109 \[hep-ex\]](https://arxiv.org/abs/hep-ex/0605109) .

[143] M. N. Achasov *et al.*, *Phys. Rev.* **D76**, 077101 (2007), [arXiv:0709.1007 \[hep-ex\]](https://arxiv.org/abs/0709.1007) .

[144] M. N. Achasov *et al.*, *Phys. Rev.* **D90**, 032002 (2014), [arXiv:1312.7078 \[hep-ex\]](https://arxiv.org/abs/1312.7078) .

[145] J. Dudek *et al.*, *Eur. Phys. J.* **A48**, 187 (2012), [arXiv:1208.1244 \[hep-ex\]](https://arxiv.org/abs/1208.1244) .

[146] J. L. Rosner, *Phys. Rev.* **D79**, 097301 (2009), arXiv:0903.1796 [hep-ph].

[147] T. K. Pedlar *et al.* (CLEO), *Phys. Rev.* **D79**, 111101 (2009), arXiv:0904.1394 [hep-ex].

[148] M. Vanderhaeghen and A. Denig, private communication (2016).

[149] P. Adlarson *et al.* (2014) See contribution from C. F. Redmer, arXiv:1412.5451 [nucl-ex].

[150] A. Hoecker, in *51st Rencontres de Moriond on EW Interactions and Unified Theories La Thuile, Italy, March 12-19, 2016* (2016) arXiv:1605.06042 [hep-ex].

[151] D. Babusci, H. Czyz, F. Gonnella, S. Ivashyn, M. Mascolo, R. Messi, D. Moricciani, A. Nyffeler, and G. Venanzoni, *Eur. Phys. J.* **C72**, 1917 (2012), arXiv:1109.2461 [hep-ph].

[152] L. Gan, *Proceedings, 8th International Workshop on Chiral Dynamics (CD 2015)*, PoS **CD15**, 017 (2015).

[153] J. J. Sakurai, *Annals Phys.* **11**, 1 (1960).

[154] J. J. Sakurai, *Currents and mesons*, second printing; 1 ed. (University of Chicago Press, Chicago, 1973).

[155] J. S. R. Chisholm, *Math. Comp.* **27**, 841 (1973).

[156] J. S. R. Chisholm and J. McEwan, *Proc. R. Soc. Lond.* **A336**, 421 (1974).

[157] R. Hughes Jones, *Journal of Approximation Theory* **16**, 201 (1976).

[158] P. R. Graves-Morris, R. Hughes Jones, and G. J. Makinson, *J. Inst. Math. Appl.* **13**, 311 (1974).

[159] A. Cuyt, *Journal of Computational and Applied Mathematics* **32**, 47 (1990).

[160] C. Alabiso and P. Butera, *J. Math. Phys.* **16**, 840 (1975).

[161] P. Guillaume and A. Huard, *Journal of Computational and Applied Mathematics* **121**, 197 (2000).

[162] C. Aubin, T. Blum, M. Golterman, and S. Peris, *Phys. Rev.* **D86**, 054509 (2012), arXiv:1205.3695 [hep-lat].

[163] A. Cuyt, J. Tan, and P. Zhou, *Math. Comp.* **75**, 727 (1990).

- [164] A. Gérardine, private communication (2016).
- [165] N. Isgur, *Phys. Rev.* **D13**, 122 (1976).
- [166] H. Fritzsch and J. D. Jackson, *Phys. Lett.* **B66**, 365 (1977).
- [167] J. F. Donoghue, B. R. Holstein, and Y. C. R. Lin, *Phys. Rev. Lett.* **55**, 2766 (1985), [Erratum: *Phys. Rev. Lett.* 61, 1527 (1988)].
- [168] F. J. Gilman and R. Kauffman, *Phys. Rev.* **D36**, 2761 (1987), [Erratum: *Phys. Rev.* D37, 3348 (1988)].
- [169] A. Bramon and M. D. Scadron, *Phys. Lett.* **B234**, 346 (1990).
- [170] P. Ball, J. M. Frere, and M. Tytgat, *Phys. Lett.* **B365**, 367 (1996), [arXiv:hep-ph/9508359 \[hep-ph\]](https://arxiv.org/abs/hep-ph/9508359) .
- [171] A. Bramon, R. Escribano, and M. D. Scadron, *Phys. Lett.* **B403**, 339 (1997), [arXiv:hep-ph/9703313 \[hep-ph\]](https://arxiv.org/abs/hep-ph/9703313) .
- [172] E. P. Venugopal and B. R. Holstein, *Phys. Rev.* **D57**, 4397 (1998), [arXiv:hep-ph/9710382 \[hep-ph\]](https://arxiv.org/abs/hep-ph/9710382) .
- [173] A. Bramon, R. Escribano, and M. D. Scadron, *Eur. Phys. J.* **C7**, 271 (1999), [arXiv:hep-ph/9711229 \[hep-ph\]](https://arxiv.org/abs/hep-ph/9711229) .
- [174] J. Schechter, A. Subbaraman, and H. Weigel, *Phys. Rev.* **D48**, 339 (1993), [arXiv:hep-ph/9211239 \[hep-ph\]](https://arxiv.org/abs/hep-ph/9211239) .
- [175] R. Kaiser and H. Leutwyler, in *Nonperturbative methods in quantum field theory. Proceedings, Workshop, Adelaide, Australia, February 2-13, 1998* (1998) [arXiv:hep-ph/9806336 \[hep-ph\]](https://arxiv.org/abs/hep-ph/9806336) .
- [176] P. Herrera-Siklody, J. I. Latorre, P. Pascual, and J. Taron, *Phys. Lett.* **B419**, 326 (1998), [arXiv:hep-ph/9710268 \[hep-ph\]](https://arxiv.org/abs/hep-ph/9710268) .
- [177] T. Feldmann, P. Kroll, and B. Stech, *Phys. Lett.* **B449**, 339 (1999), [arXiv:hep-ph/9812269 \[hep-ph\]](https://arxiv.org/abs/hep-ph/9812269) .
- [178] T. Feldmann, *Int. J. Mod. Phys.* **A15**, 159 (2000), [arXiv:hep-ph/9907491 \[hep-ph\]](https://arxiv.org/abs/hep-ph/9907491) .
- [179] M. Benayoun, L. DelBuono, and H. B. O'Connell, *Eur. Phys. J.* **C17**, 593 (2000), [arXiv:hep-ph/9905350 \[hep-ph\]](https://arxiv.org/abs/hep-ph/9905350) .
- [180] A. Bramon, R. Escribano, and M. D. Scadron, *Phys. Lett.* **B503**, 271 (2001), [arXiv:hep-ph/0012049 \[hep-ph\]](https://arxiv.org/abs/hep-ph/0012049) .
- [181] R. Escribano and J. Nadal, *JHEP* **05**, 006 (2007), [arXiv:hep-ph/0703187 \[hep-ph\]](https://arxiv.org/abs/hep-ph/0703187) .

[182] R. Escribano, P. Masjuan, and J. J. Sanz-Cillero, *JHEP* **05**, 094 (2011), arXiv:1011.5884 [hep-ph] .

[183] P. Bickert, P. Masjuan, and S. Scherer, in *8th International Workshop on Chiral Dynamics (CD 2015) Pisa, Italy, June 29-July 3, 2015* (2015) arXiv:1511.01996 [hep-ph] .

[184] X.-K. Guo, Z.-H. Guo, J. A. Oller, and J. J. Sanz-Cillero, *JHEP* **06**, 175 (2015), arXiv:1503.02248 [hep-ph] .

[185] D. Espriu and R. Tarrach, *Z. Phys.* **C16**, 77 (1982).

[186] B. A. Kniehl, A. V. Kotikov, A. I. Onishchenko, and O. L. Veretin, *Phys. Rev. Lett.* **97**, 042001 (2006), arXiv:hep-ph/0607202 [hep-ph] .

[187] J. Bijnens and G. Ecker, *Ann. Rev. Nucl. Part. Sci.* **64**, 149 (2014), arXiv:1405.6488 [hep-ph] .

[188] S. Alte, M. König, and M. Neubert, *JHEP* **02**, 162 (2016), arXiv:1512.09135 [hep-ph] .

[189] C. E. Thomas, *JHEP* **10**, 026 (2007), arXiv:0705.1500 [hep-ph] .

[190] C. Di Donato, G. Ricciardi, and I. Bigi, *Phys. Rev.* **D85**, 013016 (2012), arXiv:1105.3557 [hep-ph] .

[191] V. A. Novikov, M. A. Shifman, A. I. Vainshtein, and V. I. Zakharov, *Nucl. Phys.* **B165**, 55 (1980).

[192] J.-M. Gerard and A. Martini, *Phys. Lett.* **B730**, 264 (2014), arXiv:1312.3081 [hep-ph] .

[193] P. Bickert, P. Masjuan, and S. Scherer, *Phys. Rev.* **D95**, 054023 (2017), arXiv:1612.05473 [hep-ph] .

[194] C. Michael, K. Ott nad, and C. Urbach (European Twisted Mass), *Proceedings, 31st International Symposium on Lattice Field Theory (Lattice 2013)*, PoS **LATTICE2013**, 253 (2014), arXiv:1311.5490 [hep-lat] .

[195] S. Drell, *Nuovo Cim.* **11**, 693 (1959).

[196] S. Berman and D. Geffen, *Nuovo Cim.* **18**, 1192 (1960).

[197] D. A. Geffen and B.-l. Young, *Phys. Rev. Lett.* **15**, 316 (1965).

[198] L. Sehgal, *Nuovo Cim.* **A45**, 785 (1966).

[199] B.-l. Young, *Phys. Rev.* **161**, 1620 (1967).

[200] C. Quigg and J. Jackson, (1968).

[201] L. Bergstrom, E. Masso, L. Ametller, and A. Bramon, *Phys.Lett.* **B126**, 117 (1983).

[202] M. Scadron and M. Visinescu, *Phys.Rev.* **D29**, 911 (1984).

[203] A. Pich and J. Bernabeu, *Z.Phys.* **C22**, 197 (1984).

[204] B. Margolis, J. Ng, M. Phipps, and H. D. Trottier, *Phys.Rev.* **D47**, 1942 (1993), arXiv:hep-ph/9210259 [hep-ph].

[205] E. de Rafael, *Phys.Lett.* **B703**, 60 (2011), arXiv:1107.0226 [hep-ph].

[206] K. Babu and E. Ma, *Phys.Lett.* **B119**, 449 (1982).

[207] A. E. Dorokhov and M. A. Ivanov, *Phys.Rev.* **D75**, 114007 (2007), arXiv:0704.3498 [hep-ph].

[208] A. Dorokhov and M. Ivanov, *JETP Lett.* **87**, 531 (2008), arXiv:0803.4493 [hep-ph].

[209] A. Dorokhov, M. Ivanov, and S. Kovalenko, *Phys.Lett.* **B677**, 145 (2009), arXiv:0903.4249 [hep-ph].

[210] M. J. Savage, M. E. Luke, and M. B. Wise, *Phys.Lett.* **B291**, 481 (1992), arXiv:hep-ph/9207233 [hep-ph].

[211] D. Gomez Dumm and A. Pich, *Phys.Rev.Lett.* **80**, 4633 (1998), arXiv:hep-ph/9801298 [hep-ph].

[212] M. Knecht, S. Peris, M. Perrottet, and E. de Rafael, *Phys.Rev.Lett.* **83**, 5230 (1999), arXiv:hep-ph/9908283 [hep-ph].

[213] P. Herczeg, *Phys.Rev.* **D16**, 712 (1977).

[214] A. Soni, *Phys.Lett.* **B52**, 332 (1974).

[215] L. Bergstrom, *Z.Phys.* **C14**, 129 (1982).

[216] Y. Kahn, M. Schmitt, and T. M. P. Tait, *Phys. Rev. D* **78**, 115002 (2008), arXiv:0712.0007 [hep-ph].

[217] Q. Chang and Y.-D. Yang, *Phys. Lett.* **B676**, 88 (2009), arXiv:0808.2933 [hep-ph].

[218] P. Masjuan and P. Sanchez-Puertas, (2015), arXiv:1504.07001 [hep-ph].

[219] P. Masjuan and P. Sanchez-Puertas, *JHEP* **08**, 108 (2016), arXiv:1512.09292 [hep-ph].

[220] B. Martin, E. De Rafael, and J. Smith, *Phys.Rev.* **D2**, 179 (1970).

[221] L. Ametller, A. Bramon, and E. Masso, *Phys.Rev.* **D30**, 251 (1984).

[222] Z. K. Silagadze, *Phys. Rev.* **D74**, 054003 (2006), arXiv:hep-ph/0606284 [hep-ph].

[223] M. Knecht, *Proceedings, 17th International Conference on Quantum Chromodynamics (QCD 14)*, *Nucl. Part. Phys. Proc.* **258-259**, 235 (2015), arXiv:1412.1228 [hep-ph].

[224] P. Vasko and J. Novotny, *JHEP* **10**, 122 (2011), arXiv:1106.5956 [hep-ph].

[225] T. Husek, K. Kampf, and J. Novotný, *Eur. Phys. J.* **C74**, 3010 (2014), arXiv:1405.6927 [hep-ph].

[226] T. Husek, K. Kampf, and J. Novotny, *Phys. Rev.* **D92**, 054027 (2015), arXiv:1504.06178 [hep-ph].

[227] D. Gomez Dumm, A. Pich, and J. Portoles, *Phys.Rev.* **D62**, 054014 (2000), arXiv:hep-ph/0003320 [hep-ph].

[228] D. Gómez Dumm and P. Roig, *Eur.Phys.J.* **C73**, 2528 (2013), arXiv:1301.6973 [hep-ph].

[229] G. 't Hooft and M. Veltman, *Nucl.Phys.* **B153**, 365 (1979).

[230] R. Mertig, M. Bohm, and A. Denner, *Comput. Phys. Commun.* **64**, 345 (1991).

[231] T. Hahn and M. Perez-Victoria, *Comput.Phys.Commun.* **118**, 153 (1999), arXiv:hep-ph/9807565 [hep-ph].

[232] A. Dorokhov, *JETP Lett.* **91**, 163 (2010), arXiv:0912.5278 [hep-ph].

[233] E. Abouzaid *et al.* (KTeV Collaboration), *Phys.Rev.* **D75**, 012004 (2007), arXiv:hep-ex/0610072 [hep-ex].

[234] G. Agakishiev *et al.* (HADES), *Phys. Lett.* **B731**, 265 (2014), arXiv:1311.0216 [hep-ex].

[235] R. Abegg, A. Baldisseri, A. Boudard, W. Briscoe, B. Fabbro, *et al.*, *Phys.Rev.* **D50**, 92 (1994).

[236] R. R. Akhmetshin *et al.* (CMD-3), *Phys. Lett.* **B740**, 273 (2015), arXiv:1409.1664 [hep-ex].

[237] M. N. Achasov *et al.*, *Phys. Rev.* **D91**, 092010 (2015), arXiv:1504.01245 [hep-ex].

[238] L. Bergstrom, *Z. Phys.* **C20**, 135 (1983).

[239] N. T. Huong, E. Kou, and B. Viaud, (2016), [arXiv:1606.08195 \[hep-ph\]](https://arxiv.org/abs/1606.08195) .

[240] N. T. Huong, E. Kou, and B. Moussallam, *Phys. Rev.* **D93**, 114005 (2016), [arXiv:1511.06255 \[hep-ph\]](https://arxiv.org/abs/1511.06255) .

[241] F. Hagelstein, R. Miskimen, and V. Pascalutsa, *Prog. Part. Nucl. Phys.* **88**, 29 (2016), [arXiv:1512.03765 \[nucl-th\]](https://arxiv.org/abs/1512.03765) .

[242] H.-Q. Zhou and H.-R. Pang, *Phys. Rev.* **A92**, 032512 (2015).

[243] M. J. Ramsey-Musolf and M. B. Wise, *Phys. Rev. Lett.* **89**, 041601 (2002), [arXiv:hep-ph/0201297 \[hep-ph\]](https://arxiv.org/abs/hep-ph/0201297) .

[244] A. Crivellin, G. D'Ambrosio, M. Hoferichter, and L. C. Tunstall, *Phys. Rev.* **D93**, 074038 (2016), [arXiv:1601.00970 \[hep-ph\]](https://arxiv.org/abs/1601.00970) .

[245] A. Antognini *et al.*, *Science* **339**, 417 (2013).

[246] R. Alonso, B. Grinstein, and J. M. Camalich, *JHEP* **10**, 184 (2015), [arXiv:1505.05164 \[hep-ph\]](https://arxiv.org/abs/1505.05164) .

[247] H. Davoudiasl, H.-S. Lee, and W. J. Marciano, *Phys. Rev.* **D85**, 115019 (2012), [arXiv:1203.2947 \[hep-ph\]](https://arxiv.org/abs/1203.2947) .

[248] H. Davoudiasl, H.-S. Lee, and W. J. Marciano, *Phys. Rev. Lett.* **109**, 031802 (2012), [arXiv:1205.2709 \[hep-ph\]](https://arxiv.org/abs/1205.2709) .

[249] C. E. Carlson and B. C. Rislow, *Phys. Rev.* **D86**, 035013 (2012), [arXiv:1206.3587 \[hep-ph\]](https://arxiv.org/abs/1206.3587) .

[250] S. G. Karshenboim, D. McKeen, and M. Pospelov, *Phys. Rev.* **D90**, 073004 (2014), [Addendum: *Phys. Rev.* D90,no.7,079905(2014)], [arXiv:1401.6154 \[hep-ph\]](https://arxiv.org/abs/1401.6154) .

[251] P. A. M. Dirac, *Proc. Roy. Soc. Lond.* **A117**, 610 (1928).

[252] L. E. Kinsler and W. V. Houston, *Phys. Rev.* **45**, 104 (1934).

[253] J. E. Nafe, E. B. Nelson, and I. I. Rabi, *Phys. Rev.* **71**, 914 (1947).

[254] D. E. Nagle, R. S. Julian, and J. R. Zacharias, *Phys. Rev.* **72**, 971 (1947).

[255] G. Breit, *Phys. Rev.* **72**, 984 (1947).

[256] H. M. Foley and P. Kusch, *Phys. Rev.* **73**, 412 (1948).

[257] J. S. Schwinger, *Phys. Rev.* **73**, 416 (1948).

[258] D. Hanneke, S. Fogwell, and G. Gabrielse, *Phys. Rev. Lett.* **100**, 120801 (2008), arXiv:0801.1134 [physics.atom-ph] .

[259] K. A. Olive *et al.* (Particle Data Group), *Chin. Phys. C* **38**, 090001 (2014), see the review “Muon Anomalous Magnetic Moment — A. Hoecker and W.J. Marciano”, pp. 649-652.

[260] P. J. Mohr, B. N. Taylor, and D. B. Newell, *Rev. Mod. Phys.* **84**, 1527 (2012), arXiv:1203.5425 [physics.atom-ph] .

[261] G. F. Giudice, P. Paradisi, and M. Passera, *JHEP* **11**, 113 (2012), arXiv:1208.6583 [hep-ph] .

[262] P. von Weitershausen, M. Schafer, H. Stockinger-Kim, and D. Stockinger, *Phys. Rev. D* **81**, 093004 (2010), arXiv:1003.5820 [hep-ph] .

[263] C. S. Kim, J. D. Kim, and J.-H. Song, *Phys. Lett. B* **511**, 251 (2001), arXiv:hep-ph/0103127 [hep-ph] .

[264] M. Beneke, P. Dey, and J. Rohrwild, *JHEP* **08**, 010 (2013), arXiv:1209.5897 [hep-ph] .

[265] M. Blanke, A. J. Buras, B. Duling, A. Poschenrieder, and C. Tarantino, *JHEP* **05**, 013 (2007), arXiv:hep-ph/0702136 [hep-ph] .

[266] L. B. Okun, Sov. Phys. JETP **56**, 502 (1982), [Zh. Eksp. Teor. Fiz.83,892(1982)].

[267] B. Holdom, *Phys. Lett. B* **166**, 196 (1986).

[268] A. Petermann, *Helv. Phys. Acta* **30**, 407 (1957).

[269] C. M. Sommerfield, *Phys. Rev.* **107**, 328 (1957).

[270] C. M. Sommerfield, *Ann. Phys.* **5**, 26 (1957).

[271] S. Laporta and E. Remiddi, *Phys. Lett. B* **379**, 283 (1996), arXiv:hep-ph/9602417 [hep-ph] .

[272] M. A. Samuel and G.-w. Li, *Phys. Rev. D* **44**, 3935 (1991), [Erratum: Phys. Rev.D48,1879(1993)].

[273] G. Li, R. Mendel, and M. A. Samuel, *Phys. Rev. D* **47**, 1723 (1993).

[274] S. Laporta, *Nuovo Cim.* **A106**, 675 (1993).

[275] S. Laporta and E. Remiddi, *Phys. Lett. B* **301**, 440 (1993).

[276] A. Czarnecki and M. Skrzypek, *Phys. Lett. B* **449**, 354 (1999), arXiv:hep-ph/9812394 [hep-ph] .

[277] T. Aoyama, M. Hayakawa, T. Kinoshita, and M. Nio, *Phys. Rev. Lett.* **109**, 111808 (2012), arXiv:1205.5370 [hep-ph] .

[278] R. Bouchendira, P. Clade, S. Guellati-Khelifa, F. Nez, and F. Biraben, *Phys. Rev. Lett.* **106**, 080801 (2011), arXiv:1012.3627 [physics.atom-ph] .

[279] T. Aoyama, M. Hayakawa, T. Kinoshita, and M. Nio, *Phys. Rev. Lett.* **109**, 111807 (2012), arXiv:1205.5368 [hep-ph] .

[280] K. Fujikawa, B. W. Lee, and A. I. Sanda, *Phys. Rev. D* **6**, 2923 (1972).

[281] A. Czarnecki, B. Krause, and W. J. Marciano, *Phys. Rev. Lett.* **76**, 3267 (1996), arXiv:hep-ph/9512369 [hep-ph] .

[282] M. Knecht, S. Peris, M. Perrottet, and E. De Rafael, *JHEP* **11**, 003 (2002), arXiv:hep-ph/0205102 [hep-ph] .

[283] A. Czarnecki, W. J. Marciano, and A. Vainshtein, *Phys. Rev. D* **67**, 073006 (2003), [Erratum: Phys. Rev.D73,119901(2006)], arXiv:hep-ph/0212229 [hep-ph] .

[284] C. Gnendiger, D. Stöckinger, and H. Stöckinger-Kim, *Phys. Rev. D* **88**, 053005 (2013), arXiv:1306.5546 [hep-ph] .

[285] M. Davier, A. Hoecker, B. Malaescu, and Z. Zhang, *Eur. Phys. J. C* **71**, 1515 (2011), [Erratum: Eur. Phys. J.C72,1874(2012)], arXiv:1010.4180 [hep-ph] .

[286] K. Hagiwara, R. Liao, A. D. Martin, D. Nomura, and T. Teubner, *J. Phys. G* **38**, 085003 (2011), arXiv:1105.3149 [hep-ph] .

[287] K. Hagiwara, A. D. Martin, D. Nomura, and T. Teubner, *Phys. Rev. D* **69**, 093003 (2004), arXiv:hep-ph/0312250 [hep-ph] .

[288] A. Kurz, T. Liu, P. Marquard, and M. Steinhauser, *Phys. Lett. B* **734**, 144 (2014), arXiv:1403.6400 [hep-ph] .

[289] M. Benayoun, P. David, L. DelBuono, and F. Jegerlehner, *Eur. Phys. J. C* **72**, 1848 (2012), arXiv:1106.1315 [hep-ph] .

[290] M. Benayoun, P. David, L. DelBuono, and F. Jegerlehner, *Eur. Phys. J. C* **75**, 613 (2015), arXiv:1507.02943 [hep-ph] .

[291] M. Ablikim *et al.* (BESIII), *Phys. Lett. B* **753**, 629 (2016), arXiv:1507.08188 [hep-ex] .

[292] C. M. Carloni Calame, M. Passera, L. Trentadue, and G. Venanzoni, *Phys. Lett. B* **746**, 325 (2015), arXiv:1504.02228 [hep-ph] .

- [293] C. Aubin and T. Blum, *Phys. Rev.* **D75**, 114502 (2007), arXiv:hep-lat/0608011 [hep-lat] .
- [294] P. Boyle, L. Del Debbio, E. Kerrane, and J. Zanotti, *Phys. Rev.* **D85**, 074504 (2012), arXiv:1107.1497 [hep-lat] .
- [295] M. Della Morte, B. Jager, A. Juttner, and H. Wittig, *JHEP* **03**, 055 (2012), arXiv:1112.2894 [hep-lat] .
- [296] X. Feng, K. Jansen, M. Petschlies, and D. B. Renner, *Phys. Rev. Lett.* **107**, 081802 (2011), arXiv:1103.4818 [hep-lat] .
- [297] D. Nomura and T. Teubner, *Nucl. Phys.* **B867**, 236 (2013), arXiv:1208.4194 [hep-ph] .
- [298] E. de Rafael, *Phys. Lett.* **B322**, 239 (1994), arXiv:hep-ph/9311316 [hep-ph] .
- [299] J. Prades, E. de Rafael, and A. Vainshtein, *Adv. Ser. Direct. High Energy Phys.* **20**, 303 (2009), arXiv:0901.0306 [hep-ph] .
- [300] F. Jegerlehner, *Proceedings, Workshop on Flavour changing and conserving processes 2015 (FCCP2015)*, *EPJ Web Conf.* **118**, 01016 (2016), arXiv:1511.04473 [hep-ph] .
- [301] V. Pauk and M. Vanderhaeghen, *Phys. Rev.* **D90**, 113012 (2014), arXiv:1409.0819 [hep-ph] .
- [302] G. Colangelo, M. Hoferichter, M. Procura, and P. Stoffer, *JHEP* **09**, 091 (2014), arXiv:1402.7081 [hep-ph] .
- [303] G. Colangelo, M. Hoferichter, B. Kubis, M. Procura, and P. Stoffer, *Phys. Lett.* **B738**, 6 (2014), arXiv:1408.2517 [hep-ph] .
- [304] P. Masjuan, *Proceedings, 13th International Workshop on Tau Lepton Physics (TAU 2014): Aachen, Germany, September 15-19, 2014*, *Nucl. Part. Phys. Proc.* **260**, 111 (2015), arXiv:1411.6397 [hep-ph] .
- [305] M. Knecht and A. Nyffeler, *Phys. Rev.* **D65**, 073034 (2002), arXiv:hep-ph/0111058 [hep-ph] .
- [306] T. Blum, S. Chowdhury, M. Hayakawa, and T. Izubuchi, *Phys. Rev. Lett.* **114**, 012001 (2015), arXiv:1407.2923 [hep-lat] .
- [307] J. Green, O. Gryniuk, G. von Hippel, H. B. Meyer, and V. Pascalutsa, *Phys. Rev. Lett.* **115**, 222003 (2015), arXiv:1507.01577 [hep-lat] .
- [308] T. Blum, N. Christ, M. Hayakawa, T. Izubuchi, L. Jin, and C. Lehner, *Phys. Rev.* **D93**, 014503 (2016), arXiv:1510.07100 [hep-lat] .

[309] T. Goecke, C. S. Fischer, and R. Williams, *Phys. Rev.* **D83**, 094006 (2011), [Erratum: Phys. Rev. D86, 099901 (2012)], arXiv:1012.3886 [hep-ph].

[310] G. Colangelo, M. Hoferichter, A. Nyffeler, M. Passera, and P. Stoffer, *Phys. Lett.* **B735**, 90 (2014), arXiv:1403.7512 [hep-ph].

[311] K. Melnikov and A. Vainshtein, *Phys. Rev.* **D70**, 113006 (2004), arXiv:hep-ph/0312226 [hep-ph].

[312] A. Nyffeler, *Phys. Rev.* **D79**, 073012 (2009), arXiv:0901.1172 [hep-ph].

[313] S. Weinberg, *The Quantum theory of fields. Vol. 1: Foundations* (Cambridge University Press, 2005).

[314] A. Nyffeler, (2016), arXiv:1602.03398 [hep-ph].

[315] P. Masjuan and P. Sanchez-Puertas, *Phys. Rev.* **D95**, 054026 (2017), arXiv:1701.05829 [hep-ph].

[316] J. Bijnens, E. Pallante, and J. Prades, *Nucl. Phys.* **B474**, 379 (1996), arXiv:hep-ph/9511388 [hep-ph].

[317] J. Bijnens, E. Pallante, and J. Prades, *Nucl. Phys.* **B626**, 410 (2002), arXiv:hep-ph/0112255 [hep-ph].

[318] M. Hayakawa and T. Kinoshita, *Phys. Rev.* **D57**, 465 (1998), [Erratum: Phys. Rev. D66, 019902 (2002)], arXiv:hep-ph/9708227 [hep-ph].

[319] A. Nyffeler, *Proceedings, 6th International Workshop on Chiral dynamics*, PoS **CD09**, 080 (2009), arXiv:0912.1441 [hep-ph].

[320] B. Moussallam, *Phys. Rev.* **D51**, 4939 (1995), arXiv:hep-ph/9407402 [hep-ph].

[321] G. Ecker, P. Masjuan, and H. Neufeld, *Eur. Phys. J.* **C74**, 2748 (2014), arXiv:1310.8452 [hep-ph].

[322] E. R. Arriola, W. Broniowski, and P. Masjuan, *Proceedings, Conference on Modern approaches to nonperturbative gauge theories and their applications (Light Cone 2012)*, (2012), 10.5506/APhysPolB-Supp.6.95, [Acta Phys. Polon. Supp. 6, 95 (2013)], arXiv:1210.7153 [hep-ph].

[323] V. Pauk and M. Vanderhaeghen, *Eur. Phys. J.* **C74**, 3008 (2014), arXiv:1401.0832 [hep-ph].

- [324] P. Masjuan and M. Vanderhaeghen, *J. Phys. G***42**, 125004 (2015), [arXiv:1212.0357 \[hep-ph\]](https://arxiv.org/abs/1212.0357) .
- [325] C. C. Nishi, *Am. J. Phys.* **73**, 1160 (2005), [arXiv:hep-ph/0412245 \[hep-ph\]](https://arxiv.org/abs/hep-ph/0412245) .